Structure and Dynamics at Colloidal Boundaries

Universiteit Utrecht

ISBN 978-90-393-4763-8

Subject headings: colloids/interfaces/confocal microscopy/crystal defects/hydrodynamics.

Structure and Dynamics at Colloidal Boundaries

Structuur en Dynamica bij Colloïdale Grensvlakken

(met een samenvatting in het Nederlands)

Proefschrift

ter verkrijging van de graad van doctor aan de
Universiteit Utrecht op gezag van de rector magnificus,
Prof. dr. J.C. Stoof, ingevolge het besluit van het
college voor promoties in het openbaar te verdedigen
op 19 maart 2008 des middags te 16.15 uur

door

Jonkheer Volkert Willem Alexander de Villeneuve

geboren op 20 februari 1979 te Leidschendam

Promotoren: Prof. dr. H.N.W. Lekkerkerker

Prof. dr. W. K. Kegel

Co-promotor: Dr. A.V. Petukhov

This work is part of the research programme of the 'Stichting voor Fundamenteel Onderzoek der Materie (FOM)', which is financially supported by the 'Nederlandse Organisatie voor Wetenschappelijk Onderzoek (NWO)'.

In the field of observation, chance favours only the prepared mind.– Louis Pasteur

Cover: Artist impression of a sphere moving through an interface, as in Chapter 11

List of publications

This thesis is based on the following publications

- J.M. Meijer, V.W.A. de Villeneuve and A.V. Petukhov, In-Plane Stacking Disorder in Polydisperse Hard Sphere Crystals, Langmuir 23 (7) (2007) 3554 - 3560 (Chapter 2)
- V.W.A. de Villeneuve, P.S. Miedema, J.M. Meijer and A.V. Petukhov. Grain size effects on lateral islands in hard-sphere crystals, Eur. Phys. Lett. 79 (2007) 56001 (Chapter 2 and Chapter 4)
- V.W.A. de Villeneuve, D. Verboekend, R.P.A. Dullens, D.G.A.L. Aarts, W.K. Kegel and H.N.W. Lekkerkerker, Hard sphere crystal nucleation and growth near large spherical impurities, J. Phys.: Condens. Matter 17, S3371 (2005)(Chapter 5)
- V. W.A. de Villeneuve, R. P.A. Dullens, D. G.A.L. Aarts, E. Groeneveld, J. H. Scherff, W. K. Kegel and H. N.W. Lekkerkerker, Hard Sphere Crystal Growth Frustrated by Large Spherical Impurities, Science, 309, 1231-1233, (2005) (Chapter 5 and Chapter 6)
- V.W.A. de Villeneuve, D.G.A.L. Aarts and H.N.W. Lekkerkerker, Comparing the approach of a rigid sphere and a deformable droplet towards a deformable fluid surface, Colloids and Surfaces A: Physicochem. Eng. Aspects 282-283 61-67 (2006) (Chapter 9)
- V.W.A. de Villeneuve, J.M.J. van Leeuwen J.W.J. de Folter, D.G.A.L. Aarts, W. van Saarloos and H.N.W. Lekkerkerker, Residence and Waiting Times of Brownian Interface Fluctuations, Accepted for publication in Eur. Phys. Lett. (Chapter 8)
- V.W.A. de Villeneuve, A.B.G.M. Leferink op Reinink, J.M. Meijer, A.V. Petukhov and P. Schall, Localisation of Vacancies and Stacking Transitions in Close Packed Crystals, submitted to Eur. Phys. J. E: Soft Matter. (Chapter 3)
- R.P.A. Dullens, V.W.A. de Villeneuve, M.C.D. Mourad, A.V. Petukhov and W.K. Kegel, Structural Arrest in geometrically frustrated systems, Submitted to Eur. Phys. J. App. Phys (Chapter 7)
- V.W.A. de Villeneuve, A.B.G.M. Leferink op Reinink and A.V. Petukhov, In-Plane Stacking Disorder in Hard Sphere Crystals Part II: Continuous Transitions, to be submitted. (Chapter 3)
- V.W.A. de Villeneuve, R.P.A. Dullens, L. Derendorp, D. Verboekend, E.C.M. Vermolen, Willem K. Kegel and Henk N.W. Lekkerkerker, Grain Boundary Pinning in doped Hard Sphere Crystals, to be submitted (Chapter 6)

- V.W.A. de Villeneuve, J.M.J. van Leeuwen W. van Saarloos and H.N.W. Lekkerkerker, Statistics of Fluctuating Colloidal Fluid-Fluid Interfaces, to be submitted to J. Chem. Phys. (Chapter 8)
- V.W.A. de Villeneuve, J.W.J. de Folter, D.G.A.L. Aarts and H.N.W. Lekkerkerker, The transport of a wettable sphere through a fluid-fluid interface, to be submitted (Chapter 10)
- V.W.A. de Villeneuve, J.W.J. de Folter, D.G.A.L. Aarts and H.N.W. Lekkerkerker, The transport of a wettable sphere through a fluid-fluid interface at low and high Bond numbers, to be submitted (Chapters 10 and 11)

Other publications by the author

- G.H. Koenderink, D.G.A.L. Aarts, V.W.A. de Villeneuve, A.P. Philipse, R. Tuinier, and H.N.W. Lekkerkerker, Morphology and kinetics of phase separating transparent xanthan-colloid mixtures, Biomacromolecules, 4, 129-136, (2003)
- Nikoleta B. Simeonova, Roel P.A. Dullens, Dirk G.A.L. Aarts, Volkert W.A. de Villeneuve, Henk N.W. Lekkerkerker, and Willem K. Kegel, Devitrification of colloidal glasses in real-space, Phys. Rev. E 73, 041401-1-5,(2006)
- P.S. Miedema , Volkert W. A. de Villeneuve and A.V. Petukhov, Monte Carlo Simulations of In-Plane Stacking Disorder, Phys. Rev. E 77, 010401(R) (2008)
- Matti M. van Schooneveld, Volkert W. A. de Villeneuve, Roel P.A. Dullens, Dirk G.A.L. Aarts, Miriam L. Leunissen, and Willem K. Kegel, Formation and Collapse Dynamics of Colloidal Gels, Submitted to Phys. Rev. E
- H.N.W. Lekkerkerker, V. W. A. de Villeneuve, J.W.J. de Folter, M. Schmidt, Y. Hennequin, D. Bonn, J.O. Indekeu and D.G.A.L. Aarts, the interface in phase separated colloid-polymer mixtures, submitted to Eur. Phys. J. B

Contents

1

Introduction

1.1. Boundaries

A physical boundary separates two regions with distinctly different properties. A common example in everyday life is the interface between water and air. Clearly, the physical properties of the water and air phases, such as the density and chemical composition, are very different. More subtle boundaries occur in crystals: the grain boundary, for example, separates two crystallites which may differ in as little as the crystallite orientation, whereas a stacking fault separates two regions with different packing geometries. But boundaries are not necessarily two dimensional: within a crystal plane for example, one dimensional boundaries may separate regions with a different stacking environment [1].

Macroscopically, boundaries appear sharp. Van der Waals was the first to describe the (gas-liquid) interface in terms of a density profile [2], thereby assigning a finite width to a boundary. Fourteen years later, von Smoluchowski first realized that the interfacial height should locally fluctuate in time as well due to the Brownian motion of the particles that make up the interface [3]. Inspired by von Schmoluchowski's ideas, Mandelstam first quantitatively described this roughness [4].

In atomic and molecular systems, both the finite size and roughness of interface only become apparent on length scales of order of the particle diameter. Although this width is finite, it is not easily accessible in experiments, especially in real-space and real-time. This is where colloids come in as a well established model system for statistical physics and soft condensed matter.

In the remainder of this introduction we will first generally introduce colloids as a model system in 1.2. We will proceed by describing the two colloidal model systems

described in this thesis: hard spheres (1.3) and colloid-polymer mixtures (1.4). In 1.5 the main technique used in this thesis - confocal microscopy - is presented before we finish in 1.6 with an outline of the remainder of this thesis.

1.2. Colloids - Designer Atoms

The International Union of Pure and Applied Chemistry defines colloids as follows:

The term colloidal refers to a state of subdivision, implying that the molecules or polymolecular particles dispersed in a medium have at least in one direction a dimension roughly between 1 nm and 1 μm, or that in a system discontinuities are found at distances of that order.

The definition sets the length scale for colloids: significantly larger than atoms, which are of the order of 10^{-10} m, but small enough for the gravitational forces to be balanced by thermal energy and significantly larger than the solvent molecules they are suspended in. Wilson Poon adequately describes the potential that the intrinsic time and length scales of colloidal systems offer to the experimentalist: colloids are slow, soft and seeable [5]. The particle dynamics are sufficiently slow enough to study the dynamics and kinetics of a system. The systems have soft, mouldable potentials. They are large enough to be observed on a single particle basis by microscopic methods. Colloid scientists have an immense toolkit [6] at their disposal. Through state of the art synthesis methods the size and shape, size and size distribution of the colloids can be tailored to one's needs. By adding ions or non-adsorbing polymers charge repulsion and depletion attraction can be added to the effective potential. By changing the right solvent (mixture) the density difference between the colloids and the solvent as well as the refractive index mismatch may be controlled, effectively tuning the gravitational and dispersion forces. Finally optical, magnetic and electric external fields can be applied.

One characteristic that makes (experimental) colloids fundamentally different from atoms is that they have a size distribution. This in itself can affect the phase behaviour, for example by size fractionation as an inherent part of phase separation [7], or by preventing ordered phases from forming altogether.

In this thesis, two types of colloidal systems are studied. In the first two parts of this thesis the simplest system with a phase transition is investigated, the hard sphere. In the last two parts phase separated colloid-polymer mixtures are studied. We will introduce these two systems before we sketch the outline of this thesis.

1.3. Hard Spheres

The hard sphere is the simplest conceivable system that can undergo a phase transition: the fluid-crystal transition. Hard spheres have an interaction potential that is infinitely repulsive at distances shorter than the particle diameter and zero at distances

beyond. The potential results in excluded volume interactions only, which are entirely entropic (Fig. 1.1B). The phase diagram is athermal and only depends on the volume fraction of spheres ϕ_c.

The mere existence of a phase transition in this purely repulsive system was a topic of hot debate for years until computer simulations by Alder and Wainwright and Wood and Jacobson established that hard spheres undergo a freezing transition at sufficiently high densities [8,9] when the free volume entropy in the ordered crystal state outweighs the configurational entropy for a random configuration. Hoover and Ree were eventually able to overcome finite size limitations and establish the freezing and melting transitions which occur at volume fractions of $\phi_c = 0.494$ and $\phi_c = 0.545$ [10], as schematically shown in Fig. 1.1A. Although exact quantitative descriptions of the hard sphere fluid have not been found so far, accurate descriptions of the hard sphere fluid [11] and solid [12] have been determined from simulations.

An important experimental realization of hard sphere phase behaviour was reported in the classic work by Pusey and van Megen [13]. They are realized through for example sterically stabilized polymethyl methacrylate [14] or silica [15] particles. These particles can be made sufficiently large to be studied in real space by modern microscopy methods. By refractive-index matching the particles with the solvent they are suspended in, van der Waals interactions can be minimized. Experiments show that these particles are indeed a very good experimental approximation of the hard sphere, with a potential that drastically increase from nearly 0 to many orders of magnitude higher within a few nanometres [16], which is maximally a few percent of a colloid diameter. Furthermore, measurements of thermodynamic properties of these systems match very well with those found theoretically [17].

When a hard sphere suspension is rapidly quenched (for example by sedimentation) to a volume fraction of $\phi_c = 0.58$-0.64 a non-equilibrium glassy state is obtained (Fig. 1.1A), in which the particles are caged by their neighbours [18], although the glassy state is reportedly absent under microgravity [19]. The hard sphere crystal structure is made up of close packed hexagonal layers, with a maximum packing fraction of $\pi/(3\sqrt{2}) \approx 0.74$, as was proved only recently [20, 21]. Starting at a lateral position A of a particle within such a layer, the neighbouring particles in the layer above it may be either located at B or C positions. Both ABA and ABC types of stacking sequences may be observed, which correspond to the hexagonal close packed structure (HCP) and the face centred cubic (FCC) structures, see Fig. 1.1C. The FCC structure has a higher symmetry than HCP, but the free energy difference between FCC and HCP is tiny [22–24]: less than $10^{-3}k_BT$ per particle, with k_B the Boltzmann constant and T the Kelvin temperature. Conversely, the interfacial tension in between the HCP and FCC crystals, which is the excess free energy per unit area, is vanishingly small: roughly $\gamma \sim 3 \cdot 10^{-4}k_BT/\sigma_c^2$ [25], with σ the particle diameter. This may contribute to

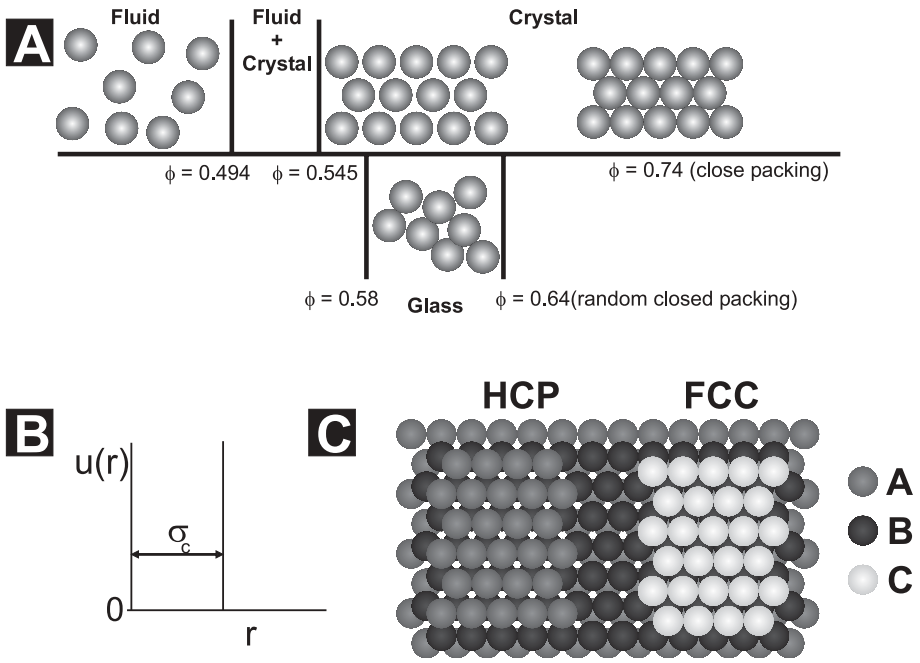

Figure 1.1. (A) The hard sphere phase diagram with the fluid and crystal phases and the non-equilibrium glassy phase. (B) The hard sphere pair interaction potential. (C) The two available close-packed structures for hard spheres: FCC (ABC type stacking) and HCP (ABA type stacking)

the frequent observation of so-called random-hexagonal close-packed (RHCP) crystal structures [26–30]. Due to the variety of possible RHCP configurations, an additional gain in entropy can stabilize the RHCP structure for sufficiently small crystals [31], although a flat wall seems to promote the FCC structure [32]. The reorganization from RHCP to FCC structure is expected to take months to years for experimental systems [25, 28]. The defects observed in these crystals are highly similar to those observed in close packed metals: vacancies, interstitials, (partial) dislocations, stacking faults and grain boundaries are all observed [1]. The low stacking fault energy [25] does affect the structure of the partial dislocations [33] which do not occur in pairs, but usually extend until the grain boundary. Moreover, kinetics may strongly increase the amount of point defects observed on an experimental time-scale and slow down the nucleation and growth processes as well [34], frequently resulting in the observation of relatively small grains in experiments. The defect structure is an important component of the first two parts of this thesis and will be introduced in more detail there.

1.4. Colloid-Polymer Mixtures

As mentioned in section 1.2, the colloid-colloid interaction potential can be engineered into a wide variety of interaction potentials. An effective attraction can be included by adding non-adsorbing polymer to the dispersion. This attraction between

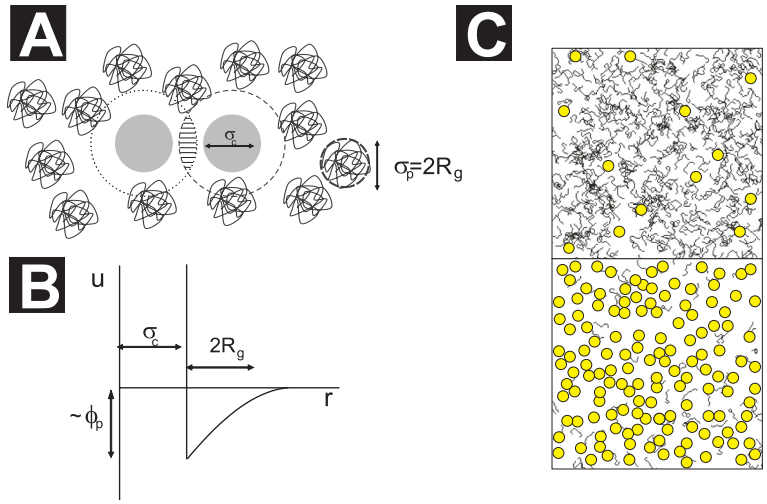

Figure 1.2. Depletion induced attraction between colloids. (A) Two nearby colloids with diameters σ_c in a sea of polymers with radius of gyration R_g. The centres of the polymers are depleted from the dashed depletion zone around the colloids. (B) Schematic representation of the depletion interaction potential, which is remarkably similar to a Lennard-Jones potential. Its depth depends on the colloid concentration, its range on the radius of gyration of the polymer. (C) By tuning the colloid-to-polymer size ratio and at the correct concentrations, colloid-polymer mixtures may phase separate in a colloid-rich and a polymer rich phase.

the colloids originates from the depletion attraction induced by the polymers. Around the colloids there is a zone entropically depleted of polymers ('the depletion zone'). If two colloids are sufficiently close such that these zones overlap, the resulting osmotic pressure imbalance pushes the particles together, as sketched in Fig. 1.2A. This phenomenon was first described by Asakura and Oosawa [35, 36] and later independently by Vrij [37]. The resulting interaction potential can be made remarkably similar to a Lennard-Jones potential (Fig. 1.2B). The depth of the attraction can be tuned by varying polymer volume fraction ϕ_p, the range of the interaction depends on the radius of gyration R_g of the polymer, which is a function of the molar weight of the polymer. At the proper colloid and polymer concentrations, three types of phases can in principle co-exist: a colloid-poor-polymer-rich phase (colloidal gas), a disordered colloid-rich-polymer-poor phase (colloidal liquid), and an ordered colloid-rich-polymer-poor phase (colloidal solid). In this thesis we will only consider one interface in colloid-polymer mixtures: the interface in between the colloidal gas and the colloidal liquid. These are widely accepted analogues of the gas-liquid interface in molecular systems [38]. For a liquid-gas phase separation, the depletion interaction needs to be at least of order of the thermal energy k_BT. Furthermore, the range of attraction should be of order of a particle diameter. It turns out that the minimum polymer to colloid diameter ratio for

liquid-gas phase separation to occur is $q = 2R_g/\sigma_c \geq 0.3$ [39]. For such interfaces, the interfacial tension becomes: The interfacial tension γ, far from the critical point follows the scaling relation [40, 41]:

$$\gamma \approx \frac{\epsilon}{\sigma^2} = \frac{k_B T}{\sigma^2} \tag{1.1}$$

with ϵ the interaction between the particles. Here ϵ is entropic and thus of order $k_B T$. Since the dimension of a colloid is much larger than that of an atom, the interfacial tension is lowered from the mN/m to the μN/m range or lower, and has been measured [42–45]. A powerful aspect of this low interfacial tension is that the interfacial roughness both in the directions perpendicular and parallel to the interface are of the order of a micrometer and the typical decay time is of the order of a second [42], as will be extensively described in Chapter 8. The roughness therefore is directly observable by microscopy, enabling a direct comparison with capillary wave theory, as in the third part of this thesis. This offers the possibility of investigating the effect of thermal fluctuations on a variety of processes [46, 47], which will be an important part of the final part of this thesis.

1.5. Laser Scanning Confocal Microscopy of Colloidal systems

The use of microscopy as a tool to extract physical quantities from particle positions dates back to Nobel Prize winner Jean Baptiste Perrin. Perrin's derivation of the Boltzmann constant from such data [48, 49], based on Einstein's seminal ideas [50] is considered to be the first proof of the existence of atoms. Presently, the existence of three-dimensional (3D) laser scanning confocal microscopy and modern algorithms that enable fast tracking of particle positions [51] and orientations [52], create possibilities that probably were beyond Perrin's wildest dreams at the time. The first such studies date from the early nineties [53, 54]. Particles with a fluorescent core and a non-fluorescent shell around it [15, 55] were an important development, resulting in an improved separation of intensity signal. 3D confocal microscopy has been used extensively in studies of for example phase transitions, interfaces and defect dynamics [17, 33, 56–60]. Interfacial phenomena have also been studied for somewhat smaller particles which are not identifiable individually [42, 61]. In these studies, the increased contrast of confocal microscopy is used to very accurately determine the local interfacial position. For a recent review of confocal microscopy of colloids see [62].

Laser scanning confocal microscopy is an optical imaging technique, which, compared to conventional optical microscopy, offers an increased contrast and the possibility to construct of 3D images by using a spatial pinhole to eliminate out-of-focus light. Marvin Minsky developed confocal microscopy as early as in 1957 ([63], but it took another 16 years before intense laser light sources enabled the construction of a laser scanning confocal microscope [64]. The technique became commercially available in the late eighties

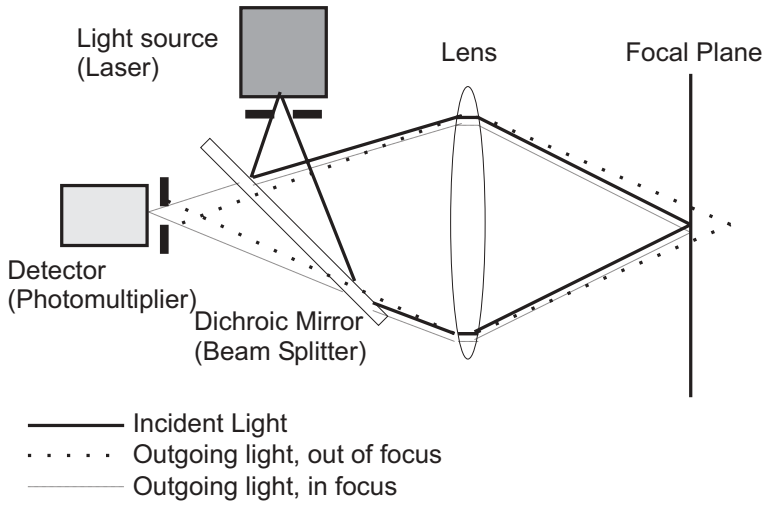

Figure 1.3. Schematic illustration of the optics of a confocal microscope. The thick solid line is incident light, the thin solid line is outgoing light (which should partly coincide with the incoming light beam, but are drawn slightly apart for clarity's sake). The dotted lines represent out of focus light that does not reach the detector. The beam splitter is a dichroic mirror that reflects the incident wavelength, whereas the outgoing wavelength passes through it.

of the previous century and was initially used for biological applications. Extensive reviews can be found in e.g. [65–67]. Here we describe the basic principle.

The principle of confocal microscopy is sketched in Fig. 1.3A. The incoming light beam passes through a pinhole to create a point source. The light is focused by an objective lens to a (diffraction limited) spot in the sample. The light originating from this illuminated spot is subsequently focused by an identical lens onto the second detector pinhole. The detector pinhole is positioned exactly at the focal plane conjugate to the imaged spot (hence the name confocal microscopy), such that the majority of light originating elsewhere in the sample does not pass through the detector pinhole. The signal corresponding to the in-focus spot of a sample reaches the (point-)detector, usually a photo multiplier tube. The lateral scanning of such points within the focal plane results in a two-dimensional (2D) cross-section image of the plane of focus. The laser as a light source improves the ability of 3D imaging. The advantages of confocal microscopy over conventional microscopy can be conveniently quantified through the point spread function $p(\rho, \zeta)$, with ρ and ζ the radial and axial optical coordinates. The optical coordinates are obtained from the radial and axial coordinates around the optical axis r and z through $\rho = r2\pi NA/\lambda$ and $\zeta = z2\pi NA^2/(n\lambda)$, where NA is the numerical aperture, λ the wavelength of the light in vacuum, and n the index of refraction of the medium. The numerical aperture $NA = n\sin(\alpha)$, with α half the angle of the cone of light passing through the objective [66]. The radial and axial limits of

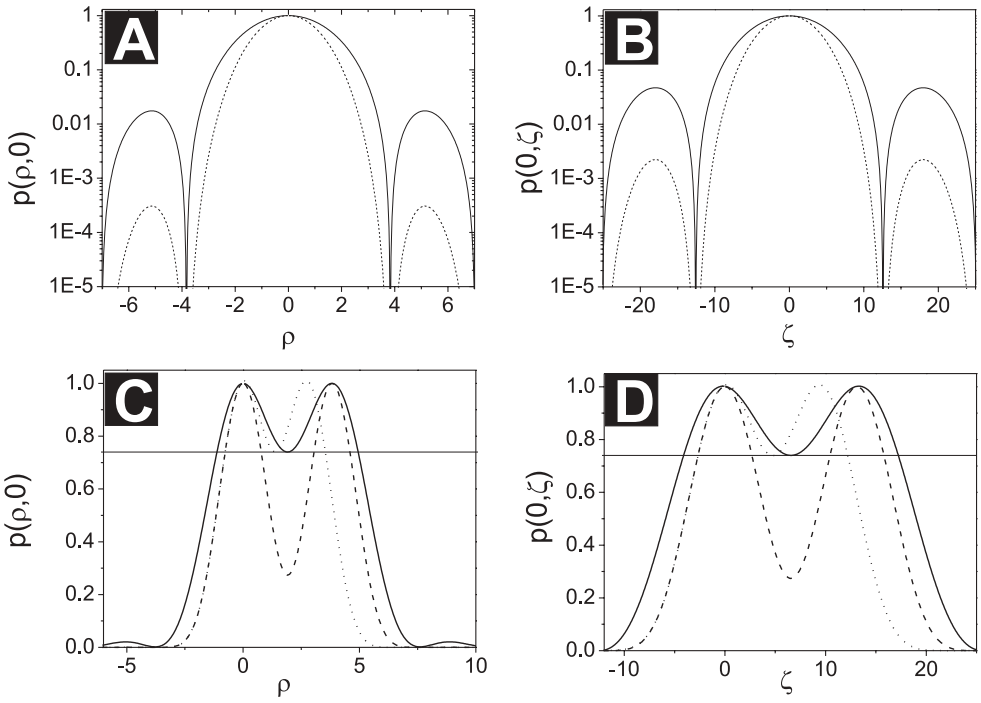

Figure 1.4. Point spread functions. For (A) and (B) the solid lines are the PSFs for regular microscopy, the dashed lines are the PSF for confocal microscopy. (A) Radial PSF $p(\rho, 0)$ for both regular and confocal microscopy. (B) Axial PSF $p(\zeta, 0)$ for both regular and confocal microscopy. Both the radial and axial PSF functions decay much faster for confocal microscopy. The subsequent two figures illustrate the Rayleigh criterion for the radial (C) and axial (D) PSF, which is based on two nearby sources. Solid lines are for regular microscopy and dashed lines for confocal microscopy, both separated by the Airy disk. The increased contrast for confocal microscopy is striking. Dashed lines are for two sources separated by the Rayleigh criterion distance for confocal microscopy, which illustrates the increased resolution. The flat solid lines at $p = 0.74$ indicate the Rayleigh criterion height.

$p(\rho, \zeta)$ are given by:

$$p(\rho, 0) = \left(\frac{2J_1(\rho)}{\rho} \right)^4 \tag{1.2}$$

with J_1 the Bessel function of the first kind and

$$p(0, \zeta) = \left(\frac{\sin(\zeta/4)}{\zeta/4} \right)^4 \tag{1.3}$$

Compared to the point spread function for regular microscopy the function is squared, which is a consequence of passing the objective twice. The Airy disc is the location where the $p(\rho, \zeta)$ first drops to zero ($p(\rho_{airy}, 0) = 0; p(0, \zeta_{airy}) = 0$), see Fig. 1.4A and B.

Table 1.1. Microscopy resolutions in the experimental systems described in this thesis. All lengths are in nm.

	regular		**confocal**	
wavelength	radial	axial	radial	axial
408	177	652	128	474
488	212	780	153	566

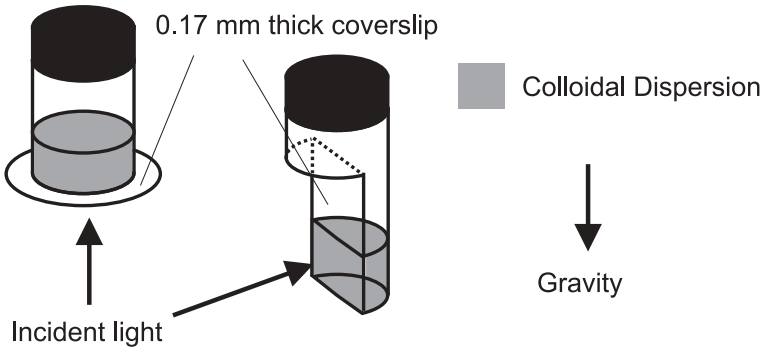

Figure 1.5. The cuvettes used throughout this thesis. They are made of small vials, part of which is sawed of and replaced by a thin cover slip, enabling high resolution microscopy.

By positioning another source at the Airy disc, a minimum occurs in between the two sources. For regular microscopy methods, this minimum is 26% lower than the maxima of the point spread functions, as indicated by the lines in Fig. 1.4C and D. The spacing in between the two point spread functions for which this 26% decrease occurs is the definition of the Rayleigh criterion, a common measure of the resolution of a microscopic method. For regular microscopy, the Airy disc resolutions are $\rho = 3.82$ and $\zeta = 13.12$. Confocal microscopy clearly higher resolutions with $\rho = 2.76$ and $\zeta = 9.53$. For the systems described in this thesis, $n \approx 1.5$, $NA = 1.4$, λ is either 408 or 488 nm. The resolutions are given in table 1.1 The improvement in resolution is highly significant, but the increase in contrast is even more powerful. The secondary maximum in $p(\rho, \zeta)$ is decreased by nearly 2 orders of magnitude (Fig. 1.4A and B), and the minimum at the Airy disc distance is decreased by roughly a factor three (Fig. 1.4C and D). The signal-to-noise ratio therefore is considerably higher. By matching the refractive index of the probe with that of the surrounding fluid, scattering is strongly suppressed of illuminating light even further, essentially limiting the depth of focus to the working distance of the objective, typically a few hundred microns.

Two main types of glass cuvettes have been used in microscopy with the focal plane either perpendicular or parallel to the direction of gravity, fabricated by the glass workshop. The sample containers are small vials, part of which is sawed off and replaced by

a 0.17 mm thick cover slip, see figure 1.5, allowing the use of high NA oil-immersion objectives and thus high resolutions.

Although they will not be described in this thesis, the evolution high speed spinning disc and swept field confocal microscopes has already opened up more experimental possibilities. At the same time the challenge to increase the lateral resolution even further is progressing as well with promising methods such as structured illumination microscopy [68].

1.6. Outline of this thesis

This thesis consists of four main parts. The first part deals with stacking disorder in hard sphere crystals. The second part deals with geometrically frustrated hard sphere crystals. The third part describes the statistics of Brownian interface fluctuations in phase-separated colloid-polymer mixtures. The final part of this thesis deals with the transport of particles through such an interface.

In the first part of this thesis we study stacking disorder in hard sphere crystals. Due to the small difference in free energy between the HCP and FCC crystal configurations, both structures can coexist within these crystals. As a result the crystals are often made up of a random combination of ABA and ABC type stacking sequences of hexagonal layers. Chapters 2 and 3 describe in-plane stacking disorder in hard sphere crystals. Here, we show that stacking can change as well within a hexagonal layer, both via abrupt transitions through line-defects (Chapter 2) and via continuous transitions through lattice deformations (Chapter 3). Therefore the hexagonal layers are made up of multiple islands of FCC or HCP stacking type. In Chapter 3 the relation between lattice vacancies and stacking transitions is investigated as well. Due to the osmotic pressure imbalance, particles are pushed slightly toward the vacancy. Furthermore, in areas where lattice deformations occur due to stacking transitions, the vacancy concentration is much higher, allowing the accommodation of lattice deformations. Chapter 4 describes the relation between grain size and typical stacking island dimension. Using methods to distinguish both the stacking type and the stacking direction, we are able to identify the typical island dimension. The fraction of FCC type particles determines the relative size of FCC and HCP type islands, which we can relate to lateral islands with an A, B or C type lateral position through simulations.

The second part of this thesis describes how geometry affects hard sphere crystals and crystallization. Chapter 5 describes the crystallization of hard spheres near large, nearly immovable objects: much larger spheres, which are in a way the simplest conceivable impurities or dopants. Crystal nucleation, the initial formation of sufficiently large crystals may be facilitated if the curvature of the dopant is sufficiently low. The subsequent crystal growth of these small crystals is retarded by the presence of impurities, but due to their high curvature, small impurities slow the crystal growth much

more down than larger ones. Chapter 6 deals with the obtained crystal structure after crystallization has completed. We introduce a frustration length which quantifies the extent of lattice distortion depending on the size of the dopants. If the dopants are sufficiently close, we show that grain boundaries may form in between directly, which is a result of the delayed growth process in between the impurities. Whether the frustration lengths persist in the sample or slowly anneal out on time depends on the impurity spacing. Chapter 7 compares lattice frustration by two methods: 1) the insertion of impurities and 2) a polygonal particle shape. Both sources of lattice frustration induce polycrystallinity.

The third part of this thesis concerns the liquid-liquid interface of phase separated colloid polymer mixtures. Such interfaces are characterised by large interface fluctuations due to the low interfacial tension γ. Experiments and theory on the residence time of a certain fluctuation above a certain height and the related waiting time in between such heights are presented in Chapter 8.

In the final part of this thesis the transport of rigid spheres through such a fluctuating interface is presented. In Chapter 9 we compare the approach of droplets and spheres to a deformable interface. The similarity of the problems shows that the approach of the sphere already captures much of the physics of the more complicated approach of a droplet. The transport of rigid spheres through interfaces is the subject of Chapters 10 and 11. We distinguish between low Bond numbers (Chapter 10) and high bond numbers (Chapter 11), which respectively represent the limits of dominant interfacial tension and gravity. The low Bond number transport configuration is characterized by a draining film in between the sphere and the interface. In the meantime the interface deforms up to maximally about half the sphere's diameter. When the sphere is sufficiently close, it is wetted by the interface and dragged through it, before it starts sedimenting away again. The high Bond number transport configuration is characterized by a thin film of gas which persists around the sphere, while the interface deforms more than half a sphere's diameter. Depending on the Bond number, two scenarios may be observed. At moderate Bond numbers the sphere leaves a V-shaped interface behind. At even higher Bond numbers, the sphere drags a column of material of the phase it was originally in behind it that eventually breaks up through a Rayleigh-Plateau instability.

Part 1

In-Plane Stacking Disorder in Hard Sphere Crystals

2

Lateral Stacking Disorder in Hard-Sphere Crystals

Part 1: Discontinuous Transitions

Abstract

We demonstrate that randomly stacked hard-sphere colloidal crystals do not merely consist of random sequences of hexagonally close-packed layers, but also of islands within the hexagonal layers with different lateral positions A, B and C. The existence of such in-plane stacking disorder was suggested by a recent observation of lateral broadening of the Bragg scattering rods in micro radian X-ray diffraction and is further confirmed here by real-space confocal microscopy in two hard-sphere colloidal systems with different sedimentation Peclet numbers. The transition from one lateral position to the other either occurs discontinuously through line-defects or continuously in a bridging area through a lattice deformation and results in transitions between hexagonally close packed and face centered cubic structures. The subsequent chapter is dedicated to the continuous transitions. In this chapter the discontinuous line-defects are characterized, up to their 3-D structure. The chance ζ to find another line-defect above a line-defect in the layer below turns out to be close to $\frac{1}{2}$ – independent of relative gravity – which can be explained by the two different stacking options above a defect. The stacking of a few sets of several line-defects situated on top of each other turns out to be predominantly FCC-like.

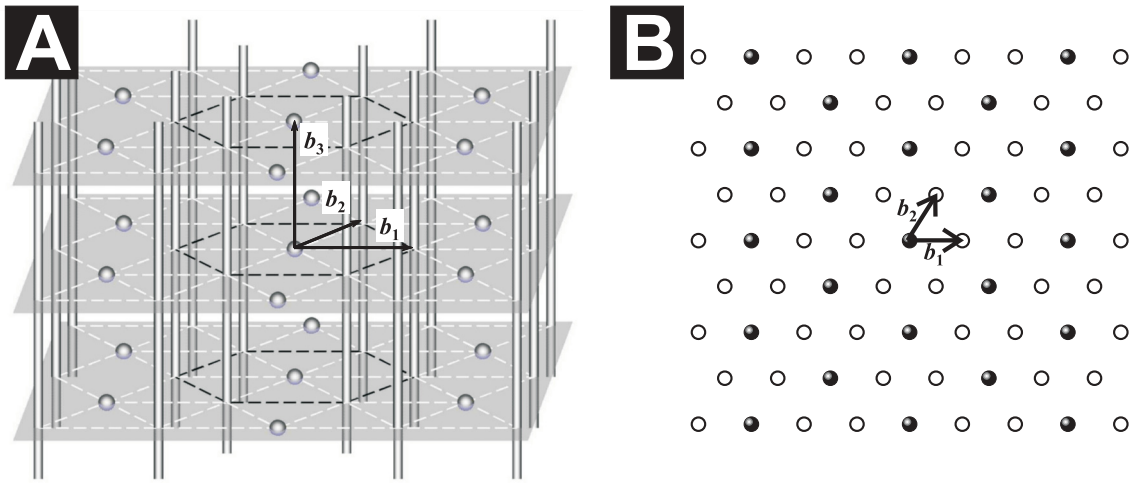

Figure 2.1. (A) Sketch of the reciprocal lattice of randomly stacked hexagonal close-packed crystals. The shadowed planes are to guide the eye. (B) Top view of the reciprocal lattice. The closed symbols correspond to lines of localized reflections (spots) while the open symbols display the position of rods.

2.1. Introduction

The formation of defect structures, such as stacking faults, grain boundaries and vacancies is inherent to the natural ordering process of colloidal crystallization. The most efficient packing of hard spheres can be achieved by arranging them into stacked hexagonal close packed layers [20]. Regular stacking sequences of ABCABC and ABABAB types respectively lead to face-centred cubic (FCC) and hexagonal close-packed (HCP) structures. Although the FCC structure provides a little bit more space for particle fluctuations, the free energy difference between FCC and HCP is tiny [22–24]: less than $10^{-3}k_BT$ per particle, with k_B the Boltzmann constant and T the Kelvin temperature. This may conribute to the frequent observation of so-called random-hexagonal close-packed (RHCP) crystal structures [19, 26–30]. Due to the variety of possible RHCP configurations, an additional gain in entropy can stabilize the RHCP structure for sufficiently small crystals [31], although a flat wall seems to promote the FCC structure [32]. Since crystal nuclei have RHCP structure and the reorganization from RHCP to FCC structure is expected to take months to years for experimental systems [25, 28], RHCP structures are quite commonly observed in hard-sphere systems.

The crystal structure can be conveniently characterized using diffraction techniques [29,69]. The diffraction wave vector $\mathbf{q} = \mathbf{k_0} - \mathbf{k}$ lies on the so-called Ewald sphere since the incident and refractive wave vectors $\mathbf{k_0}$ and $\mathbf{k}$ share the same length $2\pi/\lambda$, with λ the wavelength. Since $\mathbf{q} << \mathbf{k_0}$ for colloidal crystals, the diffraction pattern can only be observed at very small angles and $\mathbf{q}$ is nearly normal to $\mathbf{k_0}$. As a result, the relevant part of the Ewald sphere is nearly flat. The scattering wave vector $\mathbf{q}$ can be written in terms of three basis vectors $\mathbf{q} = h\mathbf{b_1} + k\mathbf{b_2} + l\mathbf{b_3}$ introduced in Fig. 2.1A, where h

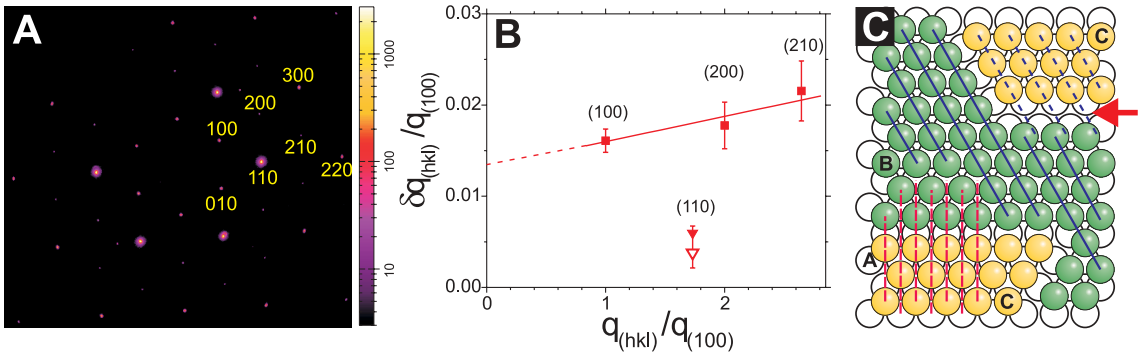

Figure 2.2. (A) A high-resolution SAXS pattern of hard-sphere colloidal crystal measured with 12.5 keV X-ray beam (λ = 1 Ångstrom). The reflections in the left-top corner are absorbed by an acute beam stop. Exposure time τ = 1 s. The strong 110-class reflections saturate the detector and their width is exaggerated at this exposure time. The Miller indices of several reflections are given. (B) Measured radial widths of the (100) (200) and (210) Bragg rods (squares) and (110) Brag spots (triangles), corrected for instrumental resolution. While the (110) peak is greatly instrument limited, the Bragg rods are clearly much broader. This graph is adapted from [69]. (C) The difference in the width of the stacking-dependent and stacking-independent reflections can be explained by the occurrence of stacking islands within a layer. The long-dashed lines in the bottom-left highlight the periodicity leading to the 110 reflection. The other lines illustrate the periodicity associated to the 100 reflection. The red arrow points to a broader line-defect in between B and C domains, which should be observed when a line defect rotates by obtuse angles of 120^0. For a rotation of 60^0 this broadening is not observed.

and k are integers due to the in-plane periodicity. For $h-k$ divisible by 3, a sequence of sharp *Bragg spots* is observed for integer values of l. When $h-k$ is not divisible by 3 and l is any real number, the irregular stacking of hexagonal layers in three lateral positions causes these features of the reciprocal lattice to be smeared out into *Bragg scattering rods* in the direction perpendicular to the hexagonal layers, as illustrated in figure 2.1 [28, 29, 70, 71].

Figure 2.2A displays an example of a high-resolution small-angle X-ray scattering (SAXS) pattern obtained at the beam line BM-26 'DUBBLE' [72] of the European Synchrotron Radiation Facility (Grenoble, France) using microradian diffraction setup [69]. The pattern is measured in a colloidal single-crystal with an X-ray beam orthogonal to the hexagonal planes (i.e., $l = 0$). The intensity of the diffraction peaks strongly decay with increasing length of the diffraction vector q mostly due to the decay of the form factor. In addition, the structure factor of the Bragg spots (e.g., 110, 220, 300) is much stronger than that of the reflections originating from the Bragg rods (e.g., 100, 210). Recently, microradian-resolution small-angle X-ray diffraction of a sedimented colloidal

single crystal revealed that the Bragg rods and Bragg spots have different widths also in the direction orthogonal to the l, as illustrated here in Fig. 2.2B [69]. Usually, one assumes that every layer has a unique lateral position and the stacking disorder is present only in the direction perpendicular to the close-packed layers. In that case both the stacking-dependent Bragg rods and the stacking-independent Bragg spots should be equally sharp in the lateral direction. The observed additional broadening of the Bragg rods within the (h,k) plane can be understood if one assumes that the close-packed hexagonal planes consist of islands with different A, B or C lateral positions of the spheres separated by characteristic line-defects as illustrated in Fig. 2.2C. The line-defect should not be confused with the class of line-defects which includes all dislocations. In fact the line-defect is a Shockley partial dislocation, with both screw and edge components, as we will discuss in Chapter 3). These line-defects separate regions within a crystal grain: by crossing the line defect positional order is lost, whereas orientational order persists across the line-defect. The stacking-independent Bragg spots, such as the 110 reflection, do not "notice" the difference between the islands and, therefore, they are not broadened by the island structure of the layers. In contrast, switching from one island to the other leads to an additional phase shift of 120^0 of their contributions to the Bragg rods, such as the 100 reflection. The lateral width of the Bragg rod should then be related to the inverse of the typical island size. Note that simulations suggest that the width of the Bragg rod itself varies along its axis due to the correlation between line-defects in consecutive layers [73]. One way to investigate the existence of stacking islands within the close-packed planes is to shift to real space. Microscopy has proved to be an extremely powerful tool to study crystallization [57], defect dynamics [33, 74] and crystal structure formed by sedimentation [75, 76] and shear [77]. The stacking of colloidal crystals has received some attention in these works, but not on the individual particle level. Line defects have been observed in previous studies [77–79], but have to date not been quantitatively studied and structurally analyzed. Additionally, microscopy can reveal information on the three-dimensional line-defect structure, which cannot be deducted straightforwardly from scattering data. It is the aim of this work to verify this interpretation of the broadening of the Bragg rods on the basis of real-space confocal microscopy results. We study the structure of line-defects and stacking islands in colloidal crystals grown by sedimentation.

2.2. Experimental section

2.2.1. Experimental Systems

In the SAXS studies presented in Figure 2.2A and in [69] sterically stabilized spherical silica colloids are used. The particle radius is 112 nm with a polydispersity of 4.1%. The density mismatch between the silica particles and solvent cyclohexane is 0.92 $g\ cm^{-3}$. We will refer to this system as SC112. Further details can be found in [29, 80].

These colloids are too small to be studied by confocal microscopy. Instead, we use poly methyl-metacrylate (PMMA) particles with a diameter of 1.2 μm, fluorescently labelled with 4-methylamino-ethylmetacrylate-7-nitrobenzo-2-oxa-1,3-diazol (NBD), which were obtained by dispersion polymerization (mass density $\rho = 1.17$ g mL^{-1}, refractive index $n_D = 1.50$) [14]. The fluorescent dye is covalently incorporated into the polymer network of PMMA and the particles are sterically stabilized against flocculation by poly(12-hydroxystearic acid). The PMMA particles were 3-5% polydisperse. This is similar to the polydispersity of the silica spheres used in the SAXS study, which is important since the polydispersity may influence the defect concentration in the crystals [81]. The PMMA particles are dispersed in two apolar solvents: the first solvent is a mixture of tetra chloromethane (Merck "for synthesis"), tetralin (Acros Organics) and cis-decalin (Merck "for synthesis") (0.35:0.35:0.30 v/v). The density of this solvent, as well as the refractive index nearly matches that of the PMMA particles (see Table 1). Despite the careful density matching, gravity is more important than in the SC112 system, as discussed in more detail in the next section. To understand the effect of the gravity, we additionally use pure cis-decalin, which has a lower density than the solvent mixture. We will refer to the systems as PT600$_{40}$ and PD600$_{30}$ respectively. The use of optically matching apolar solvents ($\Delta n_D \simeq 0.005$ (PT600$_{40}$) and 0.01 (PD600$_{30}$)) results in hard sphere interactions [17, 82].

Table 2.1. Relative gravities for the samples studied

System	Δn_D [a]	$\Delta\rho$ (g cm^{-3}) [b]	$Pe = \frac{\Delta\rho g R^4}{k_B T}$
SC112		0.92	4 10^{-4}
PT600$_{40}$	0.005	0.01	3 10^{-3}
PD600$_{30}$	0.02	0.27	9 10^{-2}

[a] Refractive index mismatch at 20^0C

[b] Density difference between particles and medium

2.2.2. Tuning Gravity

The sedimentation Peclet number, $Pe = \frac{\Delta\rho g R^4}{k_B T}$, is usually used to describe the relative importance of the gravitational field. It expresses the ratio between gravitational and thermal energy on the scale of the particle size. Since $Pe \propto R^4$, the Peclet number of the PMMA particles in PT600$_{40}$ is significantly larger ($Pe \simeq 3\ 10^{-3}$) than the Peclet number of SC112 during crystallization ($Pe \simeq 4\ 10^{-4}$). Further reduction of the gravitational field was not easily attainable. We therefore investigated the effect of gravity by increasing the gravitational field, resulting for PD600$_{30}$ in $Pe \simeq 9\ 10^{-2}$.

2.2.3. Instrumentation

Thin 2D cross sections of the sample were imaged with a Nikon Eclipse TE2000U laser scanning confocal microscope with a Nikon C1 scanning head in combination with an argon laser ($\lambda_0 = 488nm$) and an oil-immersion lens (Nikon Plan APC 100X, NA 1.4). The $\sim 0.3\ mL$ samples were stored in small vials. The bottom of the vial was removed and replaced by a microscope cover glass (Chance Propper LTd., West Mids, England, 0.11 mm thickness), which was glued to the vial using an epoxy glue (Araldit AW2101) with hardener (HW2951).

2.2.4. Preparation of the crystals

The suspensions were centrifuged at 500 g and the supernatant was removed. Assuming that the sediment has a random packing density of 0.66 for 5 % polydisperse randomly packed hard spheres [83], the samples were redispersed to a volume fraction ϕ_0. The crystals were subsequently formed by sedimentation. Heterogeneous nucleation at the sample bottom and subsequent upward growth is observed. Therefore, close to the wall, the crystal structure is solely characterized by the hexagonal plane, which enables a layer-by-layer investigation of crystal structure. By choosing initial volume fractions ϕ_0 of 0.4 ($PT600_{40}$) and 0.3 ($PD600_{30}$), the largest crystal grain sizes were obtained. The crystals were imaged from the glass sample bottom to sample heights of $\sim 30\mu m$, which corresponds to the first 20-30 layers of a crystal. Imaging was done within single colloidal crystals by selecting sufficiently large crystallites and by excluding the grain boundaries from the images. Particle positions were obtained by methods such as those used by Crocker and Grier [51].

2.3. Results and Discussion

2.3.1. Observations

Representative confocal images are shown in figure 2.3. Line-defects – and therefore stacking islands – are clearly present. In smaller grains, line-defects usually run in between the grain boundaries, where they seem to be arrested (Fig. 2.3C). Since the crystal is nearly close packed, migration of line-defects is not observed within several days. The vast majority of the line-defects are observed to form acute angles of 60^0 with each other. As shown in Fig. 2.2C an obtuse angle of 120^0 can only be occur between a pair of line-defects, of which one is significantly broader than the other. In our images, these wider defect lines are rarely observed and their length is restricted to one or two particle diameters. In fact, most apparent obtuse angles are actually two consecutive sharp angles, as illustrated in Fig. 2.3D. These broad line-defect would result in larger amount of unused crystal space and therefore are unfavourable entropically.

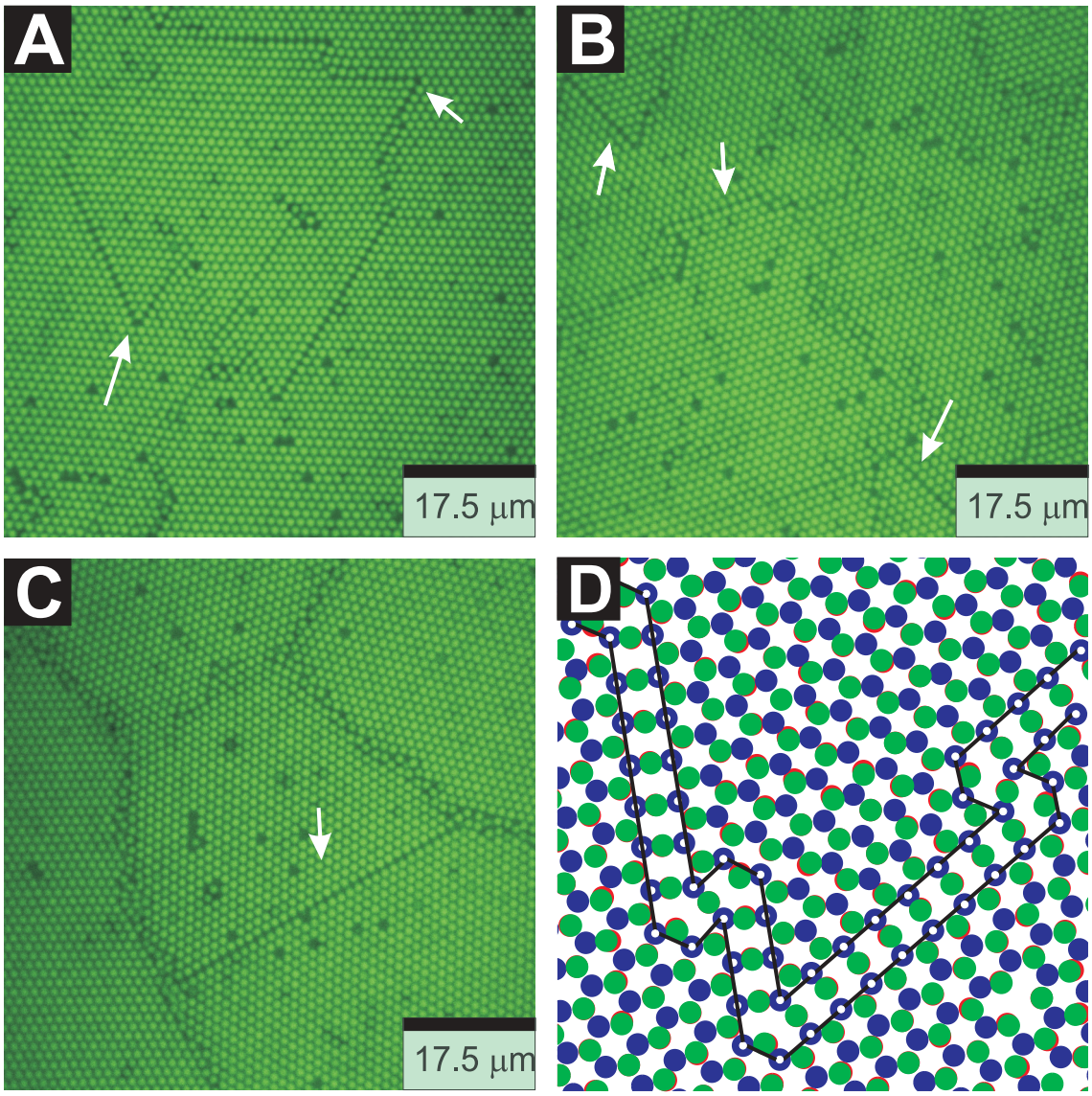

Figure 2.3. Representative confocal images of crystals in $PT600_{40}$ (A) and $PD600_{30}$ (B). The white arrows indicate line-defects in between islands with different lateral positions. (C) For small crystals, line-defects usually run across the whole grain. (D) Three consecutive layers are projected onto each other. The obtuse angles in line defects are stabilized somewhat differently than suggested in Fig. 2.2C. The black lines highlight the geometry of the lattice around apparent obtuse angles, which actually consist of two consecutive sharp angles

2.3.2. Reciprocal space

In order to determine whether $PT600_{40}$ (A) and $PD600_{30}$ show the same broadening of peaks as observed in SC112 [69], the diffraction patterns of $PT600_{40}$ were simulated. Using x,y-components of the particle coordinates r_i , the two-dimensional structure factor $S(q_x, q_y)$ was calculated:

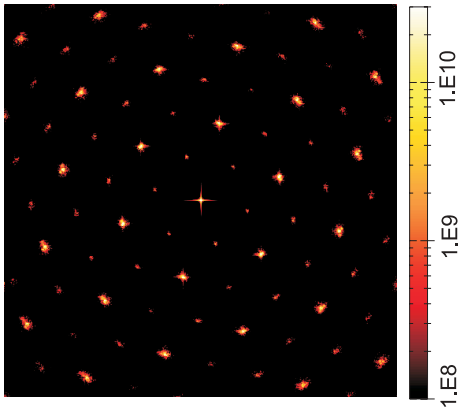

Figure 2.4. Two-dimensional structure factor pattern $S(q)$ simulated from particle coordinates in a stack of 20 layers in a $PT600_{40}$ crystal. The vertical and horizontal stripes are caused by finite-size effects

$$S(q_x, q_y) = \frac{1}{N} \sum_{n=1}^{N} \exp[i(q_x x_n + q_y y_n)]. \tag{2.1}$$

An example of the structure factor pattern is displayed in figure 2.4. It is typical for the RHCP crystal structure and its similarity with the SAXS diffraction pattern is clear. The enhanced visibility of the higher-order reflections in comparison with experimental patterns is related to the fact that the particle form factor, which strongly decays with increasing q, is not included. The stacking-independent peaks with $h - k$ divisible by 3 are much stronger. At the same time, the peaks with $h - k$ not divisible by 3 are still visible, which is caused by incomplete cancellation of the contributions in a random sequence of stacking positions. We did not observe a difference in relative widths of the reflections, which might be related to the finite size of the microscope images as well as to the presence of other types of disorder in the crystal.

2.3.3. Stacking

To quantify the extent of stacking disorder we have determined the stacking parameter α, which is the fraction of FCC stacked particles [84], using three different methods. We introduce two methods based on the determination of orientational and positional correlation of particles and additionally use the program Ballviewer [85].

The orientational correlation method compares the particle orientations of the neighbours of a particle i. All particles j in layer L are projected onto the layers $L + 1$ (above) and $L - 1$ (below) and next neighbours are identified. The relative rotation between the neighbouring particles in layers $L + 1$ and $L - 1$ is 60^0 for FCC and 0^0 for HCP (Fig. 2.5A). To express this rotation the bond orientational order parameter $\psi_3^{\pm}$

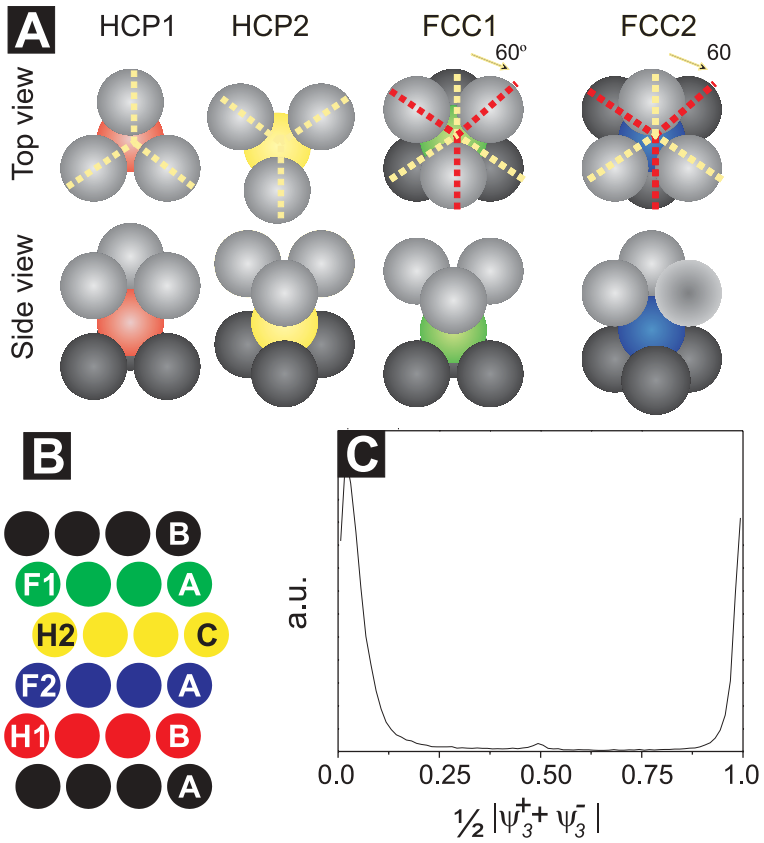

Figure 2.5. Using the ψ_3 function to distinguish between HCP and FCC: (A) Illustration of stacking type and stacking direction. The relative rotation of the particles in layers $L+1$ and $L-1$ is 60^0 for FCC and 0^0 for HCP. The change of stacking direction is characterised by a rotation of 180^0 around the direction perpendicular to the hexagonal plane, resulting in a shift from HCP_1 to HCP_2 or from FCC_1 to FCC_2. (B) Illustration of the stacking directions (side view). The different stacking directions are marked: FCC_1 (F1), FCC_2, (F2), HCP_1 (H1) and HCP_2 (H2). The lateral positions A, B and C are shown as well. (C) Typical distribution of $\frac{1}{2}|\psi_3^+ + \psi_3^-|$: The first peak at $\frac{1}{2}|\psi_3^+ + \psi_3^-| \simeq 0$ indicates the particles with FCC stacking, the second peak at $\frac{1}{2}|\psi_3^+ + \psi_3^-| \simeq 1$ the particles with HCP stacking. The small peak at $\frac{1}{2}|\psi_3^+ + \psi_3^-| \simeq 0.5$ is caused by particles lying above or below a line-defect. The configuration of the line-defect results in $|\psi_3| \simeq 0$ for the line-defect layer, see Fig. 2.3D.

is introduced:

$$\psi_3^{\pm}(\mathbf{r}_j) = \frac{1}{N^{\pm}} \sum_{k^{\pm}}^{N^{\pm}} \exp[3i\theta(\mathbf{r}_{jk^{\pm}})], \tag{2.2}$$

The summation $k^{\pm}$ runs over all $N^{\pm}$ next neighbours in the layer above (ψ_3^+) or below (ψ_3^-) of a given particle j. Next neighbours are assigned if they are within 0.8 a of the projected particle in the layer. Here, a is the lattice constant, which is determined with

the $2D$ pair correlation function $g(r)$:

$$g(r) = \frac{1}{\rho 2\pi |\vec{r}|} < \sum_{i \neq j} \delta(r - |\vec{r_i} - \vec{r_j}|) > . \tag{2.3}$$

Here, ρ is the 2D particle density and r the distance between particles i and j. The first peak of the $g(r)$ is fitted to a Gaussian to obtain an estimate of the lattice constant a. Eq. (2.4) can be exploited to distinguish stacking types FCC and HCP, by adding or subtracting the vectors resulting from projecting the particles in the layers above and below:

$$\psi^{\pm}_{3:3} = \frac{1}{2}[\psi^{+}_{3} \pm \psi^{-}_{3}] \tag{2.4}$$

Stacking can now easily be assigned: $|\psi^{\pm}_{3:3}|$ varies between 0 and 1. Depending on the sign, $|\psi^{\pm}_{3:3}| = 1$ either corresponds to FCC ($-$) or HCP ($+$). Fig. 2.5A and B shows that besides a stacking type, a stacking direction can be distinguished as well. For HCP this comes down to stacking of type HCP_1 for ABA, and stacking of type HCP_2 for BAB. Similarly, for FCC this results in stacking of type FCC_1 for ABC, and stacking of type FCC_2 for CBA. ABA is of course equivalent to BCB and CAC, BAB to CBC and ACA, ABC to BCA and CAB and CBA to BAC and ACB. Which direction is indexed by 1 or 2 is completely arbitrary, although it is insightful to realize that for perfect FCC the stacking direction is identical throughout the system, whereas for perfect HCP the orientation alternates per layer. The argument of $\psi^{\pm}_{3:3}$ can distinguish between the stacking directions of HCP and FCC. $\psi^{+}_{3:3}$ results in peaks separated by π for the distinct HCP_1 and HCP_2 directions. Similary, $\psi^{-}_{3:3}$ separates FCC_1 and FCC_2 peaks. For analysis, we additionally use the constraints that either $|\psi^{+}_{3:3}| \geq 0.8$ (HCP) or $|\psi^{-}_{3:3}| \geq 0.8$ (FCC), based on at least 1 particle in both the layer below and the layer above. The magnitude of $\psi^{\pm}_{3:3}$ can be exploited to assign stacking as well, e.g. $\frac{1}{2}|\psi^{+}_{3} + \psi^{-}_{3}| \simeq 0$ and 1 for FCC and HCP, respectively (Fig. 2.5C). The peak at $|\psi^{\pm}_{3:3}| = 1/2$ results from the configuration of particles below or above a line-defect (Fig. 2.3D), which is a first measure for defect localization as sketched out in Fig. 2.6A,B and C. On the other hand, the identification using the argument distinguished HCP_1 and HCP_2 layers on either side of a line-defect Fig. 2.6D,E and F. Apart from the line-defect, a continuous stacking transition is observed as well. These continuous transitions will be the focus of the next chapter. In either case, the stacking parameter simply is $\alpha = \frac{N_{fcc}}{N_{fcc}+N_{hcp}}$, with N_{fcc} and N_{hcp} the number of particles with FCC and HCP environment.

The positional correlation technique (Fig. 2.7A) compares the particle position distributions of particles separated by one or more layers in the z-direction. All particles i in layer $L+2$ are projected onto the layer L two layers below and the lateral xy-separation of particle i to the nearest particle j in layer L is calculated, resulting in a distance distribution $P_{xy}(r_{ij})$. Typical peaks occur at r_{ij} = 0-0.2 a (HCP) and r_{ij} = 0.6-0.8 a (FCC), with a the typical inter-particle distance within a crystal, determined in the

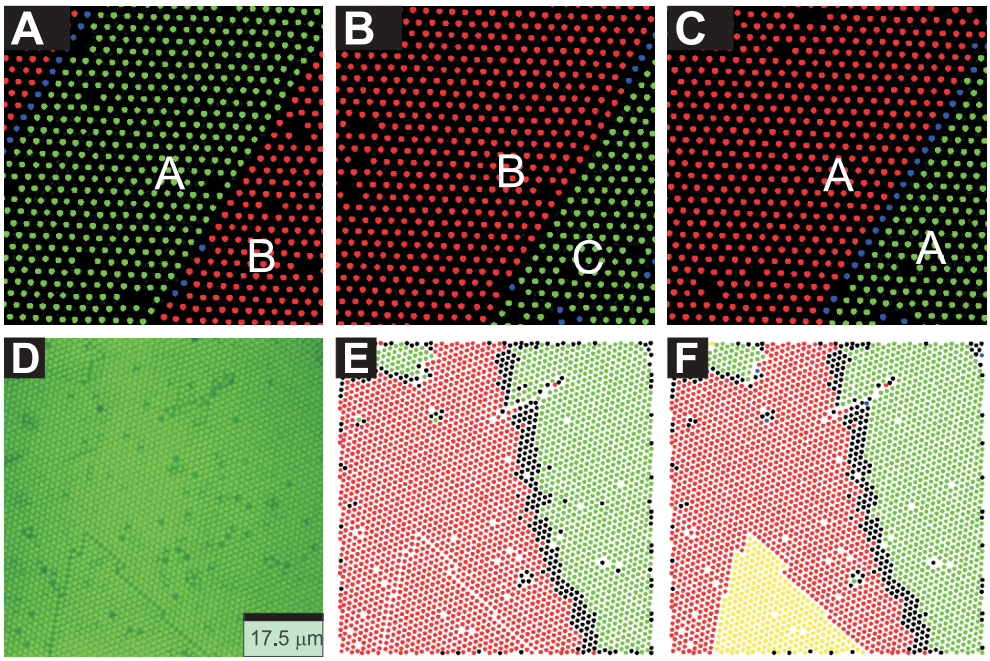

Figure 2.6. (A), (B) and (C) Stacking determined with the $|\psi_3^+ \pm \psi_3^-|$ method in three consecutive layers. The red and green circles correspond to HCP- and FCC-stacked particles respectively. Stacking could not be assigned to particles represented by purple circles and blue circles correspond to particles above or below a line-defect. A, B and C indicate the lateral positions of the layers around the line-defect. (D), (E) and (F) Stacking determined with the $|\psi_3^+ \pm \psi_3^-|$ method. (D) Confocal image of a hexagonal layer with in-plane stacking disorder. (E) The $|\psi_3^+ \pm \psi_3^-|$ method results in identification of the HCP (•) and FCC (•) islands, but particles across a line-defect are both HCP. Black symbols (•) indicate particles for which no stacking is assigned. (F) The incorporation of the argument of ψ_3 distinguishes particles on either side of the line-defect. (•) FCC_1, (•) HCP_1, (•) HCP_2, (•) no stacking assigned. No FCC_2 particles are present in this particular image. Note that (E) and (F) also reveal a non-line-defect transition. These transitions will be the subject of Chapter 3.

same way as for the orientational correlation method. The α parameter is obtained by integration of the peaks.

Ballviewer (Fig. 2.7B) distinguishes between particles with HCP, FCC and BCC (body centred cubic) environment from the distribution of angle cosines of all next neighbours [85]. The stacking parameter is again defined as $\alpha = \frac{N_{fcc}}{N_{fcc}+N_{hcp}}$. The results for the value of the stacking parameter α determined by the three methods are summarized in table 2: we find $\alpha = 0.75 \pm 0.06$ for $PD600_{30}$ and $\alpha = 0.65 \pm 0.11$ for $PT600_{40}$ while in SC112 $\alpha = 0.55 \pm 0.05$ as determined by SAXS [86]. The given errors result from comparing several sample locations. These results indicate that all

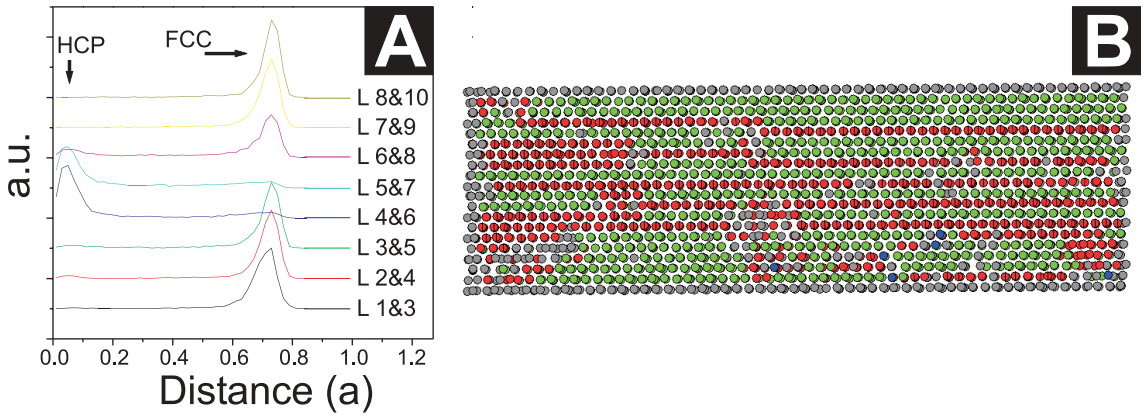

Figure 2.7. Positional Correlation and Ballviewer methods to determine the stacking parameter α: (A) The positional correlation compares the lateral particle positions of nearby particles in different hexagonal layers. From the resulting distribution function, the stacking per layer can be determined. Shown here are the resulting distribution functions for particles separated by two layers, with L referring to the layers involved. (B) Ballviewer relates the angle cosine distribution of the next neighbours of a particle. The colours red, green and blue represent HCP, FCC and BCC respectively, whereas stacking could not be assigned to grey particles.

three colloidal systems yield crystals with RHCP structure. The stacking parameter α displays a tendency toward FCC stacking, which enhances with increasing the role of the gravity. A similar effect with increasing gravity was reported for slightly charged colloids [32], suggesting either charge or the hydrodynamics of growth as its source.

Table 2.2. Overall stacking parameters obtained by positional correlation, orientational correlation and ballviewer.

Sample	SC112	Positional Correlation	Orientational Correlation	Ballviewer
SC112	0.55 ± 0.05			
$PT600_{40}$		0.68 ± 0.11	0.66 ± 0.11	0.63 ± 0.11
$PD600_{30}$		0.76 ± 0.05	0.76 ± 0.06	0.74 ± 0.06

2.3.4. Defect Identification

The confocal images, shown in figure 2.3, confirm the existence of islands of different positions in the lateral direction of the crystal. For further analysis, routines for the identification of the particles located next to line-defects are needed. The particles within a line-defect, are arranged in unusually spaced rectangles with typical distances of $\sqrt{\frac{4}{3}}a \simeq 1.15a$ and $\sqrt{\frac{7}{3}}a \simeq 1.53a$ as indicated in Fig. 2.8A. The unique set of particle

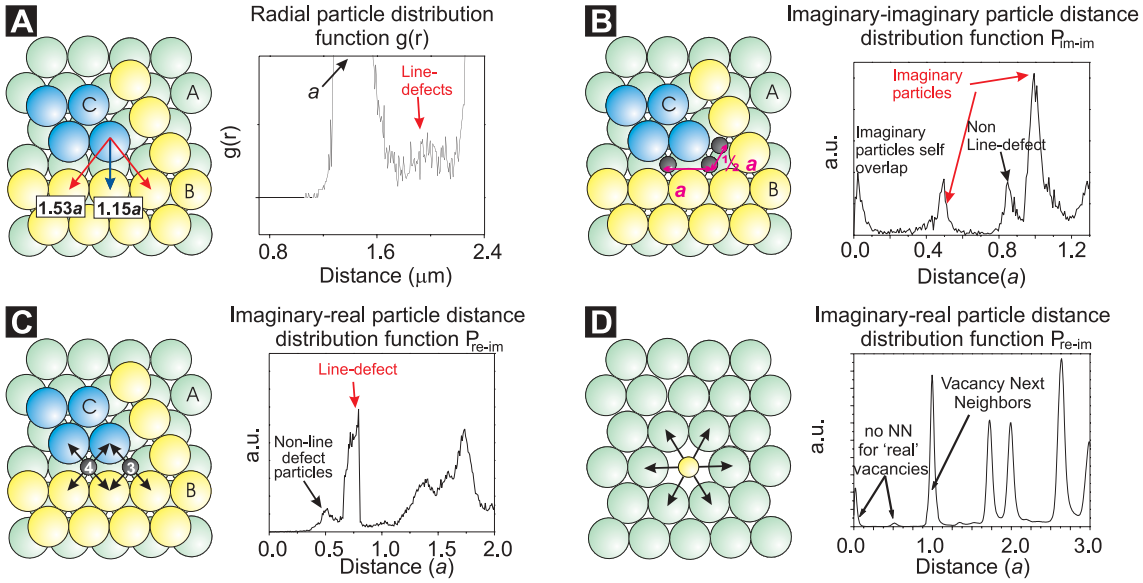

Figure 2.8. Schematic representations of the unique set of inter-particle distances around a line-defect and corresponding "line-defect radial distribution functions". (A) The typical line-defect distances. The noisy peak in between the first two peaks in the $g(r)$ function confirms the presence of these distances in the crystal. (B) The imaginary-imaginary interparticle spacings at the corner of and along line-defects are confirmed by the two peaks at respectively a and $a/2$ in P_{im-im} function (C) Imaginary particle − real particle neighbour distances, confirmed by the second peak in the P_{im-re} distribution. (D) Vacancies are identified by putting a particle in between all particles whose centres are at distances of $\sim 2a$. If no other particles are found nearby, a vacancy is identified.

distances within a line-defect provides sufficient identification criteria, which can be used to identify the particles in four steps.

In Fig. 2.8A a schematic representation of a line-defect and the 2D radial distribution function $g(r)$ are shown. As a first criterion, particles with neighbours at distances 1.32 - 1.58 a are selected. Note that the larger deviation in $g(r)$ toward lower values results from the slightly displaced particle toward the line-defect due to the osmotic pressure imbalance which pushes particles towards a line-defect. To refine the selection, an imaginary particle is positioned in between the selected particles (Fig. 2.8B). The coordinates of imaginary particles, which lie within $0.3a$ are averaged to one imaginary particle coordinate. In the imaginary particle distance distribution function $P_{im-im}(r_{ij})$ - the pair correlation function of the imaginary particles - peaks occur at a (defect line) and $0.5a$ (defect corner), as illustrated in Fig. 2.8B. Therefore, the second criterion requires imaginary particles to have imaginary neighbours at $0.91-1.09a$, but not at $0.76-0.91$ a, which corresponds to real particles slightly deviated from their ideal lattice position. The positions of the remaining imaginary particles are compared to the real particle

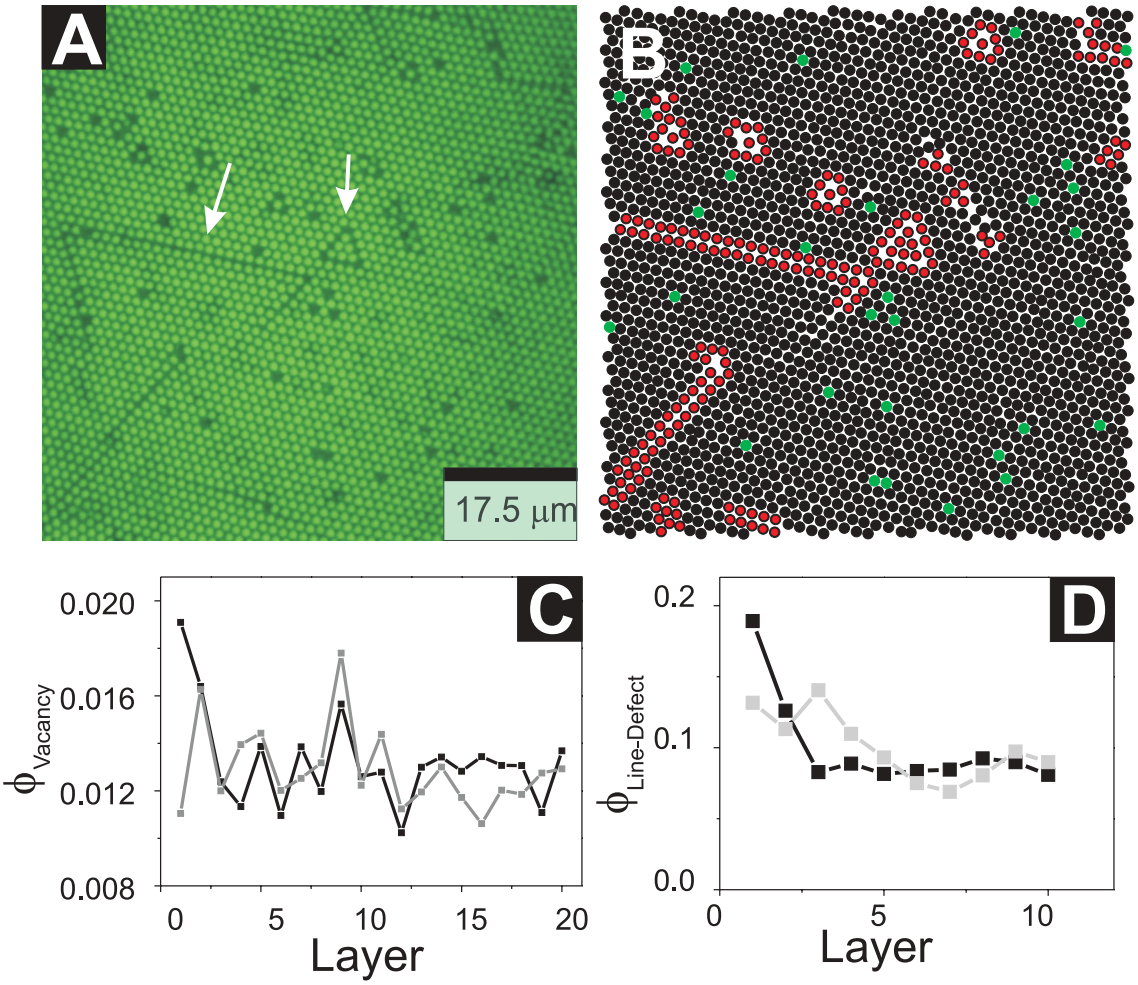

Figure 2.9. Line-defect and vacancy identification: (A) Confocal image of the 2nd layer of a $PT600_{40}$ crystal, the white arrows indicate the line-defects and islands (B) The red particles are the particles identified by the four subsequent selection criteria as line-defect particles; the green particles are vacancies. The small peak in between the first two large peaks in the $g(r)$ confirms the presence of the line-defect distances in the crystal. (C) Number of vacancies as a function of layers above the sample bottom. (D) Number of line-defect particles as a function of layers above the sample bottom. Black squares correspond to $PD600_{30}$, grey squares to $PT600_{40}$ in (C) and (D).

positions, resulting in the imaginary particle i - real particle j distance distribution function $P_{re-im}(r_{ij})$ - the pair correlation function of all real particle - imaginary particle combinations (Fig. 2.8C). Its second peak at $\sim \sqrt{\frac{7}{12}}a$ represents line-defect particles. The first peak at $\sim \frac{1}{2}a$ represents non-line-defect particles, which slightly deviate from their ideal lattice positions and were included in the initial selection criteria, but are now excluded here. Each imaginary particle within the line-defect should have three or four "real particle" neighbours at this distance. Therefore, the third criterion requires

3 or 4 real next neighbours at $0.60 - 0.82a$ and no real next neighbours at distances smaller than $0.60a$ for each imaginary particle. After these three steps, a large number of vacancy next neighbours still show up as line-defect particles. This is due to the osmotic pressure imbalance which pushes particle towards the vacancy, discussed in more detail in Chapter 3. Therefore, the final criterion excludes vacancy next neighbours as line-defects. Vacancies are identified by positioning an imaginary particle in between particles which are at distances of $1.85 - 2.30a$. If no 'real' particles are found within $0.80a$, a vacancy is localized. Positions of vacancies identified within $0.15a$ are averaged. From the vacancy position, its next neighbours are identified through a P_{im-re} correlation function, in which the imaginary particle now is a vacancy. The resulting particles are labelled as vacancy next neighbours, as illustrated in Fig. 2.8D. We set the condition that vacancy next neighbours cannot be line-defect particles. In Fig. 2.9A and B the identified line-defect particles and vacancies are shown: the line-defects are identified with high accuracy using the selection criteria.

Although the method to identify vacancies is computationally cumbersome (there are many particles spaced by $\sim 2a$ and in between a vacancy is only rarely found), it does find nearly all vacancies. The only exception arises when large agglomerations of vacancies occur in the structure. Of course, this method can easily be extended to 3D or adapted to any other crystal configuration for which the pair correlation peak at $2a$ is sufficiently isolated. Moreover, localization of e.g. di- and trivacancies is very straightforward. We will use this technique again in Chapter 3.

The relative concentrations of vacancies and particles next to line-defect provide some information on the nucleation and growth dynamics as shown in Fig. 2.9C and D. In the first two layers of the $PD600_{30}$ system, the concentration of line-defects and vacancies is much higher than in layers above. In the $PT600_{40}$ system, the amount of defects at the wall is substantially less compared to the $PD600_{30}$ system, indicating that the particles have much more time to equilibrate their particle positions, before growth sets in in the layers above.

2.3.5. The Line-Defect in Three Dimensions

With the defect particles isolated, the 3D line-defect structure can be studied. Line-defects that persist in the orthogonal direction of the crystals, all stack FCC-like (Fig. 2.10A). This is quite remarkable, since the extent to which a line-defect persists in three dimensions clearly has a large influence on the stacking parameter α. Simple geometrical arguments show that $\alpha = \frac{n}{n+2}$ around a line-defect which has FCC stacking, with n being the number of layers in which the line-defect occurs (Fig. 2.10B). For identification purposes, defect particles are projected onto the hexagonal defect layer below, with typical peaks in the resulting radial distance distribution at $(\sqrt{3}-1)a$ and $\sqrt{\frac{7}{3}}a$ (Fig. 2.10C). Defect particles are identified as caused by the layer below, when

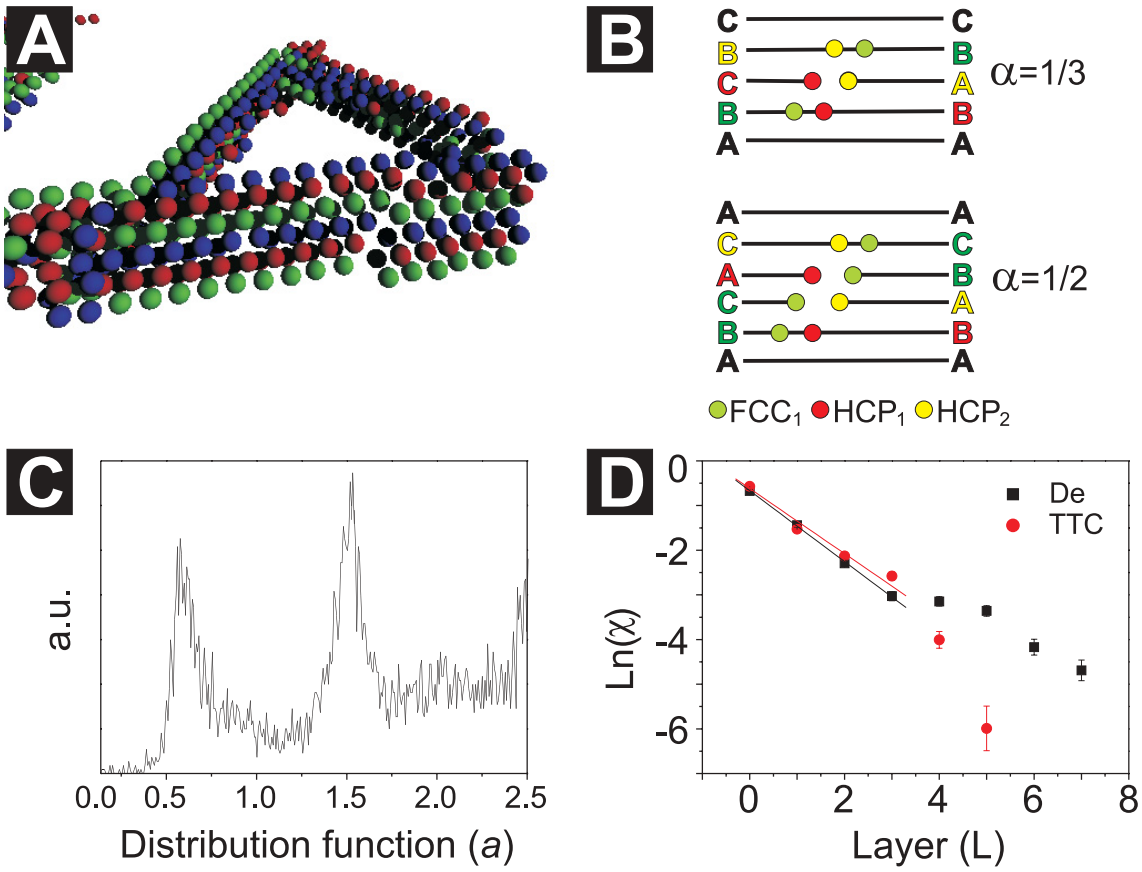

Figure 2.10. Line-defect in three dimensions. (A) 3D image of line-defect particles, green, red and blue indicate respectively A, B and C positions. FCC-like stacking is clearly visible. (B) The FCC fraction α scales as $n/(n+2)$, for a line-defect present in n consecutive layers. The colours red, yellow and green refer to HCP_1, HCP_2 and FCC_1. Note that the consecutive layers are drawn such that the FCC stacking direction is identical in the layers above and below the line-defect(s). A change of stacking direction in fact occurs with equal frequency. (C) Radial particle distribution of defect particles in subsequent layers. The first peak indicates that the closest defect particles in the subsequent layer are positioned at a lateral position of $(\sqrt{3}-1)a$. The second peak occurs at $\sqrt{\frac{7}{3}}a$. (D) Defect particle fraction χ of the defects as a function of the number of layers L in which the defect occurs below a defect particle for $PD600_{30}$ (black squares) and $PT600_{40}$ (red circles). The persistence of the defects is fitted to an exponential decay for $L \leq 4$, taking the estimated error bars into account. The plateau for $L > 4$, which is especially pronounced in De sample, is attributed to disorder that deforms the crystal lattice.

particles are found within 1.15 a or alternatively at 2.00 a, the minima after the first and second peak in the distribution function. Defects initiated at the sample bottom are analyzed separately (not presented here), due to lack of structure imposed by a layer below. The number of layers L of defect particles, below every defect particle in the $(L+1)^{th}$ layer, is determined. The fraction of defect particles in the $(L+1)^{th}$ layer of a defect is $\chi_L = \frac{N_L}{N_0}$, where N_L is the number of defect particles in the $(L+1)^{th}$ layer and N_0 is the total number of defect particles. To improve the statistics in the data, the individual datasets are combined for each system. Error bars were included to account for noise in the data, with the error for N_L estimated to be $\sqrt{N_L}$, as in a Poisson distribution. We introduce the persistence parameter ζ, which is the chance to find another line-defect particle in the layer above a line-defect particle. In Fig. 2.10D χ_L is plotted as a function of L, which fits to an exponential decay of the first order with slope $\ln(\zeta)$ for the first few layers. For the different samples, ζ is given in table 2.3. For the $PD600_{30}$-system the value of ζ does not depend on the used cut-off length values. The sensitivity of the result for $PT600_{40}$ might be related to the lower gravity force and osmotic pressure resulting in larger amplitude of particle fluctuations in $PT600_{40}$ which leads to slightly less accurate tracking of line-defect particles.

Table 2.3. Chance ζ to find another line-defect particle in a subsequent layer.

	Cut-off Distance	$PD600_{30}$	$PT600_{40}$
ζ_{bulk}	2.00 a	0.45 ± 0.03	0.48 ± 0.03
ζ_{bulk}	1.15 a	0.45 ± 0.02	0.37 ± 0.03
ζ_{wall}	2.00 a	0.38 ± 0.04	0.50 ± 0.04
ζ_{wall}	1.15 a	0.33 ± 0.05	0.50 ± 0.04

The fact that ζ is close to $\frac{1}{2}$, can be related to the kinetics of the island nucleation and growth. In random-stacking crystals the new islands are presumably randomly nucleated with one of the two possible lateral positions. The new island that grows toward the existing line-defect in the layer below has 50% chance to have a lateral position different from that in both islands below thereby closing the defect. Otherwise, by coinciding with the stacking position across the line-defect, the new island cannot grow further without changing its lateral position. This will result in persistence of the line-defect. The different persistence values found for line-defects originating at the wall for the $PD600_{30}$ and the $PT600_{40}$ samples, are likely to be a wall effect. More defects are present at the wall of the $PD600_{30}$ sample, but some of these are likely caused by the decreased crystal equilibration time. The existence of in-plane stacking disorder should

affect on the overall stacking probability α in the crystal. For example, a single line-defect, which exists only in one layer, necessarily requires an HCP environment for both islands (Fig. 2.10B), with different stacking direction. On the other hand, an increase of the number of multiple FCC-like stacked line-defects may increase the total number of particles with FCC environment and thus decrease the HCP environment. Note that in the sketch in Fig. 2.10B we have sketched identical FCC stacking directions above and below line-defects, but a change in stacking direction, also known as twinning [87] occurs with equal frequency. This marks a subtle difference between a single line-defect and a single HCP layer in between two FCC layers: in the latter case twinning always occurs, whereas this does not have to be the case for line-defects.

The persistence of the defects can also be affected by lattice deformations which cause more continuous stacking transitions compared to the discontinuous stacking transitions through line-defects. These defects will be discussed in Chapter 3. Some of the particles present in the vicinity of such a defect will have a position that strongly deviates from the ideal lattice, which complicates matters: these defects impose a non-ideal lattice for the subsequent layer, in which new defects are likely to occur. In this case the typical ζ value can be expected to be much higher. Defects that lead to such lattice deformations are present in our datasets to some extent. Some of them are identified as line-defect with our tracking method. Their presence then easily explains the plateaus that seem to occur in the persistence curves for $L > 4$, since the small fraction with higher ζ values should only markedly show up at higher L.

2.4. Discussion

The structure around line-defects can explain some experimental findings: The closure of line-defects described here easily explains the mechanism by which line-defects anneal out in the initial layers of crystals grown on patterned substrates, with lattice parameters that are slightly off [88]. Furthermore, the creation of line-defects in sheared crystals could easily explain the high degree of non-randomness in the stacking of these crystals [77].

The polydispersity of the system can increase the abundance of defects observed and should be able to (partially) stabilize line-defects. Furthermore, line-defects have somewhat shifted from their ideal lattice position, a result of the osmotic pressure imbalance near the line-defect. This again stabilizes a somewhat deformed crystal. Our observations suggest that the three-dimensional line-defect structure is FCC-wise stacking. FCC stacked defects do spread the extra line-defect space more homogeneously among the line-defect particles: in an HCP-stacked line-defect, particles at either side of the "HCP-kink" [75] do not have the same amount of "defect space" available, which should be less favourable entropically. In addition, our samples already contain a larger fraction of FCC stacked particles, which might induce the FCC-wise stacking of line-defects.

Whether the stacking islands and resulting line-defects are a thermodynamically stable situation for polydisperse spheres or an arrested state could very well depend on the extent of polydispersity. Another option – fractionation of particle sizes in different crystal grains – clearly lies outside the timescale of the present experiment [89], but should be considered for thermodynamic stability as well.

2.5. Conclusions

We explain the observed broadening of the small-angle X-ray diffraction stacking-dependent reflections in sedimented hard sphere silica crystals by the presence of island of different lateral positions. These islands result in characteristic line-defects, which we indeed observed in real space in sedimented hard sphere PMMA crystals. The line-defects persist not only in the lateral but also in the orthogonal direction of the crystal, with an FCC-like stacking structure. The persistence of the line-defects is an exponential decay, with the persistence parameter ζ, the chance to find another line-defect particle in the layer above a line-defect particle, of $\frac{1}{2}$, independent of relative gravity. The fact that ζ approaches $\frac{1}{2}$, is explained by the kinetics of island nucleation and growth, where a new island has 50% change to close the defect. Also the interaction between the lowest free energy by not having a defect in the subsequent layer and the lowest free energy for the stacking structure (FCC favoured over HCP) affects the persistence of the line-defects. Furthermore defects, which are originated by an interstitial particle, have a higher persistence in the crystal due to the difficulty of the crystal to resolve the defect.

2.6. Acknowledgement

This work resulted from a project with Andrei Petoukhov and our student Janne-Mieke Meijer. Anke Leferink op Reinink, Piter Miedema, Willem Kegel, Alan Wouterse, Job Thijssen, Roel Dullens and Jakob Hoogenboom are acknowledged for helpful discussions. Nynke Verhaegh and Gilles Bosma are acknowledged for particle synthesis. The SAXS measurements are performed with help of Maurice Mourad and Esther van den Pol and were made possible due to the technical support of Nicolas Vilayphiou, Kristina Kvashnina and their colleagues from the DUBBLE beamline. Jan Hilhorst and Roel Dullens are acknowledged for a critical reading of the manuscript.

3

In-plane Stacking Disorder in Hard-Sphere Crystals

Part 2: Continuous Transitions

Abstract

In-plane stacking disorder is not only characterised by the discontinuous transitions through line-defects presented in the previous chapter, but also by continuous transitions through lattice deformations. We introduce an interplanar bond order criterion to distinguish AB and AC type transitions between two consecutive hexagonal layers. Many of these are found to be Shockley partial screw dislocations, with a characteristic deformation that is spread across two consecutive layers. How the deformation is spread between the layers varies from case to case, which decreases positional order even more strongly than the continuous transitions presented in the previous chapter. These deformations can be traced until far away from the dislocation, both in layers above and below. The relative deformation between two consecutive hexagonal layers does have a well defined width. The deformed layers act as templates for the consecutive layers, which are deformed as well. The transitions between lateral position therefore take place even far away from the dislocation core, but the transition between AB and AC stacking does not. The full island boundary usually consists of a complex combination of both discontinuous and continuous transitions. Furthermore, we show that the regions, in which the stacking changes, contain a much higher concentration of vacancies. These vacancies cause tiny lattice deformations themselves due to the osmotic pressure imbalance caused by the missing particle, pointing towards a mechanism for the stabilisation of lattice deformations through vacancies.

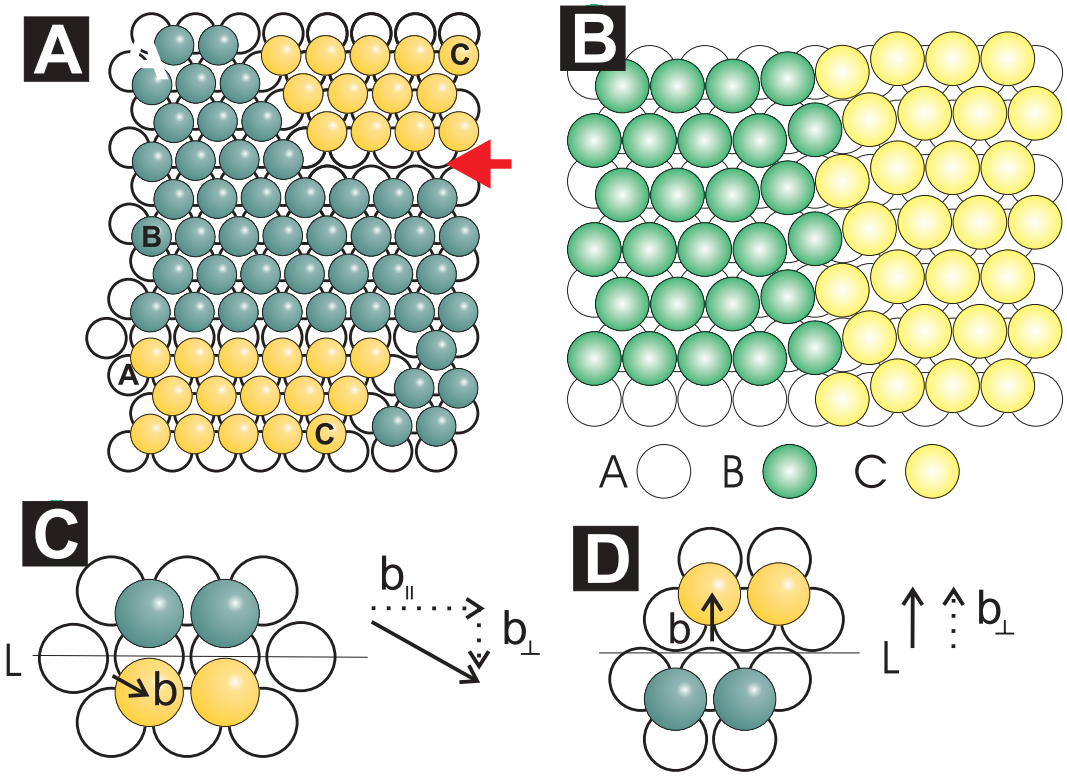

Figure 3.1. Stacking transitions within the hexagonal plane are coupled to transitions in lateral position. (A) A line-defect forms the boundary between a B and a C island within a hexagonal layer. In principle, line-defects can be broad as well as narrow. When two line-defects coincide, these either make sharp or obtuse angles. The sharp angles form between line-defects of identical width, whereas the obtuse angle form between line-defects of different width. (B) A continuous transition forms the boundary between a B and a C island. (C) and (D) Burger vectors for the narrow (C) and the broad (D) line-defect. $\vec{b}_{\parallel}$ and $\vec{b}\perp$ represent the screw and edge character of these dislocations. Whereas the narrow line-defect has a mixed character, the broad line-defect is a pure edge dislocation.

3.1. Introduction

Random hexagonally close packed (RHCP) crystals are crystals in which hexagonally close packed (HCP) and face centred cubic crystals (FCC) coexist within a single crystal. They respectively form ABA and ABC type stacking sequences of layers with hexagonal symmetry. Apart from the variation of stacking type from layer to layer, in-plane stacking disorder occurs as well within these crystals. In Chapter 2 we identified this lateral stacking disorder in sedimented hard sphere crystals. For an extended introduction to the subject we refer to the previous chapter. Within a hexagonal layer, several islands with lateral positions A, B, or C position are usually present, which induce stacking disorder within the hexagonal plane. These islands are separated by

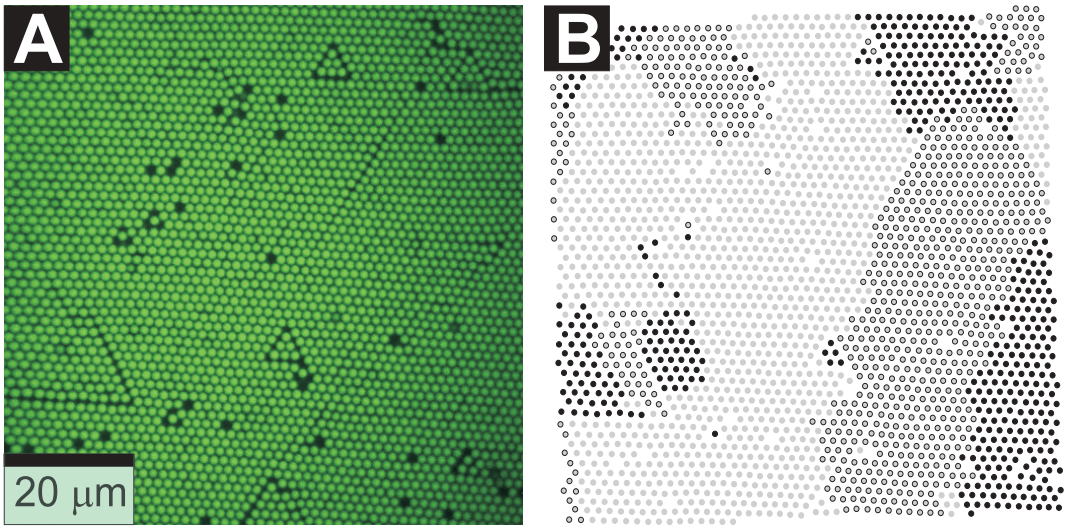

Figure 3.2. Fitting a set of particle coordinates to a lattice of ideal A, B and C positions. (A) A representative confocal image. (B) Colour assignments based on lateral position, with light grey, dark grey and black filled circles indicating the lateral positions A, B and C.

line-defects, which are characteristic of the in-plane stacking fault. Transitions from one lateral position to the other are usually coupled to in-plane transitions in stacking type or stacking direction. The stacking transition is usually of type ABC (FCC) to ABA (HCP), whereas the stacking direction transition is usually from ABA (HCP_1) to ACA (HCP_2). In principle two varieties of line-defects may occur: the narrow line-defect (a shift of one lateral position) and the broad line-defect (a shift of two lateral positions). Both are depicted in (Fig. 3.1A). In practice the overwhelming majority of line-defects are narrow line-defects, which leave less lattice space unoccupied.

This 'ideal' in-plane stacking disorder has reduced positional order since three lateral positions A, B and C are available as lattice positions instead of one. The line-defects that separate the domains of different stacking either form closed loops or run across the entire crystal grain. When fitting a set of particle coordinates Fig. 3.2A to a lattice of ideal A, B and C positions however, the lateral position often changes position without passing a line-defect (Fig. 3.2B). Furthermore, many of the present line defects appear to "dissolve in the lattice" at some point in space. Both observations in fact point to the continuous transition, which occurs through lattice deformations, such as depicted in Fig. 3.1B. The continuous transitions are evidence of the presence of partial dislocations, which occur in highly symmetric crystal structures such as FCC and HCP. Full dislocations are characterized by their Burger vector $\vec{b}$ with a magnitude b, as described for a square lattice in Fig. 3.3. Two types of dislocations are of special interest: edge and screw dislocations. The Burger vector $\vec{b}$ of an edge dislocation is perpendicular to the dislocation line L, whereas the Burger vector of a screw dislocation

is parallel to the dislocation line [87,90]. A sketch of both types of dislocations is shown in Fig. 3.1A and B, showing the Volterra constructions of both types. In practice, mixed dislocations with both edge and screw components exist as well. The edge and screw varieties can be distinguished for partial dislocations as well [87, 90, 91]. Partial dislocations differ from normal dislocations in that the length of the Burger vector is less than the unit cell dimension a' but is instead related to a shift of lateral position. Here we take the conventional FCC cubic unit cell dimension $a'[100]$ axis for reference. Partial dislocations are therefore always coupled to a stacking fault [87,90,91]. Note that in atomic systems with an FCC structure, partial dislocations nearly always occur in pairs. Due to the vanishingly small stacking fault energy [25], single partial dislocations can be easily found in hard sphere crystals.

The most common partial dislocations are the Shockley and Frank dislocations. Shockley dislocations are the result of slip: deformation within a hexagonal layer. Frank dislocations result from the agglomeration of vacancies or interstitials, resulting in half an extra layer. Schematic representations of both Shockley and Frank partials are sketched in Fig. 3.1C and D. Taking the FCC lattice as a reference, the Shockley dislocation's Burger vector is:

$$\vec{b}_{Shockley} = \frac{1}{6}[112]; \quad b^2 = \frac{a'^2}{6} \tag{3.1}$$

with a', the FCC unit cell [100] dimension. Similarly, for the Frank dislocation

$$\vec{b}_{Frank} = \frac{1}{3}[111]; \quad b^2 = \frac{a'^2}{3}, \tag{3.2}$$

and for reference purposes the full dislocation:

$$\vec{b}_{full} = \frac{1}{2}[110]; \quad b^2 = \frac{a'^2}{2}. \tag{3.3}$$

The elastic energy of a dislocation is proportional to the square of the magnitude of its Burger vector b^2 [1]. Clearly, the Frank and Shockley partials are much less costly then the full dislocation. Of the two common partial dislocations, the Shockley dislocation is the easiest to create and therefore the most commonly observed dislocation in FCC metals. Frank dislocations are always edge dislocations, Shockley dislocations have either edge, screw or a mixed character. The elastic energy of edge dislocations is roughly 3/2 times higher than that of screw dislocations [1]. The narrow line-defect is an example of mixed partial dislocation, as we have sketched in Fig. 3.1C, its burger vector has both screw $\vec{b}_{\parallel}$ and edge $\vec{b}_{\perp}$ character. The broad line-defect is an example of a pure partial edge dislocation (Fig. 3.1D).

Here we localize and characterise the lattice deformations in sedimented hard sphere crystals, to determine what type of lattice deformations and dislocations occur. We use laser scanning confocal microscopy to understand what type of partial dislocations

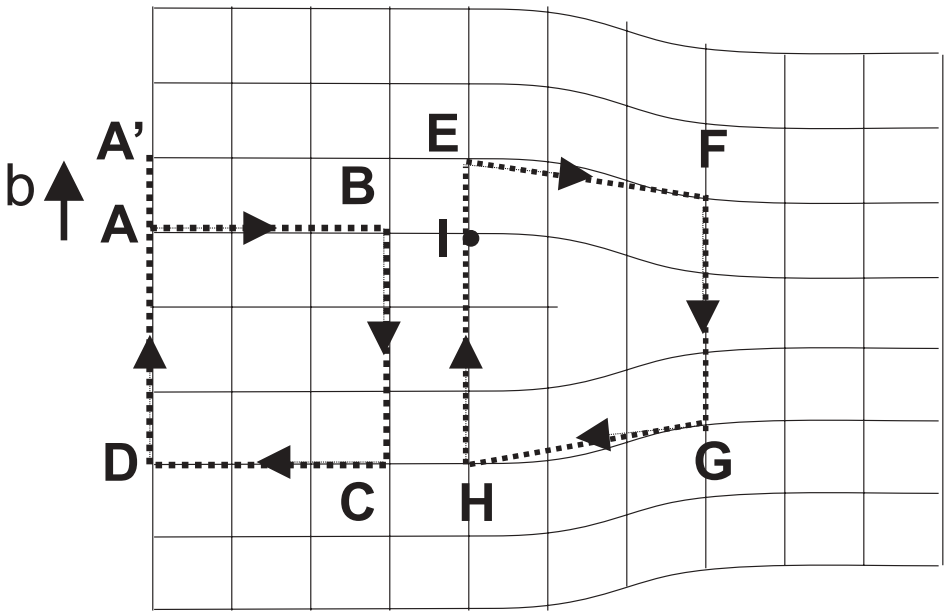

Figure 3.3. Dislocations. (A) The Burger vector $\vec{b}$ for a simple square lattice. We take the Burger circuit $EFGHIE$ around the dislocation center L. When we take an identical path in a part of the crystal which is not deformed, $ABCDA$ is identical to $EFGHI$. The part EI or AA' is needed to close the circuit is the Burger vector which shows how the lattice is distorted.

contribute to the lateral disorder, extending on works such as [75, 76, 92, 93] and Chapter 2, but also on dislocation dynamics studies such as [33, 59, 74]. Furthermore we connect local vacancy concentrations to lattice deformations, a field of study that has received some attention in 2D [94, 95], but is relatively ill-covered experimentally for hard-spheres in three dimensions.

3.2. Experimental section

Full details of our experimental methods can be found in Chapter 2. We prepared sedimented crystals of fluorescent, 0.6 μm radius poly-methyl-metacrylate spheres [14], dispersed in two apolar solvents: a mixture of tetra chloromethane, tetralin and cis-decalin (TTC) (0.35:0.35:0.30 v/v) and pure cis-decalin (De). The samples studied, were sedimented from an initial volume fraction ϕ_0 and are the samples $PD600_{30}$ and $PT600_{40}$ described in the previous chapter. Thin 2D cross sections of the sample were imaged with a Nikon Eclipse TE2000U laser scanning confocal microscope with a Nikon C1 scanning head in combination with an argon laser ($\lambda_0 = 488nm$) and an oil-immersion lens (Nikon Plan APC 100X, NA 1.4). The crystals' hexagonal layers were imaged from the glass sample bottom to sample heights of $\sim 30\mu m$, which corresponds to the first 20-30 layers of a crystal. Images were taken of complete crystal grains (samples

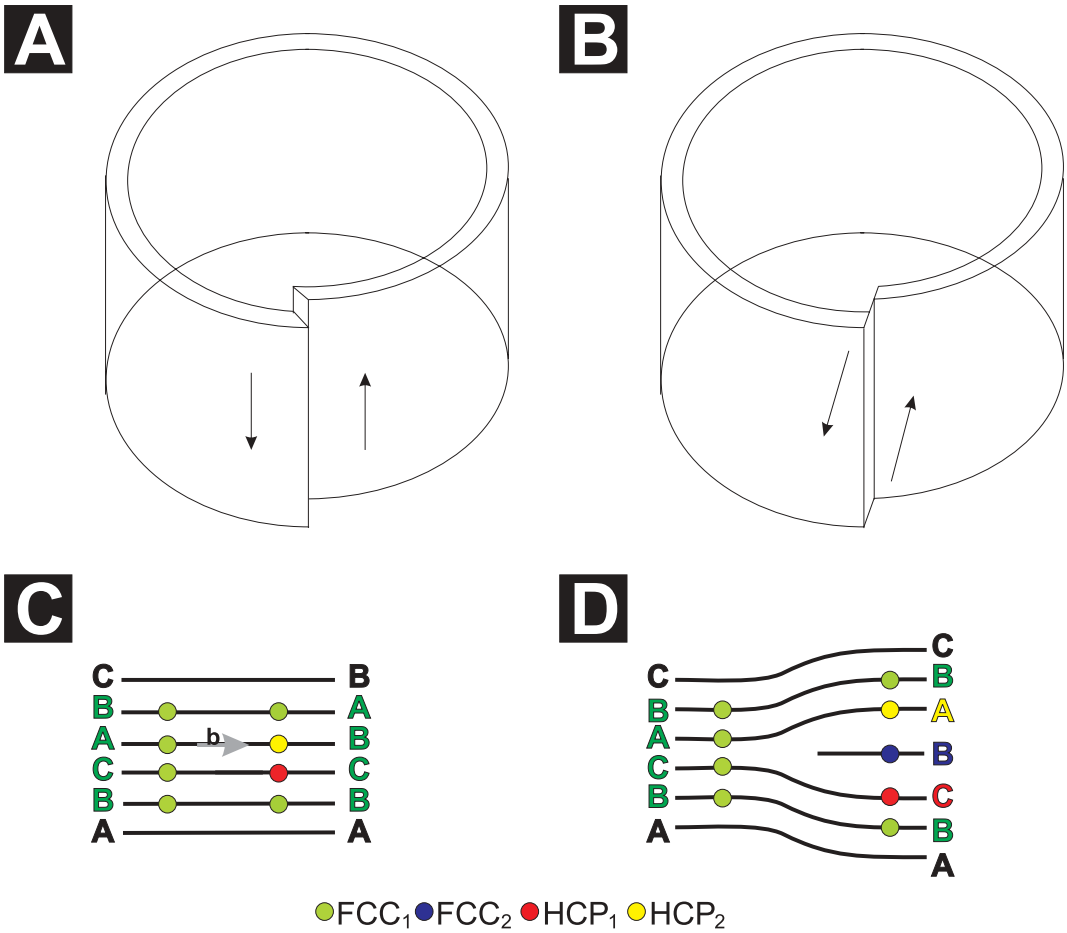

Figure 3.4. Dislocations. The Volterra constructions showing the Burger vector $\vec{b}$ and the dislocation line L for (A) the partial screw or Shockley dislocation and (B) the partial edge or Frank dislocation. Schematic representations of (C) a Shockley dislocation and (D) the Frank dislocation. The colours symbolize stacking types and directions. For (C), the Burger vector $\vec{b}$ indicates in which plane the lattice deformation takes place. The subsequent layers follow this lateral transiton. It is clear that both dislocations induce stacking disorder.

$PD600_{30}$ and $PT600_{40}$), as in Chapter 2. Particle positions were obtained by methods such as those used by Crocker and Grier [51].

3.3. Observations

The lattices in the confocal images presented in Fig. 3.5A seem fairly monodirectional at first sight, but on close inspection, the lattices contain many tiny deformations. These lattice deformations are smaller than the lattice constant a and hard to locate. 'Lattice lines' are bent, such as indicated in Fig. 3.5B, a close-up of Fig. 3.5A. It is a trace of a Shockley dislocation, which can be made more obvious by projecting three

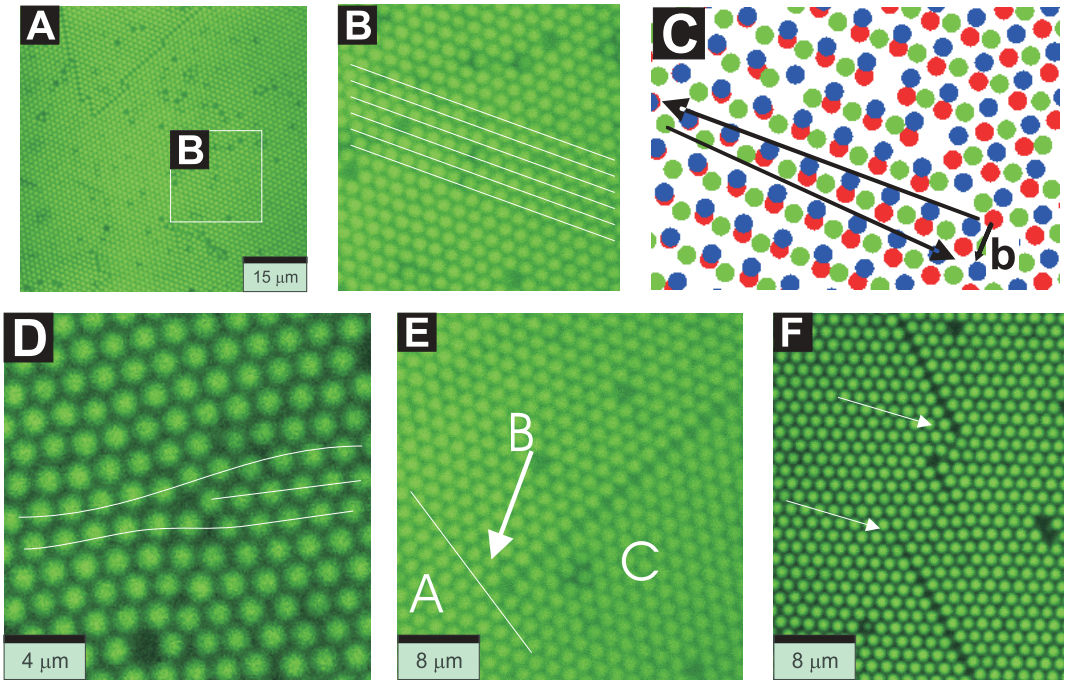

Figure 3.5. Lattice deformations in hard sphere crystals. (A) At first sight, the lattice seems perfect. Small lattice deformations smaller than the lattice constant a only become apparent on close inspection. (B) In this zoom of panel (A), we mark the lattice deformation by drawing lines parallel to the lattice orientation. (C) Three consecutive hexagonal layers (●, ●, ●). A Shockley partial screw dislocation. The Burgers vector $\vec{b}$ and the Burger circuit are shown. (the in- and out of plane parts of the Burgers circuit are not shown) causes a slow transitions from one lateral position to the other. The particles in the middle layer shown in panel (B) gradually shift from ABA to ABC environment. (D) A lattice line ends (as indicated by the lines) and the direction of deformation changes. This is a Frank partial edge dislocation, but it originates at the sample bottom in all cases studied here and therefore does not cause a stacking transition. (E) A defect similar to a Frank dislocation: a lattice line ends at a line-defect. A, B, and C lateral positions are both shown. (F) A line-defect 'disappears' into the lattice, coupled with lattice deformations.

subsequent hexagonal layers on top of each other as illustrated in Fig. 3.5C. In the subsequent hexagonal layer, the line is either bent again in the same direction, or in the opposing direction, causing a continuous stacking direction transition across the line perpendicular to the lattice line. In some cases, one of the lattice lines ends, resulting in a change of the direction of deformation such as in Fig. 3.5D, an example of a Frank dislocation. All Frank dislocations studied originate at the sample bottom, and therefore does not cause a stacking transition. The absence of Frank dislocations originating from within the lattice might well be a result of the sedimented growth

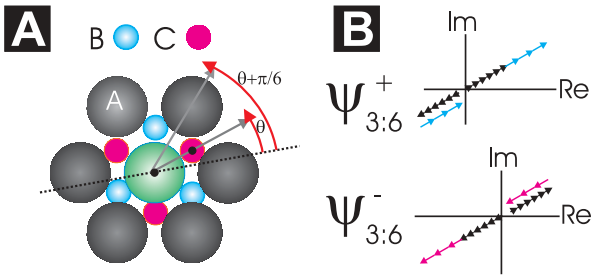

Figure 3.6. The $\psi_{3:6}$ criterion: (A) In two subsequent layers, the angle θ between an imaginary bond between a particle and a next neighbour at a B or C position is clearly shifted by $\pm\frac{\pi}{6}$ relative to a next neighbour on a lateral position A. As a result of the factor 3 in the exponent of the ψ_3 vector, a rotation of $\frac{\pi}{2}$ is required. Furthermore ψ_6 rotates by 6θ whereas ψ_3 only rotates by 3θ, which requires a second rotation. (B) To quantify the extent of disorder for both AB and AC, both $\psi^{+}_{3:6}$ and $\psi^{-}_{3:6}$ are needed, since the order in both layers contributes to the total deformation.

process and the fact that we only studied dislocations relatively close to the wall. We did find related defects which are lattice lines ending at a line-defect as shown in Fig. 3.5E. In this case, the neighbouring lattice lines both shift towards a new lateral position, but neither one passes two lateral positions but a line-defect is formed instead. Line-defects themselves also dissolve into the lattice at times, which is coupled with the change of lateral position of one of the line-defect lattice lines. With the naked eye, these deformations are not easily spotted but we have developed an algorithm to identify stacking transitions, which are usually coupled to changes in lateral position.

3.4. Localization of Stacking Transitions

The gradual character of the continuous transition makes a specific localization algorithm nearly impossible. Instead we use a method which distinguishes between AB and AC stacking. We introduce the inter-plane bond order parameter ψ_3:

$$\psi_3^{\pm}(\vec{r_i}) = \frac{1}{N^{\pm}} \sum_{j^{\pm}}^{N^{\pm}} e^{3i\theta(r_{ij}^{\pm})}. \tag{3.4}$$

Here, a particle i is projected in the hexagonal layer above (+) or below (-). The summation j runs over all $N^{\pm}$ next neighbours in the layer above or below of the given particle i. The angle between the bond vector connecting the particle with next neighbour $j^{\pm}$ and a fixed arbitrary reference axis is defined as $\vec{r}_{ij^{\pm}}$. The absolute value of ψ_3 is a representation of the crystallinity of the particle configuration. More importantly here, its argument γ_3 is a representation of the crystallite orientation and the stacking direction. The arguments of ψ_3 for AB and AC stacking are shifted by π, which suffices to distinguish between AB and AC transitions for two consecutive

layers and can be used to identify transitions within a layer. To quantify the extent of (dis)order between two consecutive layers however, we need to incorporate the in-plane bond order parameter ψ_6 as well:

$$\psi_6(\vec{r_i}) = \frac{1}{N}\sum_{k}^{N} e^{6i\theta(\vec{r_{ik}})}. \tag{3.5}$$

The summation k runs over all, in total N, in-plane nearest neighbours of particle i. $\theta(\vec{r}_{ik})$ is the angle between the bond-vector $\vec{r}_{ik}$ between particles i and k and a fixed arbitrary reference axis. The absolute value of ψ_6 represents its crystallinity (with $|\psi_6|$ on average 0.4 for a fluid and $|\psi_6| = 1$ for a perfect crystal); γ_6, the argument of ψ_6, represents a crystalline particle's orientation. If the reference axis for ψ_6 is aligned along a lattice line, the argument for ψ_3 is shifted by $\frac{\pi}{2} + 3\theta$ relative to this reference axis, as sketched in figure 3.4. We therefore define $\psi_3(\gamma_3 \pm \frac{\pi}{2})$ as the ψ_3 vector rotated by $\pm\frac{\pi}{2}$. For any other reference axis, we additionally need to compensate for the different factors in the exponent in equation (3.4) and equation (3.5), which cause ψ_6 to rotate twice as fast as ψ_3. This can be accounted for by rotating back ψ_6 by half of its argument, which we will denote by $\psi_6(\frac{\gamma_6}{2})$. We combine equation (3.4) with equation (3.4) to distinguish AB and AC stacking in between two subsequent layers:

$$\psi^{\pm}_{3:6} = \frac{1}{2}[\psi_3(\gamma_3 \pm \frac{\pi}{2}) + \psi_6(\frac{\gamma_6}{2})], \tag{3.6}$$

which results in an absolute value of 1 for (the arbitrarily assigned) perfect $AB(+)$ and $AC(-)$. While equation (3.6) represents a close expression for distinguishing the stacking direction, it is computationally cheapest to distinguish between AB and AC by using the argument of equation (3.4) and based on that use either version of equation (3.6) to quantify the extent of disorder by applying both rotations to only one vector. For analysis, we additionally use the constraint that $|\psi^{\pm}_{3:6}|$ should be 0.9 or larger, based on at least 1 particle in both the layer below and the layer above. It includes the orientation of two consecutive hexagonal planes. Note that deformations in z are not measured in this method, only the difference in orientation of the consecutive planes are incorporated. Eq. (3.4) can be exploited to identify stacking type and direction for FCC and HCP as well, by adding the vectors resulting from projecting the particles in the layers above and below.

$$\psi^{\pm}_{3:3} = \frac{1}{2}[\psi^{+}_{3} \pm \psi^{-}_{3}] \tag{3.7}$$

For full details, see Chapter 2. Stacking can now easily be assigned: $\psi^{\pm}_{3:3}$ varies between 0 and 1. Either FCC (-) or HCP (+), can be detected as such, as well as the stacking direction, which we index by 1 and 2. The determination of the direction can be obtained through $\psi^{+}_{3} + \psi^{-}_{3}$, which gives peaks separated by π for the distinct HCP_1 and HCP_2 directions. Similarly, $\psi^{+}_{3} - \psi^{-}_{3}$ can distinguish between FCC_1 and FCC_2. For analysis, we additionally use the constraints that either $|\psi^{+}_{3:3}| \geq 0.9$ (HCP) or

$|\psi^{-}_{3:3}| \geq 0.9$ (FCC). Next neighbours are assigned using the 2D pair correlation function $g(r)$:

$$g(r) = \frac{1}{\rho 2\pi |\vec{r}|} < \sum_{i \neq j} \delta(r - |\vec{r_i} - \vec{r_j}|) >, \tag{3.8}$$

with ρ the particle density and r the distance between particles i and j. The first peak of $g(r)$ is fitted to a Gaussian to obtain an estimate of the lattice constant a. The cut-off distance out-of plane next neighbours is obtained by projecting particles in the layer above or below and calculating $g(r)$, as in Chapter 2. Confocal images of several consecutive layers are shown in figure 3.7. The layer number starting with $L1$ at the sample bottom is indicated for all images. Both lattice deformations and line-defects are present in the images. We find the transitions with the $\psi^{\pm}_{3:6}$ criterion, indicating stacking transitions. The widths of these deformations vary from almost direct transitions through line-defects (left of the images in figure 3.7), to gradual transitions (right side of the images $L12$ infigure 3.7. Note that line-defects in the other layer involved in the determination of the stacking direction show up as single particle wide black lines. The $\psi^{\pm}_{3:3}$ method (bottom of figure 3.7) does not directly pinpoint the deformation between two layers since crystal stacking type (HCP or FCC) is based on 3 rather than 2 layers. The stacking transitions still clearly show up however, meaning we have developed efficient criteria for distinguishing AB and AC stacking directions, characteristic for both discontinuous and continuous transitions.

3.5. Characterisation of the Continuous Stacking Transitions

Questions that arise are:

(I) How does the deformation that characterizes the lateral transition affect stacking?

(II) What is the effect of these deformations is on crystal layers further away?

(III) Does the deformation have a well-defined width?

We will first characterise the lattice deformation itself, by tracking the lattice deformation using equation (3.5). Since the deformation to another lateral position occurs gradually, the lattice orientation locally changes during the transition, as sketched in Fig. 3.8A. For a deformation of the lattice from an A to a B position this results in a displacement of the lattice line by $\Delta_0 = \frac{a}{2\sqrt{3}}$, which is the spacing between two consecutive lattice lines at lattice positions A and B, see Fig. 3.8A. For sixfold surrounded particles, $\arg(\psi_6)$ is a measure of the local lattice orientation, which is given by $\frac{1}{6}\arg(\psi_6)$. We calculate $\arg(\psi_6)$ for all particles with six in-plane next neighbors, relative to the lattice line. To exclude other stacking transitions from showing up in our curve and for statistical averaging, we additionally divide the crystal in areas of typically 10 lattice lines. The average local orientation $\langle \arg(\psi_6) \rangle$ at a given position along the line is obtained from bins with a width d of the order of the lattice constant a.

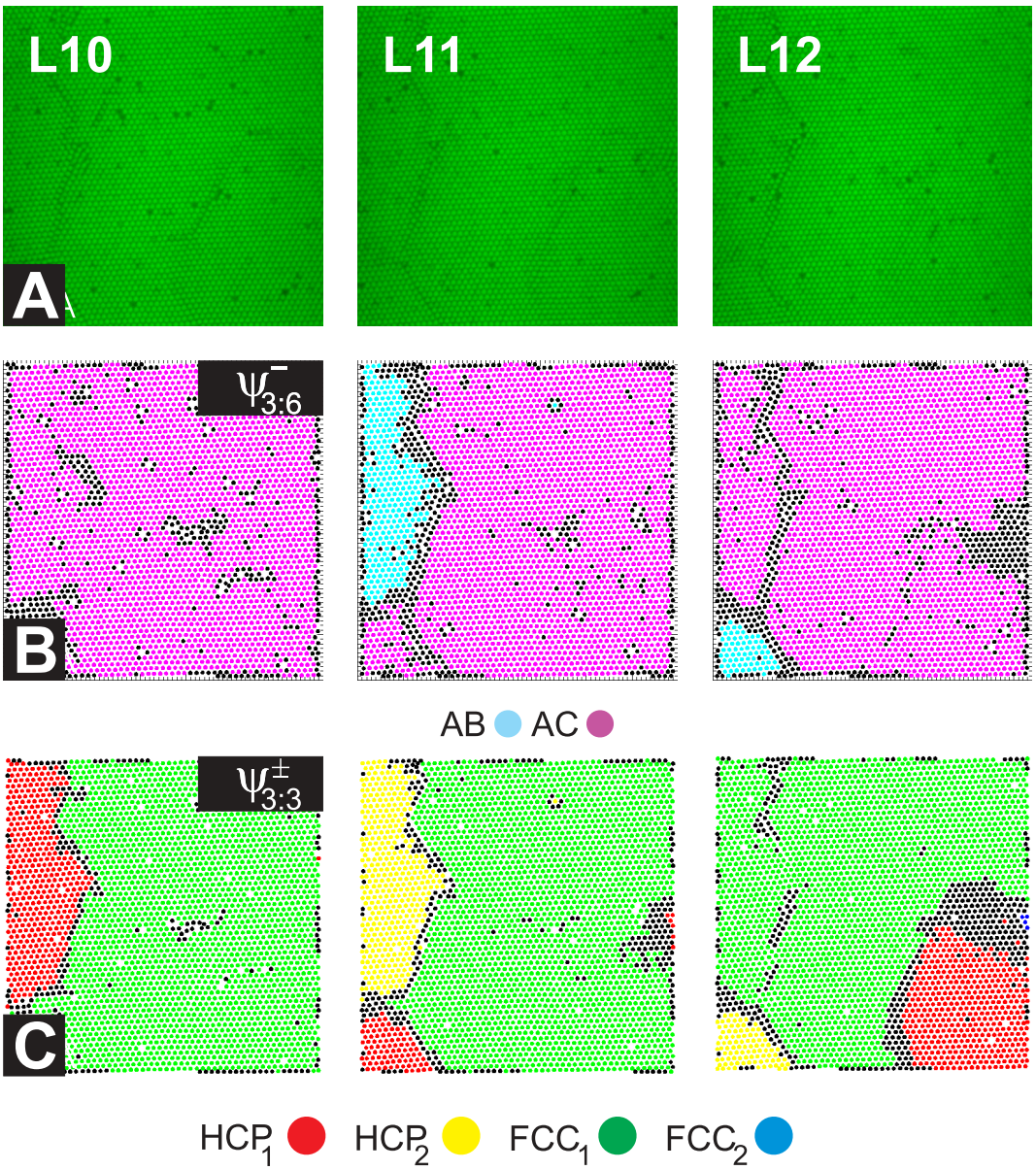

Figure 3.7. Identifying Stacking Transitions. Top: Confocal images of consecutive layers (e.g. L10 refers to the 10^{th} layer above the cover slip) with both line-defects and dislocations. Middle: Representations of $\psi_{3:6}^{\pm}$. Filled circles in cyan and magenta indicate AB and AC stacking. For black filled circles stacking could not be assigned, usually indicating a stacking transition. It is obvious that the widths of the transition vary considerably. Bottom: The incorporation of the argument of ψ_3 results in a better definition of a stacking island, since the stacking direction is involved. Green, red and yellow filled circles correspond to FCC_1, HCP_1 and HCP_2 stacking. No stacking could be assigned for black filled circles. FCC_2 particles are not present in these particular images.

The procedure is sketched in Fig. 3.8B. The magnitude of the total lattice deformation Δ between points x_1 and x_2 along the lattice line is then given by the integral in the limit of small angles:

$$\Delta = \frac{1}{6}\int_{x_1}^{x_2} \langle \arg(\psi_6) \rangle dx = \frac{1}{6}\sum_{n=1}^{N} \langle \arg(\psi_6) \rangle_n d. \tag{3.9}$$

Here, x is the distance covered along a lattice line, $\langle \arg(\psi_6) \rangle_n$ is the average orientation of bin n and N is the number of bins. When we track Δ for the deformation highlighted in Fig. 3.8B as a function of x_2 as in Fig. 3.8C, the deformation for a single layer ($L14$) is much smaller than Δ_0. By including the deformation of $L13$, the total displacement is much closer to Δ_0. The lattice deformation due to the Shockley dislocation is spread (unevenly) across two layers, as sketched in Fig. 3.8D and the deformation persists in nearly all layers below and above as shown in Fig. 3.8C. Across this continuous transition, a new part of the lattice with lateral positions A', B', C' starts, severely reducing positional order. In reciprocal space, this should contribute to the broadening of higher q-peaks of the structure factor, as is indeed observed in Fig. 2(B) in Chapter 2, a manifestation of second type disorder [96]. In comparison, line-defects reduce positional order much less: in their case the crystal switches between the same lateral positions.

As we move through the crystal, the deformation will eventually either end at the wall, end at the grain boundary, or deform again when another lattice deformation occurs. The latter is the case for $L06$ in Fig. 3.8C. At the sample bottom, there are much less restrictions to how a lattice can be deformed. If a crystal were to start growing at such a location, the first layers could easily function as a deformed crystal template for further growth. This has an important consequence for the stacking transitions in such systems. In figure 3.9 six consecutive layers are shown. Since the deformation takes place in two consecutive layers, the stacking transition for particles in either of those layers, since stacking is based on the layers which are deformed with respect to one another. For particles that are not located in one of the layers which are deformed with respect to one another, the lateral transition still takes place , whereas the stacking transition does not. As for the line defect in Chapter 2, twinning may occur, but the occurrence of in-plane stacking disorder does not necessarily induce an overall change in the crystal direction. This sufficiently answers the first two questions stated at the beginning of this section.

To quantify the total lattice distortion we determine the relative deformation τ between two consecutive layers, which is given by

$$\tau(x_2, x_1) = \Delta_a(x_2, x_1) - \Delta_b(x_2, x_1). \tag{3.10}$$

Here, the a and b subscripts referring to the layers between which the lattice is deformed. The results for three transitions are presented in Fig. 3.10A. The specific lattice deformations considered here are indicated in the $\psi^{\pm}_{3:6}$ representations in Fig. 3.10B and C.

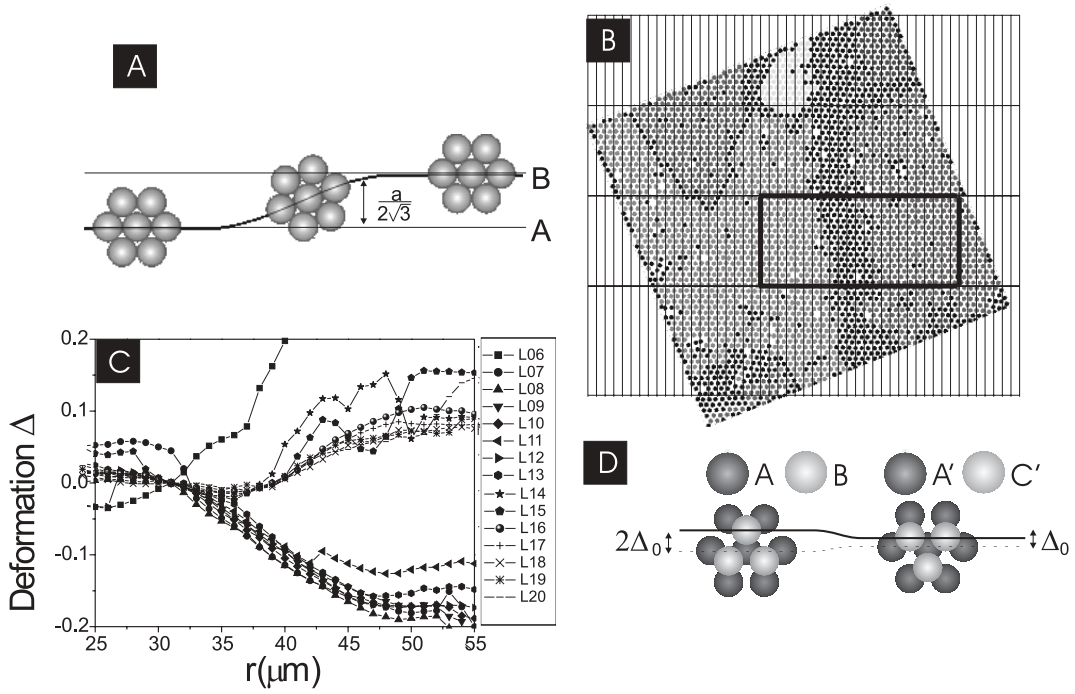

Figure 3.8. Characterisation of the rotation between consecutive layers. (A) Since the lateral position changes gradually, the lattice orientation, $\arg(\psi_6)$ changes as well for the particles in the region where the stacking transition occurs. (B) In order to pinpoint the stacking transition, we track the lattice deformation along one of the lattice lines. We divide the lattice in regions for which we calculate $\langle \arg(\psi_6) \rangle_{area}$. The area studied for lattice deformation is highlighted. (C) The lattice deformation for several consecutive layers. The deformation between two layers clearly affects both layers. The deformation persists in the layers above and below, up to as far as we can track the deformation or until another deformation occurs in the lattice. The layer numbers in the legend $L\#$ are an index for the distance to sample bottom, starting with $L01$ the first layer. (D) A sketch of a lattice deformation between consecutive layers: both layers contribute to the transition from AB to AC stacking, or rather from AB to $A'C'$ since the deformation disturbs positional order and a new reference lattice is created.

The resulting τ can be fitted to a switch function

$$\tau(r) = \frac{A}{2} \tanh \frac{r - r_0}{\xi} + \tau_0 + \frac{A}{2} \tag{3.11}$$

All variables here have a physical interpretation. r is the distance covered along the (11) axis, A is a measure for the total displacement of the lattice lines during the lattice deformation (which should ideally be Δ_0), r_0 is the location of the dislocation line and ξ is a measure for the length along the lattice line axis over which the lattice is deformed. τ_0 is an offset parameter for the net lattice deformation that has taken place further

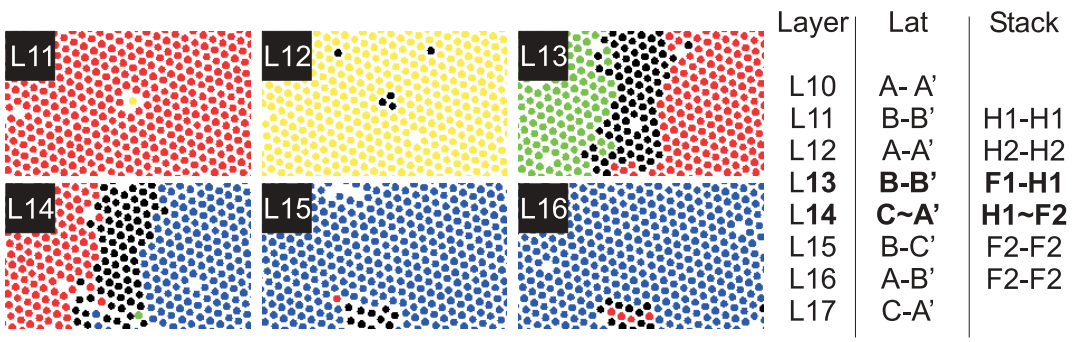

Figure 3.9. Continuous transitions and stacking. Six consecutive layers including the stacking transition studied in detail in figure 3.8. Layers above the sample bottom are indexed as $L\#$ with # referring to the layer number, starting with 01 at the sample bottom. The lattice deformation occurs between $L13$ and $L14$. Colours refer to the stacking assigned using the $\psi^{\pm}_{3:3}$, again with red, yellow, green, blue and black dots representing HCP_1, HCP_2, FCC_1, FCC_2 and no stacking assigned. The lateral positions and stacking types (H=HCP, F=FCC) are summarized in the right panel.

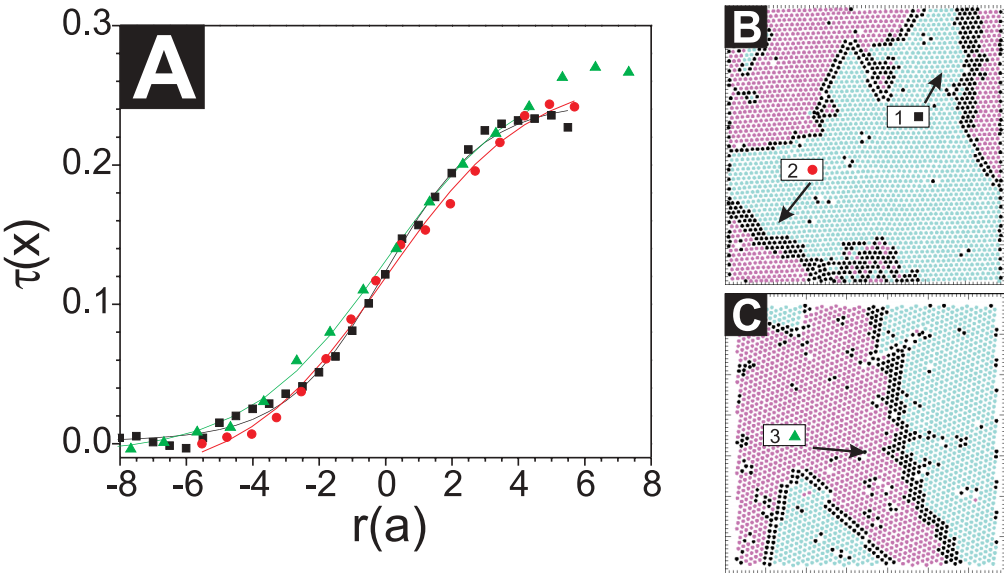

Figure 3.10. Relative deformation. (A) To extract the width of the relative deformation, the net deformation between the two layers is determined. For the three examples studied, the curves are similar, but not identical. In (B) and (C) the $\psi^{\pm}_{3:6}$ representations of the deformations studied are shown. Filled circles in cyan and magenta indicate AB and AC stacking. For black filled circles stacking could not be assigned, usually indicating a stacking transition.

away in the lattice. We additionally define $\xi_{95} = \ln(39)\xi$ which is the interval over which 95% of the deformation takes place. It gives more insight into the actual length over which the deformation takes place than ξ itself. Three Shockley partials are highlighted

in Fig. 3.10B and C. The results for the fitting parameters ξ_{95} and A of equation (3.11) of these deformations are summarized in table 3.1. The obtained curves all three cases studied are fairly similar but the total lattice deformation is substantially less for the first case. As a result the widths ξ_{95} vary somewhat. The ideal relative deformation is characterized by a deformation Δ_0 for the transition between lattice positions. A simple correction for the amplitude A with the ideal amplitude Δ_0 makes the widths even more similar (table 3.1). They are quite large, of the order of 8-9 particle diameters. Given the large amount of transitions present in the sample, this indicates that large parts of the lattice are somewhat deformed.

Table 3.1. Fitting parameters for the relative lattice deformation

Transition No.	A	ξ_{95} $[a]$	$\frac{\Delta_0}{A}\xi_{95}$ $[a]$
1	0.277	7.6	7.89
2	0.316	9.1	8.13
3	0.304	8.6	8.26

3.6. The Full Island Boundary

In Chapter 2 we presented the line-defect as boundaries between islands of different stacking. Here we have shown that continuous stacking transitions also exist. Both the discontinuous and continuous transitions have dominant screw dislocation character, which can be explained by the lower elastic energy of the screw dislocation relative to the edge dislocation. In order to investigate the full island boundary, we have depicted several examples in figure 3.11. We have used equation (3.6) to distinguish between AB and AC stacking. Note that this means that the stacking transition takes place in either the layer itself, or in the layer above or below, since the criterion is still based on two layers. Since lattice deformations take place in both layers Fig. 3.8C, this is no problem for continuous transitions, but line-defects in the layer above or below may still show up as black single particle wide lines.

The island boundaries frequently consist of a combination of both types of island boundaries. In some cases the full boundary is made up of line-defects only (left bottom corner of Fig. 3.11A) or of a full continuous transition (right of Fig. 3.11A). For obtuse island boundaries, a combination of both types of boundaries is required as in Fig. 3.11B. The system apparently prefers the continuous transitions over broad line-defects as in Fig. 3.1B. The large amount of unused lattice space is nearly enough to squeeze a particle in. Apparently this is exactly what the system does, thereby deforming the lattice. Sometimes the boundary is straight but still changes from a line-defect to a continuous transition as in Fig. 3.11C. The combination of several lattice deformations may even result in complicated island boundaries such as in Fig. 3.11D, with two consecutive continuous transitions taking place within a confined area.

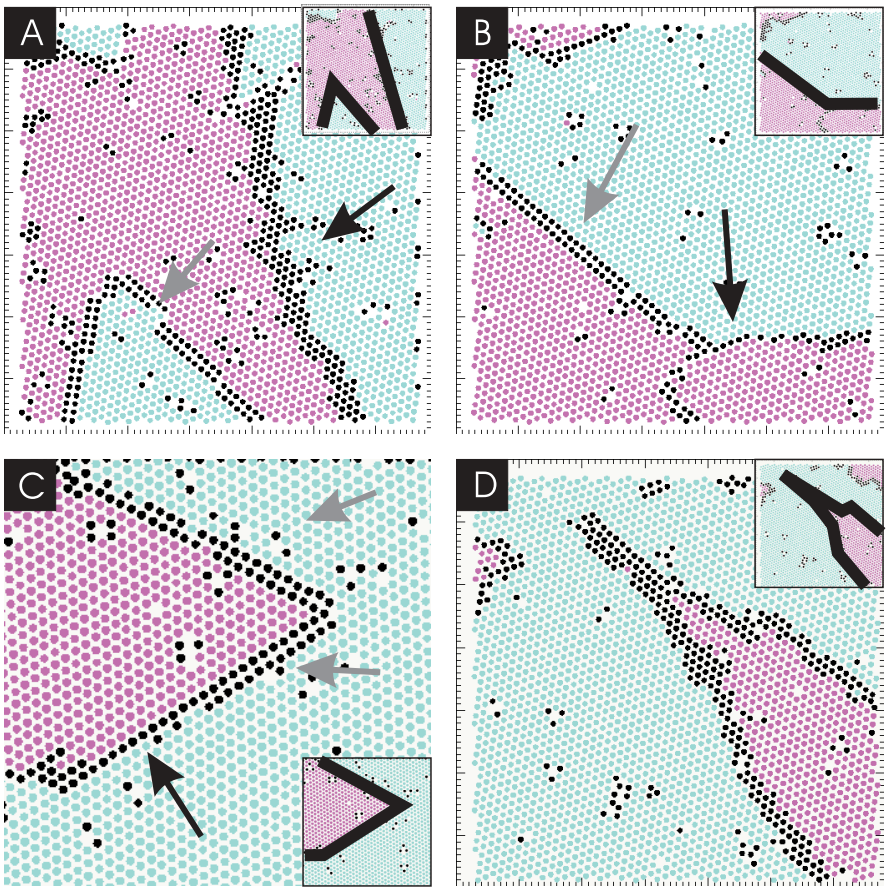

Figure 3.11. The full island boundaries. The island boundaries in hard sphere crystals are a combination of discontinuous line-defects (highlighted by grey arrows) and continuous transitions (highlighted by black arrows. The insets show the tentative shapes of the island boundaries. The colours refer to the stacking direction AB or AC, as explained in e.g. figure 3.4. (A) Both an discontinuous island boundary through a line-defect, and a continuous transition. The line-defect features a sharp edge of 60^0 (B) An obtuse angle occurring through a transition between a line defect and a continuous transition. (C) A complex island boundary is depicted, along which a line-defect gradually changes into a continuous transition. (D) A complex combination of continuous transition forms the island boundary.

3.7. Vacancies and Stacking Transitions

From the confocal images and from the analysis in Chapter 2, we find high concentrations of vacancies. In this section we investigate whether the stacking transitions and high vacancy concentrations are related. To pinpoint vacancies in the crystal lattice, we use the method in which an "imaginary particle" is positioned in between particles which are at distances of $\sim 2a$, as described in Chapter 2. In Fig. 3.12A, we also show the first peak of the radial distribution function $g(r)$ within the hexagonal plane. When

the distribution function is calculated for particle-vacancy pairs, the first peak markedly shifts towards the left by $\sim 3\%$ compared to the normal $g(r)$, for both solvents studied. This is a result of the osmotic pressure imbalance caused by the missing particle in the lattice. In a single configuration this hardly shows up since the deformation is of order of the polydispersity, which can be deducted from the overlap of the first peak of the regular and vacancy $g(r)$ distributions as well as through results presented in [97]. For some more detail on the distributions of vacancies, we determined the vacancy concentrations within HCP, FCC and defect regions as well. We identified these regions using the criteria developed earlier. We call a region a defect region if $|\psi^{\pm}_{3:3}|$ <0.9. The resulting vacancy concentrations are 2-5 times higher in defect regions than they are in FCC or HCP regions, depending on the sample. There, we also show the fraction of FCC stacked particles α (of all particles to which a stacking could be assigned).

Table 3.2. Vacancy concentrations in several parts of the crystals, as well as the FCC fraction α.

	HCP	FCC	Defect	α
$\phi_{vac}(\mathrm{PD600_{30}})$	0.0086	0.0079	0.031	0.75
$\phi_{vac}(\mathrm{PT600_{40}})$	0.0091	0.0072	0.029	0.66

The data clearly shows that the vacancy concentration is much higher in the defect regions compared to the HCP and FCC regions. The lattice deformations near these vacancies are on average identical in all regions, although the distribution of distances to next neighbours is $\sim 20\%$ broader in the defect regions, likely due to lattice deformations, see Fig. 3.12B. On the other hand, a locally higher polydispersity could also contribute to the increased width. Most of the decreased width results from the number of agglomerations of vacancies in the defect region, which decreases the height of the first peak of the vacancy $g(r)$ (Fig. 3.12B) and the number of vacancy next neighbours, which is 11.56 averaged over all samples in stacking regimes versus 11.21 in the defect regimes. The increased concentrations and widths both suggest a possible mechanism to enable lattice deformations through vacancies. It supports the view that Frank dislocations may form due to the agglomeration of vacancies [90]

3.8. Conclusions

In-plane stacking disorder is both characterised by discontinuous transitions (Chapter 2) and by continuous transitions. Both the continuous and the discontinuous transitions have a dominant Shockley screw dislocation character. These continuous lateral transitions are characterized by a lattice deformation that can be traced in layers far away from the deformation, on both sides of the dislocated planes. As a result the hexagonal planes consist of multiple domains which possess lateral positional order

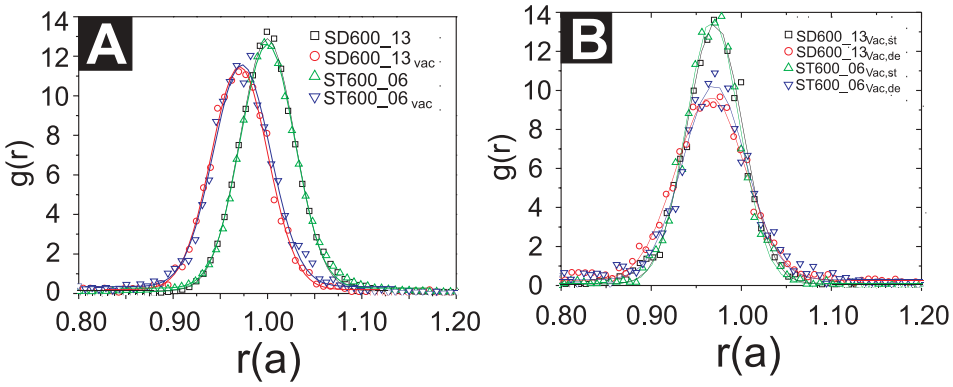

Figure 3.12. Positional order around the vacancy. (A) First peak of the g(r) calculated from particle positions (black squares, green triangles), and from the obtained vacancy positions (red circles, blue triangles) for $PD600_{30}$ (black squares, red circles) and for $PT600_{40}$ (triangles). The lines are the Gaussian fits. $PD600_{30}$ and $PT600_{40}$ subscripts refer to the sample. (B) First peak of the g(r) calculated from vacancy positions for which HCP or FCC stacking could be assigned (black squares, green triangles), and from vacancy positions for which stacking could not be assigned (red circles, blue triangles) for $PD600_{30}$ (black squares, red circles) and for $PT600_{40}$ (triangles). The lines are the Gaussian fits. $PD600_{30}$ and $PT600_{40}$ subscripts refer to the solvent. The *st* and *de* subscripts refer to the zones in the crystal where crystallinity can (stacking) and cannot (defect) be assigned respectively.

themselves, but not amongst each other. This distinguishes the continuous stacking transitions from the line-defects. The latter induce lattice positional disorder on the order of the lattice constant, but not on the order of the lateral lattice which consists of A, B and C positions. The full island boundary in fact consists of a mixture of continuous and discontinuous transitions. The island boundaries are furthermore characterised by a relatively high vacancy concentration, which points to a mechanism for the stabilization of lattice deformations.

3.9. Acknowledgement

This work resulted from a project with Andrei Petoukhov and our student Anke Leferink op Reinink. Janne-Mieke Meijer is acknowledged for part of the data acquisition. Piter Miedema is acknowledged for insightful discussions. Roel Dullens and Jan Hilhorst are acknowledged for a critical reading of the manuscript.

4

Grainsize Effects on Lateral Islands in Hard Sphere Crystals

Abstract

Due to the in-plane stacking disorder, random hexagonally closed packed hard sphere crystals consist of lateral islands with different lateral positions A, B, and C, and as a consequence, different stacking. We investigate the extent of lateral stacking disorder as a function of grain size, and as a function of the fraction of FCC-stacked particles α by laser scanning confocal microscopy and Monte Carlo simulations. We compare the simulations and microscopy data to relate stacking islands (2D domains with identical stacking type and direction) to lateral islands. Small crystals mainly contain single hexagonal planes, whereas larger crystals consist of a much larger number of lateral islands. Furthermore, the typical stacking island size is related to the FCC fraction. At high α, more FCC islands nucleate, and these are more likely to combine into larger islands than the HCP islands.

4.1. Introduction

Small crystallites are remarkably different from their large counterparts. The amount of particles at the surface is relatively high, which can drastically affect elastic [98, 99], optical [100], electric [101] and magnetic properties [102]. The change in properties is often coupled to a change in particle configuration. It is extremely difficult to study atomic systems on the single particle level, but colloidal systems are excellent reference systems: they are very similar to atomic systems [13] and enable 3D studies on the single particle level by confocal microscopy [33, 57, 76, 77, 103, 104] due to large particle size and their relative slowness. The phase diagram of colloidal hard spheres is based on excluded volume interactions only. The free energy difference between face-centered cubic (FCC) and hexagonally closed packed (HCP) structures is tiny for hard sphere crystals [22–24]: less than $10^{-3}k_BT$ per particle, where k_BT is the thermal energy. This may contribute to the frequent observation of a so-called random-hexagonal close-packed (RHCP) crystal structure in experimental hard sphere systems [19, 26–29]: the reorganization from RHCP to FCC structure is expected to take months to years [25,28]. Due to the variety of possible RHCP configurations, an additional gain in entropy can stabilize the RHCP structure for sufficiently small crystals [31].

As discussed in Chapter 2 and Chapter 3, the RHCP structure is characterized not only by randomly alternating FCC and HCP layers, but also by lateral islands with different lateral positions A, B and C, and as a result different stacking. Lateral islands (2D domains with identical lateral position A, B and C) and stacking islands (2D domains with identical stacking type HCP or FCC as well as identical stacking direction) are different quantities: stacking is based on the lateral position of three layers instead of one for lateral islands. In the previous chapters we were able to identify the line-defects and dislocations that form the boundaries between these islands, but we did not identify the typical island dimensions. Both types of transitions have a dominant screw dislocation character. Here, we investigate the extent of island formation as a function of grain size and as a function of the fraction of FCC-stacked particles α. We compare results obtained by confocal microscopy in sedimented hard sphere crystals with results of Monte Carlo simulations.

4.2. Experimental Section

Full details of our experimental methods can be found in Chapter 2. We prepared sedimented crystals of fluorescent, 0.6 μm diameter poly-methyl-metacrylate spheres [14], dispersed in two apolar solvents: a mixture of tetra chloromethane, tetralin and cis-decalin (0.35:0.35:0.30 v/v, TTC) and pure cis-decalin (De). The use of these solvents resulted in fractions of FCC α of ~ 0.6 (TTC) and ~ 0.7 (De), see Chapter 2. Crystals were grown from the sample bottom by sedimentation from intial volume fractions ϕ_0 of

0.4 (Sample $PT600_{40}$) in the solvent mixture and 0.2(Sample $PD600_{20}$), 0.3 ($PD600_{30}$) and 0.4 ($PD600_{40}$) in cis-decalin, as summarized in Chapter 3. Thin 2D cross sections of the sample were imaged with a Nikon Eclipse TE2000U laser scanning confocal microscope with a Nikon C1 scanning head in combination with an argon laser ($\lambda_0 = 488nm$) and an oil-immersion lens (Nikon Plan APC 100X, NA 1.4). The crystals' hexagonal layers were imaged from the glass sample bottom to sample heights of $\sim 30\mu m$, which corresponds to the first 20-30 layers of a crystal. Images were taken of complete grains ($PD600_{40}$, $PD600_{20}$), as well as within grains ($PD600_{30}$,$PT600_{40}$).

Table 4.1. Sample Details of the Prepared Crystals

Name	Solvent	ϕ_0	$Pe = \frac{\Delta\rho g R^4}{k_B T}$
$PT600_{40}$	TTC	0.4	$3\ 10^{-3}$
$PD600_{20}$	De	0.3	$9\ 10^{-2}$
$PD600_{30}$	De	0.3	$9\ 10^{-2}$
$PD600_{40}$	De	0.3	$9\ 10^{-2}$

4.3. Data Analysis

Particle positions were obtained by methods such as those used by Crocker and Grier [51]. We will now shortly explain how stacking islands were identified, and how particles within a single grain were isolated using IDL routines [105].

4.3.1. Identification of islands

Within a crystal layer, several islands with different lateral positions A, B and C can be present, as for example in the confocal image shown in Fig. 4.1A. Fitting such a layer to a grid of A, B and C positions is not straightforward. Although some lateral islands can be distinguished, as shown in Fig. 4.1B, over longer distance the method fails due to dislocations and slow lattice deformations, see Chapter 3. The polydispersity of the system likely enhances these effects [25]. The changes in lateral positions can be divided in discontinuous changes and continuous changes in lateral position. The discontinuous changes are characterised by line-defects which form the boundary between two lattice positions, such as illustrated in Fig. 4.1C, which are the subject of Chapter 2. The continuous changes are characterised by partial dislocations such as illustrated by the partial screw dislocation in Fig. 4.1D and are discussed in more detail in Chapter 3. Three consecutive layers are shown there, which show a marked transition of ABA stacking (left) to ABC stacking (right). The screw dislocation is characterised by a Burger vector with a direction parallel to the deformation line (the in and out of plane vectors between the first and the third plane are not shown). In practice, the two can occur simultaneously, as for example in the left bottom corner of Fig. 4.1A, where the line-defect gradually 'disappears' in the lattice. As we have shown in Chapter 3, the

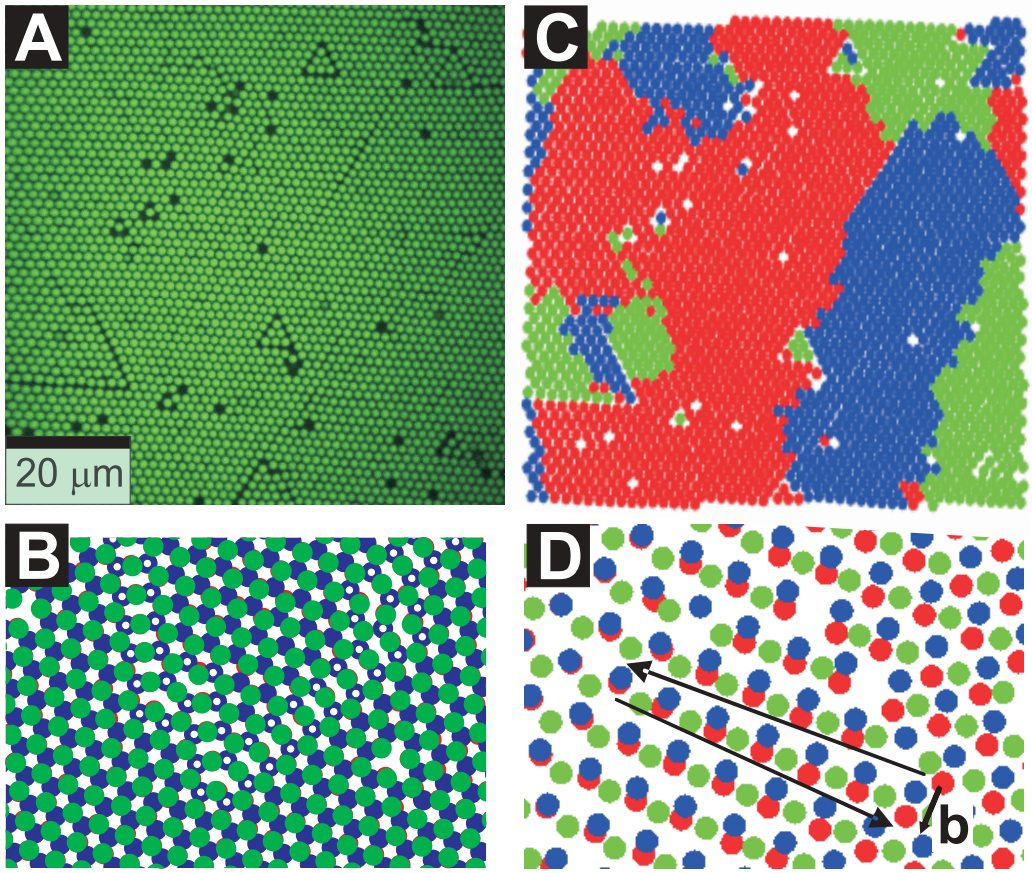

Figure 4.1. Lateral stacking disorder in hard sphere crystals. A) A typical confocal image of a close-packed crystal plane. B) A fit of the particle positions to an ideal lattice of A, B and C positions. Three consecutive layers (●, ●, ●) are shown in (C) and (D). In (C) two HCP islands are separated by a clearly visible line-defect (marked by open circles). In (D) a partial screw dislocation (with Burgers vector **b**, the in- and out of plane vectors are not shown) causes a continuous transition from one lateral position to the other. The particles in the middle layer gradually shift from ABA to ABC environment.

identification of lateral islands is therefore not feasible in large real-space datasets. A change in lateral position is usually coupled to a change in stacking (HCP or FCC). We review the orientational correlation method presented in Chapter 2 for the sake of the chapter's clarity.

The orientational correlation method compares the particle orientations of the neighbours of a particle j. All particles j in layer L are projected onto the layers $L+1$ (above) and $L-1$ (below), and next neighbours are identified. The relative rotation between the particles in layers $L+1$ and L-1 is 60^0 for FCC and 0^0 for HCP. To express this rotation the bond orientational order parameter $\psi_3^{\pm}$ is introduced:

$$\psi_3^{\pm}(\mathbf{r}_j) = \frac{1}{N^{\pm}} \sum_{k^{\pm}}^{N^{\pm}} \exp[3i\theta(\mathbf{r}_{jk^{\pm}})], \tag{4.1}$$

The summation $k^{\pm}$ runs over all $N^{\pm}$ next neighbours in the layer above (ψ_3^+) or below (ψ_3^-) of a given particle j. The angle between the bond vector connecting the particle with next neighbour $k^{\pm}$ and a fixed arbitrary reference axis is defined as $\theta_{\mathbf{rjk}}$. As a result, stacking can now easily be assigned: $\frac{1}{2}|\psi_3^+ + \psi_3^-| \simeq 0$ and 1 for FCC and HCP, respectively. Besides a stacking type, a stacking direction can be distinguished as well. For HCP this comes down to stacking of type HCP_1 of ABA, and stacking of type HCP_2 of BAB. Similarly, for FCC this results in stacking of type FCC_1 of ABC, and stacking of type FCC_2 of CBA. What direction is indexed by 1 or 2 is completely arbitrary, although it is insightfull to realize that for perfect FCC the stacking direction is identical throughout the system, whereas for perfect HCP the orientation alternates per layer. The argument of $\psi_3^+ \pm \psi_3^-$ can distinguish between the stacking directions of HCP and FCC. $\psi_3^+ + \psi_3^-$ results in peaks separated by π for the distinct HCP_1 and HCP_2 directions, as $\psi_3^+ - \psi_3^-$ does for FCC_1 and FCC_2. Examples of stacking assignments with this method can be found in Chapter 2. For analysis, we additionally use the constraints that either $|\psi_3^+ + \psi_3^-|$ (HCP) or $|\psi_3^+ - \psi_3^-|$ (FCC) should be 1.6 or larger, based on at least 1 particle in both the layer below and the layer above. For island size, a minimum island size of 10 particles was employed to reduce the noise. For samples $PT600_{40}$ and $PD600_{30}$, small islands at the border of the image were excluded from analysis since these are probably part of larger islands. The method is limited to grains with 111 planes parallel to the coverglass: no criterion to extract the 3D grain orientation is included.

Before we proceed we should point out that there are two important distinctions between stacking islands and lateral islands. First of all, a single line-defect separates two lateral islands, but causes stacking islands in the layer above and the layer below as well [93]. Stacking islands should therefore be significantly smaller than lateral islands. Similar arguments apply for a continuous transitions in lateral position, but in those cases the border between stacking orientations is broad and does not result in problems for identification. The distinction based on stacking orientation does not exclude all islands next to line-defects from having an identical stacking orientation assignment: for line-defects present in three consecutive layers [93], identical stacking is assigned to particles on either side of the middle line-defect. Furthermore, changes in lateral position due to continuous transitions such as in Chapter 3 can cause a multitude of lateral transitions without changing the stacking. This should mainly be important for large grains, where the typical distance over which lattice deformations occur is significantly smaller than the grain dimension. We will relate lateral island dimensions

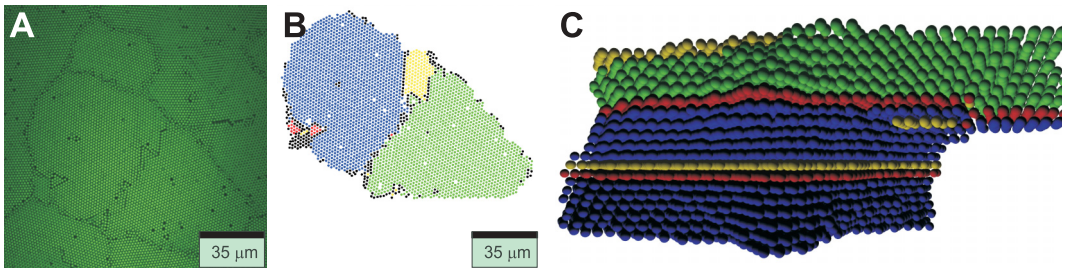

Figure 4.2. Grains Sizes and Stacking islands (A) Confocal image of a crystal with multiple grains present. (B) Stacking assignment of particles using the $\psi_3^{\pm}$ method, the particles in the grain are isolated using the argument of ψ_6. (●,●) FCC ;(●,●) HCP; (●) no stacking assigned. (C) 3D rendering of an isolated grain by, colour represent the stacking direction assignment as before.

D_{lat} and stacking island dimensions D_{FCC} and D_{HCP} as a function of crystal grain dimension D_{gr} by simulations later. We define the island dimension as the square root of the number of particles within it (either lateral or stacking) and the grain dimension D_{gr} as the square root of the average number of particles per layer of a grain.

4.3.2. Identification of Grains

To obtain good statistics of the island dimension as a function of D_{gr}, particles within a single grain can be isolated, using the argument of the local bond order parameter ψ_6:

$$\psi_6(r_j) = \frac{1}{N}\sum_{k=1}^{N} \exp[6i\theta(\mathbf{r}_{jk})], \tag{4.2}$$

where the summation k runs over all, in total N, nearest neighbours of particle j. $\theta(\mathbf{r}_{jk})$ is the angle between the bond-vector $\mathbf{r}_{jk}$ between particles j and k and an arbitrary fixed reference axis. The absolute value of ψ_6 represents its crystallinity; the argument of ψ_6 represents a crystalline particle's orientation. The latter can be used to isolate grains, since grain boundaries are characterised by an discontinuous change in crystal orientation. Since defects typically have a slightly different ψ_6 argument, an additional procedure is used to include all particles within the contours of the obtained grain. Defect particles outside of the grain which coincidentally have the same ψ_6 argument are excluded based on a next neighbour criterion. The isolation works quite well, as shown in figure 4.2. Figure 4.2C shows a 3D rendering of an isolated grain. The $\psi_3^+ \pm \psi_3^-$ method gives excellent insight into the structural changes

4.4. Simulations

On-lattice Monte Carlo (MC) simulations were performed using a layer-by-layer nucleation and growth model. To simplify simulations, we used a single lattice, which is the same for A, B and C lateral positions. Instead, the distinction between different

stacking position was performed by assigning a corresponding label (equal to 0, 1 or 2) to every occupied site j. This simplification might affect the structure at the island boundary, but was expected to reasonably reproduce the island structure. For more effective computation a list of free places was used, from which a random position j was selected at every elementary MC step. Then either a nucleation event, with a certain probability r_n or a growth attempt was performed. In all results presented here the nucleation rate $r_n = 2 \times 10^{-5}$ was used, which yields island sizes comparable to that in the experiment. The nucleation step had 100% acceptance and the position label was chosen such that the creation of the FCC environment had a chance of α_{N}. A growth step at position j was accepted if a randomly chosen neighbouring site k was occupied. The position label was then assigned to be the same as at the site k. In addition, the growth step was rejected if the position label for the new particle was equal to the lateral position in the layer below. Periodic boundary conditions (PBC) were incorporated for bulk models, however these were switched off to simulate the finite-size effects. The results of the simulations were averaged over N_{av} realizations (typically, $N_{\mathrm{av}} = 100$).

4.5. Results and Discussion

4.5.1. Bulk vs. Finite Size

Figure 4.3A shows a typical structure of a layer simulated with PBC. Since we do not include a possibility for structure re-organisation in our model, the boundaries between the islands appear rough. The fraction α_{end} of the FCC stacking in the resulting structure (Fig. 4.3B) is found to deviate from α_{N}, especially for the smallest and the largest values of α_{N}). This effect is related to the fact that an island (*e.g.* with C positions) can grow over a line-defect in the layer below (*e.g.*, between A and B islands). This changes the stacking environment and, as a result, α_{end} shifts closer to ≈ 0.5. Particles, which have at least one in-plane neigbour with a different position, are defined as defect particles. The density η of such defect particles is found to display a maximum around $\alpha_{\mathrm{N}} \approx 0.5$ (Fig. 4.3B). It decreases towards the extreme values, where the new islands are predominantly nucleated with the same stacking sequence and, therefore, have larger chance to merge without forming a line-defect.

Switching off PBC significantly affects the total number of defects and the positional distribution of defects (Fig. 4.3C). Near the grain boundary the defects are depleted. This is a result of growth from one nucleation site near the grain boundary. In the centre of the grain, growth from multiple nucleation sites usually occurs, resulting in defects where the growth fronts meet. The depleted defect zones in small crystals increase the value of α_{end} for the small grains, since relatively less line defects, that increase the line-defect concentration, occur in these crystals (Fig. 4.3D). When the grain size is smaller than the typical island size in the bulk, most layers consist of single islands and the resulting value of α_{end} is just determined by stacking probability α_{N} used in the

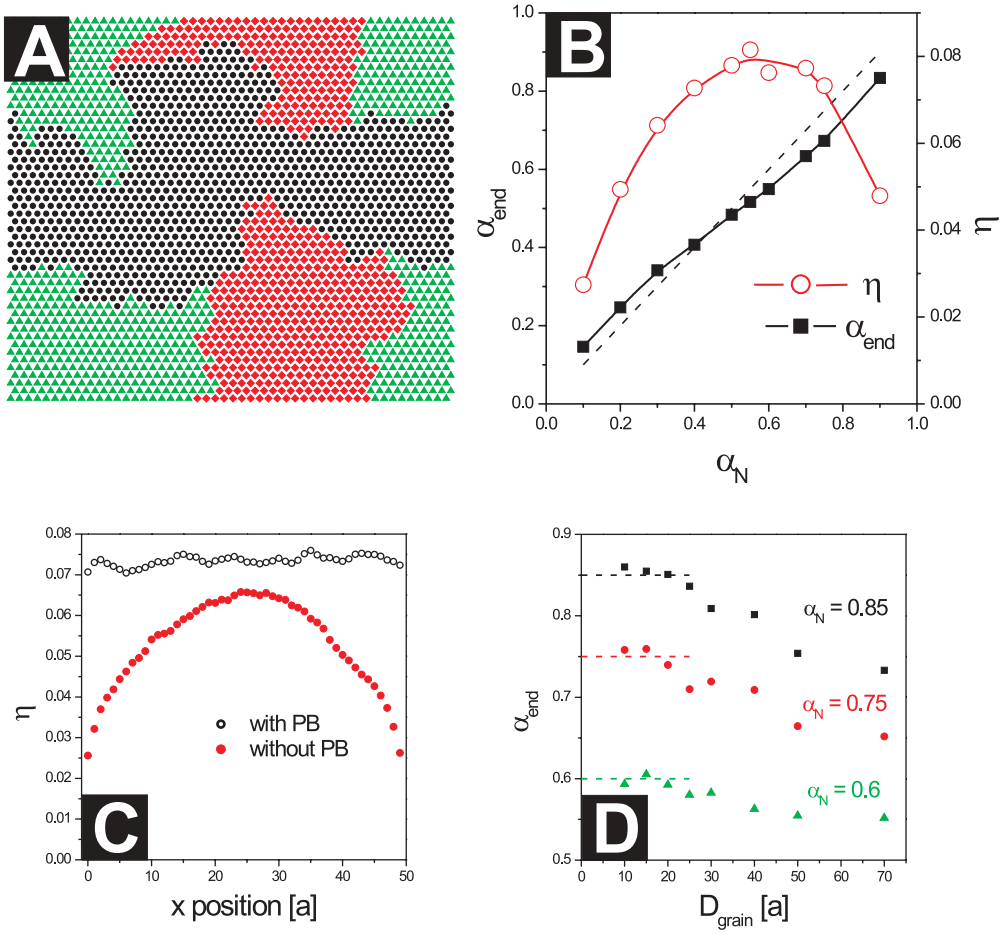

Figure 4.3. Simulation results for the bulk (A, B) and small grains (C, D). A) A typical example of island configuration in the bulk obtained with PBC for a layer containing 50×50 sites. Different symbols are used for particles with different positional label. B) Dependence of the resulting stacking probability α_{end} (■, left axis) and the defect density η (○, right axis) on α_{N}. Distribution of the defect particles along the horizontal x axis (averaged along the vertical y direction) with (○) and without (●) PBC. D) The resulting stacking probability α_{end} as a function of the grain size for three values of α_{N}. The horizontal dashed lines mark the α_{N} values.

nucleation step. Note that, in experiment, strain at the grain boundary might enhance the number of defects.

4.5.2. Stacking islands vs. Grain Size

We measured the stacking island dimensions of several grains in our samples and obtained by simulation. For our experiments, we used the $\psi_3^{\pm}$ method to identify the

stacking direction, with at least 20 crystal layers per grain. The first two layers contain more defects, which can be shown by measuring the amount of particles next to line-defects per layer, as in Chapter 2. Excluding the first two layers did not affect the measured island dimensions. The nucleation probability for FCC α_{N} was 0.75 for the simulations, typically resulting in $\alpha_{\mathrm{end}} = 0.7$ (Fig. 4.3D), similar to our experiments. In both cases, the island size initially rises with grain size (Fig. 4.4A). Above $D_{\mathrm{gr}} \approx 30$, the stacking dimension only increases very slightly (Fig. 4.4A) which means the number of islands starts to rise. D_{FCC} is usually significantly larger than D_{HCP}. Because relatively more FCC islands have nucleated within a layer, these FCC islands should more frequently combine to form larger islands than the HCP islands, which explains the observed difference in island sizes. In general the variety of island sizes found in the crystal increases with grain size. In small grains, line-defects usually run across grains. These defects are still present in larger crystals, but usually near the borders of the grain, with a sharp kink in it. Figure 4.4A contains datapoints of samples $\mathrm{PD600}_{20}$ and $\mathrm{PD600}_{40}$, and sample history clearly does not play a (large) role in determining the typical island size. The higher viscosity of the $\mathrm{PD600}_{40}$ sample slows down the particle flux by sedimentation, apparently leading to similar island nucleation and growth mechanisms.

4.5.3. Lateral islands vs. Stacking islands

We determined the relation between lateral islands and stacking islands by simulation for α_{N}= 0.75. The lateral islands were identified by procedures similar to those used to identify stacking islands, but now using the lateral position instead of the stacking to identify the island. We defined $k_{\mathrm{FCC}} = D_{\mathrm{lat}}/D_{\mathrm{FCC}}$ and $k_{\mathrm{HCP}} = D_{\mathrm{lat}}/D_{\mathrm{HCP}}$, which are plotted in Fig. 4.4B against D_{gr}. In the range of interest these relationships are approximately linear. For the smallest D_{gr} most crystal planes are perfect and $k_{\mathrm{FCC}} = k_{\mathrm{HCP}} = 1$. For much larger $D_{\mathrm{gr}} > 150$ (not shown) k_{FCC} and k_{HCP} plateau.

Using these relationships, one can determine the size D_{lat} of lateral islands out of the experimental found stacking islands dimensions as shown in Fig. 4.4C. The evaluation is separately performed on the basis of D_{FCC} and D_{HCP}. Using these results, the weight-average value of D_{lat} is also evaluated using the relative fractions of the islands of both type as the weight factor.

4.5.4. FCC Fraction

The overall stacking parameter α varies widely throughout the experimentally studied grains (Fig. 4.4D), but is on average ~ 0.7 for such crystallites. The large fluctuation of the values of α is related to the limited number of layers in the small grains. To simulate the latter effect, the value of α_{end} was determined for every realisation of the small grain, from which the average value and the standard deviation σ were determined after $N_{\mathrm{ave}} = 100$ simulations. The results are presented in Fig. 4.4D by the gray area,

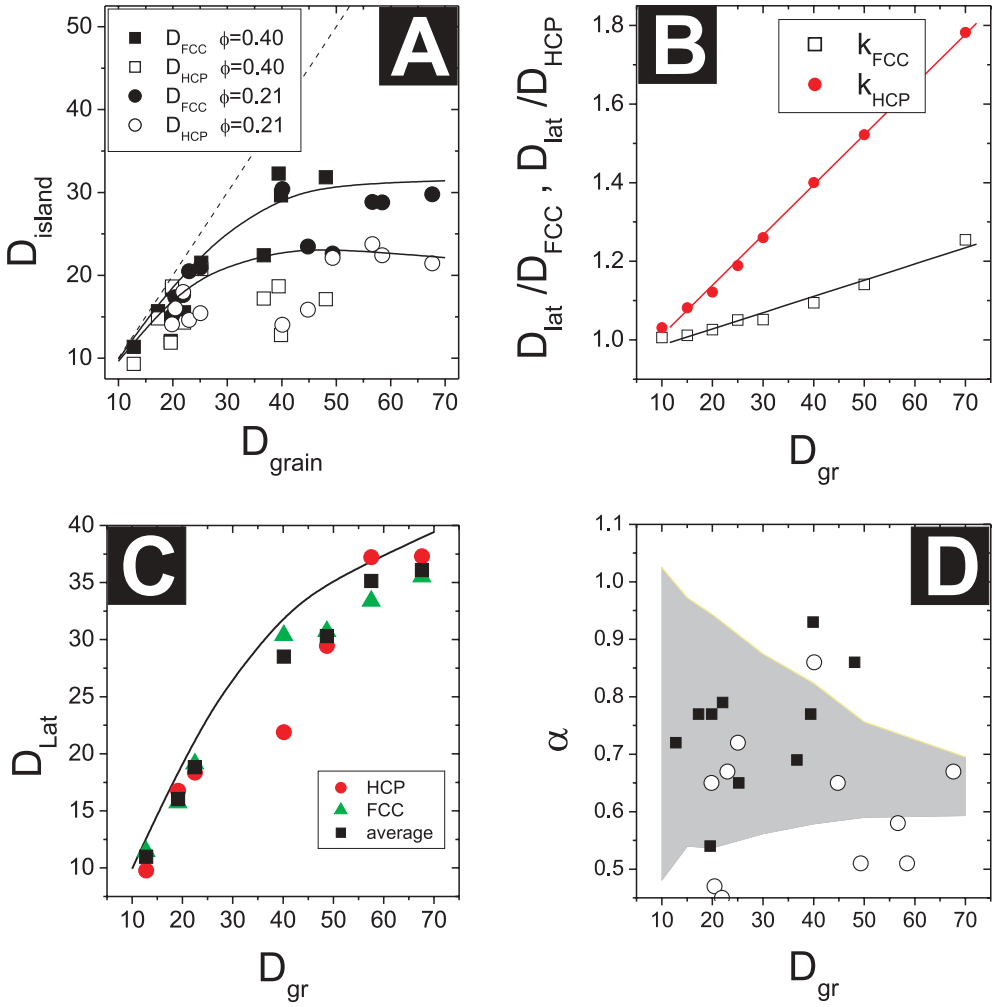

Figure 4.4. Grain size effects. A) The stacking island dimensions as a function of grain dimension; experimental FCC island dimension (filled points), experimental HCP island dimension (open points) and modelled FCC and HCP island dimension (lines). The squares refer to sample $PD600_{40}$ ($\phi_0 = 0.2$) and the circles to sample $PD600_{40}$ ($\phi_0 = 0.4$). B) The prefactors k_{FCC} and k_{HCP} as a function of grain dimension D_{gr}. C) The estimated lateral island dimension based on experimentally determined HCP stacking islands (●), FCC islands (▲) and the weight-average value (■) as function of grain dimension. The line presents the simulations results. D) The fraction of FCC stacked particles as a function of grain dimension for experimental data (points) and model data (grey shaded) for α_{N}=0.75, with grey area=2×standard deviation σ. (■) sample $PD600_{20}$; (○) sample $PD600_{40}$.

which covers $\alpha_{\text{end}} \pm 2\sigma$. Most experimental data points lie within this shaded area. On the other hand the scattered points seem to indicate a maximum around D_{gr} =45, which is close to the grain size $D_{gr} = 60$ for which simulations suggest that stacking faults anneal out most rapidly [25].

To investigate the effect of α on the island dimension, we additionally determined k_{HCP} and k_{FCC} for $\alpha_{\text{N}} = 0.6$ and 0.85. For the studied α_{N} the relationships are listed in table 4.2. α has a strong effect for these k-functions, resulting in significantly higher multiplication factors for HCP at higher α (as long as α is larger than ~ 0.5). The dependence of D_{FCC} on α is much less strong. Our results suggest that this dependency should be reversed when $\alpha < 0.5$.

Table 4.2. The relationship between the size of stacking and lateral islands.

α_{N}	k_{FCC}	k_{HCP}
0.6	$0.93 + 0.0064\, D_{\text{gr}}$	$0.90 + 0.0103\, D_{\text{gr}}$
0.75	$0.95 + 0.0041\, D_{\text{gr}}$	$0.88 + 0.0128\, D_{\text{gr}}$
0.85	$0.96 + 0.0028\, D_{\text{gr}}$	$0.84 + 0.0159\, D_{\text{gr}}$

The effect of α on the typical island dimensions was experimentally verified by measuring island sizes within several grains in TTC and De solvent. In TTC, α is ~ 0.6, slightly lower than in De where $\alpha \sim 0.7$. The crystals studied have estimated grain dimensions of 70-100 diameters, a regime where the typical stacking island size is not expected to change very much anymore with grain size (Fig. 4.4A). Since the image dimensions are identical for all measurements, we can compare the island dimensions found, even though part of the grain is not imaged (the lattice constants differ by $\sim 3\%$). The results are summarized in table 4.3. Both stacking island dimensions are smaller in TTC, which should be related to the kinetics of island nucleation and growth. In TTC, the density of the solvent is nearly matched to that of the particles, resulting in a slower flux of particles, and therefore to more nucleation events, resulting in smaller stacking island dimensions. In De, the distribution of island sizes is very broad, but FCC islands are clearly larger than HCP islands. What is important is that in De, the distribution of island sizes is very broad, but FCC islands are clearly larger than HCP islands. In TTC, both island sizes have decreased, but HCP and FCC are now much more similar, clearly supporting the observations from our simulations: The recombination of stacking islands with identical orientation indeed seems to lead to larger FCC islands at higher α.

Table 4.3. Two-dimensional Stacking island Sizes in TTC and De.

Sample	FCC island Dimension	HCP island Dimension
Decalin	26 ± 16	16 ± 12
TTC	16 ± 12	13 ± 9

4.6. Conclusion

We investigated the effect of grain size and of the fraction α of FCC particles on the size of the islands with lateral A, B or C position in RHCP sedimented hard sphere crystals by confocal microscopy and by Monte Carlo simulations. The islands were identified by assigning a stacking (HCP or FCC) and a stacking direction (1 or 2) to every particle. The dimensions of the stacking islands were correlated (islands with identical stacking) to lateral island dimensions (islands with identical lateral positions A, B or C). The lateral islands are larger than the stacking islands, since the stacking islands depend on lateral positions in three layers, compared to one layer for stacking islands. In small grains ($D_{\mathrm{gr}} <\sim 30$), the grains mainly consist of single stacking islands. In larger grains the amount of islands quickly rises and the island size seems to plateau. For $\alpha > 0.5$, FCC islands are significantly larger than HCP islands, as α approaches 0.5, the islands become smaller. This is related to the chance of finding an adjacent nucleated island with the identical stacking, which is lowest when $\alpha \sim 0.5$.

4.7. Acknowledgement

This work was a collaboration with Piter Miedema, Andrei Petukhov and Janne-Mieke Meijer. Peter Schall, Anke Leferink op Reinink and Roel Dullens are acknowledged for valuable discussions. Financial support of JMM by Schlumberger is acknowledged. Roel Dullens and Jan Hilhorst are acknowledged for a critical reading of the manuscript.

Part 2

Grain Boundaries in Geometrically Frustrated Hard Sphere Crystals

5

Hard Sphere Crystallization near Large Spherical Impurities

Abstract

Impurities affect the nucleation, growth and structure of crystals. We report the effect of large spherical poly-methyl-methacrylate impurities on the crystal nucleation and growth of monodisperse, hard poly-methyl-methacrylate colloids in a density and optically matching apolar solvent mixture. Crystallization, initiated either at the sample wall or at the impurity surface, was studied by imaging sequences of two-dimensional xy-slices in the plane of the impurity's centre with a laser scanning confocal microscope. Sufficiently large impurities can induce crystal nucleation. During crystal growth, impurities function as large immovable objects that eventually slow down growth. The resulting structure of the obtained crystals is characterized by relatively small grains.

5.1. Introduction

The crystallization process can be divided in three main stages: the nucleation, growth and the annealing of crystallites. During the first stage, small crystallites nucleate from the fluid. This is an activated process; it relies on a (rare) fluctuation, the formation of the sufficiently large, critical nucleus, with radius R. For the critical nucleus, the gain in free energy through the favourable chemical potential of the crystal ($\sim R^3$) outweighs the unfavourable creation of a solid-fluid interface ($\sim R^2$). Nucleation can proceed either through homogeneous nucleation in the bulk, or through heterogeneous nucleation at an external surface. This external surface can be thought of as for example an external wall [106], an impurity [107] or a pore [108]. A comprehensive recent review on homogeneous and heterogeneous nucleation in colloidal systems can be found in [109]. After the critical nucleus has formed, the crystallite is able to grow further, which relies on the flux of particles. The final stage occurs when crystallites meet and reorganize to form larger crystallites. This is a relatively slow process, since it either requires the growth of crystallites at the expense of others or the reorientation of a full grain.

Besides nucleation, impurities also affect the growth of crystallites as well as the eventual crystal structure, whether present as an unavoidable nuisance or intentionally added to modify a product or process. Depending on the nature of both the impurity and the main component(s), nucleation and crystal growth are either inhibited, suppressed or promoted [107, 110, 111].

For crystallization in such 'doped systems', the impurity/particle diameter ratio $\alpha \equiv (\sigma_i/\sigma_p)$ is a crucial factor. Flat walls facilitate crystallization [106,112–117]. Monte Carlo simulations show that onto hard curved impurities with $\alpha \geq 10$, crystal nucleation is observed in supersaturated hard sphere systems [107]. Furthermore, the overall translational order in two-dimensional (2D) arrays of macroscopic metal balls is significantly reduced by the presence of impurities with $\alpha \approx 3.9$ [118].

Colloidal hard sphere systems have proved useful to study the nucleation and growth [57] and sublimation [56] of crystallites, as well as the structure of a fluid -crystal interface [103]. By embedding a single large sphere into a supersaturated fluid of hard spheres, a simple geometrical model for studying the influence of impurities on crystallization is obtained. Here, we study the crystal nucleation, the crystal growth and the annealing stages in the vicinity of impurities. To this end we use fluorescently labelled spherical impurities and colloids in real-time at the particle level by laser scanning confocal microscopy.

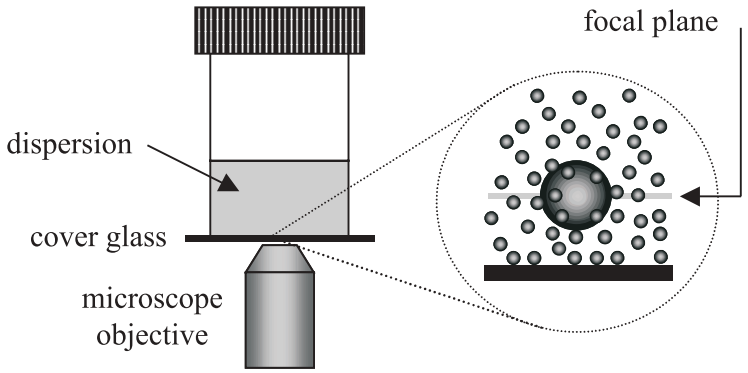

Figure 5.1. Experimental setup. Samples are imaged in the horizontal plane of the impurity's centre of mass. The focal plane is set up to 40 μm above the sample bottom, for studying heterogeneous nucleation and 15-25 μm for studying crystal growth.

5.2. Experimental system and technique

Poly-methyl-methacrylate (PMMA) particles, fluorescently labelled with 4-methyl amino ethyl methacrylate- 7-nitrobenzo- 2-oxa-1,3-diazol (NBD), were obtained by dispersion polymerization (mass density $\rho = 1.17$ g ml^{-1}, refractive index $n_D = 1.50$) [14]. The fluorescent dye is covalently incorporated into the polymer network of PMMA and the particles are sterically stabilized against flocculation by poly(12-hydroxystearic acid). 6% polydisperse 1.5 μm particles were mixed with a small amount (up to 1 wt. %) of very polydisperse (3-45 μm diameter) particles to obtain a system of monodisperse particles contaminated with a small amount of impurities of varying sizes. We will refer to impurities as I_α, with the subscript referring to the diameter ratio. A reference samples without impurities was prepared as well. The particles are dispersed in a density and optically matching apolar solvent mixture of cis-decalin (Merck, for synthesis, 30% v/v), tetraline (Merck, for synthesis, 35% v/v) and tetra chloromethane (Merck, for spectroscopy, 35% v/v), similar to [82]. The use of an optically matching apolar solvent mixture ($\Delta n_D \approx 0.0050$) results in hard sphere interactions. The low density difference (density difference $\Delta\rho \approx 0.01$ g ml^{-1}) between the solvent and the particles gives rise to a relatively large gravitational length $l_g = \frac{k_B T}{\pi/6\sigma_p^3 \Delta\rho g}$ of ~ 23 μm. Thin 2D cross sections of the sample were imaged with a Nikon Eclipse TE2000U laser scanning confocal microscope with a Nikon C1 scanning head in combination with an argon laser (λ_0=488 nm) and an oil-immersion lens (Nikon Plan APC 100X, NA 1.4). The ~ 0.3 ml samples were stored in small vials. The bottom of the vial was removed and replaced by a microscope cover glass (Chance Propper LTd., West Mids, England, 0.11 mm thickness), which was glued to the vial using an epoxy glue (Araldit AW2101) with hardener (HW2951). Sample weight was checked regularly to monitor the solvent evaporation, which was negligible.

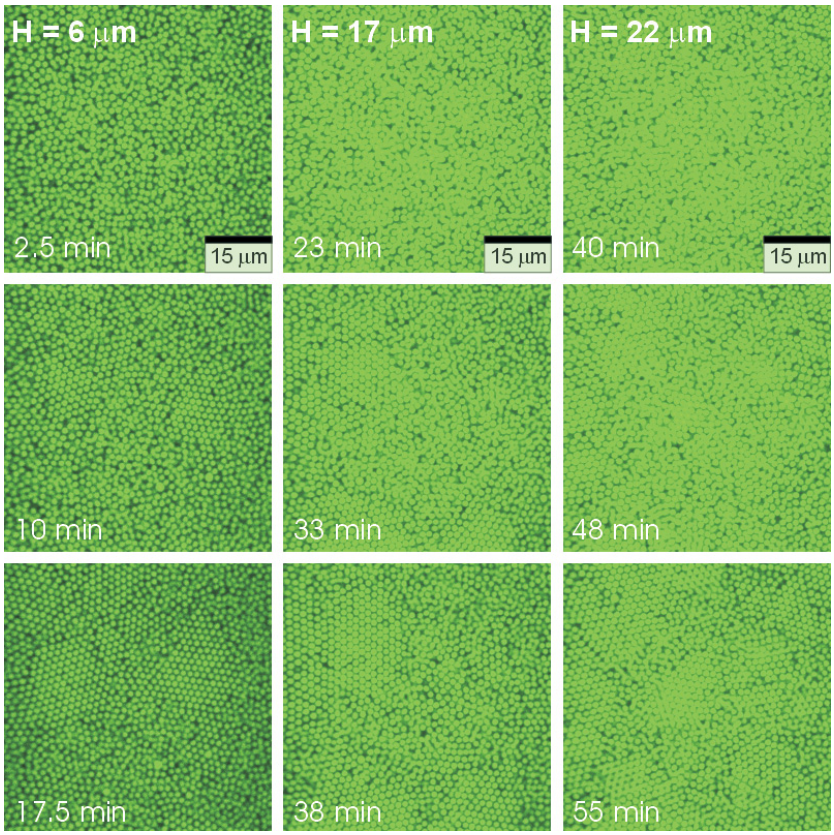

Figure 5.2. Confocal images of crystal growth in the sample without impurities at several heights H above the cover slip. The indicated times are after sample homogenisation.

In this work, we imaged the particles present at distances of 15-40 μm and 15-25 μm from the glass sample bottom (sample heights H), parallel to the flat sample bottom for respectively heterogeneous nucleation studies and for crystal growth studies. As we will subsequently show, the particle polydispersity (6%) increases the waiting time for homogeneous nucleation [106] and up to 25 μm from the wall only heterogeneous nucleation at the sample bottom and subsequent upward growth is observed. Upward growth from the sample bottom is therefore solely characterized by the hexagonal plane, which enables investigation of crystal growth by inspecting hexagonal order. By choosing a

Table 5.1. Details of the recorded confocal image sequences

Sample no	α studied	ϕ_c	H (μm)	Impurity concentration (wt%)
1	$5, 8, 11, 13, 21$	0.55	15	0.1
2	27	0.54	25	1
3	17	0.54	42	1

high volume fraction $\phi_c = 0.54$-0.55 – determined relative to the random packing density 0.66 [119] – the impurities become positionally locked in the crystal, which grows upward. Growth around the impurity can thus be studied over several hours with little impurity movement. Heterogeneous nucleation onto impurities can be studied before upward crystal growth approaches the field of view. Confocal image sequences were recorded in the horizontal plane of the impurity's center of mass, as schematically shown in figure 5.1. Details of all sequences are given in table 5.1. Particle coordinates are obtained by methods such as in [51]. The minimal translation and rotation of the impurity are tracked as well.

5.3. Results and Discussion

In this section we will investigate the dynamics of crystallization far away from impurities and near impurities. Before we discuss crystallization near the impurities, we briefly present results from the reference system without impurities.

5.3.1. Crystal Nucleation & Growth in the Sample Without Impurities

In Figure 5.2, confocal images are shown at different times for several distances H from the sample bottom. Visual inspection reveals that crystal growth starts later at greater heights and that the hexagonal plane is always parallel to the glass bottom wall. These observations suggest a scenario of heterogeneous crystal nucleation at the glass bottom wall and subsequent upward crystal growth. The hexagonal plane is parallel to the sample bottom, which enables us to quantify the crystallinity as a function of time through the two-dimensional orientational bond order parameter ψ_6 [120]:

$$\psi_6(r_i) = \frac{1}{N}\sum_{j=1}^{N} \exp[6i\theta(r_{ij})]. \tag{5.1}$$

The summation j runs over the N nearest neighbours of particle i. $\theta(r_{ij})$ is the angle between the bond-vector connecting the particles i and j and an arbitrary fixed reference axis. During crystallization, $|\psi_6|$ increases from $\sim 0.4 - 0.5$ for a typical fluid to ~ 1, which is the hexagonal order for a perfect crystal.

The crystallization curves shown for various heights in Fig. 5.3A are nearly identical in shape. Furthermore, the timescales at which $|\psi_6|$ starts to rise scale with the sample height, suggesting very similar growth mechanisms. Apparently, the particle polydispersity (6%) increases the waiting time for homogeneous nucleation [106], such that up to at least 25 μm from the wall only upward growth of the crystal, induced by heterogeneous nucleation at the sample bottom, is observed. During crystallization, the solid-fluid interface therefore rises due to crystal growth from the bottom. Precritical nuclei likely contribute to the growth, similar to [103].

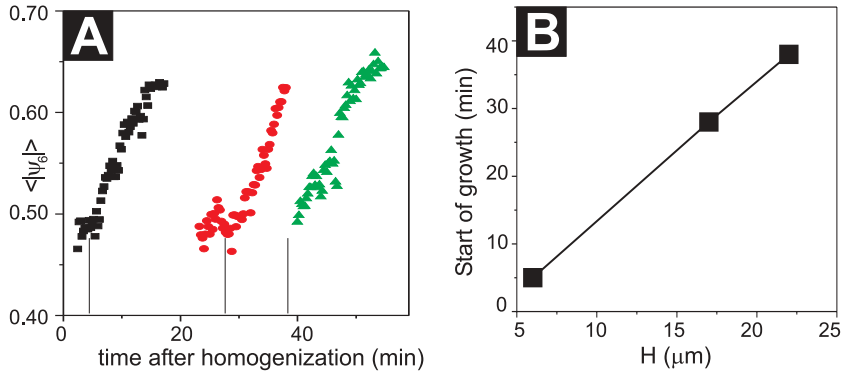

Figure 5.3. Crystal growth at different heights. (A) Heights: 6 μm (squares); 17 μm (circles); 22 μm (triangles). The vertical lines indicate the initiation times, which are obtained by extrapolating the growth curves to $\langle|\psi_6|\rangle = 0.48$, the average orientational order found in the fluid phase. (B) The initiation of crystal growth scales with the distance to the sample bottom H.

5.3.2. Heterogeneous Crystal Nucleation onto Impurities

As we will see in the subsequent section, most impurities studied do not induce nucleation in our setup. On the surface of a very large impurity (I_{27}), approximately three layers form (Fig. 5.4A1 and A2) before patches of crystal start to grow away from the impurity (Fig. 5.4A3). A series of images at different distances from the sample bottom was captured shortly before the onset of heterogeneous nucleation. The images clearly show that the system is fluid throughout the system at different heights. This confirms that it is nucleation, not crystal growth from the bottom, which is observed initially along the impurity surface (Fig. 5.4B). Pure serendipity – an impurity with a curvature that varies along the impurity surface – permits the investigation of the influence of local impurity curvature onto heterogeneous nucleation by a measurement on a single object (Fig. 5.4C). At the start of the recorded confocal image sequence, nucleation has already initiated onto this impurity with $\alpha = 17$ (Fig. 5.4C1). Crystal nuclei clearly have formed on the less curved parts of the impurity and grow away from the impurity (Fig. 5.4C3). In high curvature regions of the impurity surface, the disordered fluid phase is predominantly observed. A locally low curvature along a distance of a few particle diameters can apparently make an impurity act as a seed for heterogeneous nucleation.

To quantify the crystallisation, particles are divided in shells around the impurity, based on the distance to the impurity's surface. Averaging ($\langle\rangle$) over all particles of shell s, its hexagonal order parameter $\langle|\psi_6|\rangle_s$ is obtained, which is used to obtain a time-dependent crystal growth profile per shell (Fig. 5.5A). To analyze the nucleation onto spherical impurities, selections of the image were analyzed where the crystal's hexagonal plane was parallel to the field of view (Fig. 5.5B and C). The $\langle|\psi_6|\rangle_s$ values of the image series of the impurity with varying curvature (Fig. 5.4C) were obtained by

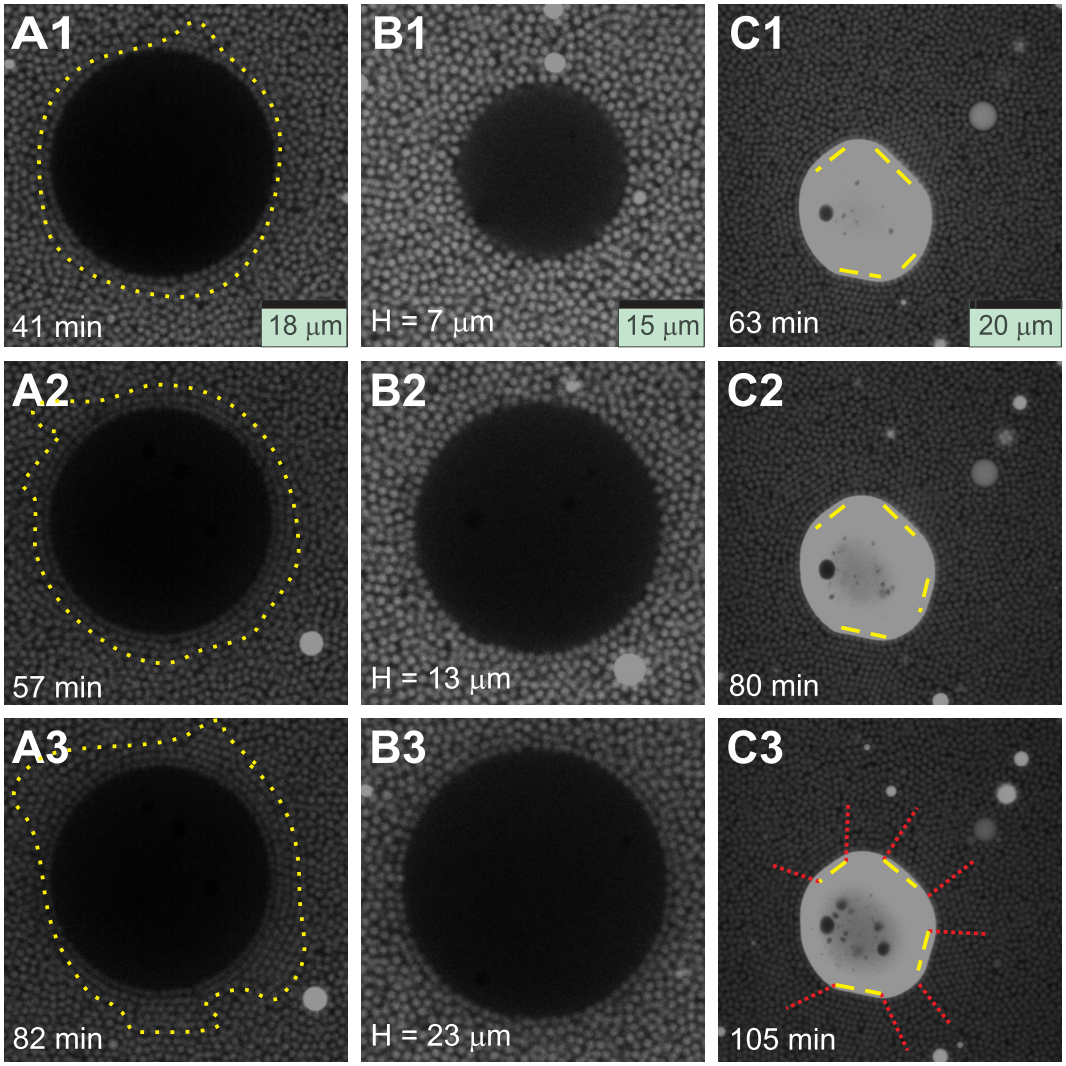

Figure 5.4. Confocal images of crystal nucleation. (A) Crystal nucleation onto an impurity with $\alpha = 27$. Nucleation takes place on the impurity surface before upward growth from the sample bottom reaches the field of view. The dotted lines roughly indicate the crystalline regions. (B) Confocal images taken after 21 minutes at different sample heights show that no upward crystal growth close to the impurity is observed shortly before nucleation is initiated. (C) Crystallites have nucleated on the less curved parts of an impurity with varying curvature: the dashed lines indicate where crystallites form on the impurity surface; the dotted lines highlight the formed crystallites.

averaging over 10 images (this is still significantly below the self diffusion time in these concentrated suspensions). Averaging enables us to show the observed trends more clearly by suppressing the relatively large fluctuations and errors in particle positions in such small datasets. For similar reasons, the $\langle|\psi_6|\rangle_s$ values of the image series in Fig. 5.4A were averaged over 10 images as well. The growth of crystallites on the

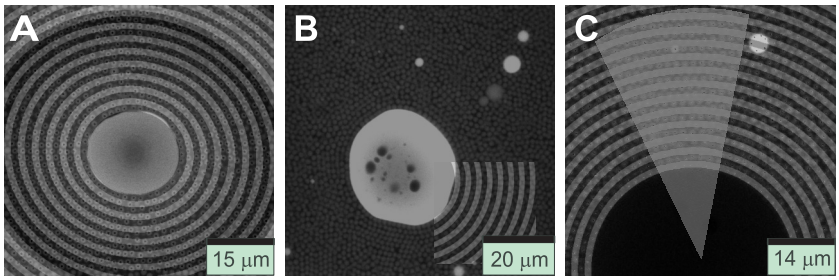

Figure 5.5. (A) Particles are divided in shells around the impurity to obtain a time and distance dependent crystallisation profile. (B) and (C) For the heterogeneous nucleation image sequences a small selection of the image is considered for analysis, where the hexagonal plane is parallel to the sample bottom. For figure (B), the square in which the shells are shown was considered for analysis. In figure (C), the shaded area is the area considered for analysis. Shells of 1.5 μm thickness are shown in all cases.

impurity with varying curvature proceeds earlier close to the impurity (Fig. 5.6A), thus layer by layer growth is observed. This is consistent with our direct observations (Fig. 5.4C). A similar trend is seen on the impurity with $\alpha = 27$ (Fig. 5.6B): the increase of order takes place earlier at 1.5-3.0 μm than at 3.0-4.5 μm, which confirms the scenario of nucleation onto and growth away from the impurity. At 5-10 μm, no increase in order is observed during the time sequence, but at 10-15 and 15-20 μm sharp increases in local order are observed when upward growth reaches the field of view. The graph also shows that increase of order further away from the impurity takes place later, when the crystal grows upward from the bottom. We will come back to this in section 5.3.4.

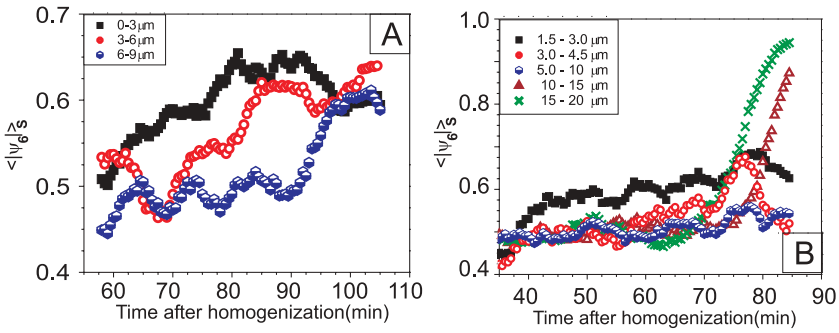

Figure 5.6. Quantitative analysis of heterogeneous nucleation. (A) Onto an impurity with varying curvature, the crystallite growth profiles suggest a layer by layer growth mechanism. (B) Onto an impurity with $\alpha = 27$, crystallite growth proceeds earlier close to the impurity. The approach of the crystal growth front towards the impurity coincides with the local decrease in $\langle|\psi_6|\rangle_6$ in the 1.5 - 3.0 μm and 3.0 - 4.5 shells μm after $\sim$ 80 minutes.

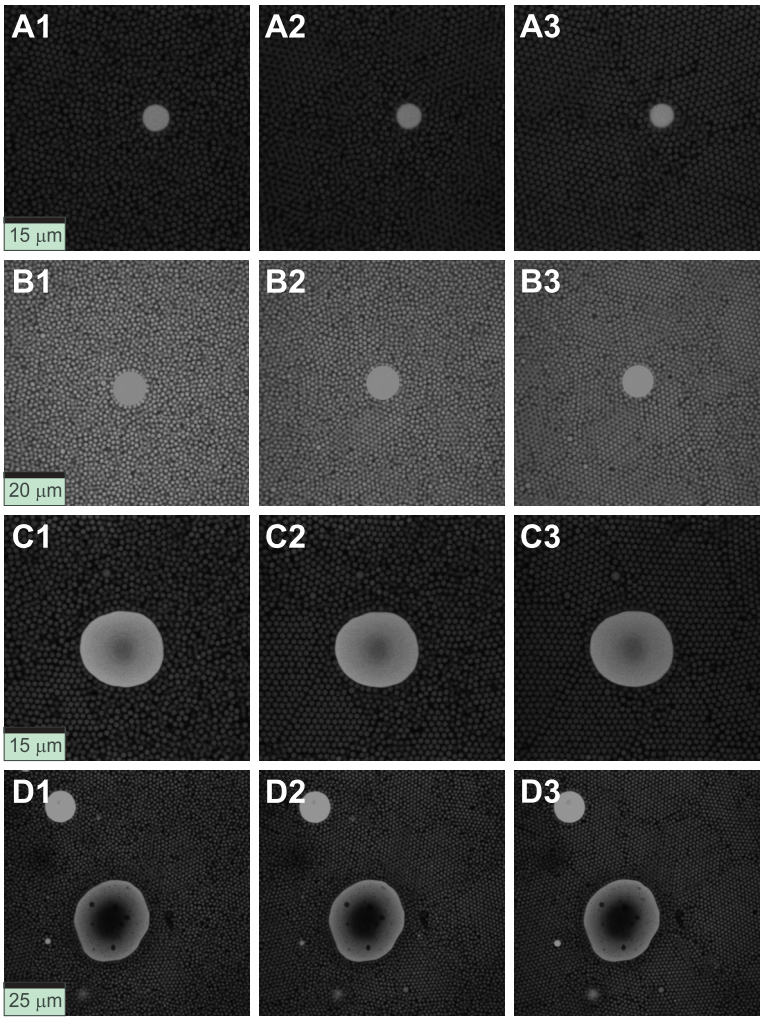

Figure 5.7. Confocal images of crystal growth near spherical impurities: (A) I_5 at (1) 31 min. (2) 50 min. and (3) 90 min.; (B) I_8 at (1) 41 min. (2) 57 min. and (3) 82 min.; (C) I_{13} at (1) 41 min. (2) 57 min. and (3) 82 min.; (D) I_{21} at (1) 74 min. (2) 82 min. and (3) 94 min. Times are after sample homogenization. Note that in our paper [104] I_8 was erroneously labelled I_{10}.

5.3.3. Crystal Growth near Impurities

Representative confocal slices of crystal growth near impurities are shown in figure 5.7. Around I_5, crystal growth is initially only observed far from the impurity (Fig. 5.7A1). The crystal front subsequently grows towards the impurity, but is clearly frustrated (Fig. 5.7A2 and A3). By frustration we mean either limited growth near the impurity (dynamic frustration) or persistent grain boundaries directed towards the impurity (static frustration). In Fig. 5.7B and C, frustration near I_8 and I_{13} is reduced: a crystal front is present, but crystal growth is observed near the impurity's shell as well (Fig. 5.7B1 and Fig. 5.7C1). Particles in the first layer around the impurity do not seem to crystallize at all; particles in the second layer crystallize only very slowly

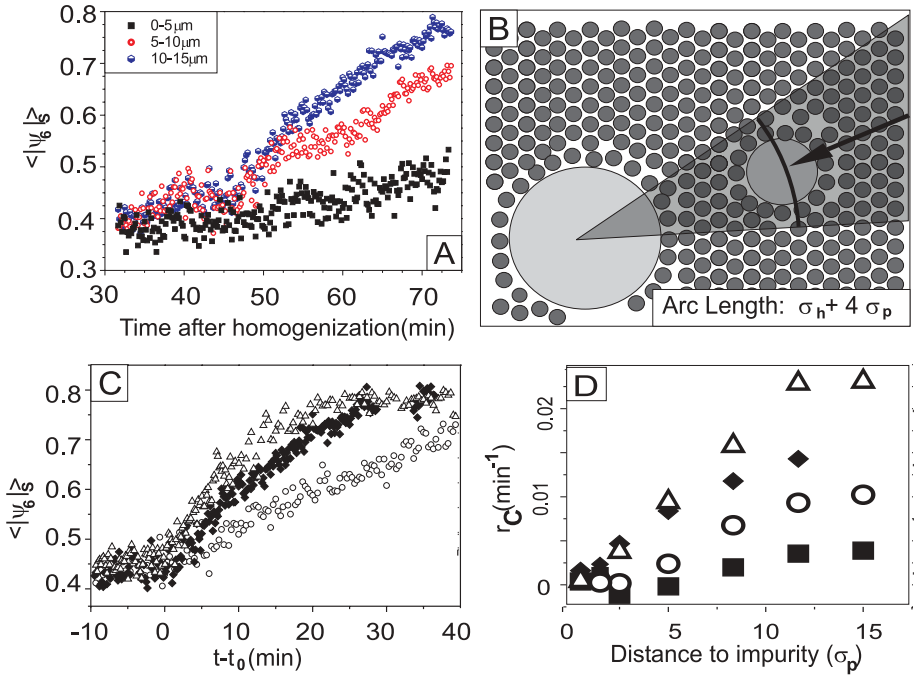

Figure 5.8. Quantitative analysis. (A) crystal growth profiles of shells around I_{13}: 0-5 μm (filled squares), 5-10 μm (open circles) and 10-15 μm (semi-filled hexagons). (B) Filtering: areas affected by other impurities are not taken into account by excluding the shaded area for analysis. (C) Crystal growth profile of the 15−20 μm shell for I_8 (circles), I_{13} (diamonds) and I_{20} (triangles). (D) Frustration of crystal growth increases both as the impurity is approached and as α is decreased. r_C close to I_5 (squares) is ~ 0 since no local increase of order occurs during the recorded image sequence. Other symbols correspond to those in panel (C). Rates at 0.5, 1.5 and 2.5 σ_p are based on shells of σ_p thickness. Other r_C values are obtained from 5μm thickness shells: r_C at $5\sigma_p$ corresponds to the 5−10 μm shell.

(Fig. 5.7B2 and Fig. 5.7C2). Here, a relatively low crystallinity during late stages of crystal growth is observed (Fig. 5.7B and Fig. 5.7C3). Finally, crystal growth near I_{21} occurs throughout the whole field of view (Fig. 5.7D). Other impurities appear in the field of view by diffusion and sedimentation for this particular sequence. These clearly affect crystal growth, as observed from the grain boundaries connecting impurities.

Typical crystal growth profiles of shells of 5.0 μm thickness around the impurity with $\alpha = 13$ are shown in Fig. 5.8A. All shells start crystallizing simultaneously, which is in contrast to the heterogeneous nucleation scenario, where the layers form by one at a time. The shells evolve from a fluid $\langle|\psi_6|\rangle_s \approx 0.4$ into a more crystalline $\langle|\psi_6|\rangle_s \approx 0.8$, where $\langle|\psi_6|\rangle_s$ plateaus. A constant $\langle|\psi_6|\rangle_s$ value is not reached for the first shell during the image sequence. Crystal growth clearly proceeds more rapidly further away from the impurity. The scenario should be the same if growth is not initiated heterogeneously

at the flat sample bottom, but homogeneously in the bulk. To compare the growth rates close to several impurities, the presence of other impurities in the I_{21} sequence was "filtered out" as sketched in Fig. 5.8B, to largely exclude the effects of the other impurities. Similar initial and final $\langle|\psi_6|\rangle_s$ values are observed for all α. As α increases, crystallinity rises faster with distance to the impurity however. This is nicely illustrated in Fig. 5.8C for the 15−20 μm shell, where t_0 indicates the time at which $\langle|\psi_6|\rangle_s$ starts steadily increasing. The increase in $\langle|\psi_6|\rangle_s$ is approximately linear right after the initial rise. We use this to define the 2D growth rate r_C of shell s (during linear rise) as:

$$r_C = \Delta\langle|\psi_6|\rangle_s/\Delta t \tag{5.2}$$

The effect of an impurity's size on the local growth rate can now be compared quantitatively (Fig. 5.8D). Several general trends can clearly be observed. First of all, a larger α results in a higher rate close to the impurity. Secondly, the rate rises faster per shell as α increases. Finally, the rates for different α apparently approach a different maximum rate at less then ∼17 particle diameters, instead of converging to a bulk rate of ∼0.02 min^{-1} at several heights in an uncontaminated sample (Fig. 5.3A) and from sample locations far (>40 μm) from impurities. Relatively far from the impurity a rough trend is observed between the growth rate and α. Note that the contribution of a single grain boundary to $\langle|\psi_6|\rangle$ is larger for inner shells than for outer shells.

We argue that grain boundaries frequently grow in between nearby impurities. A crystal may annihilate some of the its defects by running it in between two grains if nearby impurities are present, more boundaries appear. To approximate the ideal case of no nearby impurities, the image is filtered as illustrated schematically in Fig. 5.8B: grain boundaries directed toward nearby impurities are not included. The obtained increase of r_C by a factor of 1.6 for the filtered I_{21} sequence therefore is too high, whereas not filtering leads to too low values. We therefore expect the rates to converge at sufficient distance, which might very well be beyond ∼ 17 particle diameters, the practical cutoff of our measurements presented in figure 5.8. A physical reason for the decreased growth rates could partly be caused by the lower number density of the fluid state near hard curved walls [121].

5.3.4. Annealing of Crystallites

Crystallisation near the $\alpha = 27$ was imaged up to much longer times (figure 5.9). Due to the impurity curvature, grain boundaries, directed towards the impurity, separate the various crystallites on the impurity surface. Growth from the impurity surface stops when a grain boundary is formed with the approaching crystal front of the bulk crystal. The crystallites that have formed on the impurity surface reorganize afterwards to adapt to the bulk crystal's symmetry (figure 5.9). This is also observed quantitatively in Fig. 5.6B. At 5-10 μm, no increase in order is observed during the time sequence, but at 10-15 and 15-20 μm sharp increases in local order are observed when upward growth

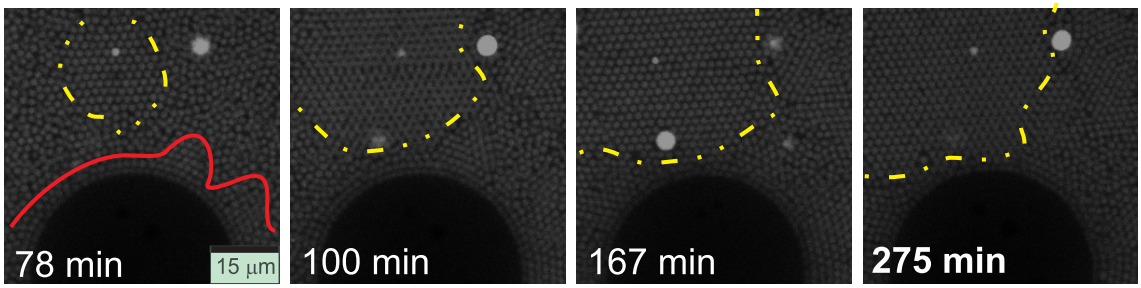

Figure 5.9. Late stages of crystallisation near an impurity with α =27: crystal growth from the bottom starts in the field of view and the crystallites on the impurity surface reorient to the bulk crystal orientation (Dark line: crystallites on the impurity surface; dotted lines bulk crystal).

reaches the field of view. The graph also shows that increase of order further away from the impurity takes place later, when the crystal grows upward from the bottom. The reorientation of the crystallites on the impurity and therefore also the displacement of the grain boundary towards the impurity coincides with a decrease in local order close to and an increase of local order far from the impurity. Growth initiated at the sample bottom is clearly dominant over growth from nuclei on curved surfaces when these two locally compete.

5.4. Conclusion

We show that two main factors control whether an impurity can act as a seed for heterogeneous nucleation in hard sphere crystals: curvature and timescales. If the surface's curvature is high, no nucleation takes place. By varying the curvature we find that nucleation (and therefore the onset of at least a single crystalline layer) occurs preferably on less curved surfaces. If bulk crystal growth has already set in close to the impurity, it will be the predominant process and crystallites formed due to heterogeneous nucleation will adjust their orientation to the bulk crystal. Quantitative analysis confirms that two very different scenarios are observed: (I) upward crystal growth which proceeds slower close to the impurity and (II) crystal nucleation onto the impurity surface and subsequent growth away from it. The higher the impurity curvature, the lower the growth rates are near the impurity.

5.5. Acknowledgement

Gilles Bosma, Hans Scherff and Esther Groeneveld are acknowledged for particle synthesis. The experiments were partly performed by Danny Verboekend during his bachelor thesis, Hans Scherff and Esther Groeneveld performed important preliminary work during their first year student internship.

6

Grain Boundary Pinning in Doped Hard-Sphere Crystals

Abstract

We report on how grain boundaries are pinned in between large spherical impurities in hard sphere colloidal crystals, studied by confocal microscopy. We introduce a frustration length ξ, connected to the extent to which the orientational order of a crystal is reduced in the vicinity of impurities. Initially, ξ increases with the impurity size ratio due to fluid particles near the impurity, but it reduces again later when particles form layers on the impurity surface. If two impurities are separated by a distance smaller than their combined frustration lengths, straight, strongly pinned grain boundaries directly form in between the impurities. At larger separations the grain boundaries can still form in between the impurities due to the enhanced stability of the fluid phase in between the impurities during crystallization, but the pinning is much weaker. Our results indicate that in between impurities, strongly pinned grain boundaries form in a well defined region in the parameter space of impurity volume fractions and impurity-to-particle size ratio.

6.1. Introduction

A hard sphere crystal packed around a larger hard sphere – the simplest conceivable impurity – nearly always results in lattice imperfections, both in two dimensions (2D) [118] and three dimensions (3D) [104,122]. Given that 2D colloidal hard sphere crystals assembled on the surface of a larger sphere contain grain boundary scars [123–125], it is intriguing to see what the resulting structure is when a 3D crystal is forced to pack around an impurity. Previous studies have shown that these impurities collect grain boundaries during crystallization [17,104,112,118,126], but the structure near the impurity surface was not investigated in detail. The extent of lattice frustration should mainly depend on the impurity to particle diameter ratio $\alpha \equiv \frac{\sigma_i}{\sigma_p}$. Two cases without frustration are a priori clear: $\alpha \to \infty$ (a flat wall) and, in a perfect crystal, $\alpha \to 1$ (no doping). In hard sphere systems with small impurity concentrations, a phase-separated system of a pure face centred cubic crystal of small spheres coexisting with a binary crystal structure is a likely candidate for thermodynamic equilibrium [127]. However, for most real systems this clearly lies beyond the typical experimental timescale: simple hard sphere crystals take months to years to reach equilibrium [25]. Given that the number of possible binary crystal structures quickly rises for $\alpha \geq 3$ [127] and that large impurities diffuse very slowly in dense systems, the experimental observation of these phases is extremely unlikely. On the contrary, if the typical crystal growth timescale is faster than the impurity diffusion timescale, two nearby impurity particles can be viewed as opposing convex walls. Since the volume fraction in the fluid phase is lowered in the vicinity of a hard curved wall [121], here, the fluid should be stabilized close to the bulk freezing volume fraction in this region: in molecular systems, a hard concave (pore)wall can stabilize the fluid beyond the melting point [128].

Here we investigate the formation of grain boundaries in between impurities during colloidal hard sphere crystallization. The intrinsic slowness of such systems and their analogy to atomic systems have resulted in excellent model systems to study freezing [57,104], melting [59] and defect dynamics [33] on the particle level.

6.2. Experimental

Our experimental approach is relatively simple: we insert large hard spherical impurities with α ranging from 3-27 in a supersaturated fluid of otherwise monodisperse hard spheres and compare these to reference samples without impurities. The system consisted of a 0.1 wt % of very large, polydisperse poly-methyl-meth-acrylate spheres (PMMA) in a suspension of 1.5 μm diameter PMMA particles in two apolar solvent mixtures with nearly matching densities and refractive: tetraline, cis-decalin and tetrachloromethane [122] and cis-decaline/cyclohexylbromide screened with tetra-butyl ammonium bromide [129]. Crystallization proceeded as in Chapter 5, at initial particle

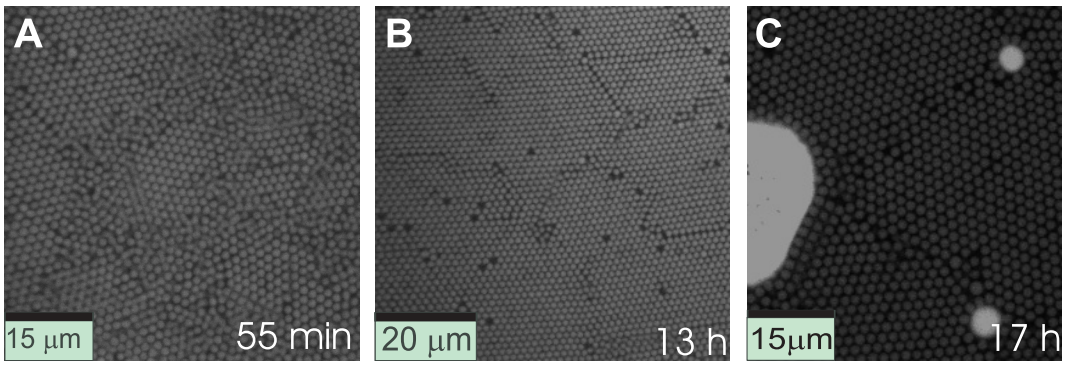

Figure 6.1. Confocal images of grain sizes. (A) Without impurities, the crystallites gradually anneal out to form large grains with typical grain sizes in the order of 100 micron such as depicted in panel (B). (C) In a sample containing impurities, the grains are much smaller. grain boundaries run from impurity to impurity. However, the grain boundaries only appear in between the large impurity and the smaller impurities. Indicated times are the times after sample homogenization.

volume fractions of 0.54-0.55. Imaging was performed with a Nikon Eclipse TE2000U confocal microscope equipped with a Nikon C1 scanning head, at distances of 15-40 μm from the glass sample bottom. Sequences of 2D xy-slices were imaged in the plane of the impurity's center of mass, near impurities with α = 3-27, over several hours. Particle coordinates are obtained by methods such as in [51].

6.3. Results and Discussion

Shortly after sample homogenization, reference samples without impurities contain many small crystallites (Fig. 6.1A). These anneal to form much larger ones within hours (Fig. 6.1B). In samples with impurities, grain boundaries persist in between impurities over similar timescales (Fig. 6.1C). Grain boundaries are present in between the larger impurity and each of the smaller impurities, but no grain boundary has formed in between the two smaller impurities, although they are at similar distances. Clearly, both the impurity size ratio and impurity spacing – in other words, concentration – are of importance for this grain boundary 'pinning'. We will discuss both aspects in the following, starting with impurity size.

Representative confocal images of frustrated crystal order near single impurities of various sizes at nearly identical particle volume fractions are shown in figure 6.2. Near smaller impurities the order is fluidlike as seen for $\alpha = 3.3$ and 8 in the Fig. 6.2A and B: upon approach of the impurity the crystal is disrupted. Near larger impurities, particles start to layer at the impurity surface, a structure that gradually adapts to the bulk crystal ($\alpha = 13$ and 27 in Fig. 6.2C and D). We should stress that except for the case of $\alpha = 27$, the crystal did not nucleate at the impurity surface, but rather formed during

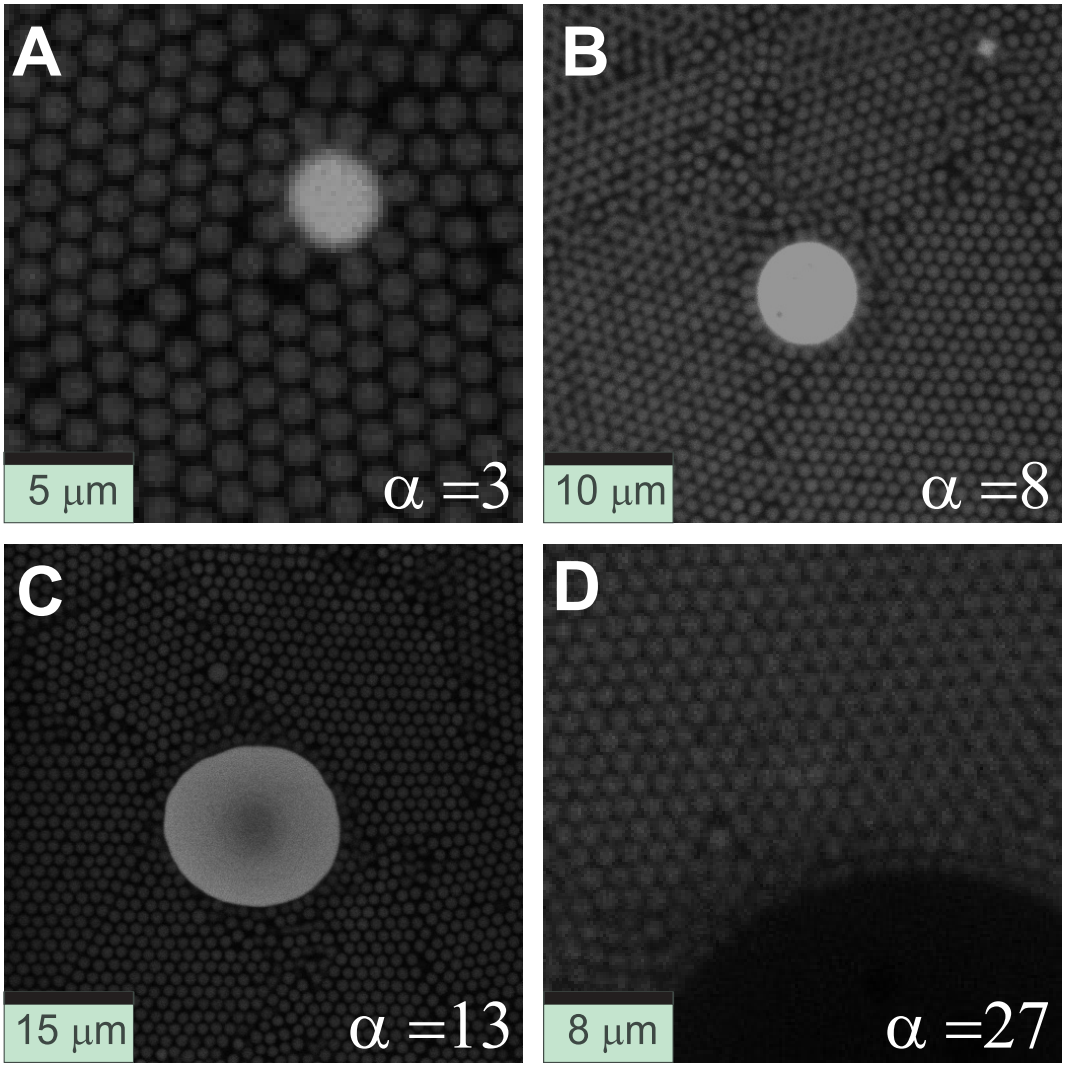

Figure 6.2. Distorted order near impurities. (A) and (B) Near the surface of small impurities the structure becomes fluidlike. (C) and (D) near the surface of larger impurities particles start to align themselves along the impurity surface.

the latter stages of crystallization [104], which is a scenario quite different from [107]. To quantify the extent of lattice frustration and extract a corresponding length scale, we compute the local orientational bond order parameter $\psi_6(\vec{r}) = \frac{1}{N}\sum_j^N e^{6i\theta(\vec{r_j})}$, where $|\psi_6| \approx 0.4$ for a typical fluid and $|\psi_6| = 1$ for a perfect hexagonal crystal slice [120]. The summation j runs over all N next neighbours of a given particle. The angle between the bond vector connecting the particle with next neighbour j and an arbitrary fixed reference axis is defined as $\theta(\vec{r_j})$. Orientational order as a function of distance to the impurity, $\langle|\psi_6|\rangle$, is obtained by averaging $(\angle\rangle)$ $|\psi_6|$ both radially over all particles at distance r from the impurity, as well as over typically 10 images. As observed in (Fig. 6.3A and B), all curves have initially low orientational order and subsequently

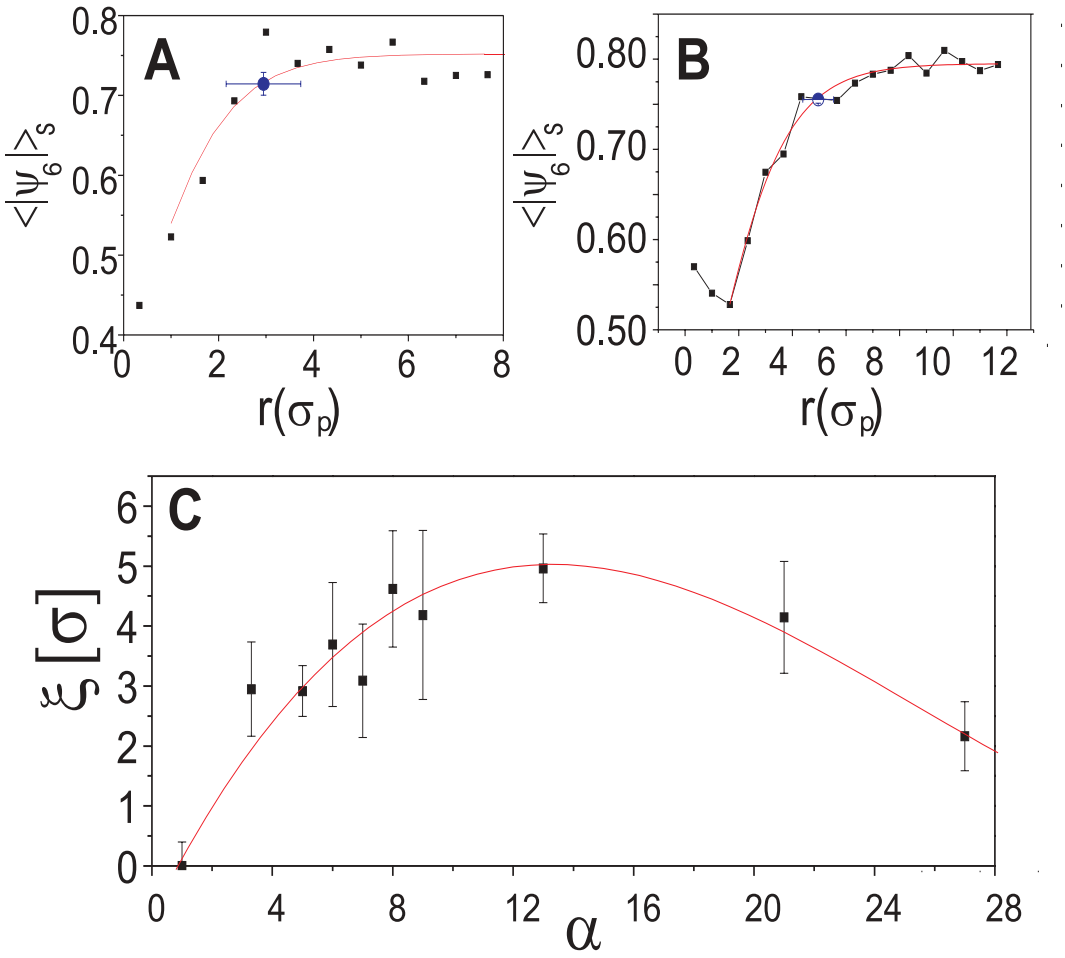

Figure 6.3. The frustration length ξ. (A) and (B) show radially and time averaged $|\psi_6|$ values as a function of distance to the impurity surface for $\alpha = 3.3$ (A) and $\alpha = 13$ (B). The obtained ξ values are shown for setting ξ at $\langle|\psi_6|\rangle(r = \xi) = 0.99\langle|\psi_6|\rangle_p$ (semifilled circles). (C) The frustration length ξ as a function of α. The competition between layering and fluidized particles results in a maximum frustration length near impurities at $\alpha \approx 14$. A 3rd order polynomial curve fit is used to estimate $\xi(\alpha)$.

rise to a plateau value $\langle|\psi_6|_p\rangle$. This distance can be interpreted as a 'frustration length' ξ, over which the impurity frustrates the crystal lattice. It is obtained by fitting the $\langle|\psi_6|\rangle(r)$ curves to an empirical fit function $\langle|\psi_6|\rangle(r) = \frac{\langle|\psi_6|_p}{1+be^{-kr}}$, with $\langle|\psi_6|_p\rangle$ the plateau value, b and k as fit parameters and r the radius from the impurity surface. Given the roughness of the data, the choice for this plateau function is arbitrary. Other plateau functions give similar results. Unless mentioned otherwise, all units of length are in σ_p. The length ξ is set such that $\langle|\psi_6|\rangle(r = \xi) = 0.99\langle|\psi_6|_p\rangle$ – the results are insensitive to the exact distance ξ is set at. Up to a distance ξ from a crystal, the crystal is frustrated, creating a frustration zone around the impurity. When comparing the frustration lengths for different size ratios, ξ is maximal for $\alpha \approx 14$ (Fig. 6.2F). This

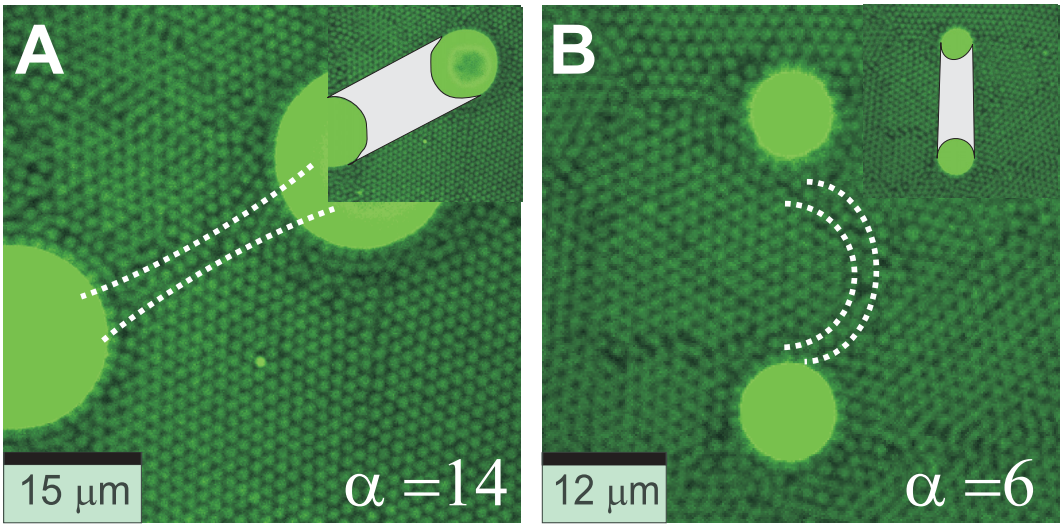

Figure 6.4. At similar impurity spacing, grain boundaries are straight for larger impurities (A) but curved for smaller impurities (B). The curved lines indicate the shape of the grain boundary. The grey areas in the inset is the region asigned as in between the impurities in figure 6.7, the rest of the image is considered as surroundings.

maximum is remarkably similar to the value of $\alpha = 10$ at which hard sphere crystals start to form precritical nuclei at the impurity surface [107]. For truly monodisperse spheres, the frustration lengths probably are larger than observed here, since polydispersity should compensate for some lattice frustration. The orientational order profiles provide even more information (Fig. 6.2E): for smaller impurities $\langle|\psi_6|\rangle_s$ quickly rises from ~ 0.4 whereas for larger impurities it is initially constant at slightly higher values of $\langle|\psi_6|\rangle_s \approx 0.5 - 0.6$. We conclude that the lower particle concentration near a highly curved surface [121] gives rise to a fluidized environment, whereas near a low curvature surface particles tend to form layers along it.

We turn to multiple nearby impurities, where the spacing in between two impurity surfaces L becomes important as well (Fig. 6.1B). The combined frustration lengths of the respective impurities might give a clue under what conditions grain boundaries form, as well as how strongly the grain boundaries are pinned. To this end we introduce the dimensionless impurity spacing $\zeta = \frac{L}{\xi_1+\xi_2}$, with ξ_1 and ξ_2 the respective frustration lengths of the impurities. grain boundaries with $\zeta \leq 1$ should be strongly pinned: many defects have to nucleate to enable the grain boundary to migrate and anneal out. Moreover, overlap of the frustration lengths should allow the system to annihilate some defects, increasing the extent of pinning. Indeed, a straight grain boundary is formed between two impurities when $\zeta = 1$ (Fig. 6.4A). Grain boundaries also appear in between impurities without overlapping frustration lengths, that is ζ¿1. These however, often have a curved shape (Fig. 6.4B), indicating that the system is locally less stable.

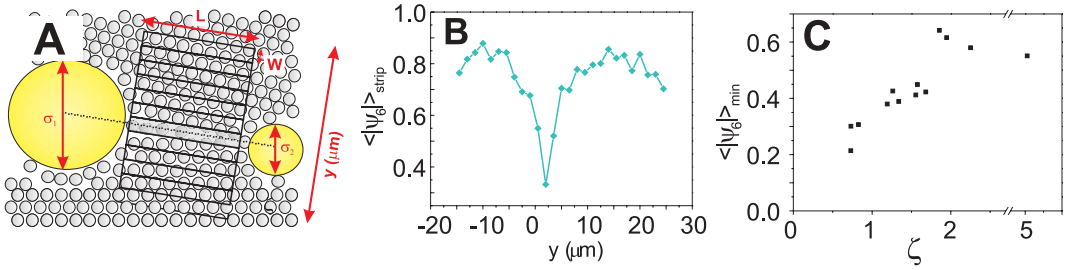

Figure 6.5. Investigating pinning: (A) division of the area in between the impurities into strips. An average $\langle|\psi_6|\rangle$ value is calculated per strip. The minimum obtained value represents how straight the grain boundaries is, that is, how strongly it is pinned. (B) A representative minimum in $\langle|\psi_6|\rangle_{strip}$. (C) $\langle|\psi_6|\rangle_{min}$ roughly increases with the dimensionless impurity spacing ζ, indicating that grain boundaries with low ζ are more strongly pinned.

To gain more understanding into the apparent grain boundary pinning, the area in between impurities was divided into thin strips with length L and width w, as illustrated in Fig. 6.5A. By calculating the average orientational order $\langle|\psi_6|\rangle_{strip}$ in every strip, a crystallinity profile is obtained such as in Fig. 6.5B. The minimum ($\langle|\psi_6|\rangle_{min}$) is more pronounced for straight grain boundaries and therefore a measure for pinning strength. For larger ζ, $\langle|\psi_6|\rangle_{min}$ indeed roughly increases (Fig. 6.6C), which points to a decrease of pinning strength. We therefore expect strong pinning for $\zeta \leq 1$, since the frustration zones overlap. This corresponds to an impurity volume fraction $\phi_i = \frac{(\frac{\alpha}{2})^3}{(\frac{\alpha}{2}+\xi)^3}$. A rough estimate for $\xi \approx \alpha$, indicates that this would occur at $\phi_i \approx 0.04$. Strong grain boundary pinning might occur for somewhat larger ζ as well. The frustration length can be considered a perturbation by the impurity on the hard sphere crystal. It is not a priori clear, however, whether these perturbations are additive, which would result in a combined length that is larger than $\xi_1 + \xi_2$: they are applied to crystals and are therefore clearly directionalised. In addition there should be a dependence on the mismatch of the orientation of the adjacent crystallites.

Further insight into grain boundary pinning is gained from the dynamics of crystal growth near impurities. Quite surprisingly, the region in between impurities initially remains fluid for separations up to $\zeta \approx 2$ (figure 6.6), clearly pointing towards enhanced kinetic stability of the fluid in between the impurities. The grain boundary directly forms in between the impurities, instead of forming and subsequently migrating towards the impurities. By dividing the particles into an area in between the impurities and the surrounding particles in the field of view, as illustrated in the insets of figure 6.4, crystallization in between the impurities and in the surrounding area was investigated: the orientational order$\langle|\psi_6|\rangle_{area}$ and $\langle|\psi_6|\rangle_{surr}$ of the respective areas was calculated as a function of time for the formation of the grain boundaries in Fig. 6.7A ($\zeta = 1.0$). Crystallization is clearly retarded in the area in between the impurities, but the

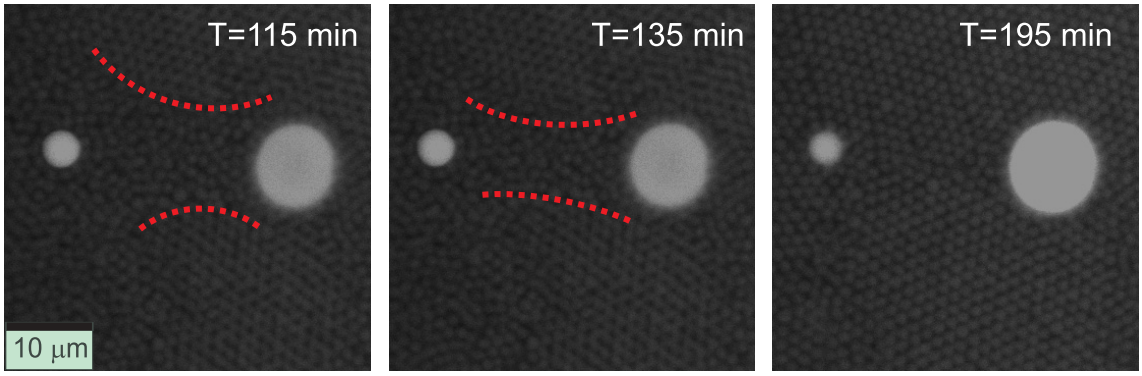

Figure 6.6. (C) The fluid bridge in between impurities gradually narrows in time and becomes a grain boundary at high density.

retardation is similar (approximately 15 minutes) for $\zeta = 1.0$ (Fig. 6.7A) and for $\zeta = 1.8$ (Fig. 6.7B). Concentrations near curved surfaces are lower in hard sphere fluids [121]. It is quite possible that two curved surfaces enhance the stability of the fluid phase such that a fluid bridge forms in between the impurity surfaces. This effectively means that the impurities capillary melt the crystal, resulting in a fluid bridge precursor for grain boundary formation. For most cases, the area in between the impurities is small and the fluctuations in the concentrations are too large to notice substantial differences in the concentration profile, but for $\zeta \approx 1.0$ (Fig. 6.7C), we obtain a clearly lowered fraction $C \equiv \frac{N\pi\sigma_p^2}{4A}$ in between the impurities, with N the number of particles and A the area of interest (Fig. 6.7C). It indeed appears that grain boundaries are formed in between impurities because the fluid phase is more stable in between the convex surfaces. Since the adjacent crystallites tend to have different orientations, a grain boundary is formed. The impurities than act as immovable objects that prevent the crystals from reorienting and annealing. This is in addition to any stabilisation of crystallite orientations along the impurity surface for sufficiently large impurities. The concentration increases as

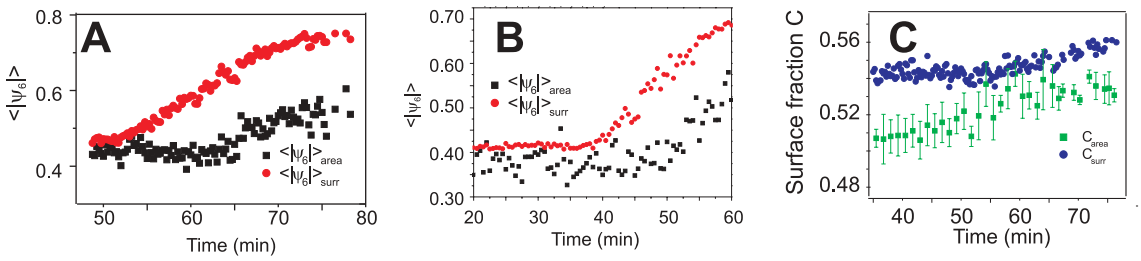

Figure 6.7. Evolution of $\langle|\psi_6|\rangle$ for $\zeta \sim 1.0$ (A) and $\zeta \sim 1.8$ (B) in between impurities ($\langle|\psi_6|\rangle_{area}$) and in the area surrounding it ($\langle|\psi_6|\rangle_{surr}$). Crystallization in between the impurities is retarded in both cases. (C) The density of particles in between impurities is lower as well for $\zeta \sim 1.0$, points are averaged over 5 time points in between impurities for clarity's sake.)

a function of time and the regions in between the impurities do eventually crystallize during the late stages of freezing (Fig. 6.7A and B), a reverse scenario of premelting at defects [59]. At carefully tuned impurity-to-particle size ratios and particle and impurity volume fractions, this could lead to a very clear regime where strongly pinned grain boundaries form directly in between impurities. This regime could be explored by computer simulations, by gradually increasing the size of two nearby particles in a hard sphere crystal. If the formation of grain boundaries in between impurities is spontaneous, a grain boundary should appear in between the enlarged spheres at a certain point. When the frustration lengths of two impurities do not overlap, the grain boundaries should anneal out in an experiment where crystallization is followed by a cycle of slight decreases and increases in volume fraction in a system of temperature-sensitive colloidal particles [59]. In fact, this probes the crystal to glass transition for binary systems: one scattering study reports a glassy system in such a regime [130], but at what point does a polycrystalline structure become glassy and according to what measures? This question is even more subtle in large size ratio binary systems and its many available binary crystal structures [127]. For thermodynamic stability of these polycrystalline systems the creation of an immense grain boundary area would have to be balanced by the alignment of crystallites along the surface of the large spheres, which seems unrealistic. An arrested state of polycrystalline grains in a 'gas' of large spheres therefore seems more likely. Depletion induced demixing of such structures would clearly take much longer than the typical experimental timescale [89].

6.4. Conclusion

In conclusion, grain boundaries in between impurities form due to the enhanced kinetic stability of the fluid particles during crystallization. We have introduced a frustration length, which characterizes up to what distance the crystal structure can 'feel' the impurity. If the resulting frustration zones of two nearby impurities overlap, defects such as grain boundaries can be trapped between the impurities. If the frustration zones do not overlap grain boundaries should anneal out again.

6.5. Acknowledgement

This work was performed with Roel Dullens, Esther Vermolen, Willem Kegel and Bachelor students Danny Verboekend and Leonie Derendorp. We acknowledge Gilles Bosma, Hans Scherff and Esther Groeneveld for particle synthesis and David Nelson, Paul Millett, Bill van Megen, Roland Roth and Dirk Aarts for valuable discussions.

7

Confocal microscopy of geometrically frustrated hard sphere crystals

Abstract

In this chapter we study the crystallization of two colloidal model systems that are geometrically frustrated in a completely different way: (I) hard colloidal polyhedrals, where crystallization is frustrated due to the incommensurate particle shape and (II) large spherical impurities in a sea of monodisperse colloidal hard spheres, where crystallization is frustrated by the introduction of impurities. As a reference system, we analyzed the crystallization of pure monodisperse colloidal hard spheres. We show that although the crystal structures of both systems are highly different on the individual particle level, both sources of geometrical frustration have a comparable effect on the grain sizes in the system. We quantitatively characterize the polycrystalline structures and study the crystallization process in time. Whereas grain boundaries persist in the frustrated systems due to structural arrest, the majority of grain boundaries anneals out quite rapidly in reference systems made up of monodisperse hard sphere crystals.

7.1. Introduction

The typical grain size of a polycrystalline material crucially influences its mechanical properties, as it is directly related to the strength of materials [131,132]. For relatively small grain sizes the strength increases with increasing grain size [132–134], while for larger grain sizes the materials strengthens if the crystallites gets smaller (Hall-Petch effect) [135,136]. Therefore, controlling the grain size, for instance by tuning the solidification rate, heating or mechanical annealing, is of paramount importance in material science [131,137,138].

Inherent to their typical size, colloidal systems provide an excellent tool to address these issues experimentally. In contrast to atomic systems, colloidal systems consist of particles with a characteristic size between a nanometre and several micrometers. This length scale makes them very suitable to be studied in real-space and real-time by microscopy techniques [15,139,140].

In this work, we consider two colloidal model systems that exhibit completely different types of geometrical frustration: The first system consists of crystals of colloidal polyhedrals that are frustrated due to incommensurate particle shape [141,142], the 'polyhedral system'. The crystals in the second system are frustrated by the addition of model impurities, as in the previous two chapters, which we will refer to as the 'impurity system'. Here, we use real-space confocal microscopy to quantitatively characterize the polycrystalline structure of geometrically frustrated colloidal crystals. Our results clearly show that both sources of geometrical frustration –which are completely different in nature– significantly reduce the grain size of the colloidal crystals in a very similar way. In addition, we investigate the arrested grain growth by identifying the (time-dependent) defect-structure during grain growth.

7.2. Experimental Section

The '*polyhedral system*' consists of crosslinked and fluorescently labeled polymethyl methacrylate (PMMA) colloids that are monodisperse in size, but exhibit a polyhedral particle shape [141,142] (see Fig. 7.1A). In our experiments, we compare the polyhedrals to a reference system of spherical and size-monodisperse reference PMMA particles of equal size [14] (see Fig. 7.1B). The diameters d of the polyhedral and reference particles are respectively $d = 2.23 \pm 0.09$ and $d = 2.33 \pm 0.07$. The '*impurity system*' consists of a sea of fluorescently labelled monodisperse PMMA particles with a diameter d_p of 1.5 ± 0.09 μm containing a small fraction of very large PMMA particles, called the impurities. The impurities were obtained by a synthesis following [14]. The resulting particles were extremely polydisperse and very large ($d_i \in 0.1 - 100$ μm) as illustrated in Fig. 7.1C. Impurities of different sizes were fractionated by repeated sedimentation. Subsequently a small amount (typically < 0.1 weight %) of impurities of the desired

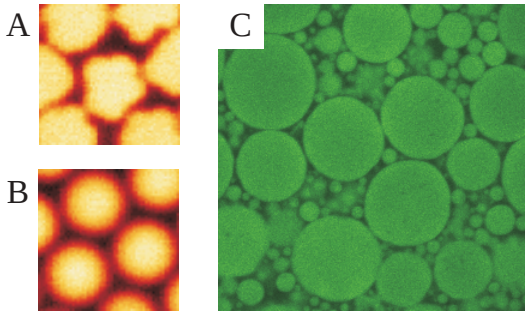

Figure 7.1. Confocal microscopy images of (A) the polyhedral particles and (B) the spherical reference particles (9×9 μm^2). (C) Confocal image of the impurities (70×70 μm^2) directly after synthesis. The larger particles (i.e. $d_i \in 7.5 - 31.5$ μm) were used as model impurities in a sea of small monodisperse particles ($d_p = 1.5$ μm).

size was added to a sea of small PMMA particles. As a result, systems of monodisperse PMMA spheres contaminated with differently sized model impurities were obtained. The reference system consists of the same monodisperse PMMA spheres ($d_p = 1.5$ μm), but now without impurities. The impurity systems are characterized by the size ratio between the particles and the impurities $\alpha \equiv (d_i/d_p)$m with d_i and d_p respectively the diameters of the impurity and the particles. In this work, we consider impurity systems with $\alpha = 5, 8, 13$ and 21.

The colloidal model systems were dispersed in a mixture of cis-decalin (Merck, for synthesis), tetralin (Merck, for synthesis) and carbontetrachloride (Merck, for spectroscopy), which simultaneously matches the refractive index and almost the mass density of the particles [122,143]. In this solvent the particles interact via a hard-sphere-like potential [17, 143]. The dispersions were contained in small homemade vials [143] and the particles were imaged using a Nikon TE 2000U inverted microscope with a Nikon C1 confocal scanning laser head. For the polyhedral colloids, samples with a volume fraction $\phi \equiv \rho v \approx 0.40$ were prepared (with ρ the number density and v the particle's volume). The impurity systems were prepared at relatively high volume fraction ($\phi \approx 0.55$) to minimize the mobility of the impurity during the measurements [104,122]. The volume fractions of the samples were defined relative to the random close packing density at the relevant polydispersity [83].

In the polyhedral, the impurity and the reference systems the colloidal crystal heterogeneously nucleates at the wall, followed by subsequent upward growth [32,103,104,122]. As a result, the hexagonal plane of the crystal is oriented parallel to the sample bottom, allowing a quantitative 2D in-plane analysis of the systems [32, 104, 117, 122, 141, 144]. The structure of the polyhedrals was analyzed after slow sedimentation had fully completed as the influence of the particle shape is most pronounced at highest density. Since the layering in the polyhedral system did not persist in bulk [141], we studied the

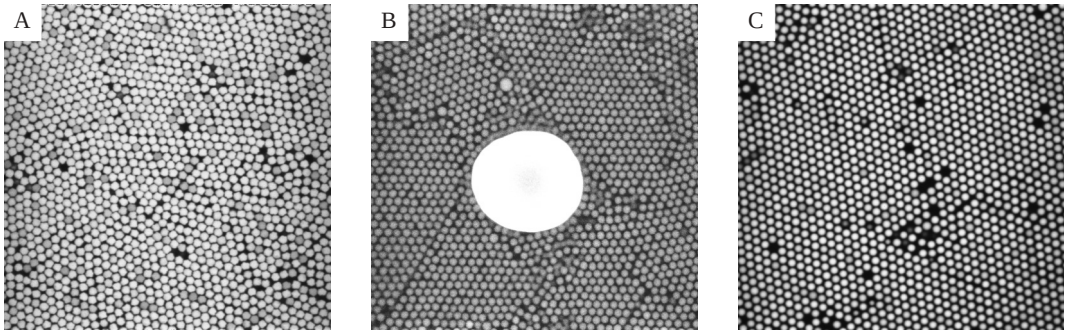

Figure 7.2. Representative confocal images of (A) the polyhedrals (75 × 75 μm^2) and (B) the impurity system for $\alpha = 13$ (60 × 60 μm^2) and (C) the reference spheres for the polyhedrals (75 × 75 μm^2). The system without impurities is highly similar to the reference system shown in panel (C).

first layer at the glass wall in this system. Although certainly interesting, the question as to how the structure of the polyhedrals evolves in the third dimension lies outside the scope of this work. The impurity system was studied in the plane corresponding to the centre of the impurity, which was typically 20 μm above the glass wall. Furthermore, we studied the time-dependent structure of both systems during crystallization. The centres of the particles were located using image-analysis software similar to that described in [51]. We verified that the polyhedral particle shape did not significantly affect the accuracy of the particle tracking.

7.3. Results and discussion

Representative confocal micrographs of the colloidal crystal formed by the frustrated and reference systems are shown in Figure 7.2. The structure of both the polyhedrals and the impurity system exhibit a much higher degree of polycrystallinity compared to the structure formed by the reference spheres. To quantify this, we computed the radial distribution function $g(r)$ (being proportional to the probability of observing a particle a distance r away from a given particle):

$$g(r) = \frac{1}{\rho} \left\langle \sum_{j \neq i} \delta(r_i - r_j - r) \right\rangle . \tag{7.1}$$

The indices i and j run over all particles. The radial distribution functions for the polyhedral, the impurity and the reference systems are shown in Fig. 7.3A1 and B1. We observe that the peaks in the $g(r)$ are markedly broadened for the polyhedrals and that the structure in the $g(r)$ decays much faster with respect to the reference $g(r)$. Nevertheless, the clear differences between the $g(r)$ of the polyhedrals and the reference $g(r)$ are not due to polycrystallinity. The polyhedral particle-shape frustrates the hexagonal crystal on the level of particle pairs: small reorientations of the lattice within the grain lead to significantly broader peaks in the radial distribution function

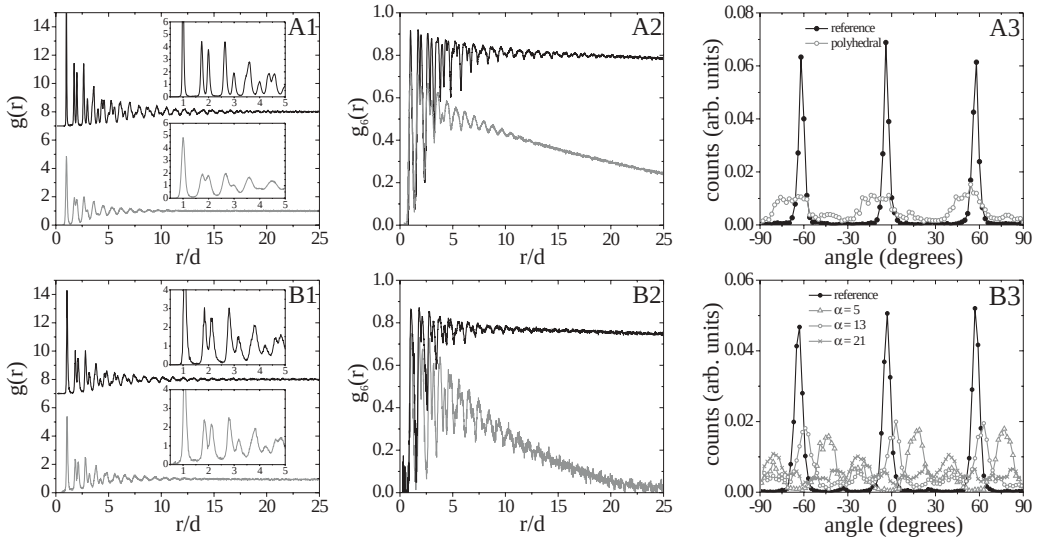

Figure 7.3. (A1) Radial distribution functions $g(r)$, (A2) bond-orientational correlation functions $g_6(r)$ and angle distributions (A3) for the polyhedrals (grey) and the reference spheres (black). (B1-B3) Same as A1-A3, but now for the impurity system (grey) and the reference system without impurities (black). (B1) and (B2): $\alpha = 21$, (B3): $\alpha = 5, 13, 21$. The radial distribution functions corresponding to the reference system have been vertically shifted for clarity. The insets in (A1 and B1) show an enlargement of the first peaks of $g(r)$ to emphasize the differences between the geometrically frustrated and reference systems.

compared to that of the reference system, especially at large r. The global structure, i.e. $g(r)$ is only slightly affected by smaller grain sizes, leading to the highly similar $g(r)$ functions for the impurity system and its reference system. The differences in the radial distribution functions observed in Fig. 7.3A1, are similar to those observed in single-crystalline regions [141]. Note that the difference between the reference radial distribution functions in Fig. 7.3A1 and B1 is due to a difference in volume fraction. Recall that the polyhedral system has been analyzed after sedimentation had fully completed, in contrast to the impurity system. The volume fraction can be quantified in terms of the two-dimensional packing fractions ($\eta = N_T A_p / L^2$, with N_T the total number of particles in the image and L^2 the area of the image). Indeed, the more pronounced peaks in the reference $g(r)$ in Figure 7.3 A1) (polyhedrals) correspond to a packing fraction of $\eta = 0.85$, which is clearly higher than $\eta = 0.74$ for the reference $g(r)$ in Fig. 7.3B1 (impurity system).

The loss of positional order shows up strongly in reciprocal space. The 2D structure factor is computed on a 2D grid of $\mathbf{q}$ -values with a sampling rate of π/L with L the size of the microscopic image, as in [96]:

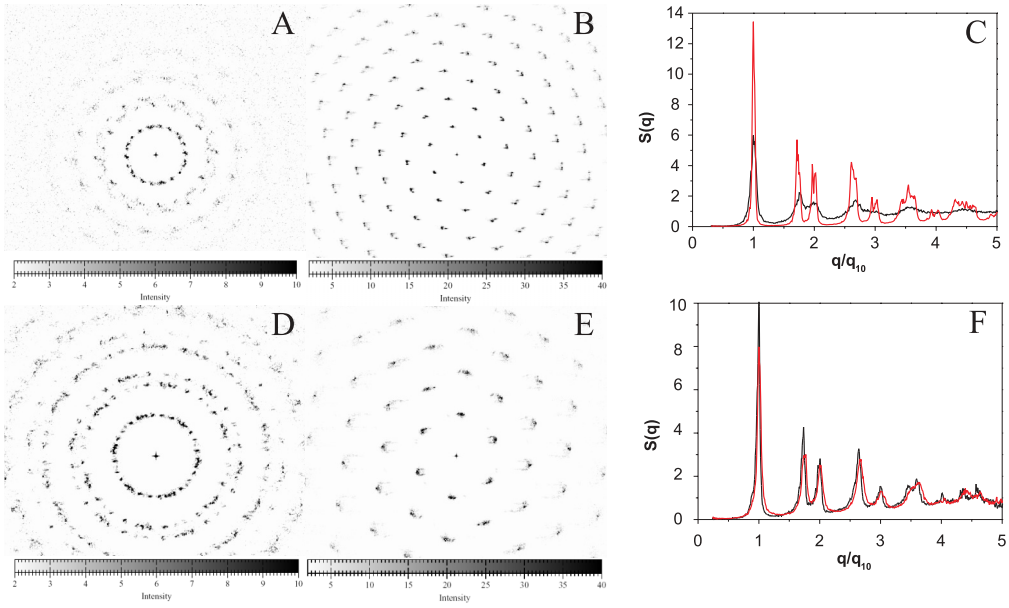

Figure 7.4. The structure factor S(q) for the polyhedral (A) and the impurity system (D). The reference structure factors for both systems are shown in panels (B) and (E). The radially averaged profiles for the frustrated systems and the reference systems are shown in panels (C) and (F) respectively. The black curves are for the polyhedral system and its reference system, the grey curves for the impurity system and its reference system The structure factor of the polyhedral system decays remarkably more rapidly than the other systems.

$$S(q_r) = \frac{1}{N}\sum_{n=1}^{N} \exp[i(\mathbf{q} - \mathbf{r_n})], \tag{7.2}$$

with $\mathbf{r_n}$ the particle coordinates and N the total number of particles. The structure factor profile $S(q)$ and the $g(r)$ profile are two related but distinctly different representations. As will be shown in more detail below, the $S(q)$ is more convenient for quantitative characterization of various types of long-range positional disorder, which is "hidden" in the details of the decay of the higher-order peaks of $g(r)$. The distinction between the finite-size effects (abrupt loss of the positional order) and the second-type disorder (monotonic deformation of the lattice) is difficult on the basis of g(r) but is easily obtainable from $S(q)$. The structure factors are presented in Fig. 7.4A and B for, respectively, the polyhedrals and the reference spheres. Whereas the spheres are monocrystalline, the $S(q)$ for the polyhedrals is powderlike, with characteristic rings instead of sharp spots. A similar trend is observed for the impurity system and its reference system in Fig. 7.4D and E. A notable difference between the impurity system and the polyhedral system shows up in the radially averaged profiles in Fig. 7.4C. As was

already clear from the $g(r)$ the positional order decays much faster in the polyhedral system. However, the angular profile of the polyhedral system is much wider than the profile of the impurity system. This also follows from the polyhedral structure factor plot Fig. 7.4A, where the intensity range used to depict the profile is much smaller than the plot for the impurity system in Fig. 7.4D. This points to orientational changes within the grain for the polyhedral system.

The bond-orientational correlation function $g_6(r)$ is significantly affected by the polycrystallinity, as is evident from Fig. 7.3A2 and B2. The bond-orientational correlation function $g_6(r)$ [120, 144] is defined as

$$g_6(r) = \langle \psi_6^*(0)\psi_6(r)\rangle \tag{7.3}$$

with

$$\psi_6(r_i) = \frac{1}{N}\sum_{j=1}^{N} \exp[6i\theta(r_{ij})]. \tag{7.4}$$

Here, ψ_6 is the local bond-orientational order parameter, where the summation j runs over all, in total N, nearest neighbors of particle i. $\theta(r_{ij})$ is the angle between the bond-vector connecting particles i and j and an arbitrary fixed reference axis. The $\langle\rangle$ in Eq. (7.3) denote averaging over all pairs of particles and the index i in Eq. (7.4) runs over all particles. For both the polyhedral and the impurity system, the $g_6(r)$ decays much faster than for the reference systems, indicating that the bond-orientational correlation is gradually lost in the frustrated systems. Indeed, polycrystallinity, where every crystallite has a different orientation, is expected to destroy the bond-orientational order on a length scale comparable to the grain size. Therefore, we determined the orientational correlation length ξ_O by fitting an exponential decaying function to the envelope of $g_6(r)$: envelope of $g_6(r) \propto \exp[-r/\xi_O]$ [118,120,144]. Hence, ξ_O is a measure for the typical size of the single crystalline domains. The orientational correlation length ξ_O being approximately 18 diameters for the polyhedrals and 9 diameters for the impurity system, indeed roughly corresponds to the grain size as can be inferred from the confocal images (Fig. 7.2A and B. Interestingly, no systematical trend in the grain size as a function of the size ratio α was found, which suggests that the impurities act as immobile obstacles during the annealing of the grain boundaries. The bond-orientational correlation functions of the reference systems show much slower, algebraic decay. The accompanying orientational correlation length ξ_O is more than 100 particle diameters for the reference systems, which points to the presence of long-range orientational order, i.e. large single-crystalline domains. Again, the (minimal) difference between the $g_6(r)$ of both reference systems can be attributed to the slightly different packing fractions.

Direct information about the polycrystallinity of a crystalstructure is also given by orientational profile of the structure factor [118]. In Figure 7.3A3 and B3, we show

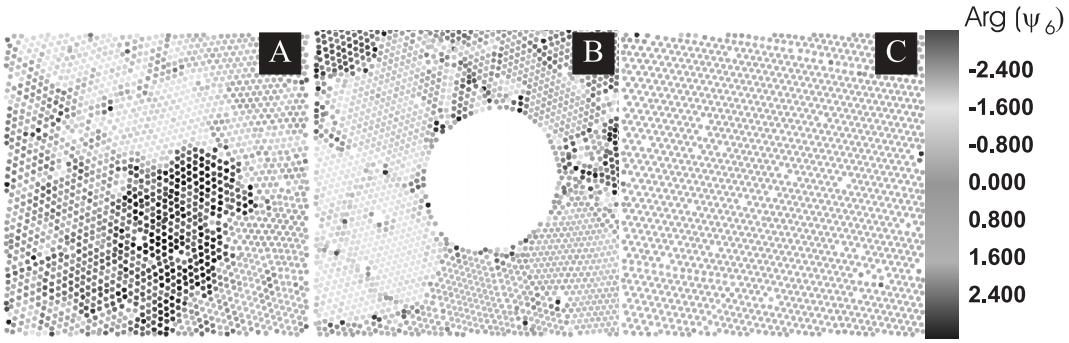

Figure 7.5. Plots of (A) the polyhedral system, (B) the impurity system and (C) the polyhedral system. Particles are assigned a color based on their ψ_6 orientation, as indicated in the legend of panel (C). Within the grains, the reference system and the impurity system have a fairly uniform orientation, whereas the distribution of orientations within the polyhedral orientations is relatively broad.

the real-space analog of this profile, that is, the distribution of angles that all nearest neighbor particles makes (with respect to an arbitrary reference axis). Clearly, in both reference systems three peaks at multiples of 60° are observed, corresponding to the three lattice orientations of a hexagonal crystal. Note that peaks with an orientational difference of 180° correspond to the same lattice orientation and are omitted for clarity. The absence of side-peaks points towards the single-crystalline structure of the reference colloidal crystals. The situation changes dramatically in the frustrated systems, where the peaks of the angle distributions are considerably broadened. Moreover, the angle distributions of the frustrated systems do not reach the zero baseline and show many other peaks. This is a direct consequence of the polycrystalline nature of the frustrated systems, as the presence of differently oriented crystalline domains results in broadening and eventually in a whole range of peaks in the angle distribution. We did not find a correlation between the orientations of the crystallites and the local curvature of the impurity, which is consistent with the absence of a relation between the grain size and the size ratio α. Note that the peaks in the angle distribution of the impurity system are generally sharper than those of the polyhedral system, which is related to the different nature of geometrical frustration in both systems: the orientation within the single grains is quite uniform in the impurity system, but changes much faster for the impurity system. This is illustrated in figure 7.5, which show plots of the particle positions with colors assigned based on the local ψ_6 orientation. Within the grains, the orientation of the polyhedral sometimes changes within several color ranges, which is certainly not the case in the impurity and reference systems.

To elucidate how the grain boundaries are formed we studied the crystallization as a function of time. In Figure 7.6 Delaunay triangulations corresponding to different

stages during crystallization are presented. The color in the triangulations corresponds to the coordination number of the particles (see caption Figure 7.6). In both the polyhedral and the impurity system, crystalline regions appear (Figure 7.6A1, B1) simultaneously in different regions of the sample. These crystallites subsequently grow (Figure 7.6A2-A4, B2-B4) and meet at a certain time. Due to the random orientations of the crystallites, grain boundaries are initially formed. This rules out the scenario that an single crystallite breaks into different crystallites due to the geometrical frustration. Interestingly, the reference systems crystallize similarly as the frustrated systems, resulting in a crystal that is initially relatively rich in grain boundaries [32,104]. However, the striking difference is that in the reference systems, the grain boundaries gradually anneal in time as is evident from Figure 7.2C, whereas they persist in the polyhedral and impurity system on our experimental time scales (Fig. 7.2A and B [104]. In other words, the time scale associated with the reorientation of the different crystallites – necessary to form a single crystal– is much larger for the frustrated systems than it is for the reference systems.

The final structure in both systems studied here is determined by a subtle interplay between geometrical frustration, crystallization and kinetic arrest. Could it be that in the geometrically frustrated crystals the grain boundaries provide a route to minimize the stress in a similar way as the grain boundary scars that appear in a hexagonal crystal on a curved surface [123, 124]? Despite their incommensurate shape, the polyhedral particles form hexagonal structures, with well defined and on average straight crystal axes [141]. Therefore, there it is unlikely that the introduction of a grain boundary reduces the stress in the crystal. However, due to the increased excluded volume with respect to a sphere, a polyhedral shape decreases the mobility of the particles, especially at high densities. As particle mobility drives the reorientation of crystallites, we argue that decreased mobility of the polyhedral particles leads to structural arrest of the crystallites, i.e. a "glass" of small, structurally arrested crystallites. An impurity locally introduces defects, but does not necessarily induce grain boundaries. Note that, if there exists a grain boundary, it is energetically favourable to annihilate some defects by locating the impurity in the grain boundary [118, 126, 145, 146]. Nevertheless, the impurities serve as immobile obstacles, which significantly slow down the reorientation-proces of the crystallites around the impurity. Consequently, this structural arrest again leads to the formation of a polycrystalline glass around the impurities.

7.4. Conclusions

Colloids provide experimental systems that can probe the microscopic origins behind macroscopic properties of nanocrystalline materials and therefore are a valuable addition to the widely used computer simulation studies. In this chapter, we have shown how colloidal crystals can be used to demonstrate that two completely different ways

of geometrical frustration both significantly decrease the grain size in materials: (I) frustration due to a polyhedral particle shape stabilizes small crystal grains on a single particle level whereas (II) frustration by the introduction of impurities stabilizes small crystallites on the single grain level. Another intriguing pathway to introduce small grains in a crystal is to introduce a 2D crystalline spherical surface with intrinsic grain boundary scars [123, 124] as seeds for heterogeneous nucleation. We expect that by increasing the roughness of the particle-shape or the concentration of the impurities, this structural arrest becomes more pronounced, which could be used to tune the grain size, to stabilize nanocrystalline materials and addressing fundamental issues in materials science [126, 145, 147]. Examples include the design of highly ductile nanocrystalline materials [126, 145, 147, 148] and tackling the microscopic origin impurity induced properties such as embrittlement [149, 150] as well as high diffusivities and catalytic properties [151].

7.5. Acknowledgements

This work resulted from a joint effort with Roel Dullens and Maurice Mourad. Hans Scherff and Esther Groeneveld are acknowledged for particle synthesis.

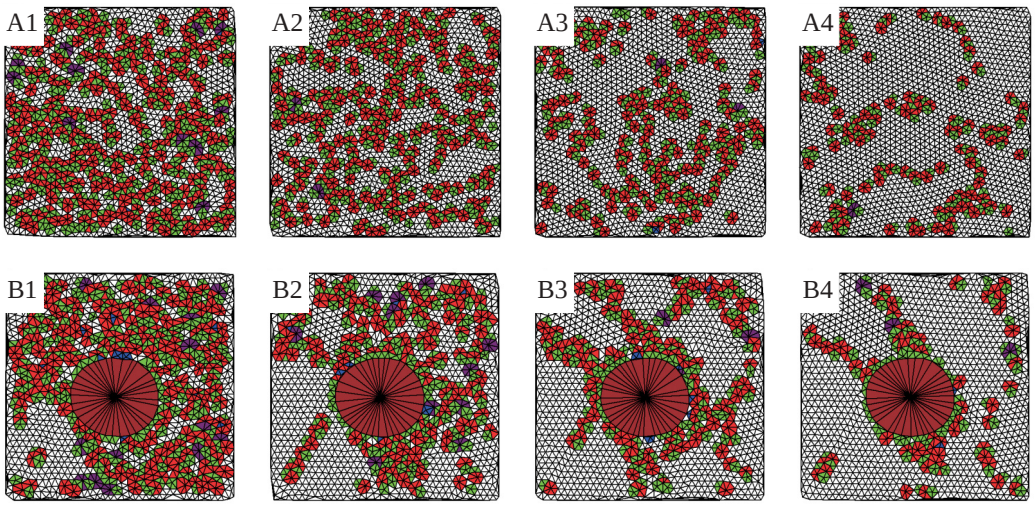

Figure 7.6. (A1-A4) Delaunay triangulations corresponding to different stages during crystallization of the polyhedral colloids ($100 \times 100\ \mu m^2$): A1-A4 respectively correspond to 0, 6, 12, 25 minutes after homogenization. (B1-B4) The same, but now for the impurity system with $\alpha = 13$ ($60 \times 60\ \mu m^2$): B1-B4 respectively correspond to 41, 60, 65, 80 minutes after homogenization. The colour code for the coordination number of the particles is as follows: four-fold: blue, five-fold: green, six-fold: no colour, seven-fold: red, eight-fold: purple and more than eight-fold: brown.

Part 3

Stochastics of Brownian Interface Fluctuations

8

Statistics of a colloidal fluid-fluid interface

Abstract

We report on measurements made by laser scanning confocal microscopy on the statistics of the interface of phase separated colloid-polymer systems. Due to the Brownian character of the process, the statistics vary with the chosen measurement interval Δt. We focus in particular on the residence times of capillary waves above a given height h and on the waiting times in between such fluctuations. The discrete scanning times are a practical cutoff and we are able to measure the waiting time as a function of this cutoff. The measurement interval dependence of the observed waiting and residence times turns out to be *solely* determined by the time dependent height-height correlation function $g(t)$. The accompanying distributions of time intervals are predictable in terms of $g(t)$ as well. We find excellent agreement between the theory presented here and the experiments.

8.1. Introduction

The frequently counterintuitive field of stochastic number fluctuations has boggled the scientist's mind for ages. Svedberg's measurement of the diffusion constant [152], based on the residence times on a fluctuating number of Brownian particles in a fixed region, inspired von Smoluchowski to develop a theoretical framework for it [153,154]. His seminal ideas were for example exploited to derive the mobility of spermatozoids [155] and white blood cells [156, 157]. Based on Einstein's [50] and Perrin's seminal papers on Brownian motion of particles [48], von Smoluchowski [3] was also the first to predict the Brownian height fluctuations of the interface. They were first quantitatively treated by Mandelstam [4] and have become an important component of modern theories of interfaces [158–161]. Note that Brownian interface fluctuations also determine properties of ordered interfaces such as grain boundaries [161].

These 'capillary waves' were initially accessed experimentally by lightscattering [4, 162–164]. A comprehensive review of this early experimental work can be found in [164]. Later, x-ray scattering of capillary waves became available as well [165–167]. On a microscopic level capillary waves were studied in computer simulations of molecular systems [168]. Recent investigations by Aarts and coworkers on colloid-polymer mixtures, [42,58,61] added another dimension to studies on capillary waves by using confocal microscopy. In these experiments, the interfacial tension γ is lowered to the nN/m range. As a consequence the characteristic length and time scale of the fluctuations are such that capillary waves can be visualized by microscopy. Microscopy furthermore enables the investigation of the effect of capillary waves on local phenomena such as rupture [46] and coalescence [47] problems and on the transport of particles through

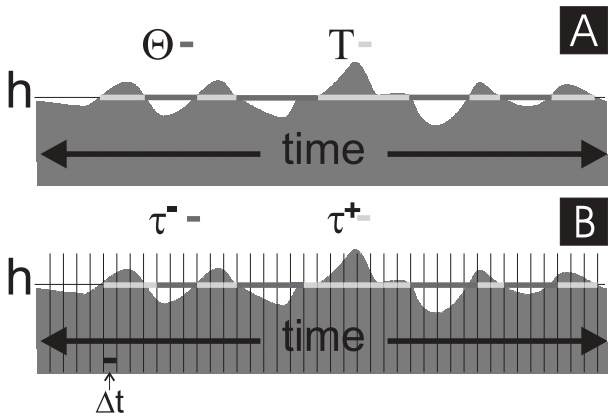

Figure 8.1. (A)Variation of the interfacial height h in time with characteristic residence times T and waiting times Θ. (B) in practice, T and Θ are determined by discrete intervals, resulting in observed residence and waiting times τ^+ and τ^-. These are determined by weighted averages of the statistics of intervals with length Δt.

the interface, as we will describe in the subsequent chapters. At a fixed location on the interface, the height is continuously fluctuating in time. Following Becker [169] and as sketched in Fig. 8.1A the waiting time Θ is the average time spent in between fluctuations above a height h and the residence time T is the average time spent above a height h:

$$\Theta(h) = \int dt p^-(h,t)t, \qquad T(h) = \int dt p^+(h,t)t \tag{8.1}$$

where $p^-(h,t)$ and $p^+(h,t)$ are the probability distributions of intervals of length t below and above the height h respectively. Such local measurements are not possible by scattering methods, since they require knowledge of continuous local stochastics which are, however, accessible by microscopy. Pioneering work by Aarts and Lekkerkerker [170] resulted in scaling relations, but did not include a full quantitative description of the process. The crux is that however fast microscopy may be, measurements always have to be taken at discrete time intervals Δt, as sketched in Fig. 8.1B, resulting in the observed waiting and residence times τ^+ and τ^-:

$$\tau^-(h) = \sum n p_n^-(h), \qquad \tau^+(h) = \sum n p_n^+(h) \tag{8.2}$$

Here, p_n^- and p_n^+ are respectively the (normalized) probability distributions on intervals of snapshots of length n, below and above height h. Note that τ^+ and τ^- are in units Δt and are therefore both dimensionless. Switching to discrete time intervals has significant implications. Due to the Brownian character of the process, the discretisation of equation (8.1) leads to statistics that depend on the chosen interval Δt. However, the necessity to be discrete saves rather than spoils the day, as it enables us to overcome the divergencies for continuous distributions. This chapter is organized as follows: we start with the brief derivation of the relevant length and timescales following standard capillary wave theory in section 8.2, before we describe our experiments in section 8.3. Results are presented in section 8.4. We develop theory in order to understand our observations in section 8.5, before we conclude in section 8.6.

8.2. Theoretical Background

Consider an interface with interfacial tension γ that separates a liquid and a gas phase, with densities ρ_l and ρ_g and viscosities η_l and η_g. The subscripts l and g denote the liquid and gas phases. We describe the interface by a mathematical sheet $\vec{s}(x,y)$. For each interfacial location there is a single height $h(\vec{s}(x,y))$, ignoring overhang effects as well as bubbles of one phase in the other. The work to create an interfacial corrugation then is:

$$\Delta F = \frac{1}{2}\int d\vec{s}(\Delta\rho g h^2(\vec{s}) + \gamma(\nabla h(\vec{s}))^2). \tag{8.3}$$

Here $\Delta\rho = \rho_l - \rho_g$ is the density difference between the phases and g the acceleration due to gravity. The first term gives the gravitational work (the displacement of matter against gravity) and the second the interfacial work (the creation of additional interfacial area). We ignore other work terms that may contribute such as the bending of the interface [159, 171] and overhang effects, an approach that describes capillary waves in colloid polymer mixtures quite well [42]. The height h may be expanded in a Fourier series in a square with length L as:

$$h(\vec{s}) = \sum_{\vec{k}} h_{\vec{k}} \exp[i\vec{k} \cdot \vec{s}]. \tag{8.4}$$

with $h_{\vec{k}}$ the Fourier coefficients for $\vec{k}(k_x, k_y)$. We additionally define $k = |\vec{k}|$. Using Parseval's theorem, we rewrite for the work:

$$\Delta F = \frac{L^2}{2} \sum_{\vec{k}} |h_{\vec{k}}|^2 [\Delta\rho g + \gamma k^2], \tag{8.5}$$

which gives the equilibrium probability on the amplitude $h_{\vec{k}}$:

$$P_e(h_{\vec{k}}) \sim \exp - \frac{L^2[\Delta\rho g + \gamma k^2]\,|h_{\vec{k}}|^2}{2k_B T}, \tag{8.6}$$

from which it follows that the mean square average of $h_{\vec{k}}$ is given by

$$\langle |h_{\vec{k}}|^2 \rangle = \frac{k_B T}{L^2(\Delta\rho g + \gamma k^2)}. \tag{8.7}$$

Here, k_B is the Boltzmann constant and T is the temperature. Since the distribution of a single k-mode is described by a Gaussian, the sum over all modes results in a Gaussian distribution of heights:

$$P_{eq}(h) = \frac{\exp[-h^2/2\langle h^2 \rangle]}{[2\pi \langle h^2 \rangle]^{1/2}}. \tag{8.8}$$

From 8.7 we can obtain the mean square height $\langle h^2 \rangle$, again applying Parseval's theorem:

$$\langle h^2 \rangle = \frac{L^2}{2\pi} \int_{k_{min}}^{k_{max}} \langle |h_{\vec{k}}|^2 \rangle \vec{k} d\vec{k} = \frac{k_B T}{4\pi\gamma} \ln \frac{k_{max}^2 + \xi^{-2}}{k_{min}^2 + \xi^{-2}}. \tag{8.9}$$

Here $\xi = (\gamma/\Delta\rho g)^{1/2}$ is the capillary length, which is the lateral correlation length scale for the capillary waves. Furthermore, $k_{max} \approx 2\pi/d$ is a cutoff related to the typical interparticle distance d and $k_{min} = 2\pi/L$ is related to the system size L.

More information from an experimental system can be extracted from the height-height correlation functions:

$$\langle h^2 \rangle\, g(\vec{s}, t) = \langle h(s', t') h(s'', t'') \rangle, \tag{8.10}$$

with $s = |\vec{s}| = |\vec{s}' - \vec{s}''|$ and $t = |t' - t''|$. By writing the correlation function as $\langle h^2 \rangle\, g(s, t)$ it is clear that for very small time and length scales, $g(s, t)$ must go to 1.

Macroscopically, one has the decaying mode for wave number k:

$$h_{\vec{k}}(t) = h_{\vec{k}}(0)\exp[-\omega_k t], \tag{8.11}$$

where ω_k is the damping coefficient. In colloidal systems capillary waves are in the overdamped regime [42, 172, 173] with a decay rate

$$\omega_k = \frac{1}{2t_c}(k\xi + (k\xi)^{-1}). \tag{8.12}$$

Here, $t_c = \xi/u_c$ is the capillary time and $u_c = \gamma/(\eta_l + \eta_g)$ is the capillary velocity. With the distribution (8.8) one can express the height-height correlation function in terms of ω_k:

$$\langle h^2\rangle g(s,t) = \frac{k_B T}{\gamma L^2}\sum_{\vec{k}}\frac{\exp[i\vec{k}\cdot\vec{s} - \omega_k t]}{k^2+\xi^{-2}} = \frac{k_B T}{\gamma(2\pi)^2}\int_{k_{min}}^{k_{max}}\frac{d\vec{k}}{k^2+\xi^{-2}}\exp[i\vec{k}\cdot\vec{s} - \omega_k t], \tag{8.13}$$

It is useful to consider the limiting cases $g(x, t = 0)$ and $g(x = 0, t)$, which we will refer to as the static and the dynamic correlation function. First we treat the static correlation function:

$$\langle h^2\rangle g(s) = \frac{k_B T}{\gamma(2\pi)^2}\int_{k_{min}}^{k_{max}}\frac{d\vec{k}}{k^2+\xi^{-2}}\exp[i\vec{k}\cdot\vec{s}], \tag{8.14}$$

switching from a summation to an integral. We next switch to cylindrical coordinates and integrate over ϕ:

$$\langle h^2\rangle g(s) = \frac{k_B T}{\gamma(2\pi)^2}\int\frac{kdk}{k^2+\xi^{-2}}\int_0^{2\pi}d\phi\exp[iks\cos\phi] = \frac{k_B T}{2\pi\gamma}\int_{k_{min}}^{k_{max}}dk\frac{k}{k^2+\xi^{-2}}J_0(ks). \tag{8.15}$$

The symbol J_0 denotes the Bessel function of the first kind. $k_{min} = 2\pi/L \simeq 0$ may be set to zero directly. Setting $k_{max} = \infty$ enables the calculation of the integral 8.15:

$$\langle h^2\rangle g(s) = \frac{k_B T}{2\pi\gamma}K_0(\frac{s}{\xi}). \tag{8.16}$$

where K_0 is the modified Bessel function of the second kind. This function diverges for $x \to 0$, but gives an accurate description for x greater than the colloid diameter σ [159]

Next we consider the height correlations in time $\langle h^2\rangle g(t)$ by setting $s = 0$. It is calculated as [42, 172, 174]:

$$\frac{k_B T}{\gamma(2\pi)^2}\int_{k_{min}}^{k_{max}}\frac{d\vec{k}}{k^2+\xi^{-2}}\exp[-\omega_k t]. \tag{8.17}$$

Here it is useful to change the integration variable into $k\xi$ and we may rewrite:

$$\langle h^2\rangle g(t) = \frac{k_B T}{2\pi\gamma}\int_{k_{min}\xi}^{k_{max}\xi}d(k\xi)\frac{k\xi}{1+(k\xi)^2}\exp[-\frac{(k\xi+(k\xi)^{-1})t}{2t_c}]. \tag{8.18}$$

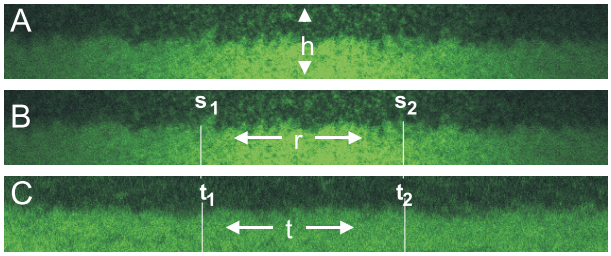

Figure 8.2. Characterizing capillary waves by confocal microscopy. Data shown are for statepoints II and IV. (A) The distributions of interfacial heights h. (B) The positional correlation between heights at several locations on the interface. (C) The time correlations between heights at different times (shown is the evolution of height in time at a fixed interfacial position).

We now have introduced three experimentally variables that characterize the system: $\langle h^2 \rangle^{\frac{1}{2}}$, $g(s)$ and $g(t)$, which give good results as shown in [42]. They are summarized in figure 8.2 with representative confocal images. Note that the image for the time correlation function (Fig. 8.2C) is in fact a sequence of 1 pixel wide height profiles measured in time. We now proceed to the experimental methods.

8.3. Experimental Section

Fluorescently labeled polymethyl-metacrylate particles were prepared using the Bosma method [14], slightly modified by using decalin (Merck, for synthesis) as the reaction solvent [175]. The particle polydispersity is around 10% from scanning electron microscopy and the dynamic light scattering particle radius is 69 nm. Polystyrene (2 10^3 kg mol^{-1}) was added as depletant polymer, with an estimated radius of gyration R_g of 42 nm [176]. At sufficiently high colloid and polymer volume fractions, respectively $\phi_c = \pi/6\sigma_c^3 n_c$ and $\phi_p = 4/3\pi R_g^3 n_p$ (with n_c and n_p the number densities of colloids and polymers respectively), this system phase separates into a colloid-rich (colloidal liquid) and a polymer rich (colloidal gas) phase. By diluting several phase separating samples with its solvent decalin, the phase diagram presented in Fig. 8.3A was constructed. The shown binodal is a guide to the eye (the theoretical binodal appears at much lower volume fractions) and the critical point is an estimate based on the ratios of the volumes of the phases.

A Nikon Eclipse E400 laser scanning confocal microscope equipped with a Nikon C1 scanhead was placed horizontally to study the colloid polymer mixture [175]. The microscope was furthermore equipped with a 405 nm laser and a Nikon 60X CFI Plan Apochromat (NA 1.4) Lens. The sample container is a small glass vial, part of which is removed and replaced by a thin (0.17 mm) glass wall. Series of 10 000 snapshots of the interface of 640 x 64 and 640 x 80 pixels (100 $\times$ 10.0 and 12.5 μm) were taken at constant intervals t_i of 0.45 s and 0.50 s of statepoints II and IV along the marked dilution line

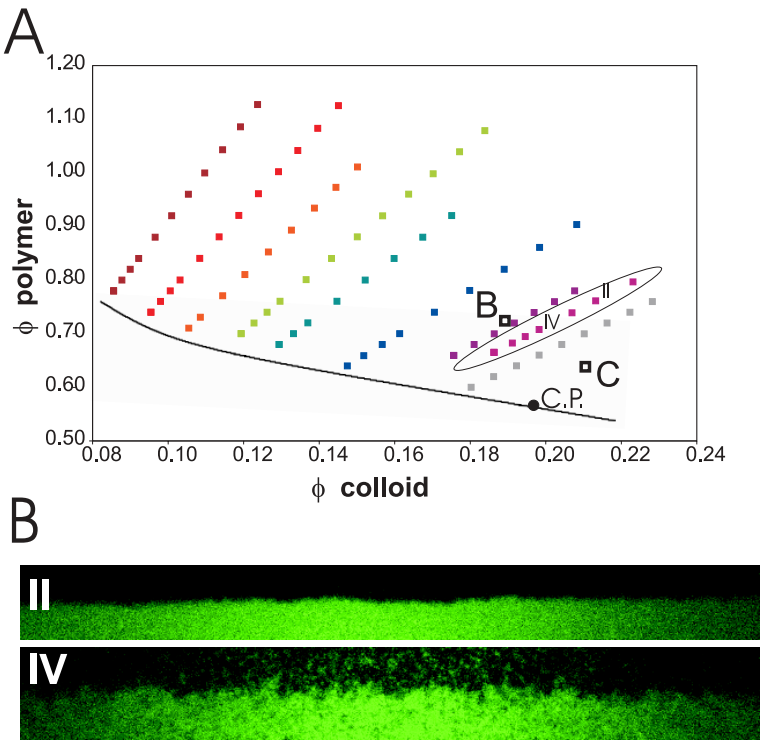

Figure 8.3. (A) Phase diagram of the system studied. The dilution line (line 11) studied here is marked. All shown state points phase separate. The indicated binodal is a guide to the eye: the theoretical binodal occurs at much lower concentrations. The marked critical point is an estimate based on the ratios of the volumes of the "liquid" and "gas" phases. Statepoints B and C will be studied in Chapter 10 and Chapter 11 respectively. (B) Confocal Images of Statepoint II and IV.

in the phase diagram, shown in Fig. 8.3A. A single scan takes approximately 0.25 s to complete (the exact scan time does vary by a few percent in time). Typical snapshots are shown for a number of state points in Fig. 8.3B. The low excitation wavelength results in resolution of $\sim$ 160 nm. The particles are $\sim$ 138 nm in diameter, hence a pixel roughly corresponds to a particle. Note that the resolution of the measured heights is significantly higher than this: the vertical location of the interface $h(s)$ is determined for each column of pixels in a frame by fitting this series of pixel values $I(z)$, which is proportional to the local colloid concentration, to a van der Waals profile $I(z) = a + b\tanh([z - h(s)]/c)$, as in [61]. The average height of the interface is set as $h = 0$. The exact resolution depends on the contrast between the phases b, which depends on the distance to the critical point, as well as on the width of the interface c. Far away from the binodal the height fluctuations are small compared to the microscopic resolution, close to the binodal the contrast between the phases reduces and the capillary waves start to show overhang effects.

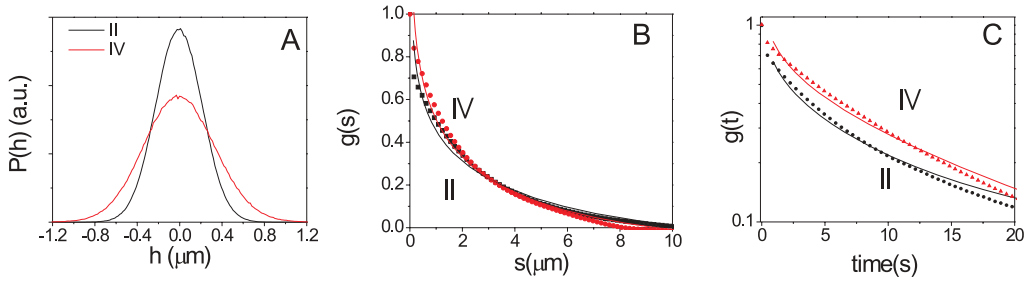

Figure 8.4. Interfacial properties determined by height distributions and height correlation functions for state points II and IV. (A) height distributions. (B) The static correlation functions, normalized by $\langle h^2 \rangle$. (C) The dynamic correlation functions, normalized by $\langle h^2 \rangle$.

8.4. Observations and Results

The wave heights h at an arbitrary point are distributed according to the Gaussian (8.8). The height distributions are shown for statepoints II and IV in Fig. 8.4A, with $\langle h^2 \rangle^{1/2} = 0.219$ and $0.336 \mu m$ for statepoints II an IV respectively. These will be used as a unit for the heights.

We find the capillary lengths from the positional correlation function $\langle h^2 \rangle g(s)$ (8.16), setting $k_{max} = \infty$ and $k_{min} = 0$. For statepoints II and IV they are shown in Fig. 8.4B, resulting in interfacial tensions $\gamma = 66 nNm^{-1}$ and $18 nNm^{-1}$ and $\xi = 11.2 \mu m$ and $7 \mu m$.

Next we consider the height correlations in time $\langle h^2 \rangle g(t - t')$ (8.18). The measured and fitted (setting $k_{max} = \infty$ and $k_{min} = 0$) dynamic correlation functions of statepoints II and IV are shown in Fig. 8.4C. From the fits, the interfacial tensions and the capillary times can be extracted, which gives $t_c = 12s$ and $\gamma = 69 nN/m$ for statepoint II and $t_c = 22s$ and $\gamma = 26 nN/m$ for statepoint IV, in reasonable agreement with the values found with the static correlation function.

The residence and waiting times are calculated through the experimentally obtained functions $p_n^{\pm}(h)$. In order to check the possible variation of waiting and residence times, we calculate the distributions for intervals of 1,2 and 4 t_i. They are shown for statepoint IV at heights $h = -1, 0$ and $1 \langle h^2 \rangle^{1/2}$ in Fig. 8.5A. Note that the x-axis has intervals as units, not time. The distributions are clearly complicated: the shortest interval of 1 time interval becomes more dominant as Δt decreases as shown in the inset of Fig. 8.5A. On the other hand, $h = -\langle h^2 \rangle^{\frac{1}{2}}$ has a surprisingly large interval of $\approx$ 2-50 interval durations, which occur most frequently for $\Delta t = 4 t_i$. It is important to realize that these are normalized distributions and that the number of intervals may strongly vary with both measurement interval and reference height. The longest intervals decay exponentially and as expected decrease most rapidly in quantity for the largest time

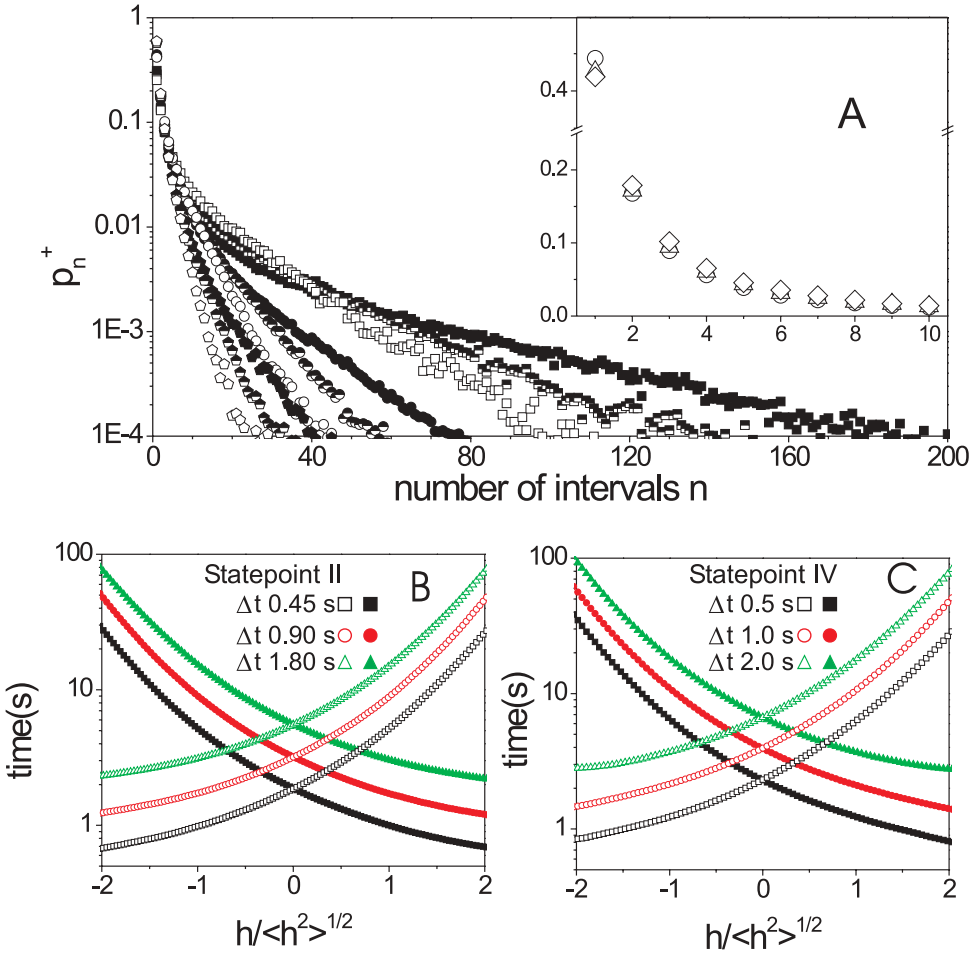

Figure 8.5. (A) The distribution of observed residence times τ^+ for statepoint IV. $p_n^+(h)$ is shown for h = -1 (squares), 0 (circles) and 1 (pentagons) $\langle h^2 \rangle^{\frac{1}{2}}$. The extent of filling corresponds to time intervals Δ t = 1 t_i (filled), 2 t_i (semi-filled) and 4 t_i (open). The inset zooms in to the distribution for short intervals for $h = 0$. Here, the symbol corresponds to time interval Δ t = 1 t_i (circles), 2 t_i (triangles) and 4 t_i (diamonds).(B) Observed waiting times (open symbols) and residence times (filled symbols), observed for statepoint II, at time intervals of 1 t_i (black squares), 2 t_i (red circles) and 4 t_i (green triangles). (C) as in panel (B), but now for statepoint IV.

intervals. As a result, the waiting and residence times, shown for statepoints II and IV as a function of height in Fig. 8.5B and C, are confusing at first sight: if we increase the time in between observations Δt to 2 or 4 t_i, the observed residence times are significantly larger!

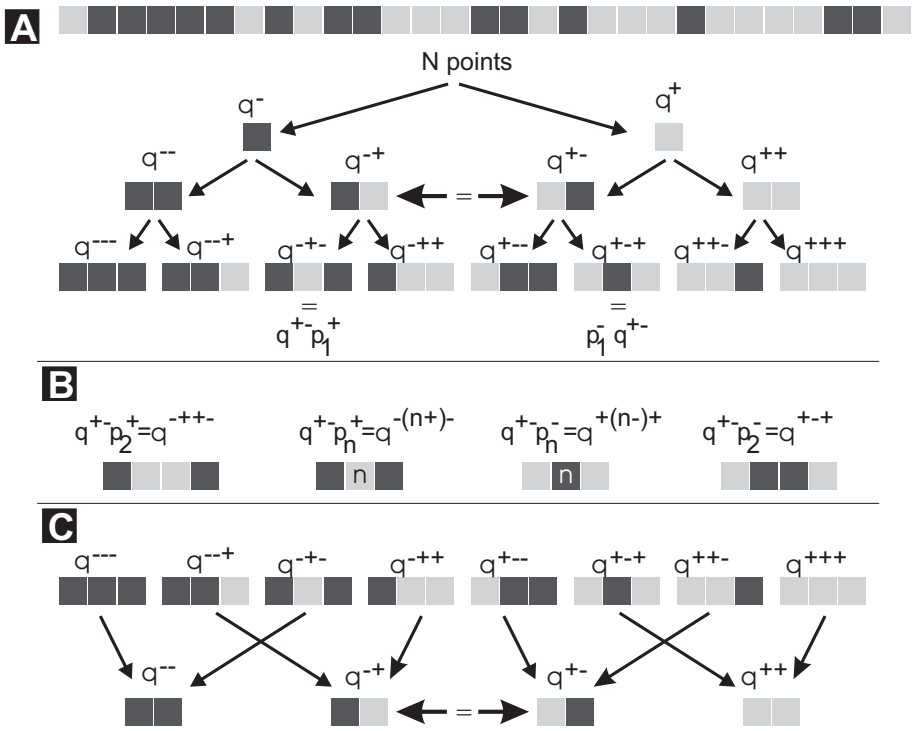

Figure 8.6. Interpretation of the measured waiting times. (A) From a measurement of N points a fraction q^+ is above (the light grey squares) h and a fraction q^- is below h (the dark grey squares). For two consecutive points, these fractions can be split up in $q^+ = q^{++} + q^{+-}$ and $q^- = q^{-+} + q^{--}$. Obviously, $q^{-+} = q^{+-}$. It is a measure for the fraction of transitions and therefore a measure for the number of hills or valleys as well. For three consecutive points we can similarly write $q^{-+} = q^{-++} + q^{-+-}$. q^{-+-} is the fraction of - + - sequences and therefore equivalent to $q^{+-}p_1^+$. (B) By extending the scheme in panel (A) we find $q^{-++-} = q^{+-}p_2^+$. Very generally, for the observation of n consecutive points above h, we can write $q^{-(n+)-} = q^{+-}p_n^+$. Completely analogous relations are shown for the valleys. (C) By increasing the time interval by a factor two, the distribution of consecutive points changes. For example q^{++} for the double time interval is made up of $q^{+++} + q^{+-+}$ of the single time interval and clearly shows that the interval time affects the measured distributions.

8.5. Interpretation and Discussion

In order to understand these observations, we need some theoretical framework. In the spirit of von Smoluchowski we start with simple counting arguments, [153, 154], in order to identify the essential object to be calculated. Consider a long measurement of N snapshots, as sketched in Fig. 8.6A. A fraction q^+ of these points is above height h (hills) and a fraction q^- is below height h (valleys). Of course these fractions can

simply be calculated from the equilibrium distribution:

$$q^+(h) = \int_h^\infty dh' P_{eq}(h') \tag{8.19}$$

and

$$q^-(h) = \int_{-\infty}^h dh' P_{eq}(h'). \tag{8.20}$$

Each of these fractions can be subdivided in heights after which either a hill or a valley follows and we obtain

$$q^+(h) = q^{++}(h, \Delta t) + q^{+-}(h, \Delta t) \tag{8.21}$$

and

$$q^-(h) = q^{--}(h, \Delta t) + q^{-+}(h, \Delta t). \tag{8.22}$$

Here q^{+-} is the fraction of hills after which a valley follows, which is equivalent to q^{-+}, since each interval in which the interface crosses the level h from above is followed by a next crossing from below. Furthermore q^{++} and q^{--} respectively are the fraction of two consecutively observed hills and valleys. q^{+-}, unlike q^+ and q^- is dependent on the measurement interval since it involves two consecutive observations, for which we have no knowledge of the history in between the measurements, see Fig. 8.6B. This means that in between two consecutive observations above h, the interface may have crossed the height any even number of times. Moreover Nq^{+-} is the total number of hills (as well as the number of valleys), which implies that $q^{+-}(h)\tau^+(h)$ is the fraction of time spent in hills:

$$q^{+-}(h, \Delta t)\tau^+(h) = q^+(h) \tag{8.23}$$

and

$$q^{+-}(h, \Delta t)\tau^-(h) = q^-(h). \tag{8.24}$$

Equations (8.23) and (8.24), independently of $q^{+-}(h, \Delta t)$, imply:

$$\frac{\tau^+(h)}{\tau^-(h)} = \frac{q^+(h)}{q^-(h)}, \tag{8.25}$$

which is experimentally verifiable. In Fig. 8.7A we show that both sides of equation (8.25) fall on a single mastercurve over nearly the full spectrum of heights for both statepoints.

For $q^{+-}(h, \Delta t)$ we need the joint probability to find the interface on level h' at $t = 0$ and on h'' at time t

$$\langle \delta(h(0,0) - h')\delta(h(0,t) - h'')\rangle = P_{eq}(h')G_c(h', 0|h'', t). \tag{8.26}$$

It is the product of the height distribution function and the conditional probability, that starting from h' at $t = 0$ one arrives at h'' a time t later.

Thermal influences can be represented by a fluctuating force $F_k(t)$ on the mode k in the Langevin equation: [177]

$$\frac{\partial h_k}{\partial t} = -\omega_k h_k + F_k(t) \tag{8.27}$$

The first term is the systematic damping force, which by itself would lead to an exponential decay of mode k. The random force $F_k(t)$ is assumed to be δ–correlated in time (white noise):

$$\langle F_k(t)\, F_{-k}(t')\rangle = \Gamma_k \delta(t-t'), \tag{8.28}$$

where Γ_k can be found from the fluctuation-dissipation theorem

$$\frac{\Gamma_k}{2\omega_k} = \langle |h_k|^2\rangle = D_k. \tag{8.29}$$

Note that the only memory of the past in (8.27) is the starting value h_k, because of the δ–correlation of the force. The only justification for the correlation (8.28) is that the thermal motion is fast with respect to the slow systematic force. With the Langevin equation all correlation functions can be calculated. Equations (8.28) and (8.29) yield the same result for $g(t)$.

The Fokker-Planck equation, which is equivalent to the Langevin equation, reads

$$\frac{\partial P(h_k,t)}{\partial t} = \omega_k \frac{\partial h P(h_k,t)}{\partial h_k} + \frac{\Gamma_k}{2}\frac{\partial^2 P(h_k,t)}{\partial h_k^2}. \tag{8.30}$$

It gives the evolution of the probability distribution $P(h_k,t)$ starting from an initial distribution $P(h_k,0)$. The solution of (8.30) provides the conditional probability on the mode $h_k(t)$, starting with the value $h_k(0)$. Linearization of the Navier-Stokes equation is justified by the relatively large difference between $\langle h^2\rangle^{\frac{1}{2}}$ and ξ, resulting in neglegible mode-coupling.

$$P_c(h_k(0)|h_k(t)) = \frac{1}{[2\pi D_k(1-e^{-2\omega_k t})]^{\frac{1}{2}}} \exp -\frac{|h_k(t) - h_k(0)e^{-\omega_k t}|^2}{2D_k(1-e^{-2\omega_k t})} \tag{8.31}$$

The result can be translated into the conditional probability on a value h' at $t = t$ from a start with h at $t = 0$:

$$G_c(h',0|h,t) = \frac{1}{[2\pi\langle h^2\rangle(1-g^2(t))]^{\frac{1}{2}}} \exp -\frac{[h - h'g(t)]^2}{2\langle h^2\rangle[1-g^2(t)]} \tag{8.32}$$

This circumvents the use of the decay frequency ω_k by using the measurable function $g(t)$. A check on (8.32) is that the correlation function $\langle h(0)h(t)\rangle$ as calculated from (8.26) and (8.32) gives the result $\langle h^2\rangle g(t)$. Figure 8.4C shows that $g(t)$ does not decay exponentially. Thus the spatial process is non-Markovian [177].

According to 8.26 $q^{+-}(h,\Delta t)$ is given by the integral

$$q^{+-}(h,\Delta t) = \int_h^\infty dh' P_{eq}(h') \int_{-\infty}^h dh'' G_c(h',0|h'',\Delta t), \tag{8.33}$$

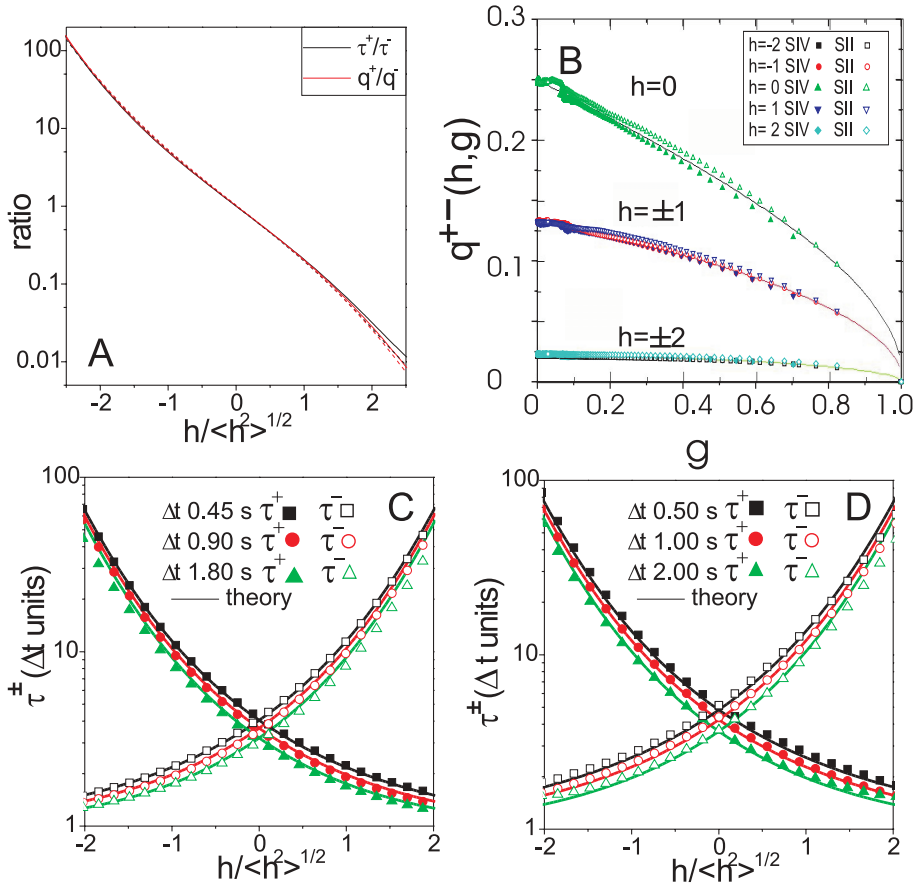

Figure 8.7. Waiting and residence times for statepoints II and IV. (A) The relation $q^+(h)/q^-(h) = \tau^+(h)/\tau^-(h)$ clearly holds over many orders of magnitude, both for statepoint II (dashed lines) and IV (non-dashed lines). (B) the probability $q^{-+}(h, g)$ as a function of g for $|h| = 0$, 1 and 2 $\langle h^2 \rangle^{1/2}$. The lines are the theoretical expressions, the points are obtained through the definition of r from the experiment. (C) Theoretical and observed time intervals for the waiting and residence times of statepoint II, with $\Delta t = 1$ (black squares), 2 (red circles) and 4 (green triangles) t_i. Open symbols are waiting times, closed symbols are residence times. The lines are the theoretical curves. (D) Theoretical and observed time intervals for statepoint IV, with $\Delta t = 1$,2 and 4 t_i. Symbols are identical to those in panel (C).

where the first integral selects the points above h with the height distribution and the second integral selects the points below h with the conditional probability given by (8.32). We have made the dependence on the interval length Δt explicit because it is an important issue. Δt enters in the calculation of $q^{+-}(h, \Delta t)$ through the value $g(\Delta t)$. We may therefore consider q^{+-} also as a function of h and $g = g(\Delta t)$, using the experimental values of $g(t)$ as input. Of course $q^{+-}(h, g)$ is experimentally measurable using its definition, that is the fraction of hills after which a valley follows. The theoretical and experimental $q^{-+}(h, g)$ are plotted in Fig. 8.7B as function of g for a few values of h for

both statepoints, resulting in a single curve for each $h/\langle h^2\rangle^{\frac{1}{2}}$. The agreement between theory and experiment is remarkable. The observed residence and waiting times for $\Delta t= 1, 2$ and $4t_i$ for statepoints II and IV, are shown in Fig. 8.7C and D in terms of units Δt. Again we find excellent agreement with the theory, using the measured values for the $g(t)$ function as theoretical input for the determination of r. Note that the y-axis has units "Δt" and is dimensionless. In terms of time, the residence time at height h increases with Δt. At sufficiently large h, the theoretical times are always larger than the experimental values, see Fig. 8.7C and D. This is at least partly due to the limited amount of time points considered, which tends to exclude the tail of the distributions $p_n^{\pm}(h)$.

With equation (8.23), equation (8.24) and the computation of $q^{+-}(h, g)$ we have determined the residence and waiting times without evaluating the distributions $p_n^{\pm}(h)$. In order to determine these we reconsider Fig. 8.6A. We focus on the shortest time interval. Using similar arguments as before:

$$q^{-+}(h, \Delta t) = q^{-++}(h, \Delta t) + q^{-+-}(h, \Delta t), \tag{8.34}$$

where q^{-+-} and q^{-++} are the fractions of hills with length one and with length longer than one respectively. This implies that

$$p_1^+(h, \Delta t) = \frac{q^{-+-}(h, \Delta t)}{q^{+-}(h, \Delta t)} \tag{8.35}$$

and more generally

$$p_n^+(h, \Delta t) = \frac{q^{-(n+)-}(h, \Delta t)}{q^{+-}(h, \Delta t)}. \tag{8.36}$$

Completely analoguous equations are easily derived for the valleys. The consequence is that an $n+2$-fold integral is required for the determination of point n of the distribution. From Fig. 8.5A it is clear that the probabilities for an interval with length n only start to decay exponentially at very large n. The calculation of the full distribution therefore requires the computation of increasingly complicated multiple correlation functions:

$$q^{-(n+)-}(h, \Delta t) = \int_{-\infty}^{h} dh_0 \int_{h}^{\infty} dh_1 ... \int_{h}^{\infty} dh_n \int_{-\infty}^{h} dh_{n+1} \\ G_{n+2}(\{h_0|0\}, ...\{h_{n+1}|(n+1)\Delta t\}), \tag{8.37}$$

The first integral guarantees that the sequence of heights starts below h, the last integral that it ends below h again as well. The other integrals require the sequence to be above h in between. Hence, G_{n+2} is a joint probability function which is analogous to (8.33). The full calculation of these integrals can be performed numerically using Monte Carlo integrations, although these become computationally expensive for large n. The best procedure is to generate a distribution according to the Gaussian integrand and to reject the points that fall outside the integration domain. Here we present the obtained

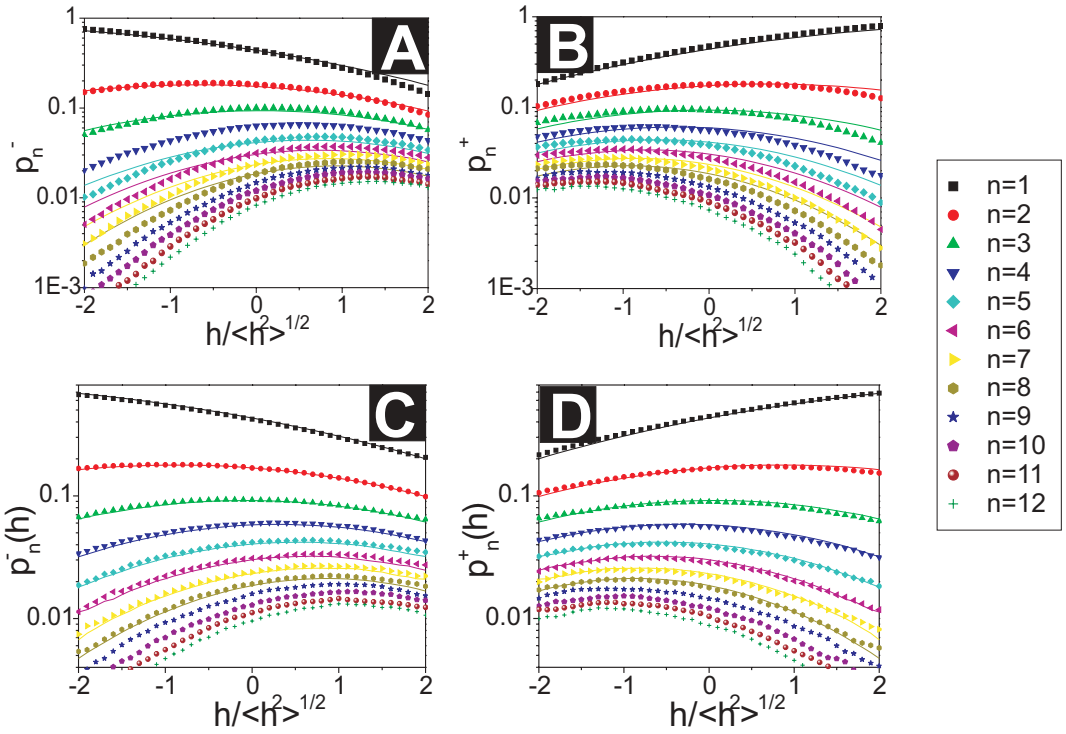

Figure 8.8. Waiting and residence time distributions. In panels (A) and (B) we show p_n^- (A) and p_n^+, both obtained through Monte Carlo integrations (curves, for n =1 up to 8) and those found experimentally (curves, for n =1 up to 12) with $\Delta t = t_i$ for statepoint II. (C) and (D) contain p_n^- and p_n^+ for statepoint IV.

results for statepoints II (Fig. 8.8A and B) and IV (Fig. 8.8C and D). In Fig. 8.8A and C and Fig. 8.8B and D the results for p_n^- and p_n^+ are shown as a function of height, with n up to 8 theoretically and up to 12 experimentally. The agreement is reasonable for statepoint II and very good for statepoint IV. The remainder of the distribution could be approximated by an exponential decay of probabilities. As this is clearly not the case until much higher n (Fig. 8.5A), which requires exhaustive computational time, we leave the matter as it is.

The higher order q fractions also reveal what changes when we increase the time interval by a factor of 2 (Fig. 8.6C). Obviously:

$$q^{++}(h, 2\Delta t) = q^{+-+}(h, \Delta t) + q^{+++}(h, \Delta t) \tag{8.38}$$

Knowledge of multiple correlation functions therefore also in principle gives information on higher order terms.

We now ask ourselves the question whether we can take the limit of $\Delta t \to 0$. If $q^{+-}(h, \Delta t)$ were to shrink proportional to Δt, the $\tau^{\pm}(h)$ would increase inversely proportional to Δt. However, analyzing the small Δt behavior of the expression (8.33),

which amounts to the limiting behavior for $g(\Delta t) \to 1$, we find

$$q^{+-}(h, g \to 1) \simeq \frac{\sqrt{1-g}}{\pi\sqrt{2}} \exp\left[-\frac{h^2}{2\langle h^2\rangle}\right]. \tag{8.39}$$

The square root in (8.39) is a reflection of the Brownian character of the fluctuations. If the initial decay of $g(t)$ is linear, $q^{+-}(h, g)$ vanishes as $(\Delta t)^{1/2}$ and consequently T and Θ vanish. Whether this vanishing is real should be doubted. At mesoscopic time scales the observed waiting time continually changes with the time interval. The behaviour of $g(t)$ at the microscopic timescale of molecular collisions could reveal the true waiting and residence times, but at those timescales the Langevin equation is not valid anymore, nor are our equations for the behaviour at small t.

Although these timescales are clearly beyond the reach of any microscopic technique, the behaviour of $g(t)$ at very small intervals could hold clues to how to relate the observed waiting times to the true waiting time. They could be related to the fastest decaying mode of the system, which depending on the system is either k_{max} or k_{min}. Measurements of the behaviour of $g(t)$ at timescales where these modes start to dominate (Fig. 8.9A) should be feasible with fast microscopy measurements.

8.6. Conclusion

We have presented confocal microscopy experiments along with theory for the microscopic waiting and residence times of heights h of the capillary waves of the fluid-fluid interface of a phase separated colloid-polymer mixture. Due to the Brownian character of the process, these times depend on the experimental measurement interval Δt. The results from this discrete time sampling are predictable in terms of the decay of the height-height correlation function $g(t)$, which in principle includes the relevant system variables interfacial tension and capillary time. The distribution of time interval lengths is predictable, although every point requires individual computation, which becomes increasingly cumbersome for longer interval lengths. We find excellent agreement between experiments and theory.

8.7. Outlook

We now attempt to put our observations in a practical context, taking droplet coalescence as an example. To relate these waiting times to the coalescence problem requires the investigation of waiting times for a fluctuation h within an area L^2 [170]. A straightforward starting point is to include the positional correlation function $\langle h^2\rangle g(s)$ which introduces the capillary length ξ as an additional scaling parameter, see Fig. 8.9B. A first approach to understand the droplet coalescence problem could include a study on the joint probabilities for two fluctuations to simultaneously occur between two surfaces locations that together cover a gap $\Delta/\langle h^2\rangle$, inducing coalescence. This could even

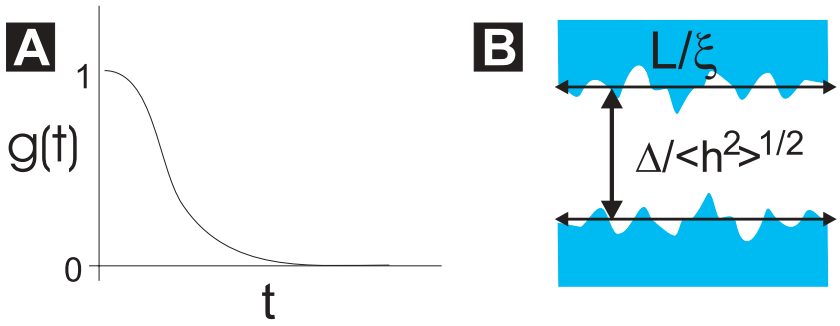

Figure 8.9. Possible future measurement: (A) At small time intervals $g(t)$ sharply bends towards $\langle h^2 \rangle$. The behaviour of $g(t)$ at small time intervals could hold clues to the true waiting times. (B) A possible future investigation could include the waiting time for the coalescence of two interfaces with length L separated by a distance Δ. Obvious dimensionless parameters are L/ξ for the length and the separation $\Delta/\langle h^2 \rangle^{\frac{1}{2}}$ respectively are the capillary length ξ and the mean square height $\langle h^2 \rangle$.

be studied experimentally by studying coalescence between two walls with thick wetting layers (such that the thickness of the layers does not affect the fluctuations too much). The full droplet coalescence problem is complicated since it involves deformed interfaces with a varying gap Δ. For interfaces with higher interfacial tensions and accordingly lower $\langle h^2 \rangle$, the distribution of locations where the coalescence events takes place should be increasingly narrow. As $\langle h^2 \rangle$ increases, the distribution of coalescence locations should increase, since the coalescence event should occur at a larger gap, with relatively less variation in the gap over the droplet surface. The Brownian character of the process complicates experimental measurements: instead of a single waiting time, a distribution of times should be expected which requires the study of the coalescence of a large number of droplets, with identical dimensions, preferrably for a few values of γ.

8.8. Acknowledgement

The theoretical part was developed in collaboration with Hans van Leeuwen and Wim van Saarloos. Dirk Aarts performed preliminary work leading to this work. Henk Blöte, Frank den Hollander, Gerard Barkema and Jan Groenewold are acknowledged for insightful discussions. The experimental system was developed by Julius de Folter during his Masters thesis. I additionally thank Chantal Vonk for assistance with particle synthesis, Stefano Sacanna for help with the electron microscopy and Bonny Kuipers for aid with the dynamic light scattering experiments.

Part 4

The Transport of Particles through a Fluctuating Interface

9

The approach of spheres and droplets towards a deformable fluid-fluid interface

Abstract

We compare the low Reynolds number approach of rigid spheres and deformable droplets of similar sizes towards a deformable fluid interface in a fluid-fluid demixing colloid polymer system. The droplets appear during the final stages of phase separation. A small amount of rigid poly-methyl-methacrylate PMMA spheres is added to the top of the sample when phase separation has (nearly) completed. Both spheres and droplets sediment towards the interface. Far away from the surface the (dimensionless) sedimentation velocity of the droplets is slightly higher than that of the spheres, since the friction experienced by the droplets is slightly reduced by inner fluid circulation. Closer to the surface velocities are strongly reduced and the effective friction increases. Furthermore, the fluid surface becomes distorted at droplet/sphere to surface separations of about one diameter. The droplets strongly deform as well. Surprisingly, the velocities of rigid spheres and droplets converge. We attribute this to an increase of the friction factor of the droplet due to droplet deformation. These data may assist in a better understanding of the transport of matter through interfaces and the process of droplet coalescence. Moreover, the similarity of the drainage of rigid spheres and fluid droplets close to the surface supports the idea that from a theoretical point of view the (simpler) drainage problem for rigid spheres already captures some of the physics.

9.1. Introduction

Both the transport of matter through a fluid interface and the process of droplet coalescence are phenomena frequently observed in everyday life. They are important in a wide variety of (industrial) processes and natural phenomena, see for example [178–186]. Recent advancements in the field of microfluidics [187], in which fluids are manipulated on a microscopic level and miniature chemical reactions can be carried out on a chip, raise a further need to study these issues.

Both the passage of a sphere through an interface and the coalescence of a droplet can be considered to consist of three stages: (i) film drainage of the continuous phase between the sphere/droplet and the surface, (ii) rupture of the film and (iii) either the further movement of the sphere or the extrusion of the droplet material into its bulk phase. The aim of this chapter is a direct comparison of step (i) of both phenomena. For droplets this first step has been studied for quite some time [188–192], but it theoretically still poses some difficulties [193]. For rigid spheres it has mainly been treated as an approximation of the first step in droplet coalescence [188, 190, 191, 194], but it has also received some attention as the initial stage of transport through an interface [195–198]. Here, we study the approach of spheres to the interface not only to shine some light on the drainage problem in droplet coalescence, but as well to understand the problem of the transport of spheres through interfaces.

As our system we use fluorescent droplets and spheres of similar sizes and essentially made up of the same material approaching the gas liquid interface of a phase-separated colloid/polymer mixture, which makes the system rather special. Moreover, the intrinsic slowness of the colloid-polymer mixture enables a direct comparison of both processes close to the interface and ensures that the Reynolds number remains much smaller than unity. The respective approaches are imaged by laser scanning confocal microscopy (LSCM).

9.2. Theoretical background

Far away from a surface, a droplet or rigid sphere with radius R of R_d or R_s, respectively, sediments with a constant velocity u_s. The sedimentation velocity is proportional to $g\Delta\rho R^2/\eta$, with g earth's acceleration, $\Delta\rho$ the density difference between the droplet/sphere and its surrounding phase (its buoyancy) and η the viscosity of the phase through which the object is sedimenting. In general, for spherical objects the sedimentation velocity is given by the Rybczynski-Hadamard result, which can be found in [199],

$$u_s = \frac{2g\Delta\rho R_d^2}{3\eta_o}\frac{\eta_o + \eta_i}{2\eta_o + 3\eta_i}, \tag{9.1}$$

where η_o is the viscosity outside and η_i the viscosity inside the object. This equation accounts for circulation of fluid inside the object as well. When $\eta_i \gg \eta_o$ the well-known Stokes equation for a rigid sphere is obtained

$$u_s = \frac{2g\Delta\rho R^2}{9\eta}, \tag{9.2}$$

and we recognize the Stokes friction factor as well: $f = F/u_s = 6\pi\eta R$ with F the force acting on the sphere. We can estimate at what size droplets will deform by considering the capillary number Ca, which reads

$$Ca = \frac{\eta u}{\gamma}, \tag{9.3}$$

and we here set $u = u_s$. Approximately, the droplet will not deform if the capillary number Ca remains smaller than unity and by filling in the estimate of u_s given above we obtain the Bond number Bo:

$$Bo = \frac{g\Delta\rho R^2}{\gamma}. \tag{9.4}$$

Hence, when $Bo < 1$ or $R < L_c \equiv \sqrt{\gamma/\Delta\rho g}$, droplets will not deform. We see that the cross-over length is equal to the capillary length L_c. From the well-known Reynolds number,

$$Re = \frac{\rho u L}{\eta}, \tag{9.5}$$

with ρ the mass density and L the characteristic length we can estimate whether or not inertial terms become important during sedimentation. Using the estimate of the sedimentation velocity and filling in typical numbers of $\rho \sim 10^3$ kg m^{-3}, $\Delta\rho \sim 10^2$ kg m^{-3}, $L \equiv R \sim 10^{-5}$ m and $\eta \sim 10^{-2}$ Pa s we find that $Re \ll 1$ during sedimentation.

Closer to the surface the velocity of the sphere/droplet reduces. The friction factor can then be written as $f = 6\pi\eta_o R\lambda$ with λ the correction to the Stokes friction. For a rigid sphere approaching a solid or free non-deformable surface exact treatments are given in [200], which describe both the undistorted fall of equation (9.2) and the velocity close to the surface:

$$\lambda = 4/3\sinh\alpha \sum_{n=1}^{\infty} \frac{n(n+1)}{(2n-1)(2n+3)} C(n,\alpha) \tag{9.6}$$

with

$$C_{rigid}(n,\alpha) = \frac{2\sinh((2n+1)\alpha) + (2n+1)\sinh(2\alpha)}{4\sinh^2((n+1/2)\alpha) - (2n+1)^2\sinh^2(\alpha)} - 1 \tag{9.7}$$

for a rigid surface and

$$C_{free}(n,\alpha) = \frac{4\cosh^2((n+1/2)\alpha) + (2n+1)^2\sinh^2\alpha}{2\sinh((2n+1)\alpha) - (2n+1)\sinh(2\alpha)} - 1 \tag{9.8}$$

for a free surface, with $\alpha = \cosh^{-1}(d/R)$ and d the distance of the sphere's center to the interface. In the limit of $z \to \infty$, the friction factor $\lambda \to 1$ in both cases. In the asymptotic limit of $h = z - R \longrightarrow 0$, where z is the minimal distance between sphere and surface, it becomes:

$$\lambda \to \frac{R}{z} \text{ and } \lambda \to \frac{R}{4z} \tag{9.9}$$

for a solid surface and for a planar free surface, respectively. These limiting equations can be found from lubrication equations as well [201, 202]. The factor 4 difference between a solid and a fluid interface is commonly observed in these type of problems. For a solid sphere approaching a deformable surface Hartland has derived expressions from lubrication theory valid for small sphere-surface separations [190]. He finds that h $\propto t^{-1/2}$. These results have later been confirmed by Jones and Wilson [193].

However, when both the fluid interface and the droplet get distorted, the description becomes more complicated: there is some constriction in the film thickness at its periphery, which slows down drainage. Furthermore, fluid circulates in the drop since it has a finite viscosity, which tends to speed up drainage as compared to a rigid sphere. These last two effects are properly treated by Jones and Wilson [193], who point out that these effects are not captured in simple lubrication theories. They predict several asymptotic regimes, which have been confirmed by Yantsios and Davis [203] using extended lubrication theories. No full analytical treatment can be obtained and the main problem in comparison with the present experimental data is that the asymptotic limits become valid for very small separations [203]. Furthermore, to pinpoint our problem we will only consider rigid spheres with $Bo < 1$, where $\Delta\rho$ now is the density difference between solid and gas and interface deformation thus does not result in a tailing configuration [196]. The Bond number can be viewed as the ratio between equation (9.2) and the capillary velocity. The latter is the characteristic interface velocity, which is given by the balance between the Laplace pressure and the viscous dissipation resulting in the capillary velocity $u_c = \gamma/\eta$. Note that the capillary velocity depends on the viscosity of both the gas and the liquid phase, whereas the bulk sedimentation rate of rigid spheres only depends on the viscosity of one phase (here, it is the gas). The viscosity of the phases therefore does somewhat affect the Bond number and therefore the extent of surface deformation. For viscosities of the same order of magnitude the effect is minimal.

Finally, it can easily be shown that during the deformation of the interface and droplet the Reynolds number remains much smaller than unity. Since the Bond number is smaller than unity in all cases, the largest velocity of importance is the capillary velocity.

Setting u in equation (9.5) equal to u_c we can estimate at what length inertia becomes as important as viscous dissipation. The length L_η at which the inertial contribution starts to dominate over viscous terms therefore is:

$$L_\eta = \frac{\eta^2}{\rho\gamma}, \tag{9.10}$$

Compared to a 'normal' fluid, a substantial increase in viscosity or decrease in interfacial tension is necessary to access the viscous regime. Here, the interfacial tension is decreased by resorting to colloid-polymer mixtures. Owing to a depletion-induced attraction [35,37], these mixtures exhibit a "gas" (colloid poor/polymer rich)-"liquid"(colloid rich/polymer poor) phase separation when the polymer/colloid diameter ratio q is sufficiently large ($q = \sigma_p/\sigma_c \geq 0.30$ [39]). Since colloidal particles have sizes of typically 1-1000 nm, these systems have much lower interfacial tensions –as experimentally verified [44,45,204,205]– than molecular systems with a magnitude proportional to [40,41]:

$$\gamma \propto \frac{k_B T}{d^2}, \tag{9.11}$$

with $k_B T$ the thermal energy and d the typical length scale at the interface, similar to the colloidal particle diameter σ_c far away from the critical point. Combining equation (9.11) with equation (9.10) shows that L_η can easily become of the order of meters and the viscous regime therefore is readily available for experimental inspection.

9.3. Experimental system and technique

The colloids used are polymethyl-metacrylate spheres (PMMA), fluorescently labelled with 4-methylaminoethyl meth-acrylate- 7-nitrobenzo-2-oxa-1,3-diazol (NBD). The particles were prepared using the Bosma method [14], slightly modified by using decalin (Merck, for synthesis) as the reaction solvent [175]. The set's polydispersity is below 10% from electron microscopy and the dynamic light scattering particle radius is 25 nm. Polystyrene (233 kg mol^{-1}) was added as depletant polymer, with an estimated radius of gyration R_g of 14 nm [176]. Very large, very polydisperse PMMA-NBD spheres (σ_c = 100 nm - 100 μm, $\rho = 1.17$g/ml) were accidentally obtained from a synthesis following [14] and subsequently size-fractionated twice in hexane (Chapter 5). The resulting 5-40 micron spheres were transferred to cis/trans decalin and diluted to a concentration of 1 wt%.

At a colloid volume fraction $\phi_c = \frac{\pi}{6}\sigma_c^3 n_c = 0.076$ of the 25 nm colloids and a polymer volume fraction $\phi_p = 4/3\pi R_g^3 n_p = 0.50$ the system phase separated into a colloid-rich (colloidal liquid) and a polymer rich (colloidal gas) phase (with n_c and n_p the number of colloids and polymers respectively) [206]. The densities of the phases were 0.90 g/ml and 0.95 g/ml with viscosities of 8 and 31 mPa s for the gas and liquid phases respectively. By analyzing the interfacial profile close to a hard wall the capillary length can be obtained [205, 207]. Since the densities of both phases are known, the surface

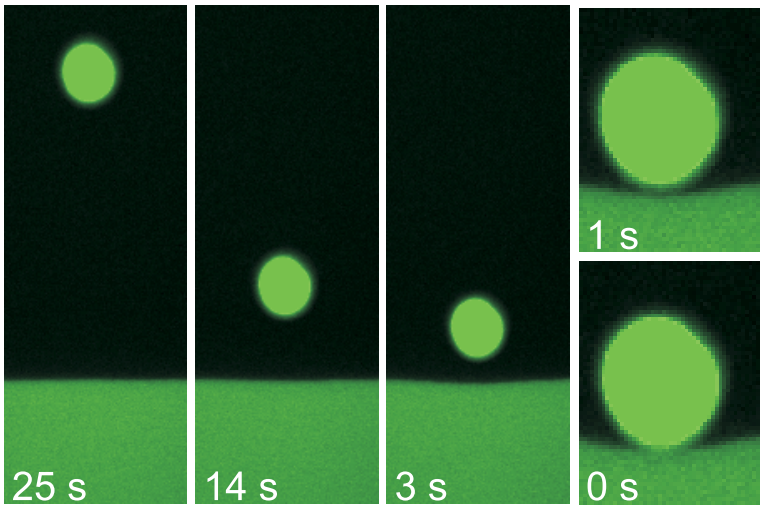

Figure 9.1. Approach of a 15 μm diameter sphere to the interface. Times are before wetting by the liquid phase. Initially the interface is undeformed (25 s). At separations smaller than the sphere diameter the interface starts to deform and the sphere slows down (14 s). As the sphere approaches the interface, the separation becomes more pronounced (3 and 2 s). At very small separations the liquid phase wets the sphere and pulls down the sphere(1 and 0 s). The analogy between sphere and droplet stops here.

tension can be estimated from the capillary length: 0.16 μN m^{-1}. By analyzing the capillary wave spectrum we found $\gamma = 0.2$ μN m^{-1} [42] in good agreement with the more suitable interfacial profile technique.

A Nikon Eclipse E400 laser scanning confocal microscope was placed horizontally to study the colloid polymer mixture [175]. The setup allows for monitoring using transmission light microscopy as well as laser scanning confocal microscopy (LSCM). A confocal scanning laser head (Nikon C1) was mounted on the microscope with a maximal capturing rate of approximately one frame (512x512 pixels) per second. The microscope was furthermore equipped with a 488 nm ArKr laser and several lenses (NIKON 20X ELWD Plan Fluor (NA 0.45) and 60X CFI Plan Apochromat (NA 1.4)). The sample container is a small glass vial, part of which is removed and replaced by a thin (0.17 mm) glass wall.

The colloid-polymer mixture was homogenised and left until a sharp interface had formed, after approximately 20 minutes [206]. Drops of colloidal liquid subsequently formed at the colloidal gas - air interface, detached from it by gravity and subsequently sedimented towards the gas-liquid interface until they coalesced with it [208].

A small amount (1.0 % v/v of the total sample volume) of very large, very polydisperse PMMA-NBD was carefully added to the top of colloidal gas phase, 16 hours after phase separation had completed. The spheres subsequently sedimented towards the gas-liquid interface.

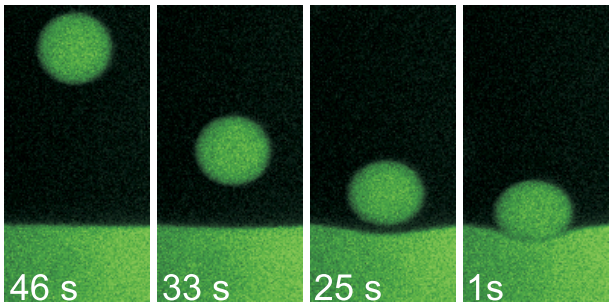

Figure 9.2. Approach of a 33 μm diameter droplet to the interface. Times are before coalescence: Initially (46 s) the interface is undeformed. At separations of approximately the droplet diameter the interface and droplet starts to deform and the droplet slows down (33 s). As the droplet approaches the interface, the separation becomes more pronounced (25 s). Right before coalescence (1s), the droplet is nearly immobile and only a very thin film separates it from its bulk phase.

9.4. Observations

Examples of spheres and droplets approaching the interface are shown in figure 9.1 and figure 9.2. Both types of objects initially sediment at a constant velocity. They start to slow down due to solvent backflow at a separation of about their own diameter and the gas-liquid interface and the droplet surface then get distorted as well. The velocity continues to decrease strongly and the surface distortion becomes more pronounced. The spheres then either break through the interface and enter a tailing mode or become wetted by the liquid phase and are dragged into it. The critical sphere radius for which $Bo = 1$ is ~ 8 μm, but we observe that even slightly larger spheres do not enter a tailing configuration [196]. The wetting occurs at about sphere-surface separations below 1 μm and the sphere is pulled down due to the interfacial tension, see figure 9.1 at 1 and 0 s. Both the tailing mode and the wetting of the sphere will be discussed in subsequent chapters. Droplets will eventually coalesce with the bulk liquid phase. There, the thin draining gas-film breaks, which is facilitated by the dynamic interface roughness [42]. The subsequent suction of the droplet into the bulk liquid is purely a capillary-viscous affair [209].

In the next section we will quantitatively analyze and discuss these observations.

9.5. Analysis & Discussion

To investigate droplet and surface deformation and droplet and sphere movement, IDL routines [105] were developed to assign gas, liquid and solid phases to each of the images' pixels, based on their intensity. The average intensities I_{gas} and I_{liq} of the bulk gas and liquid phases were used to obtain a cutoff intensity $I_{cut} = 1/2(I_{gas} + I_{liq})$ to distinguish between the gas and liquid phases. (Fig. 9.3A). Pixels with intensities

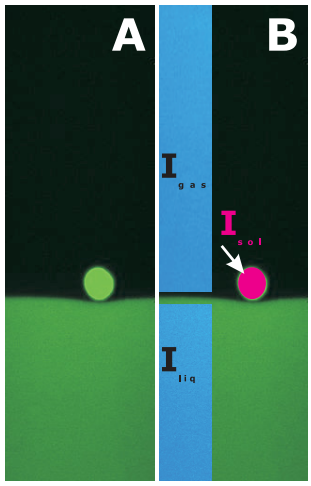

Figure 9.3. (A) Sample image of a sphere approaching the gas-liquid interface (B) the gas/liquid cutoff intensity is based on the average intensity of the bulk phases. The solid phase is assigned to pixels with intensities higher than the maximum intensity found in the liquid phase.

greater than the maximum intensity of the bulk liquid phase were assigned to the solid phase of the rigid sphere.

The (mean) radius of a sphere was obtained from its sedimentation velocity far from the interface in the gas or liquid phase (equation (9.2)). The obtained sphere velocities agree very well with the sphere radii obtained from image analysis but were sometimes slightly off because the center of the sphere was slightly out of focus.

In Fig. 9.4A and Fig. 9.4B the approach of a $15\mu m$ diameter sphere and a $26\mu m$ droplet are shown respectively. The bulk sedimentation velocities obtained from equation (9.2) and equation (9.1) agree well with the obtained values for droplets and spheres (droplets : 4.3 μms^{-1} (experiment) and 4.2 μms^{-1} (theory); spheres : 3.4 μms^{-1} (experiment) and 3.6 μms^{-1} (theory)) Once the droplets and spheres get as close to the interface as a single particle diameter they slow down. Both curves, plotted in dimensionless units (h/σ vs. F/f), are quite similar to the theoretical curve of the approach of a rigid sphere towards a free surface (Fig. 9.4C). The larger deviations in the sphere velocity data can be attributed to the slight deviation from the shape of a perfect sphere Fig. 9.4C.

The correction to the Stokes friction factor λ for droplets and spheres is plotted as a function of distance to the interface in Fig. 9.4D. It is obtained by adjacent averaging and subsequent differentiation. The theoretical curve for the approach of a rigid sphere to a free non-deformable surface is shown for comparison equation (9.6). The spheres follow equation (9.6) nearly perfectly (until the spheres are wetted by the liquid phase). The minimal deformation of the interface and the incorporation of the deformation

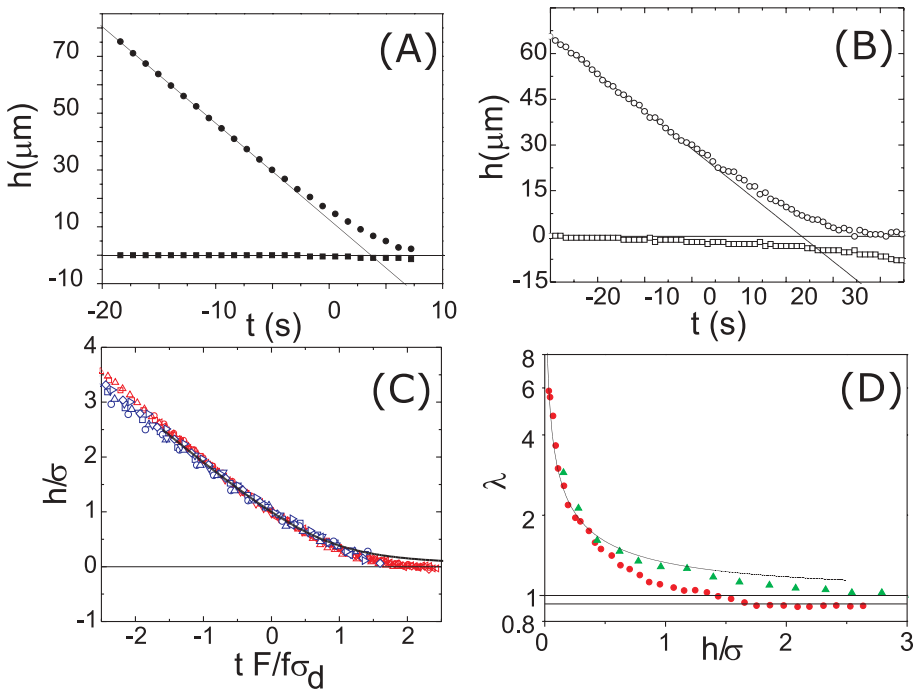

Figure 9.4. Mastercurves of droplets and spheres approaching a deformable interface: (A) approach of a 15 μm sphere relative to the deformed interface(filled circles) and the deformation of the interface (filled squares). The solid lines are the h=0 line and the fit to the positions far from the interface. (B) Approach of a 26 μm droplet relative to the deformed interface (open squares) and the deformation of the interface (open squares). The solid lines are the h=0 line and the fit to the positions far from the interface. (C) Approaches of six sets of spheres (squares) and six sets of droplets in terms of dimensionless times $tFf^{-1}\sigma^{-1}$ and heights $h\sigma^{-1}$. (D) The corrections to the Stokes friction as a function of distance to the interface. The solid line is the theoretical curve for the approach of a sphere to a non-deformable free surface from theory. λ is shown for droplets (diamonds) and rigid spheres (triangles). The λ values of 0.93 and 1.00 are indicated by the straight black lines

into the interface-sphere separation explain the agreement of the conceptually slightly different curves.

The droplets approach the interface slightly faster initially, with $\lambda \sim 0.93$, which can be obtained as well from equation (9.1). As the droplet and sphere approach the interface, λ increases due to solvent backflow, interface deformation and droplet deformation.

Interestingly, the λ values converge at very small separations, which supports the idea that from a theoretical point of view the (simpler) drainage problem for rigid spheres already captures some of the physics of droplet coalescence. The similarity is striking since the approach of a rigid sphere towards a rigid surface and a free surface result in

very different friction factors (equation (9.9)). Apparently, a second free surface (i.e. the droplet's surface) instead of a rigid surface does not affect the friction factor as strongly. We attribute the convergence of the velocities to the deformation of the droplet, which gradually cancels out the higher droplet velocity, caused by fluid circulation.

9.6. Conclusion

We present a unique approach in which similarly sized droplets and rigid spheres, essentially made up of the same material, approach the colloidal gas-liquid interface. As expected, the droplet approaches the interface slightly faster than the rigid sphere, the sphere is slower by a factor of the theoretical ~ 0.93. Interestingly, close to the interface the approach velocities converge due to deformation of the droplet, which supports the idea that from a theoretical point of view the (simpler) drainage problem for rigid spheres already captures some of the physics.

9.7. Acknowledgement

This work was carried out together with Dirk Aarts. Roel Dullens, Hans Scherff and Esther Groeneveld are acknowledged for particle synthesis.

10

The transport of a wettable sphere through a fluid-fluid interface

Part I: Low Bond numbers

Abstract

We report on the transport of a rigid sphere through the fluid-fluid interface of a demixed colloid-polymer mixture. The sphere is wettable by the colloid-rich phase it is transported to. The ultra-low interfacial tension in these phase separating mixtures results in wetting forces that are low enough to access the low-Reynolds regime. Moreover, it enables the investigation of the role of capillary waves. Rigid spheres of various sizes approach the interface by sedimenting through the polymer-rich phase toward the interface and are subsequently transported to the colloid-rich phase. Three consecutive stages can be distinguished: (i) drainage of the continuous film between the sphere and the interface, (ii) transport of the sphere through the interface and (iii) the movement away from the interface. Depending on the Bond number, which may be viewed as the ratio between gravitational force acting on the sphere and the capillary force, different transport configurations are observed. In this chapter, the drainage configuration with a dominant capillary force is discussed. The case of a dominant gravitational force is described in the next chapter.

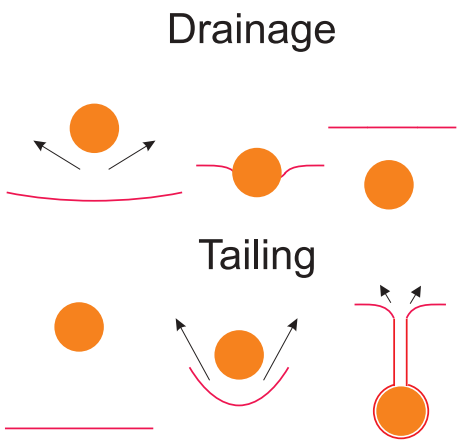

Figure 10.1. Stages of transport through the tailing and drainage configurations. The drainage configuration is characterized by a moderate interfacial deformation and a thinning film between the sphere and the interface that eventually ruptures. In the tailing configuration the sphere deforms the interface much more and the sphere leaves a long thinning tail behind in the phase it is transported to.

10.1. Introduction

The transport of rigid objects through fluid-fluid interfaces occurs at a wide range of length scales [178, 181, 184–186, 210]. The driving force is usually gravity, but can in principle be any external field. Examples include the capture of mineral particles in flotation processes [184] and the migration of magma slabs through the earths crust [186]. At high Reynolds numbers, the transport of objects through interfaces and the formation of bubbles and droplets caused by it have been studied to some extent [194, 195, 197, 210–212]. In the low Reynolds limit, the configurations that have been studied are quite limited [188, 190, 213]. The passage of a sphere through an interface can be considered to consist of three stages: (1) The film drainage between the sphere and the interface in the phase the sphere is originally in, (2) the passage of the sphere through the interface and (3) the further movement of the sphere in the phase the sphere is transported to. The Bond number $Bo = \Delta\rho g R^2/\gamma$, which may be seen as the ratio between the gravitational and capillary forces, mainly determines what transport configuration is observed. $\Delta\rho$ is the density difference between the sphere and the phase from which it approaches the interface, R is the radius of the sphere, g the gravitational constant and γ the interfacial tension between the two fluids. If the sphere density is either higher or lower than the density of both fluids, $Bo << 1$ and $Bo >> 1$ result in the *drainage* and the *tailing* configurations [196], as illustrated in figure 10.1. The drainage regime is characterized by a thinning film between the sphere and the interface, which eventually ruptures, quite similar to droplet coalescence [47, 170]. In the tailing regime, the gravitational force is dominant over the capillary force. As a result the

interface strongly deforms and the sphere leaves a column of material of the first phase behind. The first step of the process has mainly been considered as an approximation of the approach of a droplet to an interface [188,190,191,194], but it has also received some attention in the context of the transport of particles through an interface [195–197,213]. None of these studies consider the wettability of the particle. Flotation studies with spheres attached to a cantilever [214] do consider the wettability of the particles, as do studies of sphere tensiometry for the determination of the interfacial tension [215]. These studies however, are focussed on the capture of particles by interfaces and do not describe the full transport phenomenon.

Here, we consider a wettable sphere which moves through the interface of a demixed colloid polymer system. Due to the ultralow interfacial tension in these systems, the effect of capillary waves on the transport stages can be investigated as well, as was done previously for droplet coalescence [47] and the pinching of liquid threads [46]. In this chapter we study the drainage configuration in the low Bond number limit. The subsequent chapter is dedicated to the high Bond number limit. This chapter is built up as follows: in 10.2 we introduce the relevant hydrodynamics, in 10.3 we describe our experimental system and setup, in 10.4 we discuss the observed approach (10.4.1), transport (10.4.2), and moving away from the interface (10.4.3) stages. We end with a discussion in 10.5 and a conclusion in 10.6.

10.2. Theoretical Background

Consider two phases 1 and 2, characterized by viscosities η_1 and η_2 and densities ρ_1 and ρ_2. A sphere with density ρ_b and radius R in phase 2 sediments at a velocity u_s toward an interface between phases 1 and 2 with an interfacial tension γ. It is schematically shown in figure 10.2. As we will see, the sphere is wetted by a thin layer of phase 1 while it resides in phase 2. Therefore, we ignore the interfacial tension between the solid and the phases for the transport: all the capillary events occur through interactions between the film on the sphere and the interface.

We further define the density differences $\Delta\rho_{bn}$ as the density difference between the sphere and phase n, with n either 1 or 2 and $\Delta\rho_{12} = \rho_1 - \rho_2$. The b subscript refers to the rigid sphere. The sedimentation velocity u_s of a sphere in phase n is given by the well known Stokes equation:

$$u_s = \frac{2g\Delta\rho_{bn}R^2}{9\eta_n}, \tag{10.1}$$

With η_n the viscosity of phase n. The sedimentation velocity results from the equilibrated viscous and gravitational forces F_v and F_g:

$$F_v = 6\pi\eta_n R u_s, \tag{10.2}$$

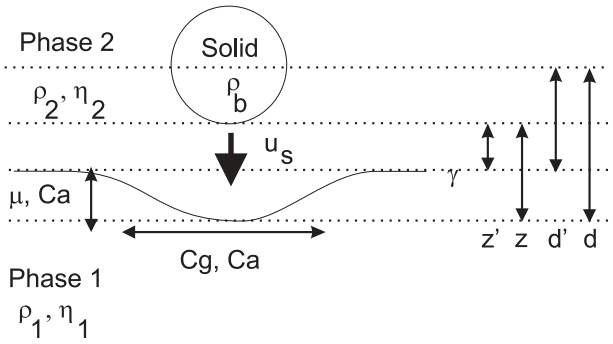

Figure 10.2. Relevant variables for the low Reynolds transport of a rigid sphere. A phase-separated system with an interface with interfacial tension γ. The phases 1 and 2 have densities ρ_1 and ρ_2 and viscosities η_1 and η_2. A sphere with density ρ_b in phase 2 with velocity u_s far from the interface approaches the interface. The width of the deformation depends on the dimensionless numbers Cg and Ca, the total deformation of the interface depends on μ and Ca. For different aspects of the process, different measures are needed for the sphere-interface distance. We define z and z' as the spacing between the sphere and the deformed and undeformed interface. Furthermore we define d and d' as respectively the distance between the sphere center and the deformed and undeformed interface.

and

$$F_g = \frac{4}{3}\pi R^3 \Delta\rho_{bn} g, \tag{10.3}$$

with g the gravitational acceleration.

As we saw in Chapter 9, for a rigid sphere approaching a free non-deformable surface exact treatments exist [200], which describe both the undistorted fall of equation (10.1) and the velocity close to the surface. Generally the velocity close to the interface may be written as

$$u_s(\alpha) = \frac{2g\Delta\rho_{bn}R^2}{9\lambda(\alpha)\eta_n}. \tag{10.4}$$

λ represents the friction increase close to the interface, and $\alpha = \cosh^{-1}(d/R)$ and d the distance of the sphere's center to the interface. The final stage of the problem – the sphere that moves away from the interface – is similar to the approach at first sight, but there are subtle differences. The solvent backflow at the interface now is in the direction of sphere motion. Furthermore, the interface may deform as the sphere moves away due to the pressure drop behind the sphere.

Following Geller et al. [196], two scenarios for transport are possible: the drainage and tailing configurations. These authors theoretically investigated the constant velocity and the constant force cases. In the limit of negligible inertial effects, the dimensional numbers that affect the configuration are the capillary number Ca, Cg and the viscosity

ratio μ:

$$Ca = \frac{u\eta_2}{\gamma}, \tag{10.5}$$

$$Cg = \frac{u\eta_2}{\Delta\rho_{12} g R^2} \tag{10.6}$$

and

$$\mu = \frac{\eta_1}{\eta_2}. \tag{10.7}$$

with u the velocity of the sphere. Ca and Cg represent the ratio of the viscous stress at the interface relative to the surface tension and buoyancy forces. Geller et al. [196] find that at high μ, interfacial deformation is reduced. High values of μ result in a "more rigid" interface and therefore less interfacial deformation perpendicular to the interface. Both depend on the capillary number as well, see figure 10.2. High values for Cg result in a relatively broad deformed area along the interface.

In our experiments, the constant gravitational force sets the velocity of the sphere far away from the interface and we work with the constant force scenarios. Since the dimensionless numbers Cg and Ca vary as the sphere slows down as it approaches the interface, we substitute $u = u_s(d = \infty)$ and we obtain the buoyancy ratio β and the Bond number Bo. β is given by:

$$\beta = \frac{\Delta\rho_{b2}}{\Delta\rho_{12}} \tag{10.8}$$

and should be larger than unity to prevent the particle from resting at the interface, such as in [188]. For the Bond number we obtain:

$$Bo = \frac{g\Delta\rho_{b2} R^2}{\gamma}, \tag{10.9}$$

which is the ratio of the gravitational force F_g and the capillary force F_c. For a sphere under a wetting angle θ the latter is given by:

$$F_c = 2\pi\gamma R\cos\theta. \tag{10.10}$$

When the capillary force is dominant, the interface only slightly deforms upon approach of the sphere due to solvent backflow. A film of phase 2 between the sphere and the interface thins until it ruptures. When the gravitational force is the dominant term, the interface deforms much more, and a thin film of phase 2 persists around the sphere in phase 1. The film again thins in time until it ruptures in the second phase. The sphere leaves a long column of phase 2 behind.

When $Bo < 1$, spheres will be transported via the drainage modus. We see that the cross-over length L_{Bo} is equal to

$$L_{Bo} = \sqrt{\frac{\gamma}{g|\Delta\rho_{b2}|}}. \tag{10.11}$$

Table 10.1. typical quantities for colloid-polymer and molecular systems

Quantity	unit	Colloidal	Molecular
η	Pa s	10^{-2}	10^{-3}
R	m	10^{-5}	10^{-3}
ρ	kg/m^3	10^3	10^3
$\Delta\rho_{b1}$	kg/m^3	10^2	10^2
γ	N/m	10^{-7}	10^{-3}
η^2/ρ	N	10^{-7}	10^{-9}
γR	N	10^{-12}	10^{-6}
$\Delta\rho g R^3$	N	10^{-12}	10^{-6}

It is remarkably similar to the capillary length $\xi = \sqrt{\frac{\gamma}{g\Delta\rho_{12}}}$, which for example determines the profile of the interface at the wall [205, 207]. The two are related through β (10.8):

$$\beta = \left(\frac{\xi}{L_{Bo}}\right)^2. \tag{10.12}$$

From the well-known Reynolds number we can estimate how important the inertial terms are for these processes compared to viscous dissipation:

$$Re = \frac{\rho u L}{\eta}, \tag{10.13}$$

with ρ the mass density, u the velocity of the sphere, η the viscosity and L the characteristic length. It may be seen as the ratio between the inertia and viscous dissipation. Setting the viscous force as a function of Re by substituting for uR and setting $L = R$ results in a force of $\sim Re\eta^2/\rho$. Therefore, a force of η^2/ρ is required to enter the high Re regime.

To estimate the magnitude of the forces involved, we insert typical values for molecular systems (table 10.1). Consider a sphere with a radius $R \equiv R \sim 10^{-3}$ m, with a density difference with the surrounding fluid $\Delta\rho_{b2} \sim 10^2$ kg/m^3, moving towards an interface with interfacial tension γ. The fluid has a density $\rho \sim 10^3$ kg/m ^{3} and a viscosity $\eta \sim 10^{-3}$ Pa s. Consequently, $\eta^2/\rho \approx 10^{-9}$N. Both the viscous and gravitational forces are of order 10^{-6}N. Compared to η^2/ρ this is much too large to end up in the low Reynolds regime. The capillary force is particularly tough to bring to the low Reynolds regime, since it only depends on R, compared to R^3 for the gravitational force. The important dimensionless numbers are shown in table 10.2 for several studies dedicated to this subject.

We reach the low Reynolds regime for interfacial forces by resorting to colloid-polymer mixtures, and working at small lengthscales. Owing to a depletion-induced attraction [35, 37], these mixtures exhibit a "gas" (colloid poor/polymer rich)-"liquid"(colloid

Table 10.2. The transport of spheres through interfaces in previous studies

Reference	Bo	β	μ	Re
Hartland [188]	0.75	0.60	4.8	3.62
Hartland [188]	0.47	0.40	46	3.62
Hartland [190]	0.47	0.60	0.022	0.003
Hartland [190]	0.15	0.40	0.21	0.045
Maru [195]	3.83	1.03-12	0.43	15
Shah [194]	2.55	7.6	0.44	801
Pitois [197]	1-10	53-235	10^{-5}-10^{-3}	$\sim$100
Manga [213]	1.4	4.3	40	< 0.1
this thesis Chapter 10	0.1-1	2.1	3.9	10^{-6}
this thesis Chapter 10	0.1-1	4.4	6.7	10^{-6}
this thesis Chapter 11	1-10	1.8	2.4	10^{-6}
this thesis Chapter 11	1-10	11	5	10^{-6}

rich/polymer poor) phase separation when the polymer/colloid diameter ratio q is sufficiently large ($q = \sigma_p/\sigma_c \geq 0.30$ [39]). Since colloidal particles have sizes of typically 1-1000 nm, these systems have much lower interfacial tensions –as experimentally verified [42, 44, 45, 204, 205]– than molecular systems with a magnitude proportional to [40, 41]:

$$\gamma \propto \frac{k_B T}{d^2}, \tag{10.14}$$

with $k_B T$ the thermal energy and d the typical length scale at the interface. The latter is similar to the colloidal particle diameter σ_c far away from the critical point. If we insert typical values for colloid-polymer mixtures: $\rho \sim 10^3 kg/m^3$, $\Delta\rho \sim 10^2 kg/m^3$, $R \sim 10^{-5} m$, $\eta \sim 10^{-2} Pas$ and $\gamma \approx 10^{-7} N/m$, we find that the capillary and gravitational forces now clearly are much lower than η^2/ρ and we are clearly in the low Reynolds regime. At the same time, the Peclet number $Pe = \Delta\rho g R^4/k_B T$ is much larger than unity, indicating that diffusion of the sphere is not important. As we saw in Chapter 8, the roughness of the interface is given by $\langle h^2 \rangle^{\frac{1}{2}} \approx \frac{k_B T}{\gamma}$, which will likely be important for the connection step.

10.3. Experimental section

10.3.1. Experimental Systems

The transport of rigid spheres was studied in two experimental systems. Both dispersions consist of fluorescently labelled poly-methyl-methacrylate particles, suspended

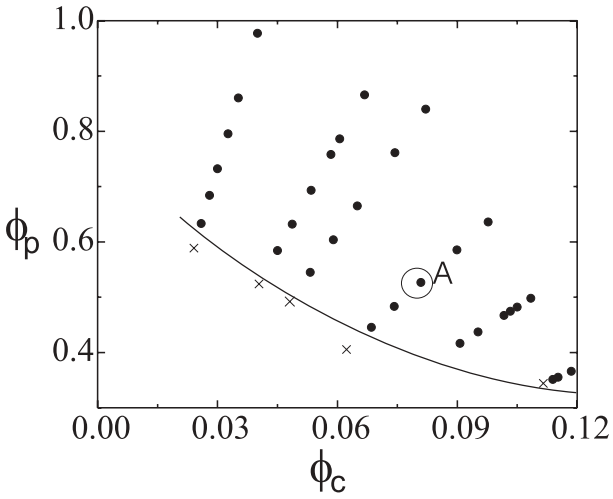

Figure 10.3. Phase diagram as constructed by dilution lines for system PN25PS14. Filled circles indicate statepoints that phase separate, crosses indicate statepoints that do not. The binodal is a guide to the eye. Measurements were performed on statepoint A. The phase diagram of PC69PS42 was shown in Chapter 8

in cis-trans decalin, with polystyrene added as a depletant. The first system was fluorescently labelled with 4-methylaminoethyl methacrylate- 7-nitrobenzo-2-oxa-1,3-diazol (NBD), the second system with (7- (diethylamino)coumarin-3-carboxylic acid N-succinimidyl ester)-aminostyrene (CAS). For the first and second system the respective radii of the particles were 25 nm and 69 nm, as determined by dynamic light scattering, with a particle polydispersity of approximately 10% as supported from scanning electron microscopy. The radii of gyration of the polymers for the first and second systen were estimated to be 14 nm and 42 nm [176]. We will refer to the first system as PN25PS14 and to the second system as PC69PS42. Phase diagrams were constructed by repetitive dilution of several phase separating samples. The phase diagram for system PN25PS14 is shown in figure 10.3. The shown binodal is a guide to the eye. Here we study statepoint A. The phase diagram for PC69PS42 was shown in Chapter 8. The statepoint studied here is statepoint B.

10.3.2. Experimental Setup

Sample PN25PS14 was studied with a Nikon Eclipse E400 microscope mounted with a Nikon C1 scanhead, with the focal plane parallel to the direction of gravity. The capturing rate was approximately one frame (512x512 pixels) per second. The microscope was furthermore equipped with a 488 nm ArKr laser and Nikon 20X ELWD Plan Fluor (NA 0.45) and Nikon 60X CFI Plan Apochromat (NA 1.4) lens.

Sample PC69PS42 was studied with an Axiovert 200M Zeiss microscope mounted with a LSM5 Exciter scanhead, again with the focal plane parallel to the direction of

gravity. The microscope was furthermore equipped with a Ar laser with both a 458 nm and a 488 nm line and a Zeiss 60x CFI Plan Apochromat (NA 1.4) lens. The capturing rate was approximately five frames (512x512 pixels) per second. In both cases the sample container is a small glass vial, part of which is removed and replaced by a thin (0.17 mm) glass wall.

Very large, very polydisperse PMMA-NBD spheres (σ_c = 100 nm - 100 μm, ρ_b=1.17 g/ml) were obtained from a synthesis following [14], and subsequently size-fractionated twice in hexane Chapter 5. The resulting 5-40 micron spheres were transferred to cis/trans decalin and diluted to a concentration of 1 wt%. A small amount of these spheres was carefully added to the top of the colloidal gas phase, 16 hours after phase separation had completed (less than 10μl or 1.0 % v/v of the total sample volume). The material was either added with a pipette or injected through a thin plastic tube. The spheres subsequently sedimented towards the gas-liquid interface and moved through it.

10.3.3. Characterisation of the experimental systems

A powerful aspect of this study is that all relevant system variables may be determined by microscopy, assuming the rheology is Newtonian. To this end we determine the bulk sedimentation velocities of the spheres and the capillary wave height-height positional and time correlation functions $g(t)$ and $g(s)$ (Chapter 8). Instead of $g(s)$ we may alternatively use the interfacial profile at the wall [205, 207]. These provide enough information to determine the interfacial tension γ as well as the densities ρ_l and ρ_g and viscosities η_l and η_g (The subscripts l and g denote the colloidal gas and colloidal liquid phases). The sedimentation velocities give $(\rho_b\text{-}\rho_l)/\eta_l = a$ and $(\rho_b\text{-}\rho_g)/\eta_g = b$. The interfacial tension γ follows directly from both correlation functions. The capillary length from $g(s)$ or the interfacial profile at the wall may be used to extract $\rho_l\text{-}\rho_g = c$ and from the capillary time we obtain $\eta_l{+}\eta_g = d$. Together this results in:

$$\rho_g = \rho_b - b\frac{ad+c}{a+b}; \quad \rho_l = \rho_b - a\frac{bd-c}{a+b}; \quad \eta_g = \frac{ad+c}{a+b}; \quad \eta_l = \frac{bd-c}{a+b} \tag{10.15}$$

In Fig. 10.4A and B, the quantities u_s/σ in the gas (A) and liquid (B) phases are shown as a function of the sphere diameter σ. The curves are fairly linear, and the fluids behave Newtonian at the shear rates applied by the spheres which are of order $u_s(d = \infty)/\sigma$. The positional and time correlation functions for capillary waves $g(s)$ and $g(t)$ are shown in Fig. 10.4C and D. For comparison, viscosities and densities of statepoint A of PN25PS14 and a statepoint similar to statepoint B of PC69PS42 were determined with a DMA 5000a density meter and an Anton Paar Physica MCR300 rheometer. These methods require quite much sample volume and are destructive, but provide a check on the quality of the data obtained from microscopy. These measurements gave highly similar results for PN25PS14, see table 10.3. For PC69PS42 the properties

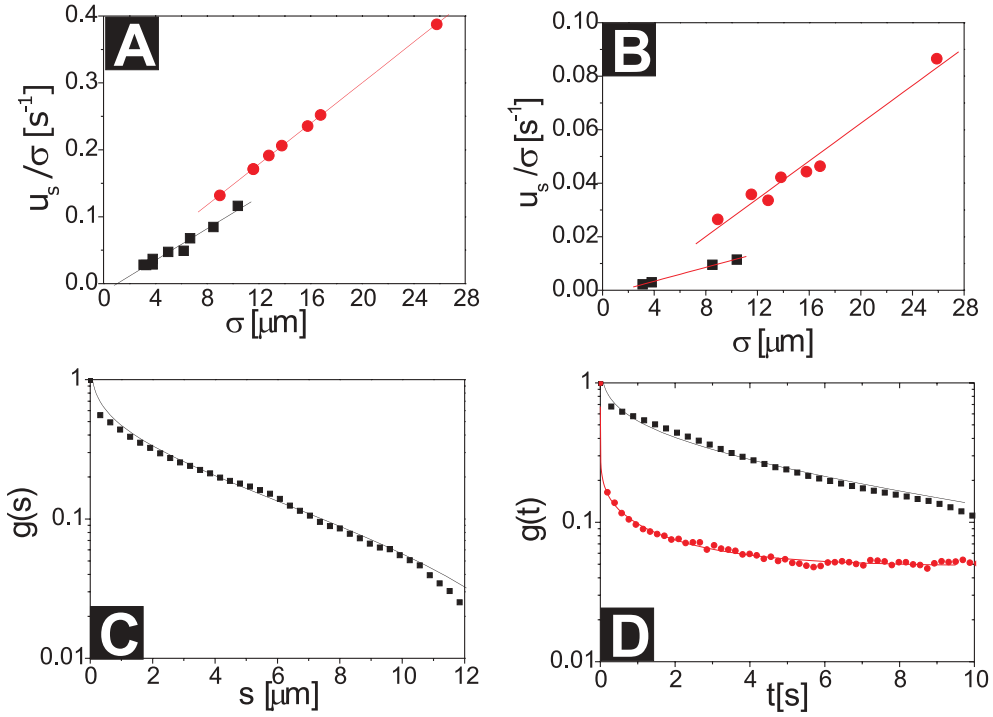

Figure 10.4. Determination of physical properties from microscopy. Squares represent the measured data for PN25PS14, circles those for PC69PS42. The lines are fitted curves. (A) Determination of $\Delta\rho_{b2}/\eta_2$ from sedimentation in the colloidal gas. (B) Determination of $\Delta\rho_{b1}/\eta_1$ from sedimentation in the colloidal liquid. (C) Determination of γ and $\Delta\rho_{12}$ from the static correlation function $g(s)$. For PN25PS14 we determined the capillary length from the profile at the wall (not shown). (D) Determination of γ and $\eta_1 + \eta_2$ from the dynamic correlation function $g(t)$.

are somewhat different, but show the correct tendency since the statepoint studied by microscopy is slightly closer to the critical point than the sample studied by the more conventional methods. Clearly we may compare the results in the systems for μ and for variation of Bo. The values for β are (unfortunately) too similar for comparison.

10.4. Results

Characteristic images of all stages are shown for both samples for spheres of respectively of $6.4\mu m$, $10.4\mu m$ diameter (both in sample PC69PS42, Fig. 10.5A and B) and for a sphere of $15.5\mu m$ radius (in sample PN25PS14, Fig. 10.5C). The respective Bond numbers are 0.18, 0.51 and 1.03. From Fig. 10.5A and B it is clear that a wetting layer of the fluid phase is present around the sphere. The layer is acquired when the sphere passes through the air-colloidal-gas interface, which is wetted by the colloidal liquid phase. Since the sample wall is wetted by the colloidal liquid due to the depletion interaction [216], it is not surprising that this layer is stable for the curved particle

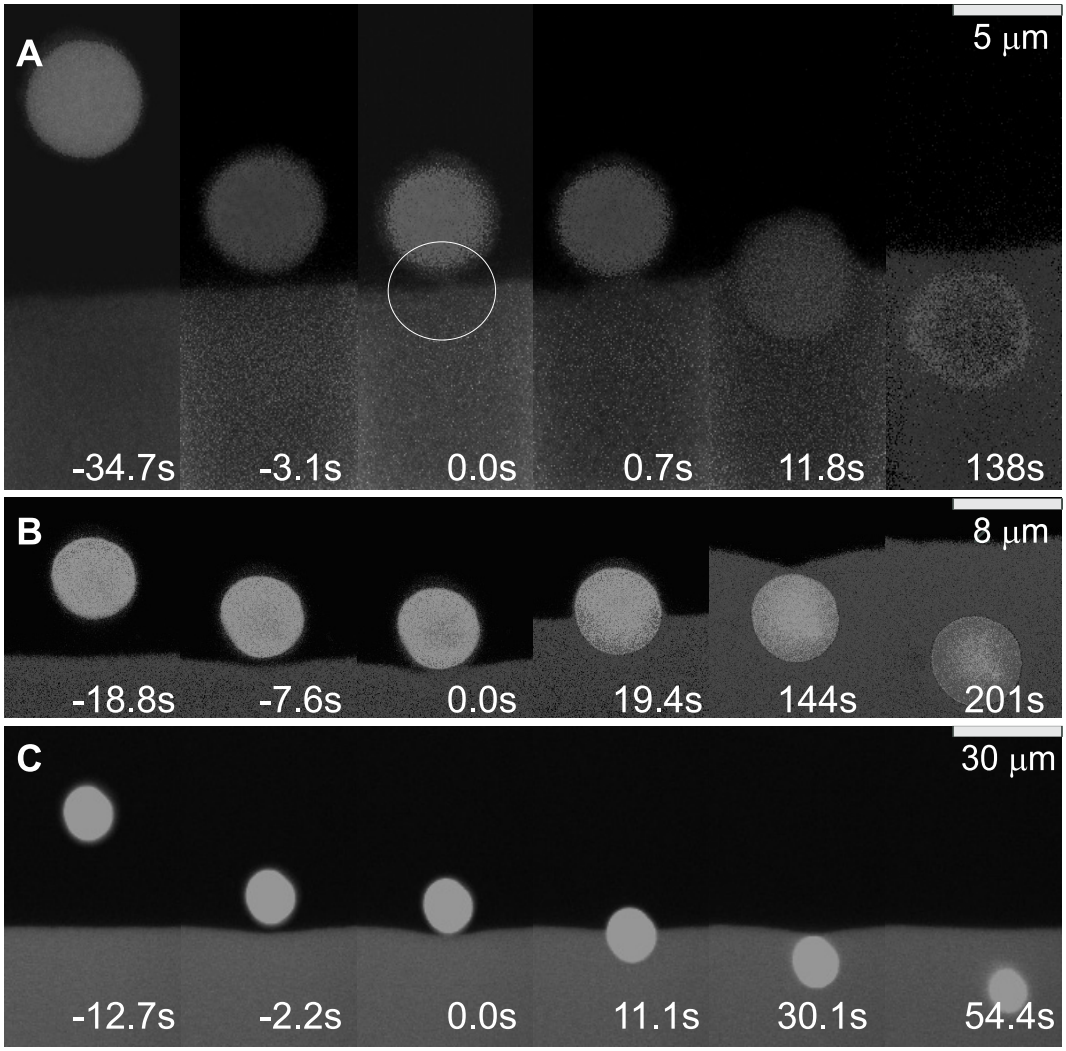

Figure 10.5. Stages of transport through the drainage mode in systems PC69PS42 (Panels (A) and (B)) and PN25PS14 (Panel (C)). (A) Transport of a 6.4 μm diameter sphere (Bo = 0.14). We can clearly distinguish the approach stage, the formation of a connection through capillary waves, the transport of the sphere through the interface through the growth of the neck, the detachment of the sphere from the interface and the acceleration of the sphere toward its bulk velocity. (B) Same as in (A), but now for a 10.4 μm diameter sphere (Bo = 0.54). Here, the interface clearly deforms during the approach and before the sphere is detached from the interface. The interface recovers after detachment. (C) A similar series, now for a 14.5 μm diameter sphere (Bo = 1.0) in system PN25PS14. The events are similar to those in (B) but the resolution in time is less and the effects in the wetting layer are less obvious because the dyes of the sphere and the colloids are identical.

Table 10.3. Physical properties of the systems studied

Method		microscopy	density & rheometer measurements	microscopy	density & rheometer measurements
Quantity	unit	PN25PS14	PN25PS14	PC69PS42	PC69PS42
ρ_l	kg/m^3	943	942	964	989
ρ_g	kg/m^3	893	889	892	887
η_l	$mPa\ s$	35	31	87	105
η_g	$mPa\ s$	9.9	8	13	6
$R_{Bo=1}$	μm	7	7	8	8
γ	nN/m	160	-	140	-
$\langle h^2 \rangle^{\frac{1}{2}}$	μm	0.065	-	0.118	-
β	-	5.2	5.2	3.8	2.7
μ	-	3.3	3.8	6.7	12.5

surface as well. At distances larger than approximately a particle diameter from the interface the sphere moves at constant velocity. Closer to the interface the sphere slows down, until the capillary waves of the interface and those on the sphere connect. This connection grows while the sphere is dragged through the interface by the wetting force. When the sphere is fully immersed in the liquid phase, the sphere detaches from the interface and the sphere speeds up towards its bulk sedimentation velocity. For sufficiently large spheres, the interface deforms during the approach. Furthermore, prior to the detachment, the sphere deforms the interface again before moving away from it. The interface regains its flat shape shortly after the sphere has disconnected from the interface. We split up the three main stages in 10 events for the drainage configuration. The approach stage may be split up in 1(A) bulk sedimentation in the gas phase, 1(B) the slowing down of the sphere and 1(C) the deformation of the interface, the latter two both due to solvent backflow. The transport stage may be divided in 2(A) the creation of a connection between the interface and the wetting layer on the sphere and 2(B) the passage of the sphere through the interface. The moving away stage is made up of 3(A) the interface deformation by the sphere after transport and 3(B) the detachment of the sphere from the interface, 3(C) the acceleration of the sphere towards its bulk velocity in the fluid, 3(D) the recovery of the interface towards its initial flat shape and 3(E) the bulk sedimentation in the liquid phase. They are sketched in figure 10.6. In the upcoming subsections we subsequently discuss all events for the approach, the transport and the moving away stages. For some processes it is more useful to consider the spacing between the deformed interface and the sphere z, for others it is more useful to consider the distance between the sphere centre and the deformed interface

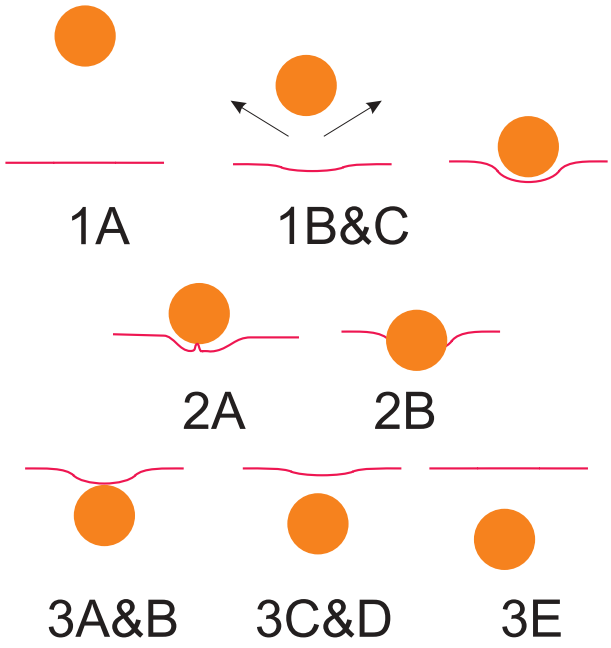

Figure 10.6. Transport events in the drainage modus. For the approach these are 1(A) sedimentation in the upper fluid, 1(B) the slowing down of the sphere close to the interface and 1(C) the deformation of the interface due to solvent backflow. For the transport process we distinguish 2(A) the creation of a connection between the interface and the wetting layer on the sphere and 2(B) the passage of the sphere through the interface. The moving away from the interface may be subdivided into 3(A) the interface deformation by the sphere after transport and 3(B) the detachment of the sphere from the interface, followed by 3(C) the acceleration of the sphere toward its bulk velocity in the fluid, 3(D) the recovery of the interface towards its initial flat shape and 3(E) the sedimentation of the sphere in the bulk phase.

d. Sometimes the undeformed interface is a more insightful reference point than the deformed interface: z' is the spacing between the sphere and the undeformed interface and d' is the distance between the sphere centre and the undeformed interface. These lengthscales are schematically shown in figure 10.2. We arbitrarily assign positive and negative distances to locations in the polymer rich and colloid rich phase. A velocity profile of the transport process shown in Fig. 10.5C is shown in figure 10.4. The velocity is shown as a function of d', made dimensionless with the sphere diameter. The sharp increase in velocity is clear, as well as the slowing down of the sphere in the gas phase and the increase in velocity after transport in the liquid phase. We observe the same phenomenology for the spheres in PC69PS42 in Fig. 10.5A and B.

10.4.1. Approach of the sphere

The approach of the sphere toward the interface was already discussed in detail in Chapter 9 for system PN25PS14 . Here, we present the results for system PC69PS42.

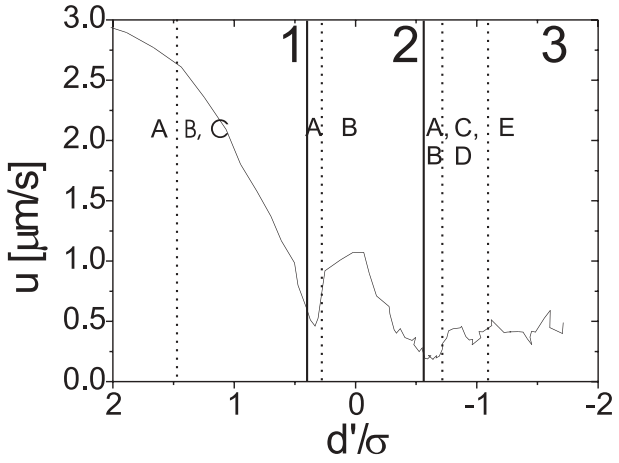

Figure 10.7. Velocity profiles during transport for the $15.5\mu m$(Bo=1.0, black curve) diameter sphere shown in Fig. 10.5C. The solid lines separate the (1) approach, (2) transport and (3) moving away stages. The dotted lines indicate transitions between the events described in figure 10.6. The numbers and letters refer to the events as assigned before.

All spheres initially sediment at constant velocity. They start to slow down due to solvent backflow at a separation between sphere and interface of about their own diameter. For larger spheres, the interface deforms. The velocity continues to decrease strongly and the surface distortion becomes more pronounced. The critical sphere radius for which $Bo = 1$ is $\sim 8\ \mu m$, but we observe that even slightly larger spheres are transported through a drainage configuration, which is both caused by the high value of μ and the slowing down of the sphere which results in a value of Ca lower than Bo. The approach and interface deformation curves for spheres with diameters $10.4\mu m$ (Bo=0.51) and $3.1\mu m$ (Bo=0.05) are shown in Fig. 10.8A and B. The height z' and the interfacial deformation δ are scaled with the particle diameter. The approach of the larger sphere is a rather smooth curve, similar to that present in Chapter 9. For the smaller particle in Fig. 10.8B, fluctuations in height appear. Here. , $Pe \approx 4$ and diffusion starts to compete with sedimentation, causing the fluctuations. The larger particle deforms the interface more than the smaller particle, also on a relative scale, as can be seen in Fig. 10.8A and B. In Fig. 10.8C we show the mastercurves for the approach with scaled heights (z/σ) and times$(tu_s(d = \infty)/\sigma)$. We set $t = 0$ as the time at which $d/\sigma = 1$. Note that the spheres studied in sample PC69PS42 are smaller than those in PN25PS14, and may be followed up to smaller values of z/σ due to the finite image resolution. While we did not see any large deviations from the theoretical curve (10.4) in Chapter 9, for smaller distances this is apparently not valid anymore, both for a deforming and a non-deforming interface. Note that we use diameters obtained from the sedimentation velocity far from the interface in the gas or liquid phase (equation (10.1)). These diameters agree well with the directly measured ones, but are

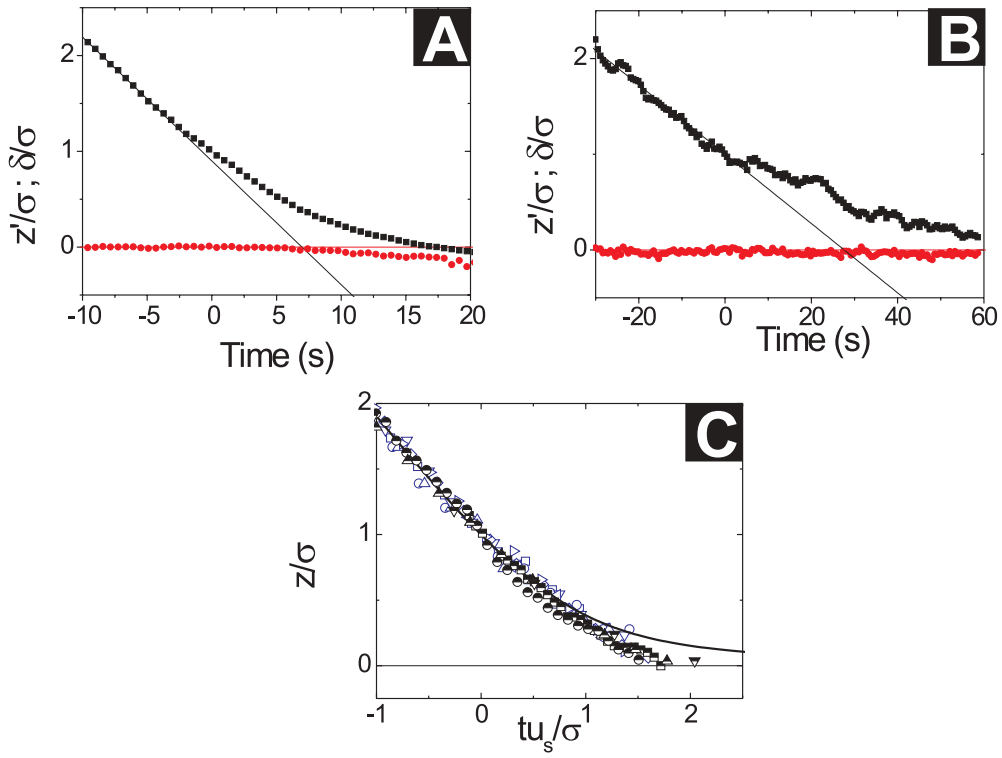

Figure 10.8. Approach of spheres toward a deformable interface and interface deformation in system PC69PS42. We scale height (z'/σ) and interfacial deformation (δ/σ). (A) Approach of a sphere with a diameter of 10.4μm (Bo = 0.51). Here the deformation of the interface is quite pronounced. (A) Approach of a sphere with a diameter of 3.1μm (Bo=0.05). Fluctuations show up in the curve due to Brownian motion of the sphere during sedimentation. The interface hardly deforms for this sphere during the approach. (C) Dimensionless mastercurves (z/σ, $tu_s(d=\infty)/\sigma$) for the approach of spheres toward the interface for PC69PS42 (semifilled symbols) and PN25PS14 (open symbols). We set $t = 0$ as the time at which $z/\sigma = 1$. The solid line is equation (10.4).

sometimes slightly off due to deviations from a perfectly spherical shape for some of the spheres.

10.4.2. Transport of the sphere

As we argued before, the transport stage of a sphere in the draining film configuration is characterized by two events: the creation of a connection between the interface and the wetting film on the sphere and the passage of the sphere through the interface. In figure 10.9 we show the events for a 4.4μm diameter sphere (Bo=0.09) in PC69PS42. The time that the connection is made is set as $t = 0$. The formation of a connection between the wetting film on the sphere and the interface is clearly mediated by capillary waves. The time for two fluctuations to cover a wetting film-interface separation Δ

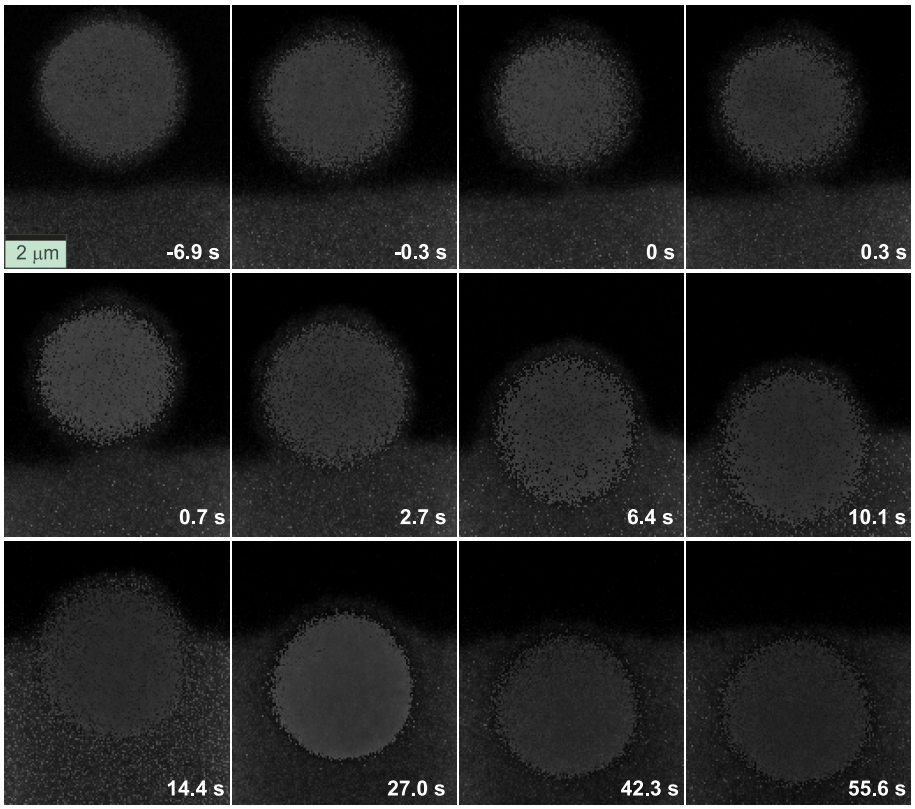

Figure 10.9. Transport of a 4.4μm diameter (Bo=0.09) sphere through the interface in PC69PS42. At $t = 0$ a connection is made between the interface of the system and the wetting film on the sphere. It is intriguing to see that the first half of the immersion of the sphere (10 s) takes place much faster than the second half (45 s). This is presumably caused by the high viscosity contrast between the phases.

should depend on the mean square interfacial roughness $\langle h^2 \rangle$. Indeed, the separation between the film and the interface at which the connection is made is approximately 200 nm, which is roughly $2\sqrt{\langle h^2 \rangle}$. The extent of interfacial deformation at the moment that the connection is made will affect the location of the connection x_c relative to the sphere center x_s. In general, the larger the deformation, the further away from the centre of the interface deformation the connection will occur and the larger the circumference length $2\pi|x_s - x_c|$ along which this minimum separation occurs [188]. The prediction of such times therefore is a tedious business, see also Chapter 8. After the connection is made, the sphere is gradually immersed in the fluid. The effective viscosity felt by the sphere clearly rises: immersion up to half the sphere's diameter takes approximately 10 s, whereas full immersion takes an additional 45 s, presumably because of the high viscosity contrast μ in this system. Indeed the contrast in breakthrough time is hardly present in PN25PS14: half immersion occurs after 9 s, full immersion after an additional 13 s. The transport velocities are shown for several sphere sizes in

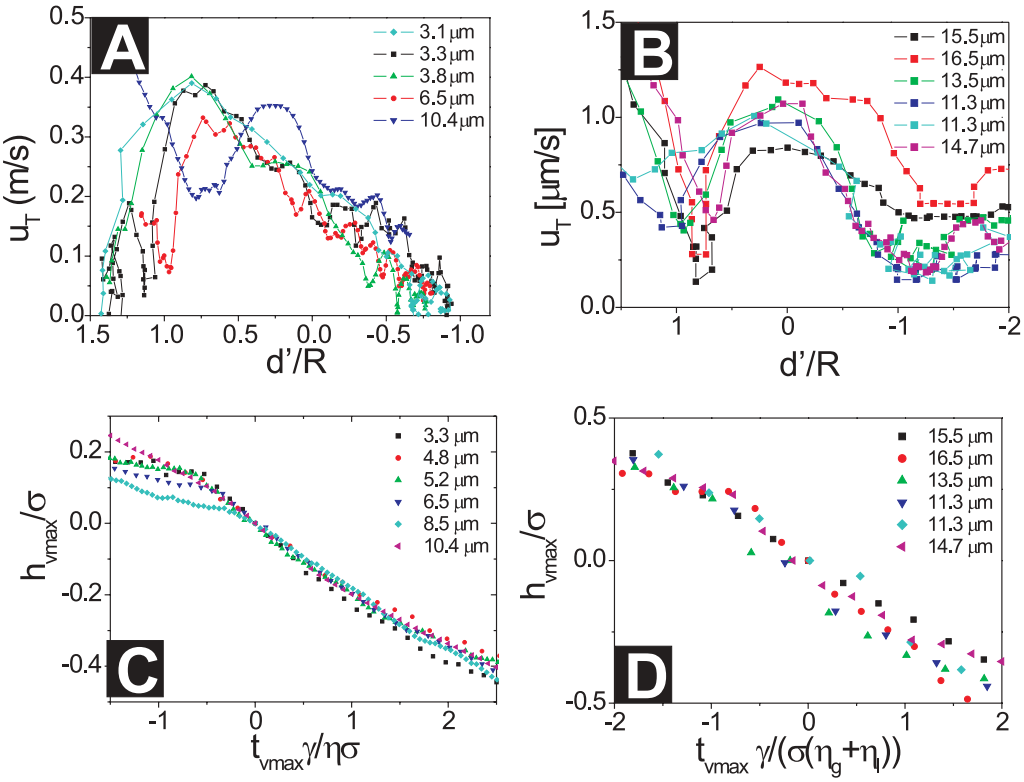

Figure 10.10. Transport through wetting. Panels (A) and (B) show the velocity profiles in respectively systems PC69PS42 and PN25PS14 of spheres as a function of d'/R. Panels (C) and (D) show the corresponding dimensionless time versus height curves, made dimensionless for the height with $d_{v_{max}}/\sigma$ and for time with $t_{v_{max}}\gamma/((\eta_1+\eta_2)\sigma)$. $t_{v_{max}}=0$ is the time of maximum observed transport velocity.

Fig. 10.10A (PC69PS42) and Fig. 10.10B (PN25PS14). We scale d' with the sphere radius R. Fig. 10.10A contains more detail in time. We see that the increase in velocity starts at d'/R slightly larger than 1 for the smaller spheres. This is roughly the distance over which the connection with the film on the sphere is made. For larger spheres the interface deforms and the velocity starts to increase only at smaller values of d'/R. For these spheres the minimum velocity before the wetting step is higher than for spheres that do not deform the interface. The maximum occurs well in the polymer rich phase for PC69PS42 and approximately at the interface for PN25PS14. The most striking feature is perhaps that the velocity does not depend on the sphere size. A sphere which is dragged at a velocity u_T through a medium with viscosity η is resisted by a viscous drag force $F_v = 6\pi\eta R u$. The wetting force F_w on a sphere is $F_w = 2\pi\gamma R\cos\theta$, with θ the wetting angle. In the quasi-static limit of the Navier-Stokes equation we may equate both forces as sketched in figure 10.11. Since the sphere is covered with a thin wetting layer of the fluid we further assume complete wetting. Together this results in

an instantaneous transport velocity $u_T(d'/R)$:

$$u_T(d'/R) = \frac{1}{3}\frac{\gamma}{\eta_{eff}(d'/R)}\sqrt{1-\frac{d'^2}{R^2}} \tag{10.16}$$

with u_T the transport velocity. η_{eff} is the effective viscosity, which is clearly a complex function of d'/R. It additionally depends on the interfacial deformation and therefore on Bo, β and λ. Since the connection is made between the interface and the wetting film we may insert the interfacial tension γ between the two phases. If we simply insert u_c for γ/η_{eff}, a maximum transport velocity of $\sim u_c/3$ should be observed. This agrees well with our observations. For PC69PS42 we find a maximum u_T of $0.41\mu m/s$ and $u_c/3 = 0.47\mu m/s$ (Fig. 10.10A). For PN25PS14 the lower resolution in time results in less accurate velocities, but we nonetheless find a maximum u_T of $0.9 - 1.1\mu m/s$ compared to $u_c/3 = 1.2\mu m/s$ (Fig. 10.10B). The asymmetry of the experimental velocity profile in Fig. 10.10A and the symmetrical velocity profile for the simple model make the agreement of the maximum velocity even more remarkable. For larger spheres the maximum velocities tend to be slightly lower. Without including a description for the effective viscosity as a function of distance to the interface, we cannot make any predictions on the full shape of the curves. with u_T the transport velocity. η_{eff} is the effective viscosity, which is clearly a complex function of d'/R. It additionally depends on the interfacial deformation and therefore on Bo, β and λ. Since the connection is made between the interface and the wetting film we may insert the interfacial tension γ between the two phases. If we simply insert u_c for γ/η_{eff}, a maximum transport velocity of $\sim u_c/3$ should be observed. This agrees well with our observations. For PC69PS42 we find a maximum u_T of $0.41\mu m/s$ and $u_c/3 = 0.47\mu m/s$ (Fig. 10.10A). For PN25PS14 the lower resolution in time results in less accurate velocities, but we nonetheless find a maximum u_T of $0.9 - 1.1\mu m/s$ compared to $u_c/3 = 1.2\mu m/s$ (Fig. 10.10B). The asymmetry of the experimental velocity profile in Fig. 10.10A and the symmetrical velocity profile for the simple model make the agreement of the maximum velocity even more remarkable. For larger spheres the maximum velocities tend to be slightly lower. Without including a description for the effective viscosity as a function of distance to the interface, we cannot make any predictions on the full shape of the curves. By defining $t_{u_{max}} = 0$ and height $d_{v_{max}} = 0$ as the time and height at which u_{max} occurs and scaling ($d_{u_{max}}/\sigma$) and time ($t_{u_{max}}u_c/\sigma$) we obtain the mastercurves for PC69PS42 (Fig. 10.10C) and for PN25PS14 (Fig. 10.10D). The mastercurves are clearly only valid for variation of the Bond number (for $Bo < 1$), but not μ and β. As a result the mastercurves for the two systems are not identical.

10.4.3. Moving away from the interface

In the moving away stage the sphere eventually speeds up to its bulk velocity in the second phase. Here, our data of the PN25PS14 are more abundant, since sedimentation

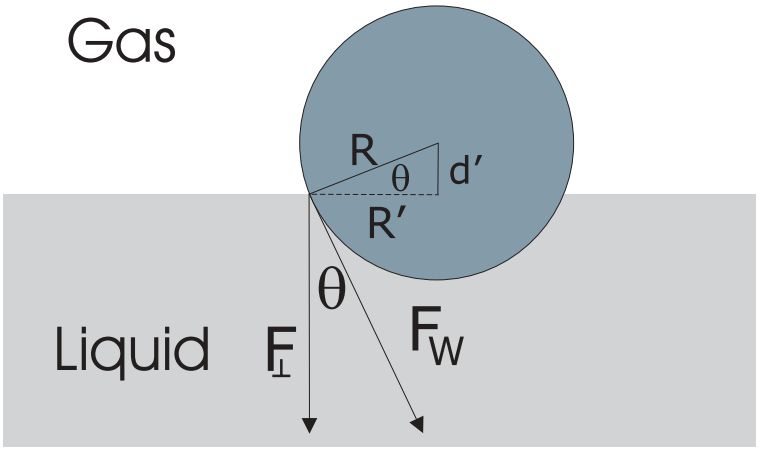

Figure 10.11. Transport of the sphere through growth of the connection made by capillary waves. The sphere is dragged down by the component of the wetting force F_w that is perpendicular to the interface $F_\perp$. The instantaneous wetting angle θ therefore determines the transport velocity. If we assume F_w to be parallel to the curvature of the sphere at the interface height (complete wetting) , we may write $\cos\theta = R'/R = \sqrt{1-(d'/R)^2}$.

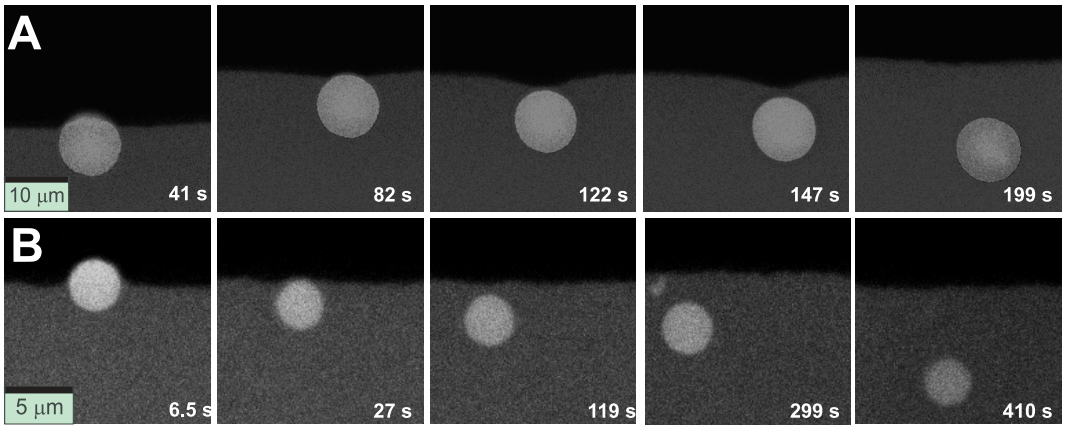

Figure 10.12. Two image series of spheres that move away from the interface in PC69PS42. (A) a sphere with a diameter of $10.4\mu m$ (Bo=0.51). The sphere drags the interface downward due to the pressure drop behind the sphere created by the flow profile (B) A sphere with a diameter of $4.4\mu m$ (Bo=0.05). The velocity of the sphere is significantly lower than for the sphere shown in (A) and the interface is not deformed by the pressure drop.

of the sphere in PC69PS42 is very slow in the second phase (of order of $10^{-2}-10^{-1}\mu m/s$ for the spheres studied), leading to long measurement times for a large spectrum of heights.

During this last stage of transport the interface may deform along while the sphere starts moving away from the interface in the second phase. In Fig. 10.12A a relatively large sphere clearly deforms the interface. In Fig. 10.12B a much smaller sphere moves

away from the interface and does not deform the interface. Gravity is the dominant driving force for the downward movement of the sphere again. As a consequence of flow, a pressure gap is created behind the sphere. As long as the capillary pressure of the deformed interface does not exceed the pressure gap behind the sphere, the interface moves along with the sphere. As gravity not only pulls the sphere but also the interface, the initial movement of the sphere is slower. Once the pressure gap behind the sphere is insufficient to deform the interface further, the sphere detaches from the deformed interface and accelerates toward its bulk sedimentation velocity in the second phase. Meanwhile, the deformed interface recovers its flat shape again. The interface deformations and sphere positions relative to the deformed and undeformed interface are shown for both spheres in Fig. 10.13A and B. The deformation for the $10.4\mu m$ sphere is obvious, that of the $4.4\mu m$ sphere is not noticeable. Scaling (z/σ and $tu_s(d = -\infty)/\sigma$) results in mastercurves for separations between the sphere and the interface larger than $z = 0$ as shown in Fig. 10.13C. It is interesting to note that when zooming in on smaller z (Fig. 10.13D), the curves are steeper for larger spheres. The largest sphere does not follow this tendency however: it passes the interface relatively slow, although it is wettable like the other spheres. The film between the sphere and the interface is too thick for transport through wetting to occur, however. For this sphere $Bo = 2.7$ and a tailing configuration is observed. This will be the focus of the final chapter of this thesis. The friction factor λ for the 10.4 μm diameter sphere in PC69PS42 as it moves away from the interface is shown in Fig. 10.14. It clearly evolves very differently than the theoretical curve (9.6). The experimental curve has a much higher friction factor at short distances. A possible explanation is again the pressure drop behind the sedimenting sphere, that causes a net attraction between the sphere and the interface.

10.5. Discussion

The particles which are transported through the interface are clearly completely wettable. The origin of the layer either originates from the thin wetting layer present at the air interface at the top of the sample, or from the condensation of colloidal liquid on the sphere surface due to the depletion interaction.

A straightforward question is what would happen if the spheres were non-wettable or only partially wettable by the phase they are transported to. The first part of the question is easily answerable. The Bond number would again set the scale. For $Bo > 1$, gravity would still overcome interfacial tension and the transport would again proceed through a tailing modus. For $Bo < 1$, interfacial tension is dominant, and the sphere would rest at the interface.

One may wonder at what point the Brownian forces will balance the capillary forces. Clearly, the Brownian forces are of order of k_BT/σ and the capillary forces are of order

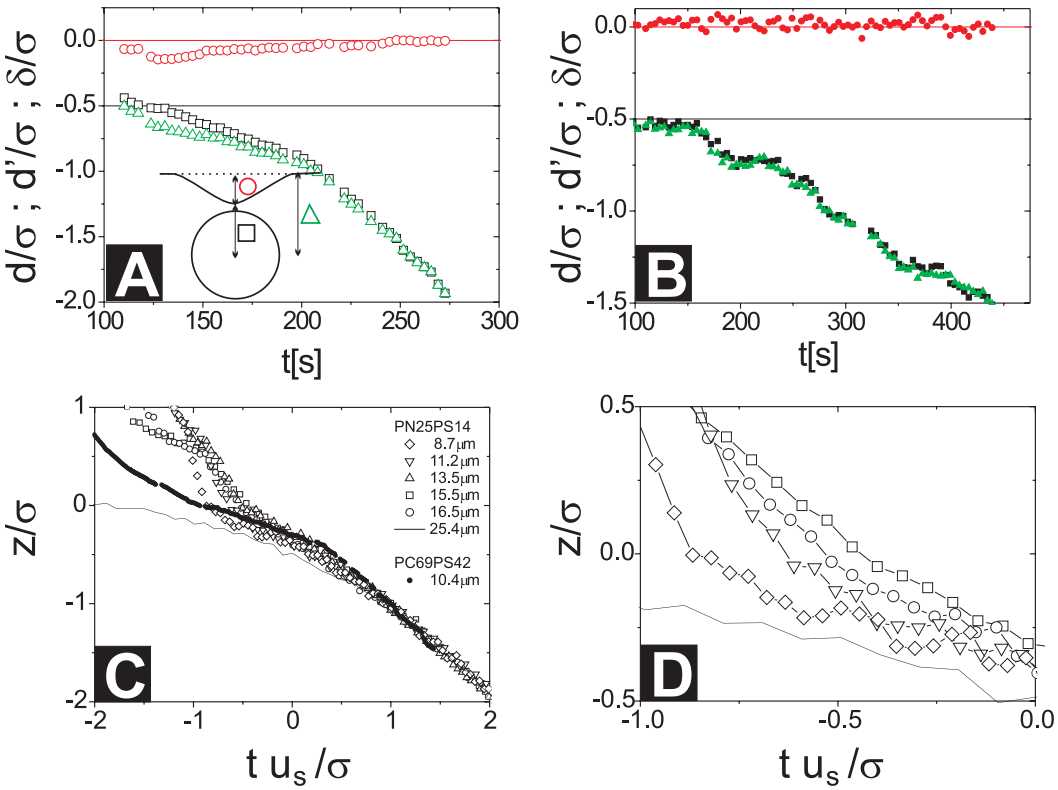

Figure 10.13. Quantitative analysis of the moving away of a sphere from the interface. (A) Moving away of a $10.4\mu m$ diameter sphere (Bo=0.51) and interfacial deformation. The height is dimensionless. The straight lines indicate the interface (at $\delta = 0$) and $d = \sigma/2$, when the sphere is attached to the interface. The sphere clearly deforms the interface before it detaches. (B) as in (A) but now for a $4.4\mu m$ diameter sphere (Bo=0.09). The interface does not deform since the gravitational force on the sphere is much lower here. (C) Dimensionless time ($tu_s(d = -\infty)/\sigma$) versus height (z/σ) for spheres in systems PN25PS14 and PC69PS42. The curves all scale for sufficient interface-sphere separations of half a diameter. In PC69PS42 the sphere spends much more time close to the interface. (D) Zoom of Fig.(C) showing the behaviour close to the interface. Here, the curves increase more steeply for larger particle sizes. Only the largest sphere does not follow the trend: it is a $25.2\mu m$ diameter sphere for which $Bo = 2.7$. Counterintuitively, the transport of this sphere is the slowest since it is not transported through wetting.

$\gamma\sigma$. The transition would then take place at $\sigma = \sqrt{\frac{k_B T}{\gamma}}$. This dimension is the thermal length, which is a measure for the height of the interface fluctuations. Therefore, Brownian forces will only be important for the transport of particles which are of order of the colloid diameter or smaller. For rigid spheres in this system, this would make them indistinguishable from the colloids that make up the system, except for density.

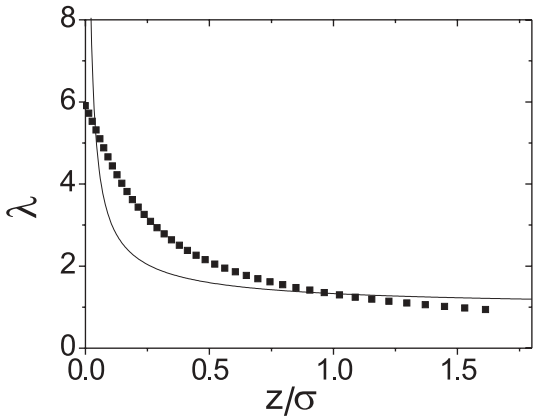

Figure 10.14. Friction factor λ as a function of z/σ for a sphere that moves away from the interface. The datapoints are obtained from the moving away of a 10.4 μm diameter sphere, the solid line is the prediction for the approach toward a free interface. The friction is clearly much stronger in the experiment than in the prediction.

10.6. Conclusion

We describe the low Bond number, low Reynolds number transport of a rigid sphere through the interface of a colloid polymer mixture, which enables the investigation of the effect of capillary waves on the process. The spheres are wettable by the colloidal liquid phase they are transported to. The spheres are covered by a thin wetting layer of the colloidal liquid phase. The spheres initially sediment at their Stokes velocity in the gas phase. Upon approach of the interface the spheres slow down. For larger spheres with $Bo > 0.1$ the interface deforms as well. At a separation of approximately twice the root mean square roughness of the interface a connection between the wetting film on the sphere and the interface is made, after which the sphere is dragged through the interface through the capillary force. The maximum transport velocity is independent of sphere size and approximately a third of the capillary velocity. Due to the pressure gap behind the moving sphere, the interface may be dragged along by the sphere if it is sufficiently large. After the sphere has detached from the interface, the sphere accelerates toward its bulk velocity in the second phase.

10.7. Acknowledgement

This work was done in collaboration with Dirk Aarts and Master Student Julius de Folter. Roel Dullens, Hans Scherff and Esther Groeneveld are acknowledged for particle synthesis. Salima Rafaï, Thomas Bickel, Paul Bartlett and Raymond Bergmann are acknowledged for insightful discussions. Julius de Folter and Dirk Aarts are acknowledged for a careful reading of the manuscript.

11

The transport of a wettable sphere through a fluid-fluid interface

Part II: high Bond numbers

Abstract

In the previous chapter, we studied the transport of wettable spheres through the interface of a demixed colloid-polymer mixture at low Reynolds and Bond numbers by confocal microscopy. Here we consider the high Bond number - low Reynolds number scenario. The sphere approaches the interface from the polymer-rich phase and is eventually transported to the colloid-rich phase. In the high Bond number limit, wetting forces do not play a large role in the transport, even though the spheres are wettable by the colloid-rich phase. Depending on the Bond number, we find two scenarios. At moderately high Bond numbers, the sphere leaves a V-shaped interface behind, which recovers due to interfacial flow. At higher Bond numbers, the so-called tailing regime is observed. In this regime, the spheres leave long columns of gas behind, which break up through a Rayleigh-Plateau instability. Furthermore we find that the theoretical expression for the approach of a sphere toward an undeformable free interface holds surprisingly well for strongly deforming interfaces.

11.1. Introduction

An introduction to the transport of particles through interfaces at constant force and low Reynolds numbers was given in Chapter 10. The initial configuration is as follows: we consider an interface between two fluid phases 1 and 2 with viscosities η_1 and η_2 and densities ρ_1 and ρ_2. A sphere with density ρ_b and radius R in phase 2 sediments at a velocity u_s toward the interface between phases 1 and 2 with an interfacial tension γ. It is schematically shown in figure 10.2 in Chapter 10. As in Chapter 10, the sphere is wetted by a thin layer of phase 1 while it resides in phase 2. Therefore, we ignore the interfacial tension between the solid and the phases for the transport: all the capillary events occur through interactions between the film on the sphere and the interface. We further define the density differences $\Delta\rho_{bn}$ as the density difference between the sphere and phase n, with n either 1 or 2 and $\Delta\rho_{12} = \rho_1 - \rho_2$. What transport configuration is observed strongly depends on the Bond number, the ratio between the gravitational and capillary forces:

$$Bo = \frac{g\Delta\rho_{b2}R^2}{\gamma}, \tag{11.1}$$

In the case of a dominant capillary force, the drainage configuration is usually observed. It consists of three characteristic consecutive stages: (1) the approach of the sphere to the interface, (2) transport from the second to the first phase and (3) moving away of the sphere from the interface, as extensively described in Chapter 9.

In the high Bond number limit the gravitational force is dominant and the tailing configuration is frequently observed. What other factors affect the observed transport configuration will be discussed shortly. In the tailing configuration, the interface strongly deforms and a thin film of phase 2 persists around the sphere in phase 1. The film thins in time until it ruptures in the second phase. Meanwhile, the sphere leaves a long column of phase 2 behind. For this configuration, we may assign the same stages as for the drainage configuration. However, the scenario is more complicated, since the rupture of the film between the wetting layer on the sphere and the bulk phase only occurs when the sphere is well in the second phase (if it occurs at all). Thus separation in time of the second and third stages is not always possible. Experimental studies have in fact not observed the rupture of the film around the sphere due to the finite size of the experimental setup [194, 195, 197, 213] and the spheres are covered with a thin film of fluid of the second phase throughout their movement in the first phase. While the sphere moves through phase 1, the thin film of phase 2 thins and the sphere leaves a column of fluid of phase 2 behind. The break-up of the column may be seen as a fourth stage, although it may also be seen as part of the interface recovery process. The four stages are summarized in figure 11.1. In this chapter we will see that in between the drainage and tailing stage the V-mode configuration occurs. In this mode the sphere

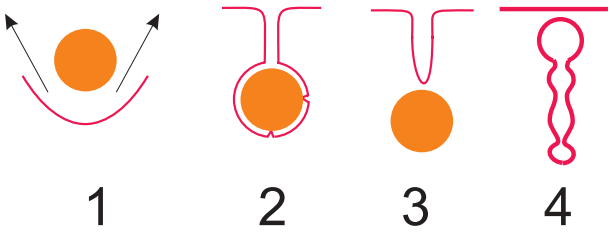

Figure 11.1. Stages of transport through the tailing configuration: (1) approach of the sphere coupled with strong interfacial deformation; (2) rupture of the remaining film between the sphere and the bulk phase; (3) further movement of the sphere in the phase it is transported to; (4) The break-up of the column may be considered as the final part of the transport stage.

leaves a strongly deformed interface behind but no gas column is created. The wetting force does play some role, but not as large a role as in the drainage configuration.

Apart from the Bond number other dimensionless numbers that affect the transport configuration are the buoyancy ratio β

$$\beta = \frac{\Delta\rho_{b2}}{\Delta\rho_{12}} \tag{11.2}$$

and the viscosity ratio μ.

$$\mu = \frac{\eta_1}{\eta_2} \tag{11.3}$$

The effect of these dimensionless numbers on the transport configurations was theoretically studied for rigid spheres [196] and for non-miscible droplets of a third phase approaching the interface [213]. The buoyancy ratio β describes the ratio between the buoyant forces acting on the sphere in the second phase and those acting upon a deformed interface. A large value of β results in an increased width of the interfacial deformation. If $\beta < 1$ a tailing configuration is never observed since the sphere will rest at the interface. A high viscosity ratio μ results in a more "rigid" interface, i.e. the restoring force of the interface is relatively large compared to the viscous drag force of the sphere. High values of μ therefore result in a reduced interfacial deformation and possibly a drainage configuration as in Chapter 10, despite a relatively high Bond number. A fourth factor that affects the transport is the typical film thickness at which film rupture occurs, for example through capillary waves or van der Waals interactions.

As we saw in Chapter 10, the high Reynolds regime is entered at a force of order η^2/ρ, with η the viscosity and ρ the fluid density. For molecular systems we typically find $\eta = 10^{-3}$ Pa s and $\rho = 10^3$ kg/m^3, resulting in a force of order 10^{-9}N. However, inserting typical numbers of $\gamma = 10^{-2}$N/m and $R = 10^{-3}$m for the capillary force, $\gamma R \sim 10^{-5}$N and clearly in the high Reynolds regime. In such systems, the low Reynolds regime is only obtained for particle radii of $R = 10^{-7}$, for which the particles are clearly Brownian and which are presently inaccessible by microscopic methods. Experimental studies of

the high Bond number limit at low Reynolds numbers in molecular systems require high viscosities [213]. We use a different approach and access the low Reynolds regime for interfacial forces by resorting to colloid-polymer mixtures, and by working at small length scales. Owing to a depletion-induced attraction [35,37], these mixtures exhibit a "gas" (colloid poor/polymer-rich)-"liquid"(colloid rich/polymer poor) phase separation when the polymer/colloid diameter ratio q is sufficiently large ($q = \sigma_p/\sigma_c \geq 0.30$ [39]). The interfacial tension in demixed colloid-polymer mixtures is typically of order 10^{-8} N/m in the systems studied here. With $\eta \sim 10^{-2}$ Pa s and $\rho \sim 10^3 \mathrm{kg/m^3}$, inertia becomes important at $\eta^2/\rho = 10^{-7}N$. We use spheres with $R = 10^{-5}$ m, which results in $F_c \sim 10^{-13}$ N. Typically, we further find $\Delta\rho_{b2} \sim 100\mathrm{kg/m^3}$ and we obtain $F_g \sim 10^{-12}$N for the gravitational force. It is dominant over the capillary force, but clearly still in the low Reynolds regime. At the same time the Peclet number $Pe = \frac{\Delta\rho g R^4}{k_B T} >> 1$ and diffusion is not important.

In comparison, nearly all cases studied for high Bond numbers are at least in one phase in the high Reynolds limit. The only experimental low Reynolds number - high Bond number study is based on high viscosities [213]. Studies such as [194, 195, 197] have Reynolds numbers larger than 1 in the phase where the tailing occurs.

Here, we present a quantitative high Bond - low Reynolds number study by confocal microscopy of the transport of spheres through the interface. This chapter is organised as follows: in section 11.2 we describe our experimental system and setup, in 11.3 we discuss the results for the approach, transport, moving away and column break-up stages. We end with a discussion in 11.4 and conclude in 11.5.

11.2. Experimental System

The transport of rigid spheres was studied in two experimental systems. Both dispersions consist of fluorescently labelled polymethyl methacrylate particles, suspended in cis-trans decalin, with polystyrene added as a depletant. The first system was fluorescently labelled with 4-methylaminoethyl methacrylate- 7-nitrobenzo-2-oxa-1,3-diazol (NBD), the second system with (7- (diethylamino)coumarin-3-carboxylic acid N-succinimidyl ester)-aminostyrene (CAS). For the first and second system the respective radii of the particles were 71 nm and 69 nm, determined by dynamic light scattering, with a particle polydispersity of approximately 10% from scanning electron microscopy. The radii of gyration of the polymers used for the first and second system were estimated to be 43 nm and 42 nm [176]. We will refer to the first system as PN71PS43 and to the second system as PC69PS42. The second system, PC69PS42 was extensively described in Chapter 8 and Chapter 10. Phase diagrams were constructed by repetitive dilution of several phase separating samples. The phase diagram for system PN71PS43 is shown in figure 11.2. The shown binodal is a guide to the eye. Here we study statepoint D. The phase diagram for PC69PS42 was shown in Chapter 8. The statepoint

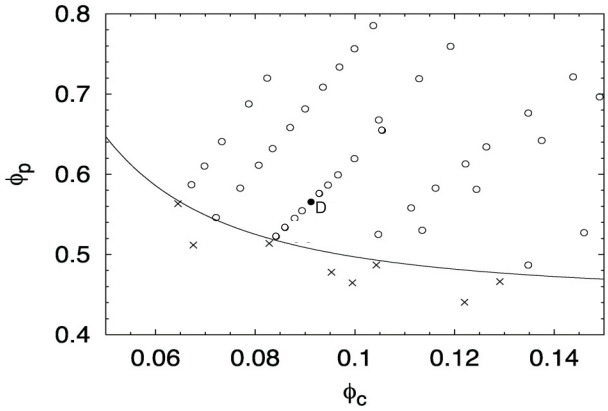

Figure 11.2. Phase diagram for system PN71PS43. Circles indicate statepoints that phase separate, crosses indicate statepoints that do not. The binodal is a guide to the eye. Measurements were performed on statepoint D, marked by the filled circle. The phase diagram of PC69PS42 was shown in Chapter 8

Table 11.1. Physical properties of the systems studied

Quantity	unit	PC69PS42	PN71PS43
ρ_l	kg/m^3	957	930
ρ_g	kg/m^3	931	906
η_l	$mPa\ s$	25	60
η_g	$mPa\ s$	6	6
$R_{Bo=1}$	μm	4	3
γ	nN/m	45	24
$\gamma/(\eta_l+\eta_g)$	$\mu m/s$	1.5	0.36
$\langle h^2\rangle^{\frac{1}{2}}$	μm	0.10	0.32
β		9	9
μ		4	10

studied here is statepoint C. The addition of the spheres and subsequent microscopy measurements were performed as in Chapter 10. PC69PS42 was studied with the Zeiss setup and PN71PS43 was studied with the Nikon setup described there.

11.2.1. Characterisation of the experimental systems

We determined the relevant system variables for all statepoints from capillary wave height-height correlation functions and bulk sedimentation rates of spheres, as in Chapter 10.They are summarized in table 11.1. Note that we again set the l and g subscripts for the colloidal liquid and the colloidal gas. Clearly we may compare the results in the systems for variation of Bo and μ, but not β. The root mean squared interfacial roughness $\langle h^2\rangle^{\frac{1}{2}}$ is much higher for the statepoint C of PC69PS42 than for statepoint

D of PN71PS43, which means that we can compare events mediated by capillary waves as well.

11.3. Results and Discussion

Depending on the Bond number, we observe two different transport configurations. In section 11.3.1 we examine the transport at moderate Bond numbers of Bo=2-3 resulting in what we will refer to as the V-mode. Higher Bond numbers result in tailing configurations, which are discussed in 11.3.2. A quantitative analysis of the height of the sphere versus time for both modes is presented in 11.3.3.

11.3.1. V-mode

Three series of images of transport at moderate Bond numbers (2-3) are shown in figure 11.3. The interface strongly deforms upon approach of the sphere. When the top of the sphere has reached the height of the undeformed interfacial position, the interface has not fully recovered yet, and the sphere leaves a V-shaped interfacial profile behind. Note that this is different from the sphere which drags the interface along in the drainage mode, encountered in Chapter 10. In the latter case, the interface has fully recovered by the time the sphere is fully below the undeformed interfacial position, but deforms again through the pressure gap behind the sphere. Initially the recovery of the interface takes place by lateral fluid motion and is driven by the hydrostatic pressure imbalance between the polymer-rich phase in the V-shaped neck and the colloid rich phase around it. Subsequently the colloid-rich phase flows upward as well, minimizing the interfacial area. The film of polymer-rich phase around the sphere ruptures relatively close to the interface at multiple locations. This frequently leads to trapped bubbles of polymer-rich phase below the sphere. We do not see any bubbles trapped below the sphere in Fig. 11.3B, but this might very well take place outside of the field of view. In Fig. 11.3C we do see several connections forming simultaneously between the wetting film on the sphere and the bulk phase. As a result, part of the polymer-rich film is initially trapped under the sphere. In time, the gas bubbles flow along the sphere surface as the sphere sediments downward and eventually detach from its surface. The sphere sediments further downward in the bulk phase, the bubbles move upward and eventually coalesce with the interface. The latter is extensively described in [209]. The effect of the roughness of the interface is clear as well: in Fig. 11.3B and C the deformed interface has a much rougher shape. It appears that the film ruptures much earlier in PC69PS42, but since we do not see the entire process due to confocal slicing, this cannot be deduced without further quantitative analysis. Despite the very different value of μ, the transition to the tailing mode takes place at similar Bond numbers (somewhere in between Bo=3 and Bo=4). In summary, we may divide the transport stages into several events, which are schematically shown in figure 11.4. The approach stage consists of

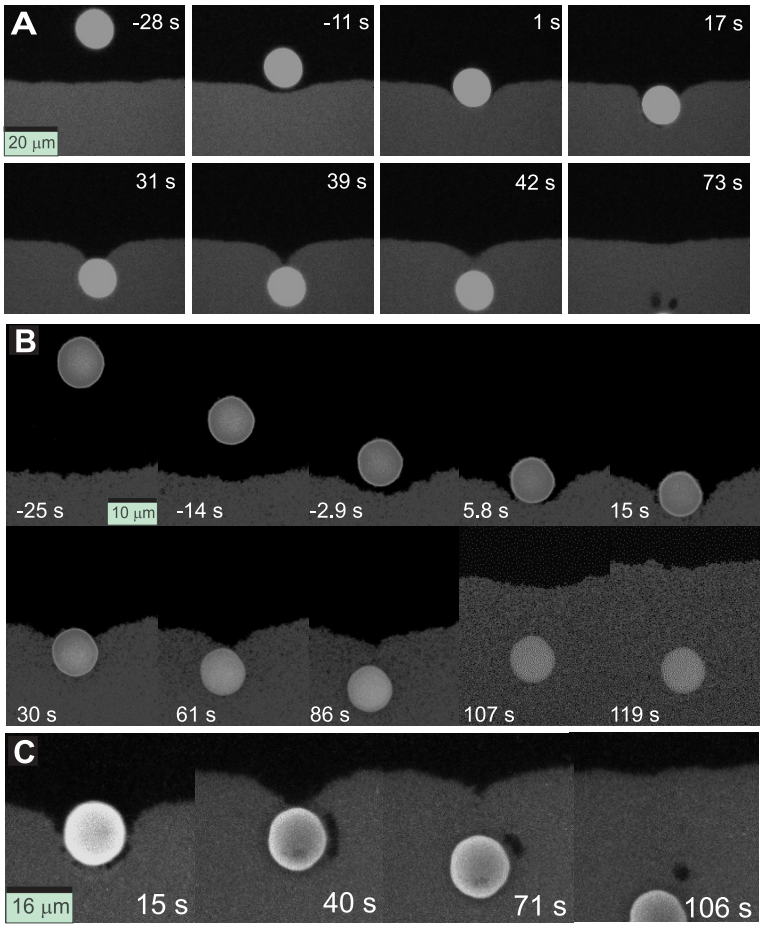

Figure 11.3. Transport through the V-configuration. $t = 0$ is set as the time when the sphere centre reaches the position of the undeformed interface. (A) Approach of a 14.6 μm diameter particle (Bo=3.2) in PN71PS43. During the approach of the sphere, the interface strongly deforms due to solvent backflow. When the sphere is completely below the position of the undeformed interface, the interface has not fully recovered yet and has a V-shaped profile. The connection between the film on the sphere and the bulk phase is made relatively far from the interface. The droplets formed during the break up of the film are seen in the last image. (B) An event similar to (A): Approach of a 9.6 μm diameter particle (Bo=3) in PC69PS42. (C) An event similar to (B). Here, however, the connection between the film on the sphere and the bulk phase is made simultaneously at several locations. As a result, part of the gas phase is trapped under the sphere and gradually slips past the sphere. It eventually becomes a gas bubble which will sediment upward and coalesce with its bulk phase.

1(A) the sedimentation of the sphere far from the interface, 1(B) the deformation of the interface and 1(C) the slowing down of the sphere due to solvent backflow. The transport stage consists of 2(A) the nearly simultaneous rupture of the film at several

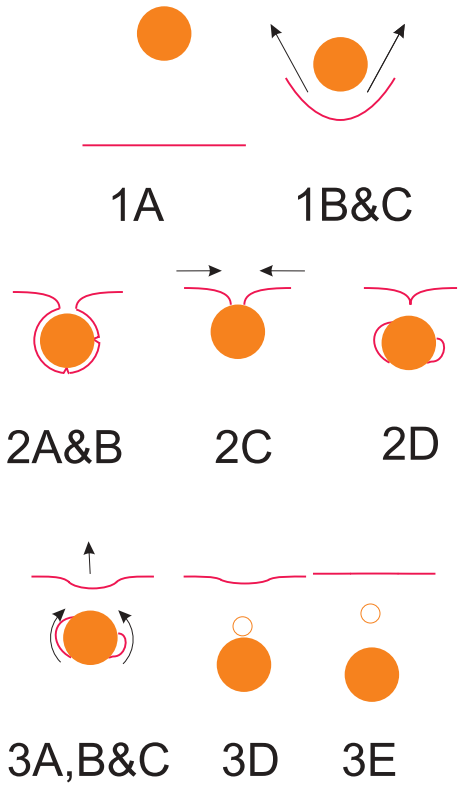

Figure 11.4. Subdivision of the approach, transport, moving away and column break-up stages in events in the V-mode configuration. They are described in detail in the text. The wetting layer on the particle is not shown.

locations around the sphere, 2(B) the growth of these connections that may drag the sphere downward depending on the location where the connections are made, 2(C) the decrease of width of the gap above the sphere; . The relatively large distance of the sphere to the interface usually leads to 2(D) the formation of gas bubbles that are trapped under the sphere. The moving away stage consists of 3(A) the speeding up of the sphere in the colloidal liquid, 3(B) the further restoration of the interface through minimization of the interfacial area, 3(C) the movement of gas bubbles along the sphere interface, 3(D) the detachment of the bubbles from the sphere and 3(E) the further movement of the sphere in the colloidal liquid phase.

11.3.2. Tailing mode

At values of $Bo > 4$, we observe a tailing configuration as shown for a 24 μm diameter sphere (Bo=9)in PN71PS43 and for a 40μm sphere-like object (Bo=45) in PC69PS42 in Fig. 11.5A and B. While the sphere moves through the interface it entrains a film of the polymer-rich phase around it and a column of the same material behind it. The film around the sphere thins and breaks up into bubbles, feeding the column. The connection between the bulk fluid and the colloidal liquid film on the sphere is usually made simultaneously at several locations, but apparently such that the net wetting

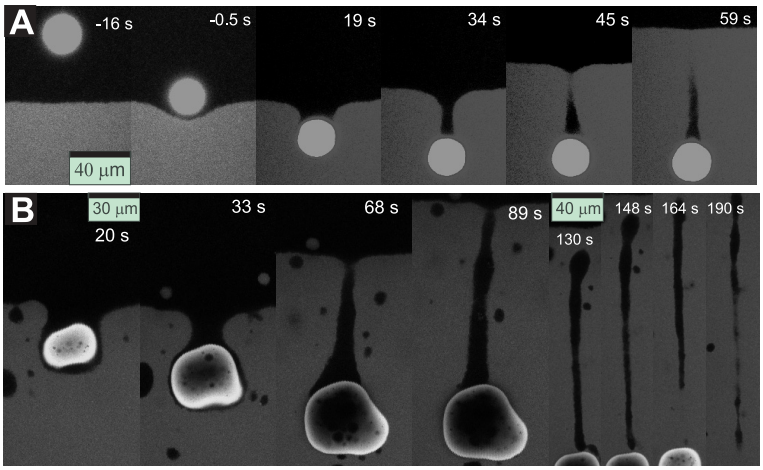

Figure 11.5. Transport through the tailing configuration. t=0 is set as the time when the sphere centre reaches the position of the undeformed interface. (A) The transport of a 24 μm sphere (Bo=9) through the interface in PN71PS43. The sphere clearly leaves a long column of colloidal gas behind. (B) Transport of a roughly 40 μm (Bo=45) sphere-like object through the interface in PC69PS42. Again, the object leaves a column of colloidal gas behind, which it extends through thinning of the film around it, but also by dragging it along. The film made up of colloidal gas thins until it eventually ruptures and breaks up into bubbles which flow around the object.

force on the sphere is negligible as no sudden increase in velocity is observable. While the sphere moves downward the column elongates and thins and closes near the bulk interface. This is likely due to the high Laplace pressure of the locally curved interface. Eventually the sphere disconnects from the column. The column width at which this occurs should be related to the roughness of the interface: when the width of the column above the sphere is sufficiently thin for fluctuations to bridge the column width, the sphere breaks away. The confocal slicing method sometimes obscures certain events, as can for example clearly be seen in the last few images of Fig. 11.5B. In principle this can be solved by sufficiently fast 3D confocal microscopy or by optical microscopy at somewhat lower resolution.

Two representative image series of the break-up of the column are shown in figure 11.6. The column (with a diameter smaller than the capillary length) breaks up as a Plateau-Rayleigh instability, which is driven by the interfacial tension [217, 218]. The break-up pattern is strongly reminiscent of the break-up of threads at ultralow interfacial tension [46, 219], with for example the absence of satellite droplets. The only difference with these studies is that here the surrounding fluid is the more viscous phase.

In Fig. 11.6A, for a sphere with Bo=10 the break-up results in only three droplets (and an additional droplet which is released from the film). The break-up in Fig. 11.6B

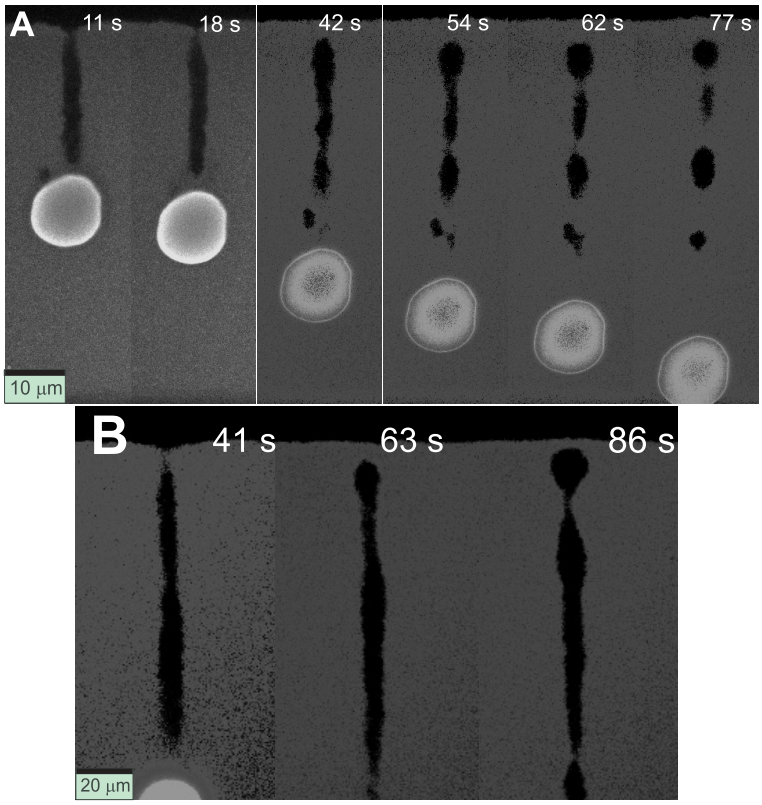

Figure 11.6. Break-up of gas columns. For panel (A) the time is the time after which the sphere has detached from the column, for panel (B) $t = 0$ is set as the time at which the sphere position equals the undeformed interface position. (A) an 18 μm diameter sphere (Bo=10) in PC69PS42 leaves a large column of colloidal gas material behind. The column eventually breaks up into several droplets. (B) Break-up process of a colloidal gas column in PN71PS43, formed behind the 24 μm sphere (Bo=5) presented in Fig. 11.5A.

stretches beyond our measurement time but clearly results in a larger amount of droplets, despite the lower Bond number (Bo=8). Clearly both the viscosity ratio μ and the increased thermal roughness may play a role here: an increased viscosity reduces the extent of interfacial deformation, while the thermal roughness affects the length of the column through coalescence events. The break-up time t_b of the cylinder for $\mu = 10$ is roughly described by $t_b = 100\eta_2 R_c/\gamma$ with R_c the radius of the column [43, 217, 220]. Note that the column here is extending while it breaks up, which should enhance the stability of it [218]. For Fig. 11.6A we find $t_b = 50$ s which is in good agreement with our observations.

We now summarize the events taking place during the approach, transport, moving away and column break up stages in the tailing regime (figure 11.7). Although the events that take place are all clearly observable, the order of the events also depends on the dimensionless parameters Bo, β, μ and $\langle h^2 \rangle^{\frac{1}{2}}$. During the approach stage, the

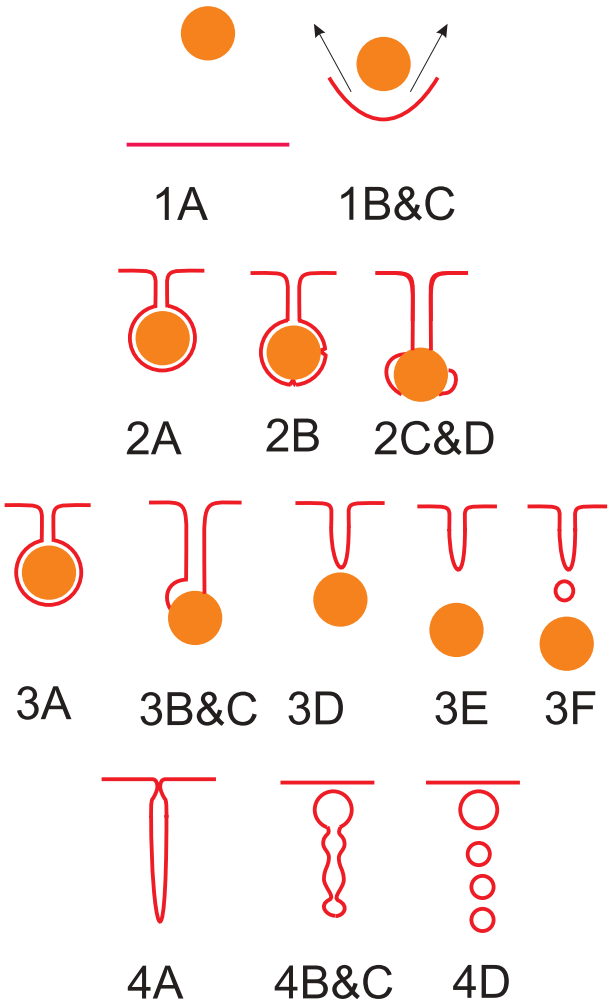

Figure 11.7. Subdivision of the approach, transport, moving away and column break-up stages in events in the tailing configuration. They are described in detail in the text. The wetting layer on the particle is not shown.

spheres initially sediment at constant velocity through the fluid (1(A)). At a spacing of $d \sim 1-2$ the interface begins to deform (1(B)) and the sphere slows down due to solvent backflow (1(C)) until it reaches a minimum velocity (1(D)). The transport events are the events leading up to the rupture of the film around the sphere. These are 2(A) the thinning of the film around the sphere in the colloidal liquid, 2(B) the rupture of the film at multiple locations, which leads to 2(C) the formation of droplets around the sphere's surface. The wetting step hardly if at all affects the particle velocity. The moving away stage may be subdivided in 3(A) the speeding up of the sphere in the liquid and creation and extension of the column (these occur before rupture). After the rupture of the film (3B), gas bubbles flow around the sphere which 3(C) coalesce with the column, 3(D) the release of the column from the sphere and 3(E) the further movement of the sphere in the colloidal liquid phase. Usually 3(F), the sphere still releases a few bubbles after

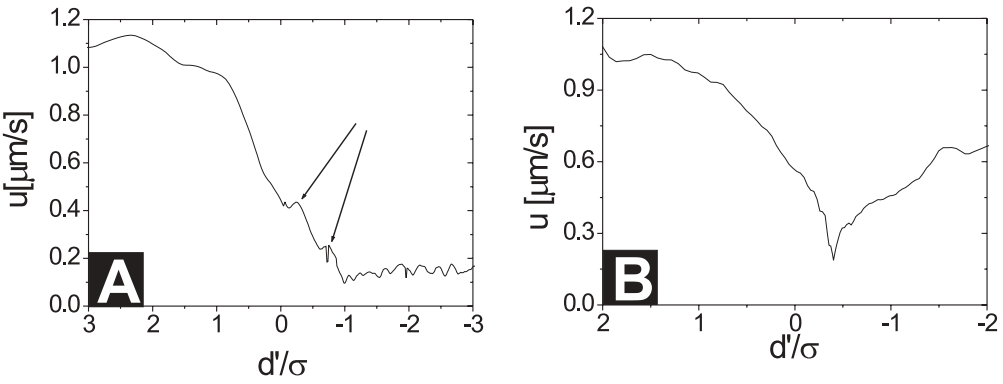

Figure 11.8. Velocity as a function of distance to the undeformed interface d' for the V-mode in PC69PS42 (A) and in PN71PS43 (B). (A) a 9.6 μm diameter sphere (Bo=2.6); (B) a 14.6 μm diameter sphere (Bo= 3.2); In panel (A) two wetting steps clearly show up. The Bond number is comparable to that in (B), but $\langle h^2 \rangle^{\frac{1}{2}}$ is much higher causing the film to rupture much earlier. In (B) the film breaks as well. The velocity far away from the interface is much lower in the colloidal liquid of PC69PS42, due to its higher viscosity. The arrows in (A) indicate the tiny increases in velocity due to wetting.

it has released the column. Again the gas bubbles will sediment upward and coalesce with the interface as in [209]. The break-up of the column starts with 4(A) the closure of the interface above the tail, 4(B) the creation of undulations in the column that decrease the interfacial area, 4(C) the break up of the column into bubbles, 4(D) the upward movement of the bubbles toward the interface and 4(E) the coalescence with the interface.

11.3.3. Quantitative Analysis of the sphere height vs. time

In this section we present a quantitative analysis of the sphere height in time. As in the previous chapter, it is not always straightforward what reference point to the interface should be taken. We follow the terminology in the previous chapter, with z the separation between the interface and the sphere surface along the symmetry axis of the sphere parallel to the axis of gravity. We further define the separation between sphere $z' = z - \delta$ as the separation between the sphere and the undeformed interface, with δ the interfacial deformation along the same symmetry axis. Similarly we have $d' = d - \delta = d + R - \delta$, with R the sphere radius, and d and d' the distance between the sphere centre and respectively the deformed and undeformed interface along the same symmetry axis, as illustrated in figure 10.2 in Chapter 10.

Two representative velocity profiles throughout the V-mode transport process, are shown in Fig. 11.8A and B as a function of d' for PC69PS42 and PN71PS43. In both figures, the velocity clearly reduces close to the interface. In Fig. 11.8A two tiny wetting

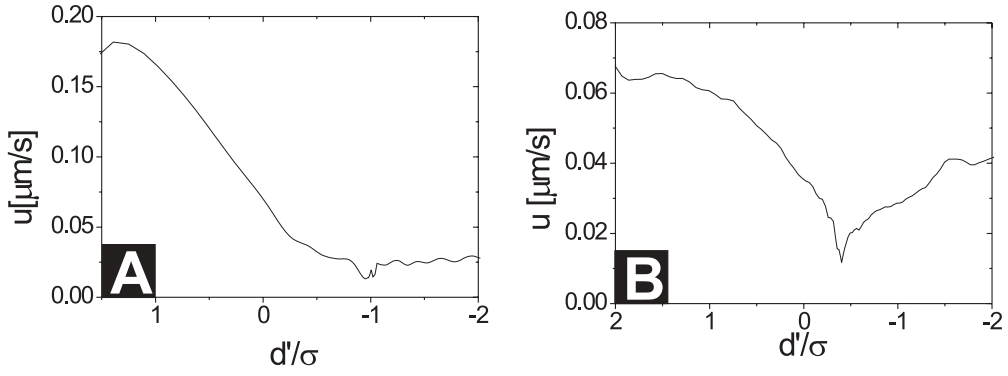

Figure 11.9. Velocity as a function of distance to the undeformed interface d' for the tailing configuration in PC69PS42 (A) and in PN71PS43 (B). (A) a 13.3 μm diameter sphere (Bo=5.0); (B)) a 24.2 μm diameter sphere (Bo = 8.8).

steps are subsequently observed, which coincide with the observation of rupture events. In Chapter 10 the maximum velocity was well described by $u_c/3$. In this system, $u_c/3 = 0.12\mu m/s$, which is significantly larger than the observed increases in velocity. This supports the scenario of multiple more or less simultaneous rupture events at the side of the sphere. The release of droplets from the sphere in Fig. 11.3A confirms that the film around the sphere is ruptured, but this does not show in the velocity profile. Here the capillary velocity is larger, $u_c/3 = 1.5\mu m/s$, but the sedimentation velocities are larger as well. Moreover the reduced resolution in time, the identical dyes of the sphere and the colloids and the smaller interfacial roughness hinder the observation of rupture events. Apparently the wetting events take place more or less at the side of the sphere, and wetting hardly contributes to the downward velocity, which is representative for all spheres in this system. In Fig. 11.9B the increase in velocity after passage of the interface is clear. In Fig. 11.9A it is hardly observable, again a consequence of the different viscosities. Clearly, as Bo increases and γ becomes less important, the minimum should vanish at some point and the velocity profile should become a simple transition from one velocity to the other.

Two representative velocity profiles of the tailing transport process, are shown in Fig. 11.9A and B as a function of d'/σ for PC69PS42 and PN71PS43. Both curves show a clear decrease of velocity upon approach of the interface. The minimum velocity of the sphere occurs approximately a diameter below the interface. No wetting events are observable in either system. Finally, in both systems the spheres accelerate toward their eventual sedimentation velocity in the colloid-rich phase.

The full approach curve (z'/σ) and interfacial deformation (δ/σ) are shown for a 10.3 μm sphere as a function of time in Fig. 11.10A. $t = 0$ is the time at which z'/σ=1. The

deformation is clearly much more pronounced than those presented in Chapter 9 and Chapter 10 for the drainage mode, easily over half a particle diameter. Despite this, the dimensionless approach curve (z/σ vs. $tu_s(d=\infty)/\sigma$ still agrees remarkably well with equation (9.6) for an undeformable free interface from Chapter 9, as shown for several approaches in Fig. 11.10B. Here, $t = 0$ is the time at which z/σ=1. The data covers spheres from both the V-mode and the tailing regime. In Fig. 11.10C we present the moving away of the sphere from the interface for several spheres. The curves are made dimensionless (z'/σ vs. $tu_s(d=-\infty)/\sigma$), but close to the interface we do see neither scaling behaviour nor a systematic trend as a function of particle diameter. A possible explanation comes from the tiny wetting events during the rupture of the film of the colloid-rich phase, described earlier: the location where the connection is made should contain some randomness, which should translate to the acceleration events. Further away from the interface, that is $z > \frac{\sigma}{2}$, scaling is observed.

Confocal microscopy is not particularly well suited for studies of the break-up of the gas column. From an image the local width of the column can be determined with high accuracy, but confocal slicing causes the true diameter of the column to be frequently out of focus. Optical microscopy is a better candidate to capture the full break-up, such as in [46], but reduces the lateral resolution. Fast 3D confocal microscopy is an alternate, but is experimentally challenging.

11.4. Conclusion

We describe the high Bond number, low Reynolds number transport of a rigid sphere through the interface of a colloid polymer mixture, which enables the investigation of the effect of capillary waves on the process. The spheres are wettable by the colloidal liquid phase they are transported to. The spheres are covered by a thin wetting layer of the colloidal liquid phase. The spheres initially sediment at their Stokes velocity in the gas phase. Upon approach of the interface the spheres slow down and the interface strongly deforms. Nevertheless, the approach is still very well described by the approach of a sphere toward a free surface. For moderate Bond numbers a minimum velocity is observed at the interface, but upon increase of the Bond number this minimum becomes less pronounced. At moderate Bond numbers of 2-3 the sphere leaves a V-shaped interface behind, which gradually recovers. At higher Bond numbers, the sphere leaves a long tail of colloidal gas material behind in the colloidal liquid phase. The column eventually breaks up in droplets through a Rayleigh-Plateau instability.

11.5. Acknowledgement

This work was done in collaboration with Dirk Aarts and Master Student Julius de Folter. Roel Dullens, Hans Scherff and Esther Groeneveld are acknowledged for particle

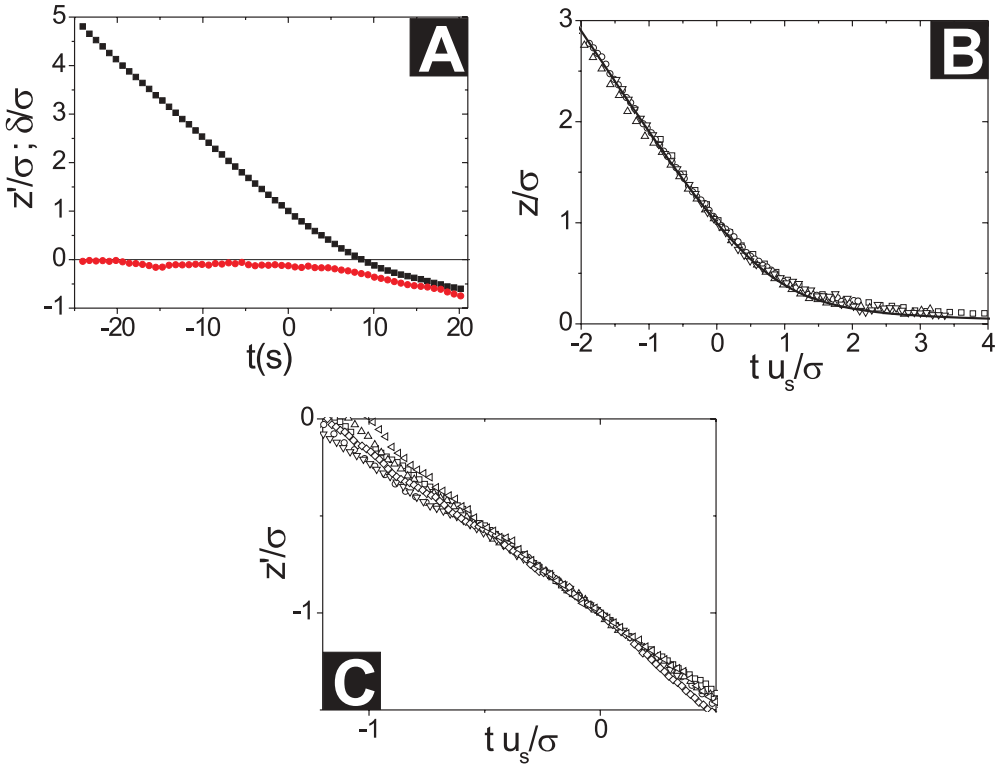

Figure 11.10. Spheres approach toward and moving away from the interface at high Bond numbers. (A) Dimensionless separation between the sphere and the undeformed interface d'/σ and interfacial deformation δ/σ for the approach of a 10.3 μm sphere (Bo=3). (B) Dimensionless separation between the sphere surface and the deformed interface (d/σ) versus dimensionless time $(tu_s(d = \infty)/\sigma)$ for several spheres approaching the interface. (C) Dimensionless separation between the sphere surface and the undeformed interface (d'/σ) versus dimensionless time $(tu_s(d = \infty)/\sigma)$ for several spheres moving away from the interface. The solid line is the theoretical curve for the approach of a rigid sphere to a free non-deformable interface, given in Chapter 8.

synthesis. Yves Hennequin, Salima Rafaï, Thomas Bickel, Paul Bartlett and Raymond Bergmann are acknowledged for insightful discussions. Julius de Folter and Dirk Aarts are acknowledged for a careful reading of the manuscript.

Bibliography

[1] D. Hull and D. J. Bacon. *Indroduction to Dislocations*. Pergamon, New York, 1984.

[2] J. D. van der Waals. *Z. f. Phys. Chem.*, 13:657, 1894.

[3] M. von Smoluchowski. *Ann. Phys.*, 25:205, 1908.

[4] L. Mandelstam. *Ann. Phys.*, 41:609–624, 1913.

[5] W. C. K. Poon. 1998.

[6] P. Bartlett. 2005.

[7] M. Fasolo and P. Sollich. *Phys. Rev. Lett.*, 91:068301, 2003.

[8] B. J. Alder and T. E. Wainwright. *J. Chem. Phys.*, 27:1208, 1957.

[9] W. W. Wood and J. D. Jacobsen. *J. Chem. Phys.*, 27:1207, 1957.

[10] W. G. Hoover and F. H. Ree. *J. Chem. Phys.*, 49:3609, 1968.

[11] N. F. Carnahan and K. E. Starling. *J. Chem. Phys.*, 51:635, 1969.

[12] B. J. Alder, W. G. Hoover, and D. A. Young. *J. Chem. Phys.*, 49:3688, 1968.

[13] P. N. Pusey and W. van Megen. *Nature*, 320:340–342, 1986.

[14] G. Bosma, C. Pathmamanoharan, E. H. A. de Hoog, W. K. Kegel, A. van Blaaderen, and H. N. W. Lekkerkerker. *J. Colloid Interface Sci.*, 245:292, 2002.

[15] A. van Blaaderen and P. Wiltzius. *Science*, 270:1177, 1995.

[16] G. Bryant, S. R. Williams, L. Qian, I. K. Snook, E. Perez, and F. Pincet. *Phys. Rev. E*, 66:060501, 2002.

[17] R. P. A. Dullens, D. Aarts, and W. K. Kegel. *PNAS*, 103:529–531, 2006.

[18] W. van Megen and S. M. Underwood. *Nature*, 362:616, 1993.

[19] J. Zhu, M. Li, R. Rogers, W. Meyer, R. H. Ottewill, S.-S. S. Crew, W. B. Russel, and P. M. Chaikin. *Nature*, 387:883, 1997.

[20] N. J. A. Sloane. *Nature*, 395:435–436, 1998.

[21] T. Aste and D. Weaire. *The pursuit of perfect packing*. IOP Publishing, Bristol, 2000.

[22] P. G. Bolhuis, D. Frenkel, S. C. Mau, and D. A. Huse. *Nature*, 388:235, 1997.

[23] A. D. Bruce, N. B. Wilding, and G. J. Ackland. *Phys. Rev. Lett.*, 79:3002, 1997.

[24] S. C. Mau and D. A. Huse. *Phys. Rev. E*, 59:4396, 1999.

[25] S. Pronk and D. Frenkel. *J. Chem. Phys.*, 110:4589–4592, 1999.

[26] P. N. Pusey, W. van Megen, P. Bartlett, B. J. Ackerson, J. G. Rarity, and S. M. Underwood. *Phys. Rev. Lett.*, 63:1989, 1989.

[27] W. K. Kegel and J. K. G. Dhont. *J. Chem. Phys.*, 112:12, 2000.

[28] I. P. Dolbnya, A. V. Petukhov, D. G. A. L. Aarts, G. J. Vroege, and H. N. W. Lekkerkerker. *Europhys. Lett.*, 72:962 – 968, 2005.

[29] A. V. Petukhov, I. P. Dolbnya, D. G. A. L. Aarts, G. J. Vroege, and H. N. W. Lekkerkerker. *Phys. Rev. Lett.*, 90:028304, 2003.

[30] N. A. M. Verhaegh, J. S. Vanduijneveldt, A. Vanblaaderen, and H. N. W. Lekkerkerker. *J. Chem. Phys.*, 102:1416–1421, 1995.

[31] S. Auer and D. Frenkel. *Nature*, 409:1020, 2001.

[32] J. P. Hoogenboom, P. Vergeer, and A. van Blaaderen. *J. Chem. Phys.*, 119:3371 – 3383, 2003.

[33] P. Schall, I. Cohen, D. A. Weitz, and F. Spaepen. *Science*, 305:1944–1948, 2004.
[34] P. Sollich. *J. Phys. Condens. Matter*, 14:R79 – R117, 2002.
[35] S. Asakura and F. Oosawa. *J. Chem. Phys.*, 22:1255, 1954.
[36] S. Asakura and F. Oosawa. *J. Pol. Sci.*, 33:183, 1958.
[37] A. Vrij. *Pure Appl. Chem.*, 48:471, 1976.
[38] W. C. K. Poon. *J. Phys.: Condens. Matter*, 14:R859, 2002.
[39] H. N. W. Lekkerkerker, W. C. K. Poon, P. N. Pusey, A. Stroobants, and P. B. Warren. *Europhys. Lett.*, 20:559, 1992.
[40] J. S. Rowlinson and B. Widom. *Molecular theory of capillarity*. Clarendon Press, Oxford, 1982.
[41] P. G. De Gennes. *Scaling concepts in polymer physics*. Cornell University Press, Ithaca, 1979.
[42] D. G. A. L. Aarts, M. Schmidt, and H. N. W. Lekkerkerker. *Science*, 304:847, 2004.
[43] E. H. A. de Hoog and H. N. W. Lekkerkerker. *J. Phys. Chem. B*, 105:11636, 2001.
[44] E. H. A. de Hoog and H. N. W. Lekkerkerker. *J. Phys. Chem. B*, 103:5274, 1999.
[45] G. A. Vliegenthart and H. N. W. Lekkerkerker. *Prog. Colloid Polym. Sci.*, 105:27, 1997.
[46] Y. Hennequin, D. Aarts, J. H. van der Wiel, G. Wegdam, J. Eggers, H. N. W. Lekkerkerker, and D. Bonn. *Phys. Rev. Lett.*, 97:44502, 2006.
[47] D. G. A. L. Aarts. *Soft Matter*, 3:19–23, 2007.
[48] J. Perrin. *Ann. de Chim. Phys.*, 18:5, 1908.
[49] J. Perrin. *Les Atomes*. Libr. Felix Alcan, Paris, 1920.
[50] A. Einstein. *Ann. Phys.*, 17:549, 1905.
[51] J. C. Crocker and D. G. Grier. *J. Colloid Interface Sci.*, 179:298, 1996.
[52] A. Mohraz and M. J. Solomon. *Langmuir*, 21:5298–5306, 2005.
[53] H. Yoshida, K. Ito, and N. Ise. *Phys. Rev. B*, 44:435, 1991.
[54] A. Van Blaaderen, A. Imhof, W. Hage, and A. Vrij. *Langmuir*, 8:1514–1517, 1992.
[55] R. P. A. Dullens, E. M. Claesson, D. Derks, A. van Blaaderen, and W. K. Kegel. *Langmuir*, 19:5963, 2003.
[56] J. R. Savage, D. W. Blair, A. J. Levine, R. A. Guyer, and A. D. Dinsmore. *Science*, 314:795–798, 2006.
[57] U. Gasser, E. R. Weeks, A. Schofield, P. N. Pusey, and D. A. Weitz. *Science*, 292:258–262, 2001.
[58] C. P. Royall, D. G. A. L. Aarts, and H. Tanaka. *Nature Physics*, 3:636–640, 2007.
[59] A. M. Alsayed, M. F. Islam, J. Zhang, P. J. Collings, and A. G. Yodh. *Science*, 309:1207–1210, 2005.
[60] D. Reinke, H. Stark, H. H. von Grunberg, A. B. Schofield, G. Maret, and U. Gasser. *Physical Review Letters*, 98, 2007.
[61] D. Derks, D. G. A. L. Aarts, D. Bonn, H. N. W. Lekkerkerker, and A. Imhof. *Phys. Rev. Lett.*, 97:038301, 2006.
[62] V. Prasad, D. Semwogerere, and E. R. Weeks. *Journal of Physics Condensed Matter*, 19, 2007.
[63] M. Minsky, 1957.
[64] P. Davidovits and M. D. Egger. *Appl. Opt.*, 10:1615–1619, 1971.
[65] C. J. R. Sheppard and D. M. Shotton. *Confocal Laser Scanning Microscopy*. BIOS Scientific Publishers, Oxford, 1997.
[66] R. H. Webb. *Rep. Prog. Phys.*, 59:427, 1996.
[67] T. Wilson. *Confocal Microscopy*. Academic Press, London, 1990.
[68] M. G. L. Gustafsson. *Journal of Microscopy-Oxford*, 198:82–87, 2000.

[69] A. V. Petukhov, J. H. J. Thijssen, D. C. t Hart, A. Imhof, A. van Blaaderen, I. P. Dolbnya, A. Snigirev, A. Moussaid, and I. Snigireva. *J. Appl. Cryst.*, 39:137–144, 2006.
[70] A. J. C. Wilson. *X-ray Optics*. Methuen & Co. Ltd., London, 1949.
[71] C. Dux and H. Versmold. *Phys. Rev. Lett.*, 78:1811, 1997.
[72] W. Bras, I. P. Dolbnya, D. Detollenaere, R. van Tol, M. Malfois, G. N. Greaves, A. J. Ryan, and E. Heeley. *J. Appl. Cryst.*, 36:791 – 794, 2003.
[73] P. S. Miedema, V. W. A. de Villeneuve, and A. V. Petukhov. *Submitted*, 2007.
[74] P. Schall, I. Cohen, D. A. Weitz, and F. Spaepen. *Nature*, 440:319–323, 2006.
[75] M. S. Elliot, B. T. F. Bristol, and W. C. K. Poon. *Physica A*, 235:216–223, 1997.
[76] J. P. Hoogenboom, A. K. van Langen-Suurling, J. Romijn, and A. van Blaaderen. *Phys. Rev. E.*, 69:051602, 2004.
[77] T. Solomon and M. J. Solomon. *J. Chem. Phys.*, 124, 2006.
[78] M. S. Elliot and W. C. K. Poon. *Adv. Colloid Interface Sci.*, 92:133–194, 2001.
[79] W. C. K. Poon and P. N. Pusey. Phase transition of spherical colloids. In M. Baus, L.F. Rull, and J.P Ryckaert, editors, *Observation, Prediction and Simulation of Phase Transitions in complex fluids*, pages 3–51. Kluwer, 1995.
[80] A. V. Petukhov, I. P. Dolbnya, D. Aarts, and G. J. Vroege. *Phys. Rev. E*, 69, 2004.
[81] S. Pronk and D. Frenkel. *J. Chem. Phys.*, 120:6764–6768, 2004.
[82] E. H. A. de Hoog. *Interfaces and Crystallization in Colloid-Polymer Suspensions*. PhD thesis, Utrecht, 2001.
[83] K. Schätzel and B. J. Ackerson. *Phys. Scri.*, page 70, 1994.
[84] A. J. C. Wilson. *Proc. Roy. Soc. London A*, 180:277, 1942.
[85] G. J. Ackland and A. P. Jones. *Phys. Rev. B*, 73:054104, 2006.
[86] A. V. Petukhov, D. G. A. L. Aarts, I. P. Dolbnya, E. H. A. de Hoog, K. Kassapidou, G. J. Vroege, W. Bras, and H. N. W. Lekkerkerker. *Phys. Rev. Lett.*, 88:208301, 2002.
[87] J. Friedel. *Dislocations*. Addison-Wesley Series in Metallurgy and Materials. Pergamon, Reading, 1964.
[88] W. Lee, A. Chan, M. A. Bevan, J. A. Lewis, and P. V. Braun. *Langmuir*, 20:5262–5270, 2004.
[89] R. P. Sear. *Phys. Rev. Lett.*, 82:4244–4247, 1999.
[90] H. Föll. Defects in crystals, www.uni-kiel.de, 2007.
[91] S. Amelinckx. *The direct observation of dislocations*, volume 6 of *Solid State Physics - Advances in research and application*. 1964, New York and London, 1964.
[92] J. P. Hoogenboom, C. Retif, E. de Bres, M. V. de Boer, A. K. van Langen-Suurling, J. Romijn, and A. van Blaaderen. *Nano Letters*, 4:205–208, 2004.
[93] J. M. Meijer, V. W. A. de Villeneuve, and A. V. Petukhov. *Langmuir*, 23:3554–3560, 2007.
[94] A. Pertsinidis and X. S. Ling. *Nature*, 413:147, 2001.
[95] A. Pertsinidis and X. S. Ling. *New J. Phys.*, 7:33, 2005.
[96] R. P. A. Dullens and A. V. Petukhov. *Europhysics Letters (EPL)*, 77:58003, 2007.
[97] V. W. A. de Villeneuve, A. B. G. M. Leferink op Reinink, J. M. Meijer, A. V. Petukhov, and P. Schall. *Eur. Phys. J. B*, submitted, 2007.
[98] X. Wu, Y. T. Zhu, M. W. Chen, and E. Ma. *Scripta Materialia*, 54:1685–1690, 2006.
[99] H. Van Swygenhoven, P. M. Derlet, and A. G. Froseth. *Nature Materials*, 3:399–403, 2004.
[100] C. P. Collier, R. J. Saykally, J. J. Shiang, S. E. Henrichs, and J. R. Heath. *Science*, 277:1978–1981, 1997.

[101] B. Gilbert, F. Huang, H. Zhang, G. A. Waychunas, and J. F. Banfield. *Science*, 305:651–654, 2004.
[102] V. F. Puntes, K. M. Krishnan, and A. P. Alivisatos. *Science*, 291:2115–2117, 2001.
[103] R. P. A. Dullens, D. Aarts, and W. K. Kegel. *Phys. Rev. Lett.*, 97:228301, 2006.
[104] V. W. A. de Villeneuve, R. P. A. Dullens, D. G. A. L. Aarts, E. Groeneveld, J. H. Scherff, W. K. Kegel, and H. N. W. Lekkerkerker. *Science*, 309:1231–1233, 2005.
[105] Interactive data language, research systems, inc. (http://www.ittvis.com/).
[106] S. Auer and D. Frenkel. *Phys. Rev. Lett.*, 91:015703, 2003.
[107] A. Cacciuto, S. Auer, and D. Frenkel. *Nature*, 428:404, 2004.
[108] A. J. Page and R. P. Sear. *Phys. Rev. Lett.*, 97:065701, 2006.
[109] R. P. Sear. *J. Phys. Condens. Matter*, 19:033101, 2007.
[110] N. Kubota. *Crystal Research And Technology*, 36:749–769, 2001.
[111] T. A. Land, T. L. Martin, S. Potapenko, G. T. Palmore, and J. J. De Yoreo. *Nature*, 399:442–445, 1999.
[112] A. Kose and S. Hachisu. *J. Colloid Interface Sci.*, 55:487, 1976.
[113] A. Gast, W. Russel, and C. Hall. *J. Colloid Interface Sci.*, 55:161, 1986.
[114] P. D. Kaplan, J. L. Rouke, A. G. Yodh, and D. J. Pine. *Phys. Rev. Lett.*, 72:582, 1994.
[115] A. Dinsmore, P. Warren, W. Poon, and A. Yodh. *Europhys. Lett.*, 40:337, 1997.
[116] V. C. Martelozzo, A. Schofield, W. C. K. Poon, and P. N. Pusey. *Phys. Rev. E*, 66:021408, 2002.
[117] R. P. A. Dullens and W. K. Kegel. *Phys. Rev. Lett.*, 92:195702, 2004.
[118] D. R. Nelson and M. Rubinstein. *Philosophical Magazine A.*, 46:105 – 126, 1982.
[119] W. Schärtl and H. Sillescu. *J. Stat. Phys.*, 77:1007, 1994.
[120] D. R. Nelson. *Defects and geometry in condensed matter physics*. Cambridge University Press, Cambridge, 2002.
[121] P. M. Konig, P. Bryk, K. Mecke, and R. Roth. *Europhys. Lett.*, 69:832–838, 2005.
[122] V. W. A. de Villeneuve, D. Verboekend, R. P. A. Dullens, D. G. A. L. Aarts, W. K. Kegel, and H. N. W. Lekkerkerker. *Journal of Physics-Condensed Matter*, 17:S3371–S3378, 2005.
[123] P. Lipowsky, M. J. Bowick, J. H. Meinke, D. R. Nelson, and A. R. Bausch. *Nat. Mater.*, 4:407–411, 2005.
[124] T. Einert, P. Lipowsky, J. Schilling, M. J. Bowick, and A. R. Bausch. *Langmuir*, 21:12076–12079, 2005.
[125] M. J. Bowick, A. Cacciuto, D. R. Nelson, and A. Travesset. *Phys. Rev. B*, 73, 2006.
[126] P. C. Millett, R. P. Selvan, S. Bansal, and A. Saxena. *Acta Mater.*, 53:3671–3678, 2005.
[127] J. V. Sanders and M. S. Murray. *Phil. Mag. A*, 42:721, 1980.
[128] L. D. Gelb, K. E. Gubbins, R. Radhakrishnan, and M. Sliwinska-Bartkowiak. *Rep. Prog. Phys.*, 62:1573–1659, 1999.
[129] A. Yethiraj and A. van Blaaderen. *Nature*, 421:513, 2003.
[130] A. Imhof and J. K. G. Dhont. *Phys. Rev. Lett.*, 75:1662, 1995.
[131] S. E. Offerman, N. H. van Dijk, J. Sietsma, S. Grigull, E. M. Lauridsen, L. Margulies, H. F. Poulsen, M. T. Rekveldt, and S. van der Zwaag. *Science*, 298:1003–1005, 2002.
[132] S. Yip. *Nature*, 391:532–533, 1998.
[133] J. Schiotz, F. D. Di Tolla, and K. W. Jacobsen. *Nature*, 391:561–563, 1998.
[134] H. van Swygenhoven. *Science*, 296:66, 2002.
[135] E. O. Hall. *Proc. Phys. Soc. Lond. B*, 64:747, 1951.
[136] N. J. Petch. *J. Iron Steel Inst.*, 174:25, 1954.

[137] H. Gleiter. *Acta Materialia*, 48:1–29, 2000.
[138] Q. H. Wei and X. L. Wu. *Physical Review E*, 70, 2004.
[139] W. K. Kegel and A. van Blaaderen. *Science*, 287:290, 2000.
[140] E. R. Weeks, J. C. Crocker, A. C. Levitt, A. Schofield, and D. A. Weitz. *Science*, 287:627, 2000.
[141] R. P. A. Dullens, M. C. D. Mourad, D. G. A. L. Aarts, J. P. Hoogenboom, and W. K. Kegel. *Phys. Rev. Lett.*, 96:028304, 2006.
[142] R. P. A. Dullens, E. M. Claesson, and W. K. Kegel. *Langmuir*, 20:658 – 664, 2004.
[143] E. H. A. de Hoog, W. K. Kegel, A. van Blaaderen, and H. N. W. Lekkerkerker. *Phys. Rev. E*, 64:021407, 2001.
[144] C. A. Murray. Experimental studies of melting and hexatic order in two-dimensional colloidal suspensions. In K.J. Strandburg, editor, *Bond-orientational order in condensed matter systems*, pages 137–215. Springer-Verlag, New York, 1992.
[145] P. C. Millett, R. P. Selvam, and A. Saxena. *Acta Mater.*, 54:297–303, 2006.
[146] Y. Ishida, S. Okamoto, and S. Hachisu. *Acta Met.*, 26:651, 1978.
[147] C. E. Krill, R. Klein, S. Janes, and R. Birringer. *Mater. Sci. Forum*, 179-181:443, 1995.
[148] J. Weissmueller and J. Markmann. *Adv. Eng. Mat.*, 7:202, 2005.
[149] R. Schweinfest, A. T. Paxton, and M. W. Finnis. *Nature*, 432:1008–1011, 2004.
[150] G. Duscher, M. F. Chisholm, U. Alber, and M. Ruhle. *Nature Materials*, 3:621–626, 2004.
[151] C. Suryanarayana. *Advanced Engineering Materials*, 7:983–992, 2005.
[152] T. Svedberg. *Z. f. Phys. Chem.*, 77:147, 1911.
[153] M. von Smoluchowski. *Wien. Ber.*, 123:2381, 1914.
[154] M. von Smoluchowski. *Wien. Ber.*, 124:339, 1915.
[155] L. Rothschild. *J. Exp. Biol.*, 30:178, 1953.
[156] R. J. Nossal and Y. T. Chang. *J. Mechanochem. Cell*, 3:247, 1976.
[157] S. L. Brenner, R. J. Nossal, G. H. Weiss, and 1978. . *J. Stat. Phys.*, 18:1–18, 1978.
[158] F. P. Buff, R. A. Lovett, and F. H. Stillinger. *Phys. Rev. Lett.*, 15:621, 1965.
[159] K. R. Mecke and S. Dietrich. *Phys. Rev. E*, 59:6766, 1999.
[160] A. Milchev and K. Binder. *Europhys. Lett.*, 59:81, 2002.
[161] Z. T. Trautt, M. Upmanyu, and A. Karma. *Science*, 314:632–635, 2006.
[162] C. V. Raman. *Nature*, 112:281, 1923.
[163] C. V. Raman and L. A. Ramdas. *Proc. Roy. Soc (London), Ser. A*, 108:561, 1925.
[164] A. Vrij. *Adv. Coll. Interf. Sci.*, 2:39–64, 1968.
[165] C. Fradin, A. Braslau, D. Luzet, D. Smilgies, M. Alba, N. Boudet, K. Mecke, and J. Daillant. *Nature*, 403:871, 2000.
[166] M. K. Sanyal, S. K. Sinha, K. G. Huang, and B. M. Ocko. *Phys. Rev. Lett.*, 66:628, 1991.
[167] A. Braslau, P. S. Pershan, G. Swislow, B. M. Ocko, and J. Als-Nielsen. *Phys. Rev. A*, 38:2457, 1988.
[168] J. H. Sikkenk, J. M. J. van Leeuwen, E. O. Vossnack, and A. F. Bakker. *Physica A*, 146A:622633, 1987.
[169] R. Becker. *Theorie der Wärme*. Springer-Verlag, Berlin, 1966.
[170] D. G. A. L. Aarts and H. N. W. Lekkerkerker. *J. Fluid. Mech.*, submitted, 2007.
[171] J. Kuipers and E. M. Blokhuis. *Journal of Colloid and Interface Science*, 315:270–277, 2007.
[172] U. S. Jeng, L. Esibov, L. Crow, and A. Steyerl. *J. Phys.: Condens. Matter*, 10:4955, 1998.
[173] V. W. A. de Villeneuve, J. M. J. van Leeuwen, W. van Saarloos, and H. N. W. Lekkerkerker. *Submitted*, 2007.

[174] J. Meunier. Experimental studies of liquids at interfaces: classical methods for studies of surface tension, surface wave propagation and surface thermal modes for studies of viscoelasticity and bending elasticity. In J. Charvolin, J. F. Joanny, and J. Zinn-Justin, editors, *Liquids and Interfaces*, pages 327–369. North-Holland, New York, 1988.

[175] D. G. A. L. Aarts and H. N. W. Lekkerkerker. *J. Phys.: Condens. Matter*, 16:S4231, 2004.

[176] B. Vincent. *Colloids Surf.*, 50:241, 1990.

[177] N. van Kampen. *Stochastic Processes in Physics and Chemistry*. Elsevier, 3rd edition, 2007.

[178] L. F. Phillips. *Accounts of Chemical Research*, 37:982–988, 2004.

[179] E. Dickinson. *Journal Of Dairy Science*, 80:2607–2619, 1997.

[180] K. L. Hoy. *Journal Of Coatings Technology*, 68:33–39, 1996.

[181] W. T. Shin, S. Yiacoumi, and C. Tsouris. *Current Opinion In Colloid & Interface Science*, 9:249–255, 2004.

[182] L. J. Lewis, P. Jensen, and J. L. Barrat. *Physical Review B*, 56:2248–2257, 1997.

[183] A. E. Brandes, G. F. Zhang, and J. Vivekanadan. *J. Appl. Meteorology*, 43:461, 2004.

[184] H. J. Stechemesser and A. V. Nguyen. *Int. J. Miner. Process.*, pages 117–132, 1999.

[185] R. Lande and A. M. Wood. *Deep-Sea Res.*, pages 61–72, 1987.

[186] M. Manga, H. A. Stone, and R. J. O'Connell. *J. Geoph. Res.*, pages 19979–19990, 1993.

[187] H. A. Stone, A. D. Stroock, and A. Ajdari. *Annu. Rev. Fluid Mech.*, 36:381, 2004.

[188] S. Hartland. *J. Coll. Int. Sc.*, 26:383, 1968.

[189] S. Hartland. *Can. J. Chem. Eng.*, 47:221, 1969.

[190] S. Hartland. *Chem. Eng. Sci.*, 24:987, 1969.

[191] S. Hartland. *Chem. Eng. Sci.*, 24:611, 1969.

[192] S. Hartland, B. Yang, and S. A. K. Jeelani. *Chem. Eng. Sci.*, 49:1313, 1993.

[193] A. F. Jones and S. D. R. Wilson. *J. Fluid Mech.*, 87:263, 1978.

[194] S. T. Shah, D. T. Wasan, and R. C. Kintner. *Chemical Engineering Science*, 27:881–893, 1972.

[195] H. C. Maru, D. T. Wasan, and R. C. Kintner. *Chemical Engineering Science*, 26:1615–1628, 1971.

[196] A. S. Geller, S. H. Lee, and L. G. Leal. *Journal Of Fluid Mechanics*, 169:27–69, 1986.

[197] O. Pitois, P. Moucheront, and C. Weill. *Comptes Rendus De L Academie Des Sciences Serie Ii Fascicule B-Mecanique Physique Astronomie*, 327:605–611, 1999.

[198] O. Pitois and X. Chateau. *Langmuir*, 18:9751–9756, 2002.

[199] H. Lamb. *Hydrodynamics*. Cambridge University Press, Cambridge, 1932.

[200] J. Happel and H. Brenner. *Low Reynolds number hydrodynamics*. Martinus Nijhoff Publishers, Dordrecht, 1986.

[201] O. Reynolds. *Philos. Trans. R. Soc. London*, 177:157, 1886.

[202] G. E. Charles and S. G. Mason. *J. Coll. Sc.*, 15:236, 1960.

[203] S. G. Yiantsios and R. H. Davis. *J. Fluid Mech.*, 217:547, 1990.

[204] B. H. Chen, B. Payandeh, and M. Robert. *Phys. Rev. E*, 62:2369, 2000.

[205] D. G. A. L. Aarts, J. H. van der Wiel, and H. N. W. Lekkerkerker. *J. Phys.: Condens. Matter*, 15:S245, 2003.

[206] D. G. A. L. Aarts, R. P. A. Dullens, and H. N. W. Lekkerkerker. *New J. Phys.*, 7:40, 2005.

[207] D. G. A. L. Aarts. *J. Phys. Chem. B*, 109:7407, 2005.

[208] D. G. A. L. Aarts. *The interface in demixed colloid-polymer systems: Wetting, waves and droplets*. PhD thesis, University of Utrecht, 2005.

[209] D. G. A. L. Aarts, H. N. W. Lekkerkerker, H. Guo, G. H. Wegdam, and D. Bonn. *Phys. Rev. Lett.*, 95:164503, 2005.

[210] R. Bergmann, D. van der Meer, M. Stijnman, M. Sandtke, A. Prosperetti, and D. Lohse. *Phys. Rev. Lett.*, 96:154505, 2006.

[211] A. N. Srdic-Mitrovic, N. A. Mohamed, and H. J. S. Fernando. *Journal of Fluid Mechanics*, 381:175–198, 1999.

[212] N. Abaid, D. Adalsteinsson, A. Agyapong, and R. M. McLaughlin. *Physics of Fluids*, 16:1567–1580, 2004.

[213] M. Manga and H. A. Stone. *Journal of Fluid Mechanics*, 287:279–298, 1995.

[214] H. J. Butt. *Journal of Colloid and Interface Science*, 166:109–117, 1994.

[215] L. Zhang, L. Ren, and S. Hartland. *Journal of Colloid and Interface Science*, 180:493–503, 1996.

[216] Y. Hennequin, D. G. A. L. Aarts, J. O. Indekeu, D. Bonn, and H. N. W. Lekkerkerker. *Phys. Rev. Lett.*, submitted, 2007.

[217] S. Tomotika. *Proc. R. Soc. Ser. A*, 150:322, 1935.

[218] S. Tomotika. *Proc. R. Soc. Ser. A*, 153:302–318, 1936.

[219] M. Moseler and U. Landman. *Science*, 289:1165, 2000.

[220] F. D. Rumscheidt and S. G. Mason. *J. Coll. Sc.*, 17:260269, 1962.

Summary

This thesis deals with the structure and dynamics at the boundaries of two colloidal model systems: colloidal hard spheres and colloid-polymer mixtures. A general introduction on these systems as well as the main technique used here, confocal laser scanning microscopy is presented in Chapter 1.

The remainder of the thesis consists of four main parts. In the first part, stacking disorder between the hexagonal close packed (HCP) and face centered cubic (FCC) structure is investigated (Chapters 2-4). The second part deals with geometrical frustration in hard sphere crystals (Chapters 5-7). The third part treats local height fluctuations of the 'gas-liquid' interface of a demixed colloid polymer mixture (Chapter 8). The final part deals with the transport of a rigid sphere through such interfaces (Chapters 9-11).

In the first part of this thesis we investigate transitions between the HCP and FCC structure within the hexagonal plane in close packed hard sphere crystals. This disorder occurs as a result of the availability of three different lateral positions A, B and C. We find two main types of transitions: discontinuous transitions with characteristic line-defects (Chapter 2) and continuous transitions through partial dislocations (Chapter 3). The full island boundary in fact consists of a mixture of continuous and discontinuous transitions. The island boundaries are furthermore characterised by a relatively high vacancy concentration, which points to a mechanism for the stabilization of lattice deformations. In Chapter 4 we find that the relative sizes of these 2D domains with HCP or FCC stacking are related to the fraction of FCC-stacked particles, which is related to the chance of two adjacent domains to have the same type of stacking during the formation of the crystal.

In the second part of this thesis the effect of geometrical frustration on crystallisation and crystal structure is investigated. The main sources of geometrical frustration studied are hard spherical impurities of which we vary the size ratio. In Chapter 5 we investigate the effect of these impurities on crystal nucleation and growth. If the impurity is small, the high curvature prevents nucleation from taking place. The curvature of impurities with a diameter of order 20 times larger than the spheres is sufficiently low to enable nucleation onto the sphere. Growth of crystals is affected as well: The higher the (local) impurity curvature, the lower the growth rates are near the impurity. In Chapter 6, we investigate a hard sphere crystal containing impurities. We can describe the extent of lattice frustration by the impurity with a frustration length, which characterizes up to what distance the crystal structure can 'feel' the impurity. If the

frustration zones of two nearby impurities overlap, defects such as grain boundaries can be trapped between the impurities. Moreover, during growth, these defects appear directly in between the impurities. In Chapter 7, we demonstrate that two different ways of geometrical frustration both significantly decrease the grain size in materials with colloidal crystals: (I) frustration due to a polyhedral particle shape stabilizes small crystal grains on a single particle level whereas (II) frustration by the introduction of impurities stabilizes small crystallites on the single grain level.

In the third part of this thesis the focus is shifted to the gas-liquid interface in colloid polymer mixtures. Due to the ultra-low interfacial tension, the height fluctuations can be tracked in time using confocal microscopy, which is the topic of Chapter 8. We find that the waiting time for a fluctuation of a certain critical height depends on the measurement interval, since the interface is fluctuating even on the smallest timescale. The results from this discrete time sampling are very well predicted in terms of the decay of the height-height correlation function, as we show using theory which is presented here along with the theory.

In Chapter 9, we present experiments on the approach of fluid droplets and rigid spheres, similar in size and composition, toward the colloidal gas-liquid interface. We find good agreement with theory, as the droplet approaches the interface slightly faster than the rigid sphere. Interestingly, close to the interface the approach velocities converge due to deformation of the droplet, which supports the idea that from a theoretical point of view the (simpler) drainage problem for rigid spheres already captures some of the physics.

In Chapters 10 and 11 we describe the observed transport configurations for the low Reynolds number passage of a sphere through the interface of a colloid polymer mixture, as a function of the Bond number, which is the ratio of gravitational and interfacial forces. The low ($Bo < 1$) and high ($Bo > 1$) Bond numbers are treated in Chapters 10 and 11. The low Bond number configuration is as follows: The spheres initially sediment at their Stokes velocity in the gas phase. Upon approach of the interface the spheres slow down. For larger spheres with $Bo > 0.1$ the interface deforms as well. Close to the interface a connection between the wetting film on the sphere and the interface is made, after which the sphere is dragged through the interface through the capillary force. After the sphere has detached from the interface, the sphere accelerates toward its bulk velocity in the second phase.

In the high Bond number limit, the spheres again initially sediment at their Stokes velocity in the gas phase. Upon approach of the interface the spheres slow down and the interface strongly deforms. At moderate Bond numbers of 2-3 the sphere leaves a V-shaped interface behind, which gradually recovers. At higher Bond numbers, the sphere leaves a long tail of colloidal gas material behind in the colloidal liquid phase. The column eventually breaks up in droplets through a Rayleigh-Plateau instability.

Samenvatting voor Iedereen

In dit hoofdstuk zal ik een poging doen om de inhoud van dit proefschrift op begrijpelijke wijze voor een algemeen publiek te presenteren. Het is belangrijk om je daarbij te realiseren dat het onderzoek vooral van fundamentele aard is. Dat betekent dat de vraag 'hoe werkt het nu eigenlijk' en daarom vergroting van de kennis het hoofddoel is. Aan de andere kant staan de fundamentele en meer toegepaste kanten van de colloïdwetenschap dicht bij elkaar. Voorbeelden voor een toepassing op de lange termijn zouden kunnen liggen in de fotonica, materiaalkunde of voedselchemie. Mijn belangrijkste drijfveer in deze jaren is echter de 'verbazing' over hoe de wereld in elkaar steekt geweest.

Genoeg over de aard van dit onderzoek. "Structure and Dynamics at Colloidal Boundaries" laat zich ruwweg vertalen in het Nederlands als 'Structuur en Dynamica bij Colloïdale Grensvlakken'. Ik zal colloïden introduceren, colloïdale fasen, en colloïdale fasegrenzen. Structuur en Dynamica slaan op het zowel bekijken van een instantane ordening van deeltjes, als naar de ontwikkeling van een dergelijke structuur in de tijd.

Colloïden zijn deeltjes met een afmeting tussen de miljoenste en een duizendste millimeter. Dat is zeer klein, maar aanzienlijk groter dan een atoom of doorsnee molecuul. Aan de andere kant zijn ze aanzienlijk kleiner dan zand. Wat deze deeltjes bijzonder maakt is dat ze net als atomen en moleculen onder invloed van temperatuur continu bewegen in de ruimte en niet als een blok naar beneden vallen door de zwaartekracht. Dat doen ze doorgaans in een (moleculaire) vloeistof als water of olie. De term "colloïden" wordt nauwelijks in het dagelijks leven gebruikt, maar toch komen ze veel voor om ons heen. Bekende voorbeelden zijn rode bloed lichaampjes, vele vormen van verf (pigmentdeeltjes in een vloeistof), zepen (micellen), melk, slasaus en mayonaise (oliedruppels in water).

Doordat colloïden in de ruimte rondzweven gaan ze op zoek naar hun 'thermodynamisch meest gunstige toestand' - de energetisch meest voordelige situatie. Dit kan net als voor atomen en moleculen een gas, vloeistof of kristal zijn. Dit maakt dat colloïden ook prachtige modelsystemen voor moleculaire systemen zijn, want ze hebben bovendien enkele aantrekkelijke eigenschappen: Ze zijn zacht, langzaam en zichtbaar. Daarmee bedoel ik het volgende. In tegenstelling tot atomen kunnen we colloïden met moderne microscopie technieken (zichtbaar) op deeltjes niveau volgen in de tijd (langzaam). Processen die in een atomair systeem binnen een fractie van een seconde plaatsvinden, kunnen in een colloïdaal systeem makkelijk minuten of uren duren. Daarnaast kunnen we de manier waarop ze elkaar aantrekken en afstoten afstellen naar wens

(zacht), bijvoorbeeld elektrische lading, magnetisme of deeltjesvorm. De experimenten die hier beschreven zijn maken van vooral de eerste twee aspecten optimaal gebruik. We gebruiken de confocale microscopie techniek. Met deze techniek kun je hele locale informatie zeer scherp in beeld krijgen. Door de focus te wijzigen kan zo zelfs een 3D beeld gereconstrueerd worden De deeltjes worden daarbij zichtbaar gemaakt door er een fluorescent verfje in te stoppen.

In dit proefschrift zijn experimenten aan twee van dit soort systemen beschreven: zogenaamde 'harde bollen' en colloïd-polymeer mengsels.

Om te beginnen de harde bollen. Dit zijn eigenlijk niet meer dan in de ruimte rondzwevende knikkers: ze stoten elkaar alleen af wanneer ze met elkaar in botsing komen. Toch kunnen ze een kristal vormen bij een voldoende hoge concentratie. Dit kun je ook zien gebeuren als je een knikkerpot geleidelijk met knikkers van dezelfde afmeting vult - hoe meer knikkers er inzitten, hoe meer de knikkers zich ordenen. Als je ze er allemaal tegelijk in stort, ontstaat echter een wanordelijke structuur, met een minder efficiënte pakking dan een dicht gepakt kristal, wat maar aangeeft dat de gunstigste toestand in realiteit lang niet altijd bereikt wordt. Bij lagere concentraties kunnen harde bollen zich vrij bewegen en vormen een wanordelijke vloeistof. Dit zijn de drie (vloeistof, glas, kristal) typen structuren waarin harde bollen voor kunnen komen, ook wel fasen genoemd.

Het andere modelsysteem dat in dit proefschrift beschreven wordt is een colloïd-polymeer systeem. hier zweven naast de knikkers ook polymeren in de vloeistof. Polymeren zijn zeer lange moleculen. In de vloeistof hebben ze doorgaans de gedaante van een wanordelijk kluwen. Door de aanwezigheid van deze kluwens, worden de knikkers naar elkaar toe geduwd als ze dicht bij elkaar in de buurt zijn. Dit gebeurt wanneer de knikker zo dicht bij elkaar in de buurt zijn dat er geen kluwen meer tussen past: de kluwens buiten deze 'verboden' zone duwen de knikkers naar elkaar toe. In het 'wetenschappelijks' heet dat depletie attractie. Deze vorm van attractie lijkt sterk op de aantrekking tussen moleculen. Het heeft tot gevolg dat colloïd-polymeer mengsels nog veel meer verschijningsvormen hebben dan harde bollen alleen. Bij voldoende hoge concentraties van zowel de knikkers als de kluwens kunnen deze systemen bijvoorbeeld ontmengen in twee wanordelijke fasen, één met vooral kluwens en één met voornamelijk knikkers. Dit zijn colloïdale equivalenten van een gas (lage concentratie wanordelijke bollen) en een vloeistof fase (hoge concentratie wanordelijke bollen).

Tussen deze fasen bevinden zich grensvlakken, zoals het grensvlak tussen lucht en water, olie en water, of tussen ijs en water. Dit is niet anders bij colloïden. Ze zien er zo op het oog zeer scherp uit, maar wanneer je met een zeer sterke microscoop het grensvlak zeer gedetailleerd in beeld brengt – wat door de grootte en de traagheid van colloïden kan – kun je, wordt al snel duidelijk dat het grensvlak een overgangsgebied is tussen de twee fasen. Daarnaast fluctueert de positie van het grensvlak in de tijd.

Deze aspecten komen allebei uitgebreid aan bod in dit proefschrift. Overigens is de verscheidenheid aan type grensvlakken veel rijker in de geordende kristalfase. Zo kunnen daar ook grenzen ontstaan tussen domeinen met een verschillend type stapeling (zoals in deel 1 van dit proefschrift) of tussen domeinen met een verschillende oriëntatie van het kristal (deel 2 van dit proefschrift).

Dit proefschrift is in vier delen onderverdeeld. De eerste twee delen gaan over kristallen van harde bollen. In deel drie en vier wordt het grensvlak van een ontmengd colloïd-polymeer mengsel bekeken.

Deel drie beschouwt de statistiek van hoogtefluctuaties, veroorzaakt door de temperatuur van het systeem. In deel 4 wordt gekeken naar bollen die door de zwaartekracht door het grensvlak heen vallen.

In deel één wordt gekeken naar de structuur van defecten binnen het harde bollen kristal, en dan met name naar de overgangen tussen twee vormen van de meest efficiënt mogelijk gepakte structuren: de zogenaamde 'hexagonal close packed' en 'face centered cubic' structuren, kortweg HCP en FCC. Theoretisch zijn ze energetisch zo goed als even gunstig, al kan uit de manier waarop het kristal groeit een duidelijke voorkeur naar één van de twee structuren ontstaan. Het blijkt dat er twee hoofdtypen van overgangen tussen beide structuren bestaan: abrupte overgangen (hoofdstuk 2), gekarakteriseerd door duidelijke lijndefecten in het kristal, en meer geleidelijke overgangen, die met het oog veel lastiger te detecteren zijn (hoofdstuk 3). We introduceren een aantal analysemethodes om deze 'fouten' in het kristal te detecteren, waarmee we kristallen goed kwantitatief kunnen analyseren, en meer leren over de totale defectstructuur. In hoofdstuk 4 worden de domeingroottes van de FCC en HCP structuren bekeken, en vergeleken met totale hoeveelheid aan FCC en HCP gestapelde deeltjes. Bij een relatief grotere hoeveelheid aan FCC gestapelde deeltjes, zijn de FCC domeinen ook groter dan de HCP domeinen. Dit kunnen we relateren aan het groeiproces van het kristal: als er meer domeinen met FCC ontstaan, dan is de kans dat ze tot een groter domein hercombineren ook groter.

Deel 2 beschrijft defectstructuren die ontstaan wanneer het kristal 'gefrustreerd' wordt. Dat betekent dat het kristal zijn structuur moet aanpassen, omdat de ordening belemmerd wordt. We veroorzaken deze frustratie door de toevoeging van een groter deeltje, of door de vorm van het deeltje veranderen van een rond naar een veelhoekig deeltje. In hoofdstuk 5 kijken we naar hoe zo'n grotere bol (als het ware een bonk in een zee van kleinere knikkers) de vorming van het kristal beïnvloedt. Daarbij kijken we naar twee fases: de vorming van zeer kleine kristalletjes uit de vloeistoffase, en de verdere groei van deze kristalletjes. De vorming van de kristalletjes wordt vanaf een grofweg 20 keer zo grote bonk bevorderd, voor kleinere bonken zie we dit niet. De groei van de kristalletjes in de buurt van de bonken wordt geremd. Hierbij is de kromte van

de bonk belangrijk. Hoe groter de kromte, dus hoe kleiner de bonk, hoe meer de kromming geremd wordt. In hoofdstuk 6 wordt bekeken hoe de uiteindelijke structuur in een kristal vol bonken eruit ziet. De gebiedjes met de zelfde oriëntatie, korrels genoemd, zijn veel kleiner in deze kristallen. Daarbij lopen de korrelgrenzen, die de grens vormen tussen gebieden met verschillende oriëntatie, zeer vaak tussen de bonken. De bonken stabiliseren kennelijk deze defecten. Hoe sterk de defecten gestabiliseerd worden, kunnen we bepalen aan de hand van een frustratie lengte van een bepaalde bonkgrootte. Daarvoor zijn twee effecten belangrijk: de destructie van orde door de kromming, en het vormen van kristallijne laagjes langs de bol. Het eerste vermindert de orde, het tweede vergroot de orde. Daarom vinden we een maximum van de frustratielengte bij een bonk die grofweg 13 keer zo groot is als de gewone knikkers. In hoofdstuk 7 vergelijken we het frustreren door toevoeging van bonken met de frustratie door veelhoekige deeltjes. Ondanks de compleet verschillende oorsprong van de frustratie vinden we een vergelijkbare structuur van kristallen met kleine korrelgroottes.

De laatste twee delen van het proefschrift zijn studies van fasegescheiden colloïd-polymeer mengsels. Deel 3 beschrijft de spontane hoogtefluctuaties van het grensvlak, veroorzaakt door de temperatuur. Deze fluctuaties zijn bijvoorbeeld belangrijk voor het voorspellen van de samensmelttijd van druppels. We kijken daarbij naar de zogenaamde wacht- en verblijfstijden voor een fluctuatie van een bepaalde hoogte. Deze tijden geven de gemiddelde tijd tussen twee van zulke fluctuaties in en de gemiddelde duur van een dergelijke fluctuatie aan. Onze bevindingen tonen aan dat deze tijden lastig te voorspellen zijn: ze zijn namelijk afhankelijk van het tijdsinterval waarmee we meten. We kunnen ze echter wel zeer goed voorspellen voor een gegeven intervaltijd, waarbij we alleen gebruik maken tussen de correlatie (samenhang) tussen twee opeenvolgende hoogte metingen.

In het laatste deel van het proefschrift bekijken grote bollen, die door de zwaartekracht zakken door een fluctuerend grensvlak. In hoofdstuk 9 wordt de nadering van bollen vergeleken met de nadering van druppels. Volgens de theorie vallen druppels (relatief) sneller doordat er binnen de druppel vloeistofcirculatie plaatsvindt en onze experimenten bevestigen dat.

Dankwoord

In dit gedeelte van het proefschrift wil ik graag iedereen bedanken die op zijn of haar manier heeft bijgedragen aan dit proefschrift.

Henk, ik heb ongelooflijk veel vrijheid gekregen (wellicht ook wel genomen) wat betreft de invulling van dit proefschrift. Met als gevolg behoorlijk uiteenlopende onderwerpen. Op sommige punten heeft dat de diepgang wellicht belemmerd, maar zeker niet overal. Ik bewaar dan ook uitstekende herinneringen aan de langdurige sessies met u en Hans van Leeuwen over het huidige hoofdstuk 8. U bent een zeer betrokken begeleider met het vermogen om in een oogopslag de zwakke punten in een manuscript te duiden. Ik heb menigmaal versteld gestaan als u weer een antiek manuscript uit een van uw laatjes viste: uw kennis van de oude literatuur is fenomenaal.

Andrei(tje), weinigen kunnen zeggen dat ze jarenlang kamergenoot(je) zijn geweest van hun compromotor(tje)! Op de dag dat ik langs je beeldscherm(pje) liep en daar een plaatje van een bolstapeling(etje) zag, kon ik niet vermoeden dat een opmerkinkje van mijn kant(je) ('Dat zie ik ook onder mijn microscoop') uiteindelijk zou resulteren in het eerste deel(tje) van dit proefschrift(je) en de inmiddels vele gemeenschappelijke publicatie(tje)s. Je enthousiasme(tje) is meeslepend: het is altijd een groot plezier(tje) om met je te werken.

Willem, tijdens mijn eerste jaar kwam jij (als copromotor, maar dat niemand je kennelijk toen nog verteld) met het idee voor een eerstejaars project. Dit heeft uiteindelijk geleid tot wat nu deel 2 van dit proefschrift is. Ook dat hadden we toen nooit kunnen vermoeden. Tijdens een impulsieve brainstormsessie weet je regelmatig een wilde link te leggen naar een ander vakgebied. Ik vertrok dan ook iedere keer vol goede moed en nieuwe ideeën na zo'n bijeenkomst. Ook de lachsessies met Paul van der Schoot erbij zal ik niet snel vergeten: ik was welliswaar nooit aanwezig bij die ontmoetingen, maar het gelach bulderde op zo'n vrijdagmiddag dan zo hard en aanstekelijk door het hele lab, dat er geen ontkomen aan was. Vergelijkbare taferelen vonden overigens plaats bij het 'kale gozer' incident. Daarnaast blijkt je huis ook bijzonder geschikt voor het creëren van sigaren walmen tijdens de whiskey proef avonden. Wordt je nieuwe huis ook zo ingehuldigd?

De Stichting voor Fundamenteel Onderzoek der Materie heb ik in deze jaren leren kennen als een uitzonderlijk professionele en betrokken werkgever, die in alle fasen van de promotie er actief naar streeft hun werknemers zoveel mogelijk breed te ontwikkelen en een goede basis voor hun verdere carrière mee te geven.

Een bijzondere dank ben ik ook verschuldigd aan Dirk Aarts en Roel Dullens. Ik had me geen enthousiaster collega's kunnen wensen om het pad voor me te banen en mij als het ware te lanceren. Jullie zijn altijd betrokken geweest bij de diverse onderwerpen die ik tijdens mijn promotie aangesneden heb, ook nadat jullie uit het lab vertrokken waren. Ook buiten het lab waren het goede tijden. Ik hoop snel weer eens in Oxford langs te komen voor een pint/cassis - de monsters stuur ik voortaan per post. Dirk, je bent daarnaast schuldig aan mijn inwijding in de 'wondere wereld der colloïden' tijdens mijn bijvak: ik had het daar niet beter kunnen treffen.

Veel van de resultaten die dit proefschrift gehaald hebben zijn tot stand gekomen in samenwerking met een of meerdere studenten. Om te beginnen waren er natuurlijk de eerstejaars Esther Groeneveld en Hans Scherff, die mijn gehele promotietraject eigenlijk overhoop gegooid hebben: een synthese waar een groot assortiment van wel heel grote bollen uit voortkwamen. De gevolgen ervan had ik op dat moment nooit kunnen voorspellen. Ze verschijnen in dit proefschrift in maar liefst zes van de tien hoofdstukken: het is maar dat jullie weten wat je op je geweten hebt. Ook de daarop volgende eerstejaars projecten, dat van Chris Evers en Anika Jonker en dat van Sander Filon en Micah van der Vaart, heb ik met veel plezier begeleid. Mijn Bachelorstudenten Danny Verboekend, Leonie Derendorp, Janne-Mieke Meijer, Anke Leferink op Reinink en Jos van Rijssel en Masterstudent Julius de Folter kwamen allemaal met uitstekend materiaal. Danny, jij was mijn eerste student. Je nucleatie experimenten leiden nog steeds tot enthousiaste reacties. Leonie, ik hoop dat je ondanks alles uiteindelijk terugkijkt op een succesvolle periode. Janne-Mieke, wat jij in 3 maandjes voor elkaar hebt gebokst, gedreven door een grenzeloze nieuwsgierigheid en motivatie, is fenomenaal. Julius, ik had me geen betere master-student kunnen wensen. Je oog voor detail en georganiseerdheid zullen je ongetwijfeld nog veel succes brengen. Ik weet niet of je ooit nog mij zult vertrouwen om je samples mee naar Oxford te nemen. Anke, het is heerlijk om zo'n flapuit als studente te begeleiden – zeker als het er een is die het daarnaast ook nog eens goed doet. Jos, ik heb zelden een student zo eigengereid bij zijn bijvak het lab in zien stappen. Naast deze studenten heb ik ook met veel plezier bijgedragen aan de studentenprojecten van Piter Miedema en Matti van Schooneveld. Piter - de volgende keer dat ik je in de stad tegenkom graag in niet-beschadigde toestand. Matti - ik bewaar nog uitstekende herinneringen aan onze 'gezellige' trip naar Milaan en ik wens je veel succes met jouw promotie.

De mannen van de glasblazerij en de instrumentmakerij stonden altijd klaar voor het ontwerpen en smeden van diverse microscoop-attributen: ook jullie ben ik veel dank verschuldigd! Daarnaast was de audiovisuele dienst onder leiding van Jan den Boesterd altijd plezierig om mee samen te werken – jammer dat jullie van de zevende zijn vertrokken.

Mijn kamergenoten door de jaren heen – naast Andrei waren dat Annemieke ten Brinke, Mark "Chanceless Klokko" Klokkenburg, Daniela "Frau" Kraft en Jan 'Lederhose' Hilhorst – bedank ik voor de gezelligheid, discussies, grappen, lunchpauzes en wat al niet meer. Annemieke, je had altijd een luisterend oor. Mark, ik ben persoonlijk van mening dat we die whiskyavond (daar is ie weer) er toch echt in moeten houden. Daniela, ik vrees dat je regelmatig het slachtoffer van onze flauwe grappen bent geweest – van het luchtalarm tot het 'efficiënte' Duitse virus – maar je bent een fantastische collega. Jan, het is goed om zo'n enthousiaste collega verder te zien werken aan kristaldefecten met Andrei: veel succes en ik ben benieuwd naar de resultaten!

Maar ook de overige collega's door de jaren heen wil ik bedanken: op het van't Hoff lab is niemand te beroerd om elkaar verder te helpen wat een uitstekende werksfeer oplevert. Daarbij wil ik in ieder geval generatiegenoten Karel Planken, Stefano Sacanna, Maria Claesson en Alan Wouterse noemen en daarnaast Maurice Mourad, Lia Verhoeff, Nikoleta Simeonova, Mircea Raşa (vocabular romaneşte), Emile Bakelaar, Bonny Kuipers, Chantal Vonk en Martijn Oversteegen noemen, maar natuurlijk ook alle anderen.

Een van de grote voordelen van het bedrijven van de colloïdkunde te Utrecht is de aanwezigheid van de Soft Condensed Matter groep. Daarbij denk ik in eerste instantatie aan het tweezeren van de grote bollen met Esther Vermolen. De experimenten zijn nooit helemaal tot wasdom gekomen, maar ik heb er desalniettemin behoorlijk wat van geleerd. Daarnaast was het altijd gezellig met Didi, Carmen (& Toni!), Mirjam (kinderliedjes zingen in Han-sur-Lesse), Teun (Als het voor ons in de wetenschap niet lukt kunnen we altijd nog reisleiders op Corsica worden), Eduardo (thanks for the Spanish holiday tips), Job en alle anderen.

Ook van buiten de universiteit Utrecht heb ik van vele kanten hulp gekregen. Zonder de Leidse tandem Hans van Leeuwen en Wim van Saarloos had hoofdstuk 8 dit proefschrift nooit gehaald. Dat de theorie zo goed met het experiment zou overeenkomen, hadden we van tevoren nooit kunnen bedenken. Daarnaast is er ook voor Peter Schall, Salima Rafaï en Yves Hennequin in Amsterdam een dikke merci. Thomas Bickel, merci pour tout tes idées! Furthermore I am grateful to Paul Bartlett, Roland Roth, Paul Millett and David Nelson for insightful discussions.

Voor de 7^{de} verdieping heb ik met veel plezier met Chantal Christis en Mayken Wadman BBQ's georganiseerd. Els de Hoog, Jan Klok en Hans Tromp, bedankt voor de aangename tijd tijdens de metingen op het NIZO.

Dan een woord voor mijn vrienden en familie. Als ik iemand vergeet te noemen dan spijt mij dat – ik ben immers behoorlijk verstrooid.

To my 'Norwegian' friends I say tusen takk, det var kjempegøy!. Astrid en Wouter, zonder jullie (en de kinderschare) had ik mijn lieve meisje natuurlijk nooit leren kennen! Maar los daar van staan jullie altijd klaar voor ons. Geweldig!

Trupa din România, Neta, Oana, Claudiu, Teo, Alexică, Oana, Ina, Edi, Ana, Johanna, Eva, Oriana, Wim şi Maud şi alţii, acum am timp pentru a studia romaneşte, nu mai am nici o scuză!

Daan, Stefan, Thijs en Lars, ik bewaar met name goede herinneringen aan onze jaarclubtrip naar Ierland, maar ook aan de vele andere bijeenkomsten. De Utrechtse vriendenkring: Judith, Martin, Dirk, Elles, Marjolijn, Rudy, Chantal, Birgit, Sipke, Suzanne, Hanneke, Martijn, Bjorn, Mieke, Mara, Raoul, Johan, Marije en alle anderen – het was altijd goed bijkomen met jullie, of het nu op weekendje weg, in de kroeg, bij een hapje eten of bij een concert was. Simone, het is wel heel bizar dat wij zonder het met elkaar af te spreken op dezelfde middag promoveren. Rudy en Hanneke, bedankt dat jullie vandaag mijn paranimfen willen zijn. Dat we er nog maar regelmatig op mogen proosten!

Bart (+Josine, Evy en Saartje), Jan (+Kelly), Jeroen (+Lizette), Oliver, Nicolas (+Kim) en Hugo: onze vriendschappen gaat heel ver terug. We kunnen elkaar tijden niet zien en toch is het altijd als vanouds. Dat is heel waardevol.

Onze kat Tonks, sorry dat ik je zo vaak van het toetsenbord gemept hebt toen je er demonstratief op ging zitten tijdens het schrijven van dit proefschrift. Het heeft me wellicht van de RSI gered.

Ik heb het geluk een zeer hechte en betrokken familie te hebben: dat is een voorrecht. En Maria, daar mag jij je ook toe rekenen.

Opa, u stak nooit onder stoelen of banken dat u vond dat ik na mijn studie serieus over een promotietraject moest denken. Ik wilde er destijds niets van weten. Des te trotser ben ik dat u bij mijn verdediging aanwezig zult zijn. Oma, u heeft mij gelukkig nooit verteld dat u vond dat ik moest promoveren, maar betrokken was u altijd. Ik ben er net zo trots op dat ook u er bij zult zijn.

Bogdan şi Laura, am obţinut frate şi sora. Virgil şi Elena, tatul meu şi mama mea, sunteţi tare dulci. Vą port mereu în inima.

Pappa, Mamma, Erwin & Wendy, Marie-Louise en Roseline & Luca. Ik heb niet veel tijd voor jullie gehad het laatste half jaar, maar jullie hebben me altijd door dik en dun gesteund. Jullie zijn me enorm dierbaar.

Gabriela Cristina, soţia mea dragă cu ochi frumoşi. Sunt foarte mândru de noi. Nu ai idee cât de mult m-ai ajutat tu cu teza aceasta. Mulţumesc pentru tot, tigroaica mea, tu ai fost cu mine tot timpul.

Curriculum Vitae

De schrijver van dit proefschrift is geboren op 20 februari 1979 in Leidschendam. In 1997 behaalde hij het gymnasium diploma aan het Christelijk Gymnasium Sorghvliet (cum laude) en studeerde hij een jaar Engineering aan Queen's University in Kingston, Ontario, Canada. Het jaar daarop begon hij met de studie Scheikunde aan de Universiteit Utrecht. Het propedeuse examen werd een jaar later behaald. In 2004 legde hij het doctoraalexamen scheikunde af met als hoofdvak anorganische chemie en een bijvak fysische en colloïd chemie, behorende tot het Debye instituut. Per 1 januari 2004 trad hij in dienst van stichting FOM (Fundamenteel Onderzoek der Materie) als onderzoeker in opleiding (OIO). Hij deed zijn promotieonderzoek in het van't Hoff Laboratorium voor Fysische en Colloïd Chemie, behorende bij het 'Debye Institute for nanomaterials', onder begeleiding van prof. dr. H.N.W. Lekkerkerker, prof dr. W.K. Kegel en dr. A.V. Petukhov. De resultaten van dit onderzoek zijn beschreven in dit proefschrift.

Resultaten van dit proefschrift werden onder meer gepresenteerd in Lunteren (Wetenschappelijke Vergadering Statistische Fysica, 2005), Utrecht (6^{th} Liquid Matter Conference, 2005), Obergurgl (Solid/Fluid Interfaces, Oostenrijk, 2006), Carghèse (Colloids in External Fields Summer School, Corsica, 2006), Veldhoven (Physics@FOM, 2007), Grenoble ($10^{\text{ème}}$ Colloque SFmu, uitgenodigigd spreker, Frankrijk, 2007) en Aken (International Soft Matter Conference, Duitsland, 2007).

Sinds 1 januari 2008 is hij als post-doctoraal medewerker verbonden aan het van't Hoff Laboratorium voor Fysische en Colloïd Chemie aan de Universiteit Utrecht.

Resumé

The author was born on February 20, 1979 in Leidschendam. He graduated from high school in 1997 at 'Christelijk Gymnasium Sorghvliet' (cum laude), a grammar school. In the subsequent year he studied Engineering at Queen's university, Ontario, Canada, before he started his chemistry studies in 1998 at the Universiteit Utrecht in the Netherlands. He obtained his Masters degree in inorganic chemistry in 2004 with a bachelor in physical and colloid chemistry. As of january 2004 he started his PhD under supervision of prof. dr. H.N.W. Lekkerkerker, prof. dr. W.K. Kegel and Dr. A.V. Petukhov. The project was financed by the FOM foundation (Stichting voor Fundamenteel Onderzoek der Materie - Foundation for Fundamental Research of Matter) and carried out at the van't Hoff laboratory for physical and colloid chemistry. The results of this project are described in this thesis and were amongst others presented in Lunteren, the Netherlands (Wetenschappelijke Vergadering Statistische Fysica, 2005), Utrecht, the Netherlands (6^{th} Liquid Matter Conference, 2005), Obergurgel, Austria (Solid/Fluid Interfaces, 2006), Carghèse, Corse (Colloids in External Fields Summer School, 2006), Veldhoven, the Netherlands (Physics@FOM, 2007), Grenoble, France ($10^{\text{ème}}$ Colloque SFmu, invited speaker, 2007) and Aachen, Germany (International Soft Matter Conference, 2007).

As of the january 2008 he is a post-doctoral fellow at the van't Hoff laboratory for physical and colloid chemistry in Utrecht, the Netherlands.

Color figures

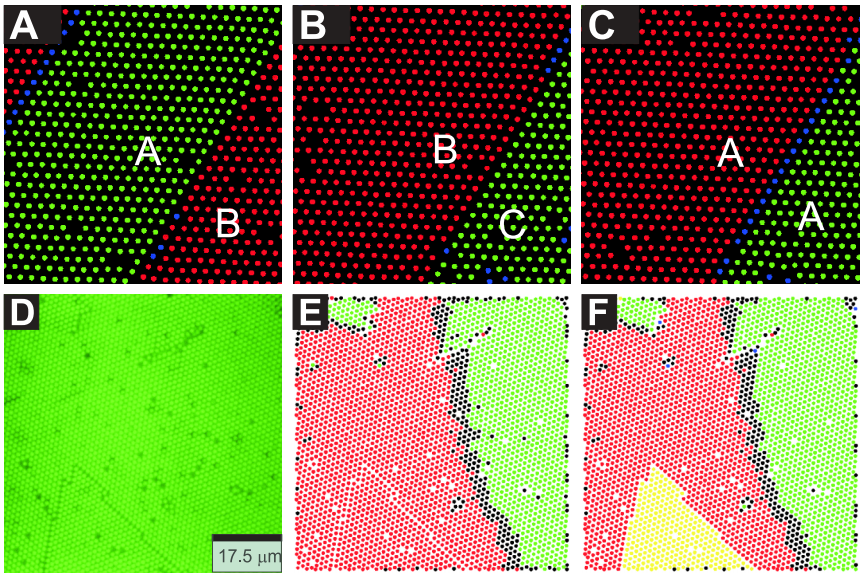

Figure 2.6

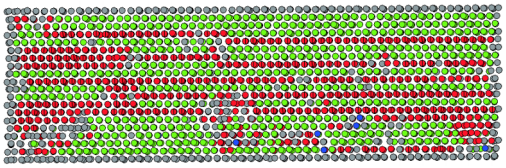

Figure 2.7b

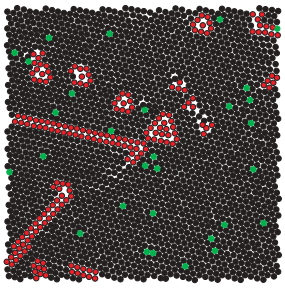

Figure 2.9b

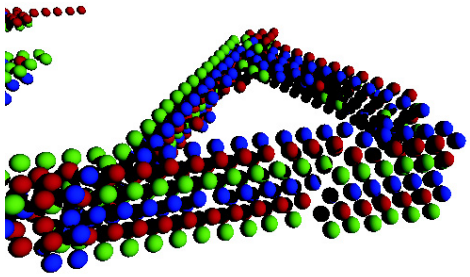

Figure 2.10a

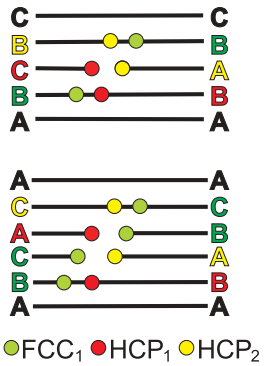

Figure 2.10b

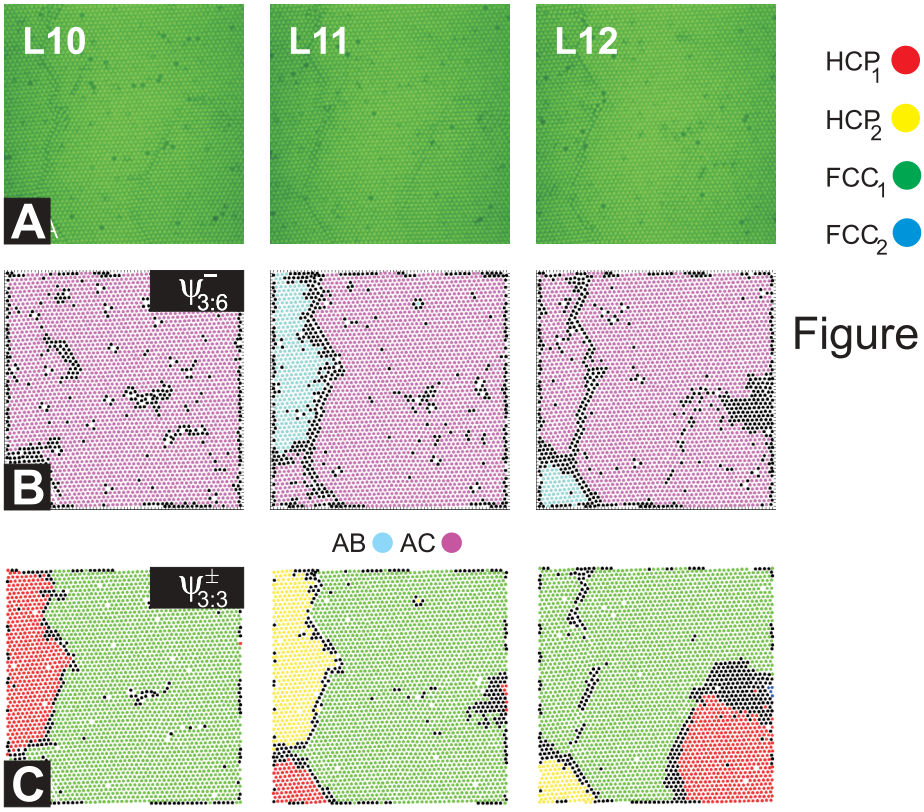

Figure 3.7

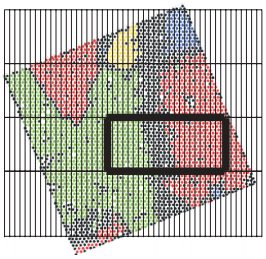

Figure 3.8b

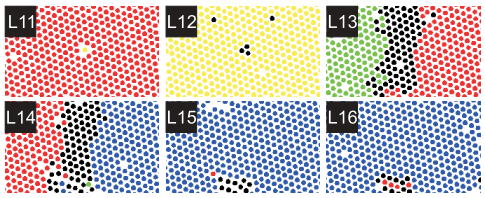

Layer	Lat	Stack
L10	A- A'	
L11	B-B'	H1-H1
L12	A-A'	H2-H2
L13	**B-B'**	**F1-H1**
L14	**C~A'**	**H1~F2**
L15	B-C'	F2-F2
L16	A-B'	F2-F2
L17	C-A'	

Figure 3.9

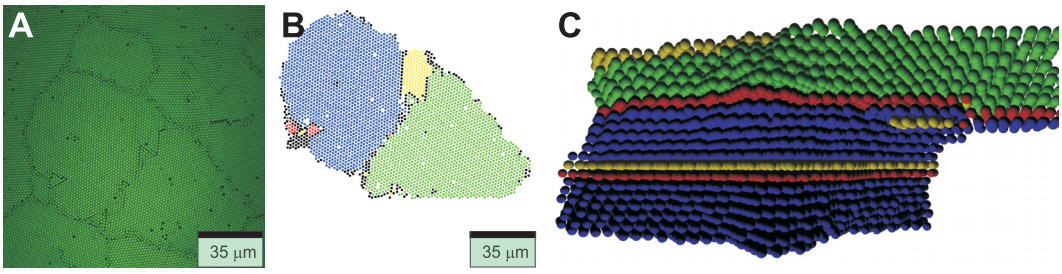

Figure 4.2

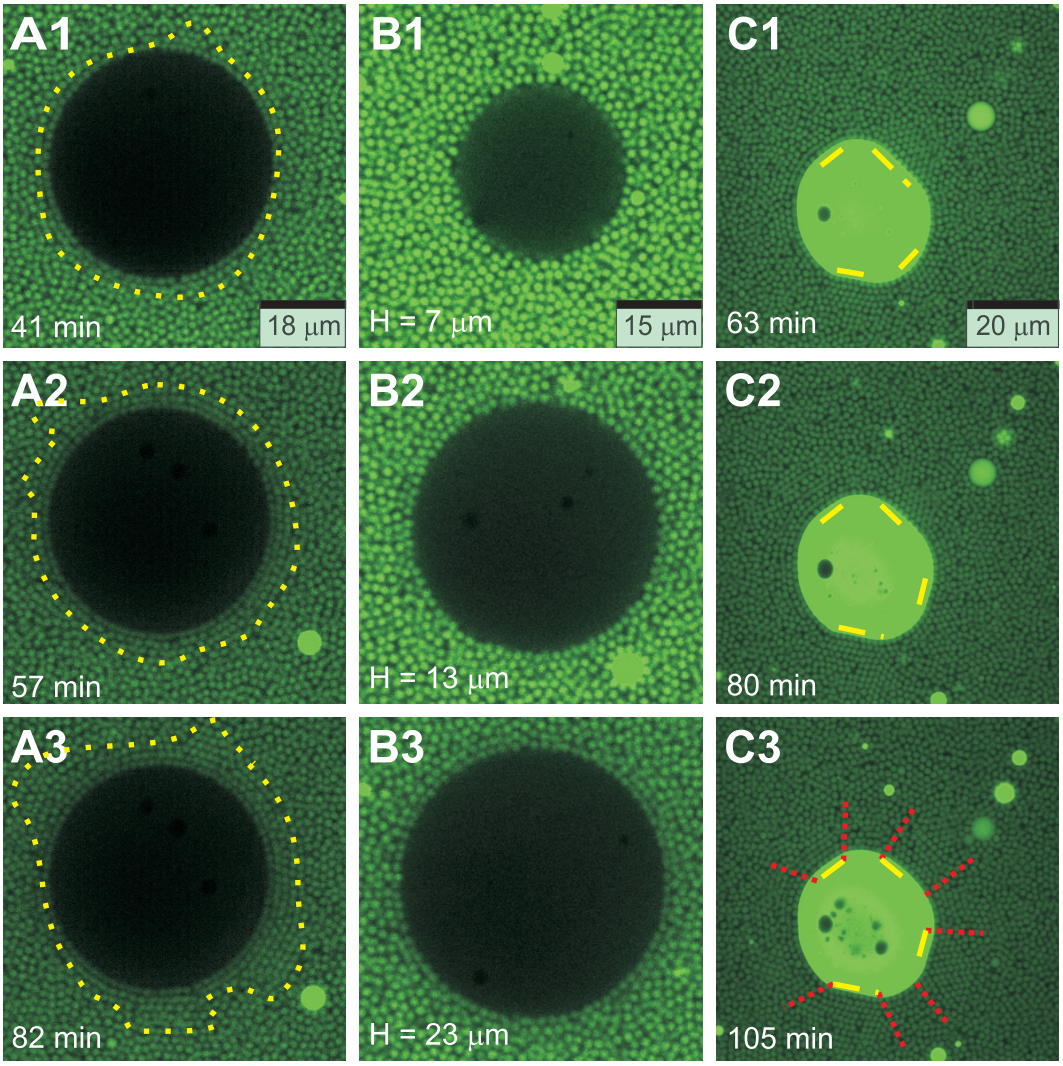

Figure 5.4

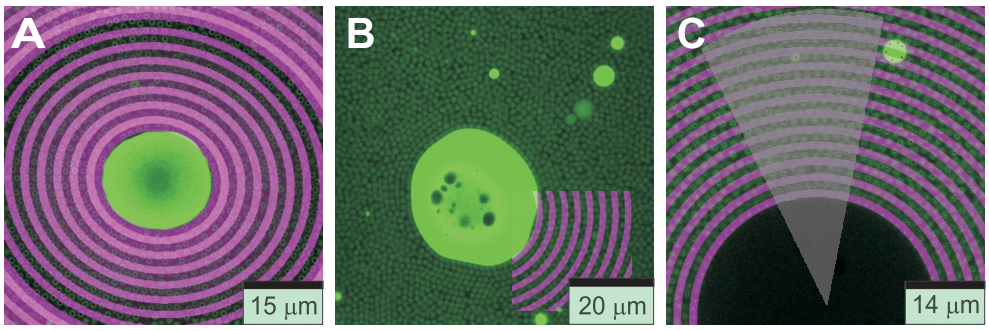

Figure 5.5

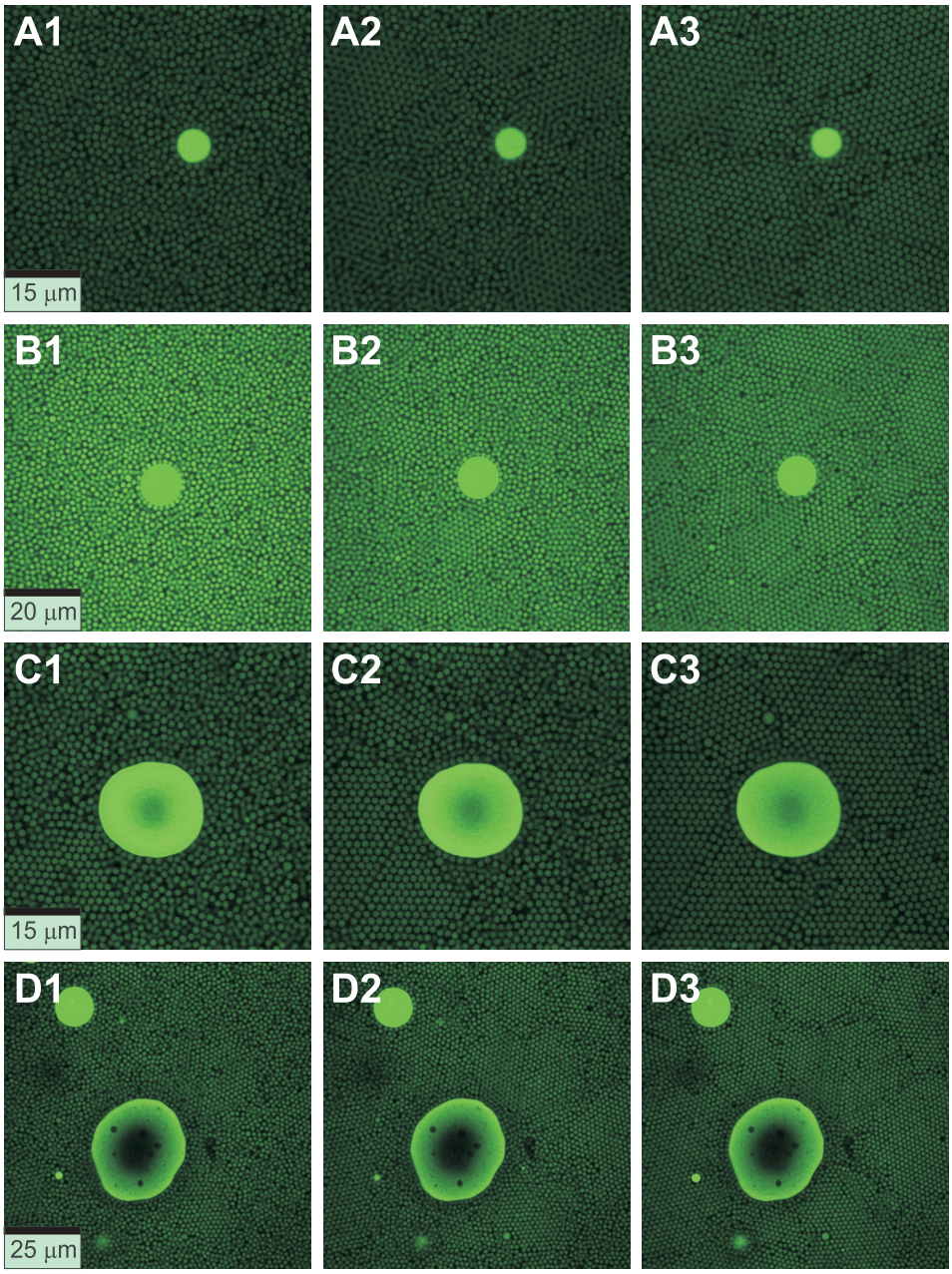

Figure 5.4

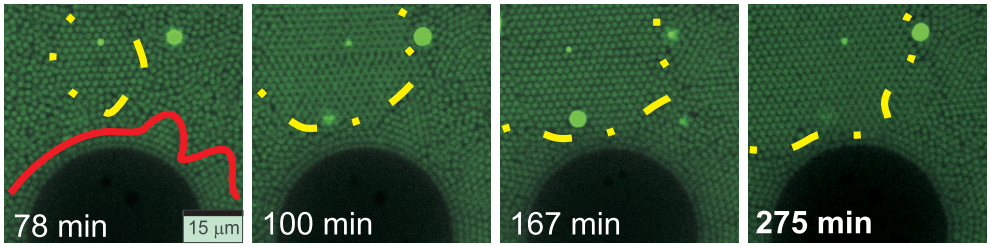

Figure 5.9

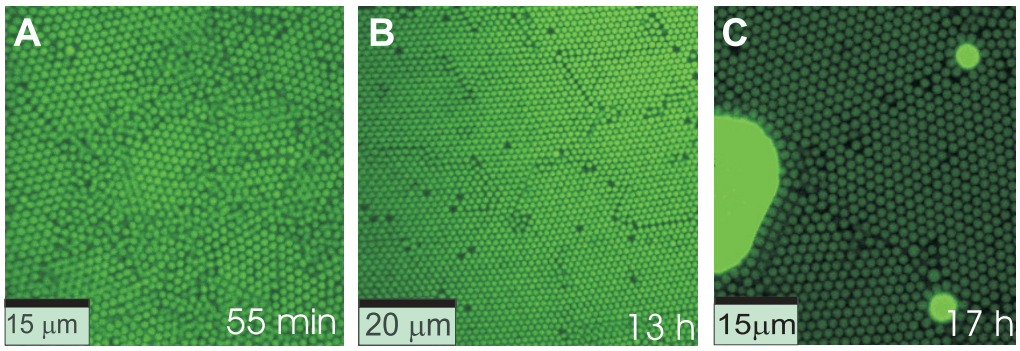

Figure 6.1

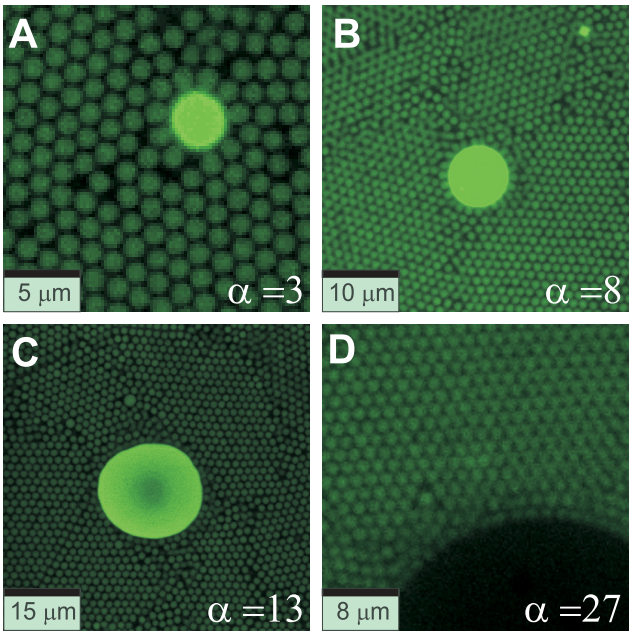

Figure 6.2

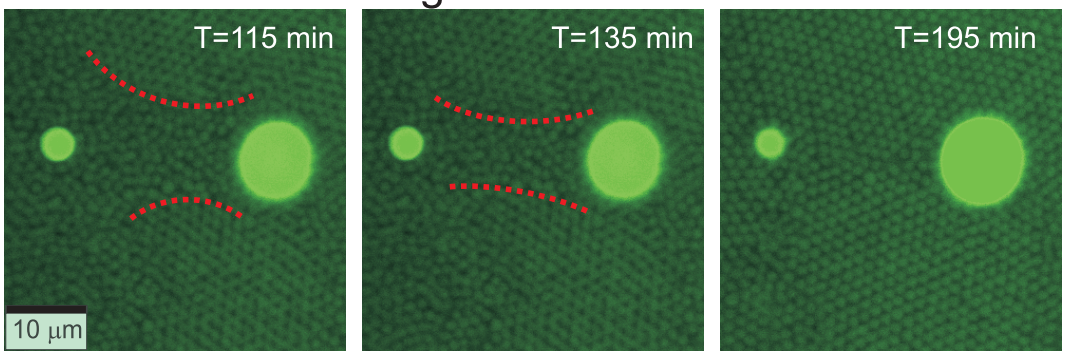

Figure 6.6

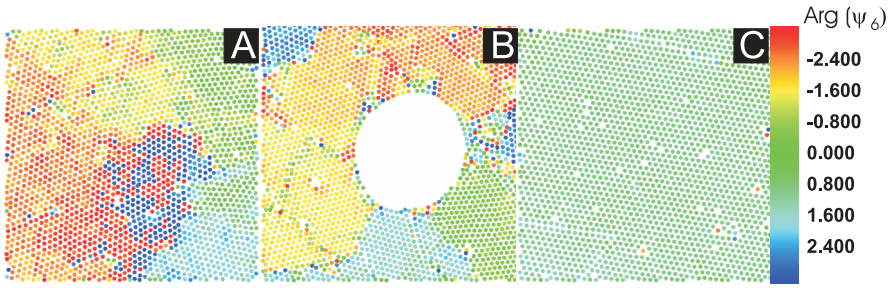

Figure 7.5

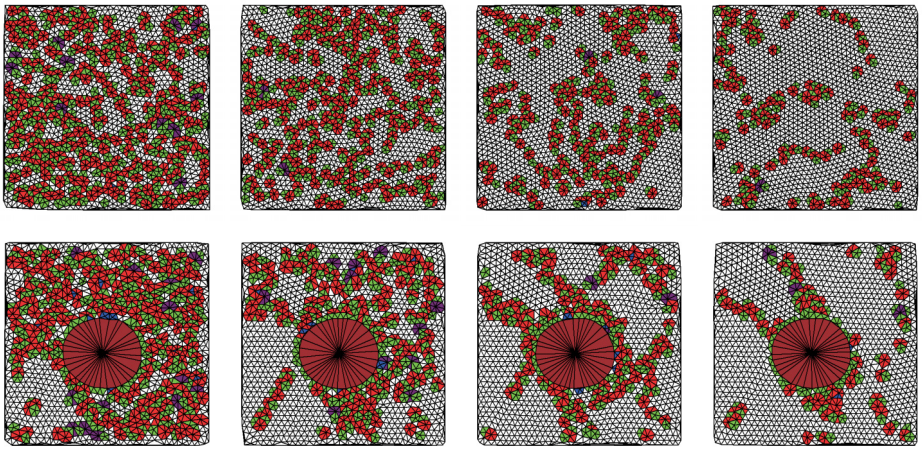

Figure 7.6

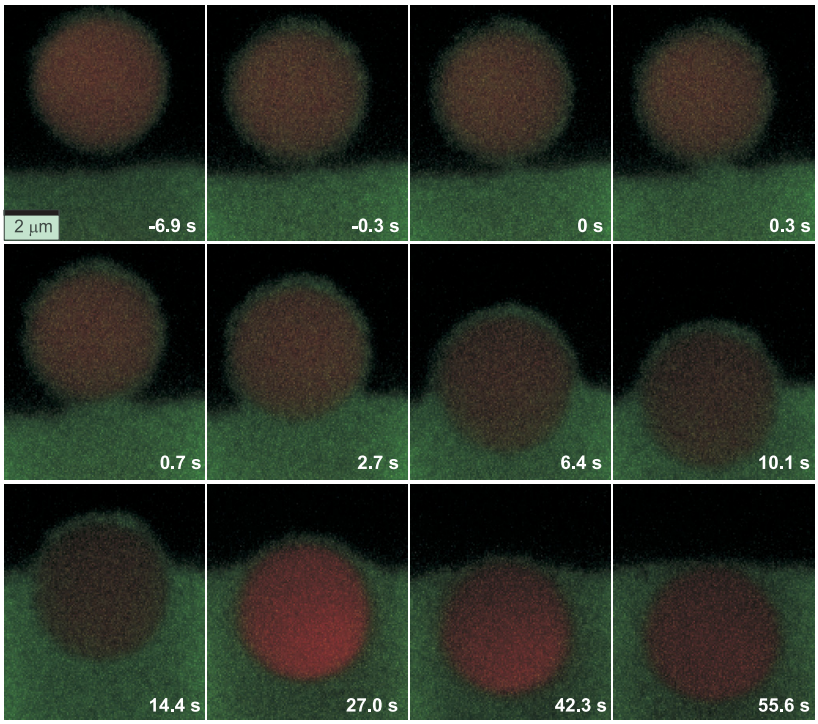

Figure 10.9

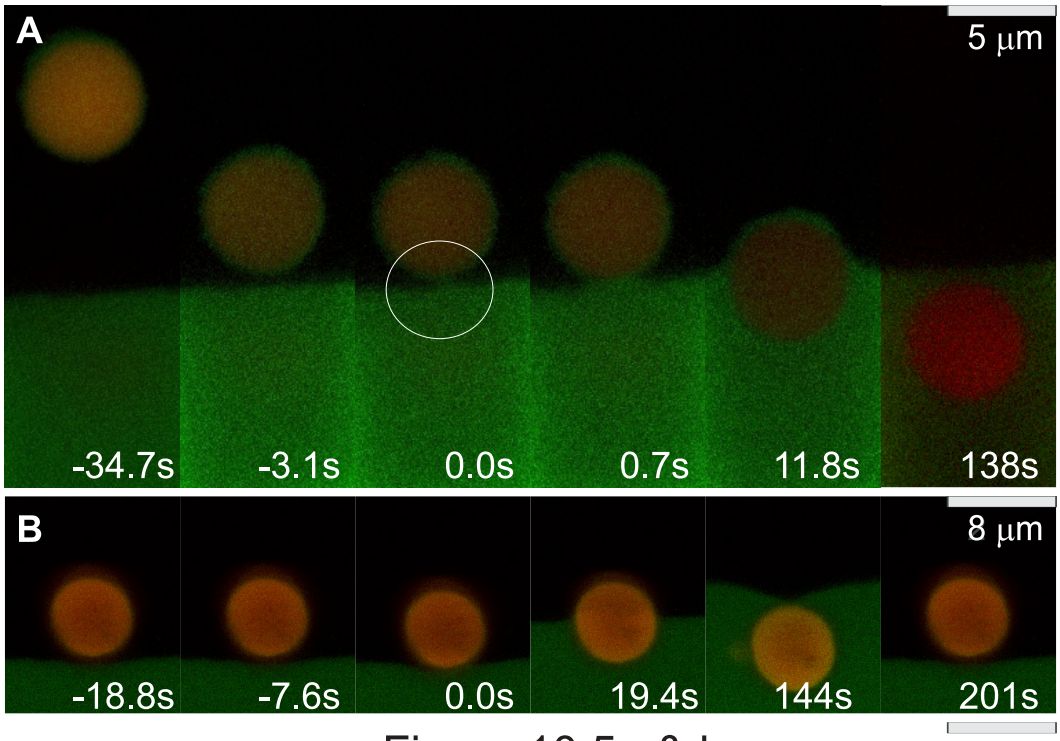

Figure 10.5a & b

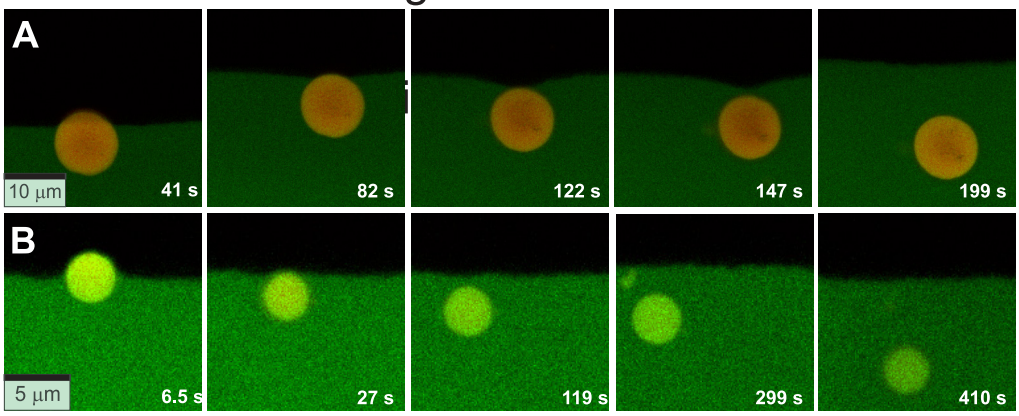

Figure 10.12

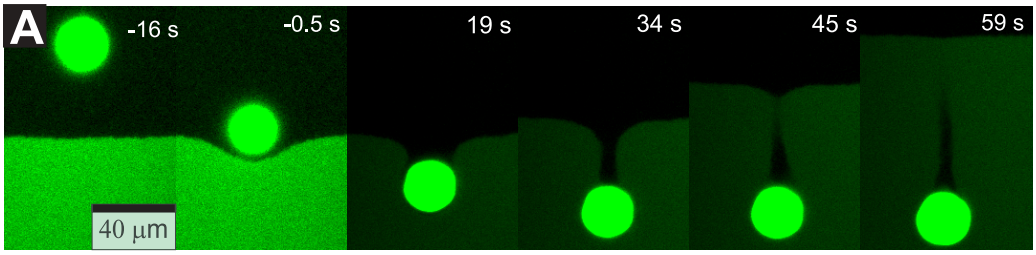

Figure 11.5a

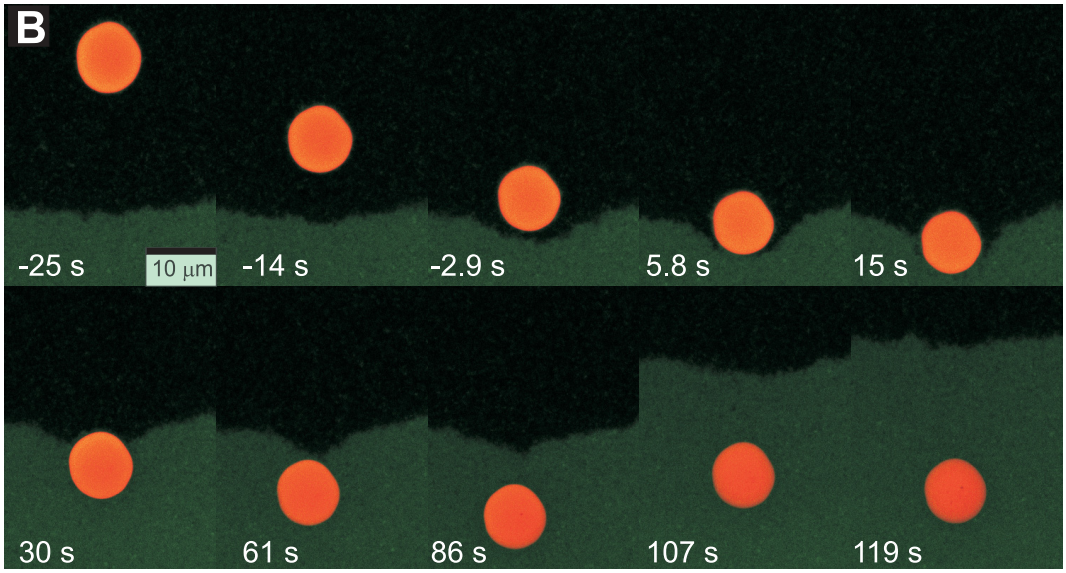

Figure 11.3b

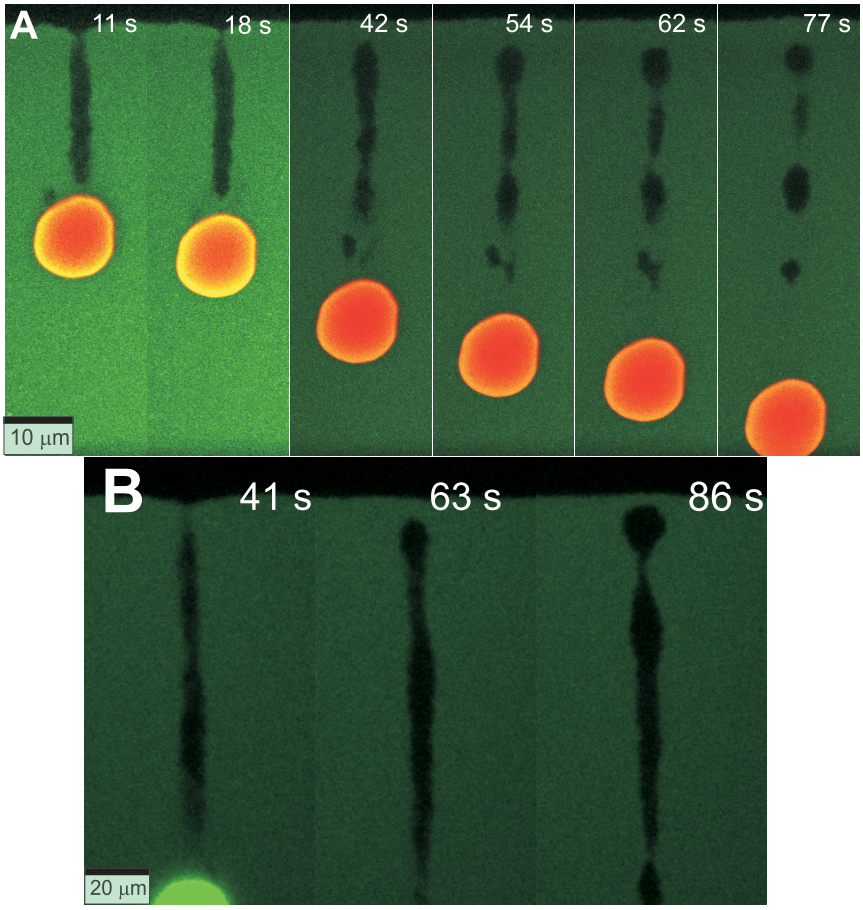

Figure 11.6